UNIVERSITY OF CAPE TOWN

PhD THESIS

PHYSICAL AND BIOGEOCHEMICAL PROPERTIES OF SEASONAL SEA ICE IN THE ATLANTIC SECTOR OF THE ANTARCTIC MARGINAL ICE ZONE

Author:
Riesna R. **AUDH**

Supervisors:
Prof. Marcello **VICHI**
A/Prof. Sarah E. **FAWCETT**

A thesis submitted in fulfilment of the requirements

for the degree of Doctor of Philosophy

in the

Department of Oceanography

November 2024

This page is intentionally left blank

Declaration of Authorship

I, Riesna R. AUDH, declare that this PhD thesis titled, "Physical and Biogeochemical Properties of Seasonal Sea Ice in The Atlantic Sector of The Antarctic Marginal Ice Zone" and the work presented in it are my own. I confirm that:

- This work was done wholly or mainly while in candidature for a research degree at this University.
- Where any part of this thesis has previously been submitted for a degree or any other qualification at this University or any other institution, this has been clearly stated.
- Where I have consulted the published work of others, this is always clearly attributed.
- Where I have quoted from the work of others, the source is always given. With the exception of such quotations, this thesis is entirely my own work.
- I have acknowledged all main sources of help.
- Where the thesis is based on work done by myself jointly with others, I have made clear exactly what was done by others and what I have contributed myself.

Student Name:	**Riesna R. Audh**	**Student Number:**	**ADHRIE001**
Signature:		**Date**:	

This page is intentionally left blank

Declaration on the Inclusion of Publications

I, Riesna R. AUDH, confirm that I have been granted permission by the University of Cape Town's Doctoral Degrees Board to include the following publication(s) in my PhD thesis, and where co-authorships are involved, my co-authors have agreed that I may include the following publication(s) in my PhD thesis:

1. **Audh, R.R.**, Fawcett, S.E., Johnson, S., Rampai, T. and Vichi, M., 2023. Rafting of Growing Antarctic Sea Ice Enhances In-Ice Biogeochemical Activity in Winter. *Journal of Geophysical Research: Oceans*, 128(12), p.e2023JC019925.
2. Johnson, S., **Audh, R.R.**, de Jager, W., Matlakala, B., Vichi, M., Womack, A. and Rampai, T., 2023. Physical and morphological properties of first-year Antarctic sea ice in the spring marginal ice zone of the Atlantic-Indian sector. *Journal of Glaciology*, pp.1-14.

Student Name:	**Riesna R. Audh**	**Student Number:**	**ADHRIE001**
Signature:		**Date**:	

This page is intentionally left blank

“Here was a crystalline world of azure and emerald, indigo and alabaster - dazzling to the eye, disturbing to the soul.”

P. Berton, describing the Ross expedition’s first encounter with sea ice, 1818.

This page is intentionally left blank

Abstract

The study of Antarctic sea ice biogeochemistry has largely focused on samples collected from pack ice during summer, with few winter data available. Measurements from the Antarctic marginal ice zone (AMIZ) have proven even more difficult to obtain. The AMIZ is a broad, circumpolar feature of the Southern Ocean where sea ice begins to form during winter. The incorporation of seawater during sea-ice growth along with chemical and biological processes operating within the ice results in a complex biogeochemical environment within the sea ice matrix. This thesis presents the first biogeochemical datasets for sea ice collected in the Atlantic AMIZ during winter and spring, including measurements from young pancake ice, consolidated first-year ice and brash ice. It also proposes a revised set of standard operating procedures for conducting interdisciplinary sampling in complex marginal ice conditions. Measurements of sea-ice temperature, salinity, crystal structure, $\delta^{18}O$, chlorophyll and nutrient concentrations were combined with model simulations to decipher the conditions under which the ice formed and grew, how these conditions influenced the subsequent biogeochemical environment and how the sea-ice properties evolved from winter to spring. Our findings confirm that winter sea ice is biologically active and further suggest that the growth of sea ice in the AMIZ is not a linear progression of thickness with habitat space reduction as sea ice consolidates. Instead, sea ice consolidates and thickens as a result of multiple cycles of breaking and rafting of young ice, and the biogeochemical signatures of the young ice are conserved in the reformed, consolidated ice cover. Novel nitrate and particle δ^{15}N measurements enabled us to investigate the seasonal evolution of sea-ice nitrogen cycle dynamics in the AMIZ, revealing that processes such as nitrate assimilation and nitrification are ongoing during winter. A comparison of our data to previous studies suggests a temporally advanced nitrogen cycle compared to pack ice in the region. Finally, the first measurements of winter pancake ice and spring brash ice biogeochemistry are highlighted and illustrate the seasonal influence on the sea ice environment and surface ocean in the AMIZ. The work detailed in this thesis significantly advances the available data and knowledge base for the AMIZ, particularly related to the biogeochemistry of sea ice, and will help to improve and validate future modelling efforts by providing observations in a severely understudied region.

This page is intentionally left blank

Acknowledgements

I extend my deepest gratitude to my supervisor, **Prof. Marcello Vichi**. When I first inquired about the only Antarctic project available to our honours class in 2017, I had no idea what I was getting into. Now, seven years later, I have seen the Antarctic, walked on sea ice, and grown both personally and professionally. I cannot thank you enough for the opportunities you have provided and your guidance over the years.

I am equally grateful to my co-supervisor, **A/Prof. Sarah E. Fawcett**. You were there when I used a pipette for the first time, sampled from a Niskin bottle for the first time, and most notably, took my first sea ice core. I am so appreciative of your presence and influence on my research journey. Learning from you in the laboratory and in the field has been a privilege.

This research was supported by the **National Research Foundation of South Africa** through the **South African National Antarctic Program** (grant nos. 118745 and 129232). This work also received funding from the European Union's Horizon 2020 research and innovation programme under grant agreement no. 101003826 via project **CRiceS** (Climate Relevant Interactions and Feedbacks: the key role of sea ice and Snow in the polar and global climate system) and the **Whales and Climate research program** (https://whalesandclimate.org). I also acknowledge the **South African Department of Science and Innovation's Biogeochemistry Research Infrastructure Platform** and the **South African Polar Research Infrastructure** for research infrastructure support.

I would like to acknowledge the **Marine Biogeochemistry Lab** at the University of Cape Town. My appreciation also goes to **Dr. Raymond Roman (and the SEAL5000), Hazel Little, Dr. Brett Kuyper, Dr. Adam West, Joshua Mirkin, and Dayna Collins**. Thank you for your support in the laboratory throughout my sample analysis. Additionally, to **Dr. Raquel Flynn**—your support, both in and out of the lab, has been invaluable. I would also like to thank **Cashifa Karriem, Nadia Jabaar, and Sharon Bosma** for their administrative support throughout my postgraduate journey.

In 2019, I spent a combined 165 days aboard the S.A. Agulhas II during the SANAE58/2019 Weddell Sea Expedition and the 2019 SCALE winter and spring cruises. I would like to thank the **Sea Ice teams** from all voyages. Your support and manual labor contributed significantly to this thesis, and my dataset would not be as extensive without all of you. My thanks and respect go to the **Captain and crew of the *S.A. Agulhas II*** on those voyages. Their knowledge and expertise in the harsh conditions of the Antarctic and Southern Ocean are unmatched.

This thesis reflects the support and boundless love I received from my **friends** throughout this challenging academic pursuit. I owe an immense debt of gratitude to each of you, with special mention for **Siobhan Johnson, Mark Hambrock, Justin Pead, Do Yeou Ku, Kurt Spence, Shantelle Smith, Jessica Burger, Kirsten Petzer, Leandrea Naidoo, Mishka Rawatlal,** and **Danielle Shay**. Thank you for checking in, for the tea, and for the company. To my team at **NRF-SAEON (Egagasini) and SAPRI**, thank you for your patience and encouragement in this final year.

To my **parents**: you have sacrificed so much to get me here. Thank you for your unwavering support. To **Nitara** and **Hassan**, thank you for your encouragement. To **Yazia**, I cannot wait to tell you all about sea ice and Antarctica. To **Basil** and **Ecco**, you have seen me through my darkest days.

To **Timothy Gwynn**: thank you for the hours of practice presentations, proofreading, and code troubleshooting; for the hours you spent at East Pier waiting for the ship to return; and later, when Basil and Ecco came, for loving them while I was away. Thank you for being with me through the highs and lows—especially the lows. You held me together, and in moments when I couldn't recognize myself, you could always see me.

This page is intentionally left blank

Contents

List of figures

List of tables

Chapter 1

1. Introduction

1.1. Sea ice in the global system

Although sea ice exists primarily in the polar regions, its influence is not limited to these regions. The annual expansion and retreat of sea ice in the Antarctic polar region of the Southern Ocean is one of the largest seasonal variations on the planet (Shepherd et al., 2018) (Figure 1.1). Sea ice plays an important role in the global system and climate by influencing heat exchange and the surface albedo, ocean circulation, and marine ecosystems. Sea ice has a high albedo which results in its surface reflecting more incoming solar radiation compared to the open ocean, thus regulating the global heat budget. The dynamic interactions between the ocean, atmosphere and sea ice that occur in the region (e.g., wind and wave action) and the freezing and thawing of sea ice affects seawater density, thus contributing to the formation and renewal of deep water in the oceans and the redistribution of heat and moisture throughout the connected ocean basins. Sea ice also provides a habitat and substrate for a wide range of microorganisms, including algae, bacteria and viruses and contributes to the nutrient availability and productivity of the surface polar ocean (Dieckmann & Hellmer, 2003; Arrigo, 2014). From a biogeochemical perspective, sea ice influences the nitrogen, phosphorus, and iron cycles of the surface ocean. These nutrients are sequestered, transported and recycled within the ice and surrounding seawater and can limit the growth of algae and other primary producers, which can have cascading effects on the entire food web (Arrigo, 2014).

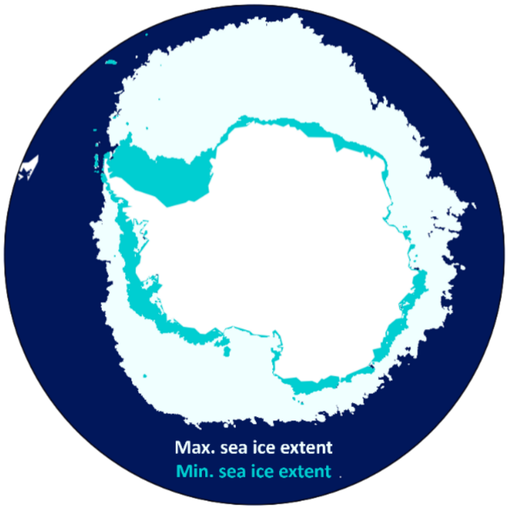

Figure 1.1. Map of the Antarctic polar region overlaid with the maximum and minimum sea ice extent derived from the AMSR2 satellite product for 2019 (Spreen et al., 2008).

Sea ice also serves as both a driver and indicator of climate variability and global climate change. Sea ice is highly sensitive to changes in temperature and other environmental factors, which makes it a good indicator of climate change (Dieckmann & Hellmer, 2003). The growth of sea ice also contributes to the sequestration of carbon from the atmosphere to the deep ocean through deep water formation from brine expulsion (De Vries, 2022), while the presence of sea ice influences the exchange of gasses between the ocean and the atmosphere by acting as a semi-permeable layer on the ocean surface (Clarke & Ackley, 1984).

Sea ice is a dynamic and constantly changing environment that influences and is influenced by the global system. While existing research has contributed significantly to our understanding of the physical properties and dynamics of Antarctic pack ice, a notable gap persists in our knowledge of the sea ice that grows in the Antarctic marginal ice zone (AMIZ). The aim of the following literature review is to examine the current state of knowledge of the AMIZ and the physical and biogeochemical dynamics of the sea ice that grows in the region.

1.2. The Antarctic Marginal Ice Zone

The Antarctic marginal ice zone (AMIZ) is a circumpolar boundary region that marks the transition between the open ocean and the sea-ice covered ocean (Figure 1.2). The AMIZ is characterised by intense interactions between the ocean and the atmosphere through wind and wave dynamics that arise from the combination of open water and sea-ice cover (Muench, 1989; Vichi, 2022). These interactions influence how the sea-ice cover grows (e.g. morphological properties) and eventually consolidates, thickens, and results in the AMIZ being composed of a combination of free drifting pancake ice, frazil ice and different first-year ice types (Toyota et al., 2011; Vichi, 2022).

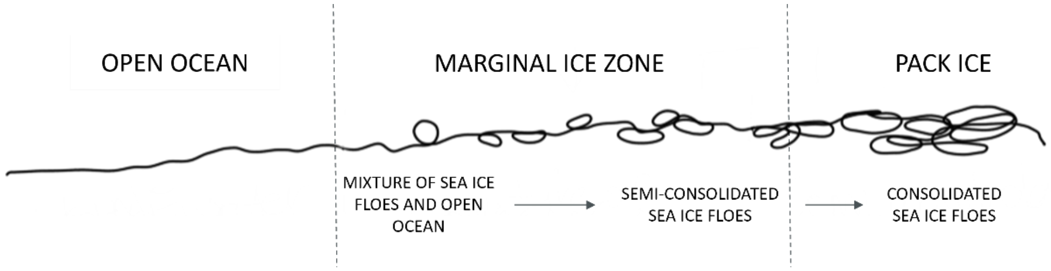

Figure 1.2. Illustration depicting the transition from the ice-free open water to the marginal ice zone that has a combination of ice floes and open water spaces to semi-consolidated sea-ice cover and finally consolidated conditions (pack ice).

The AMIZ is a highly variable environment that can change rapidly over short time scales (Vichi, 2022) (Figure 1.3), particularly during the ice-growth season when extensive sea-ice cover renders the region largely inaccessible. Despite the challenges posed by its harsh conditions, the AMIZ holds significant scientific importance due to its critical role in the Antarctic ecosystem. Phytoplankton and ice algae thrive in the AMIZ sea ice and serve as a primary food source for krill and other marine organisms, while also acting as a temporary storage of carbon. Furthermore, the AMIZ plays a crucial role in the global climate system, exhibiting high temporal and spatial variability in heat, moisture, and gas exchange between the ocean and atmosphere. Its thinner and more mobile ice is particularly susceptible to melting, breakup and re-freeze, changing the buoyancy of the surface ocean and releasing nutrients.

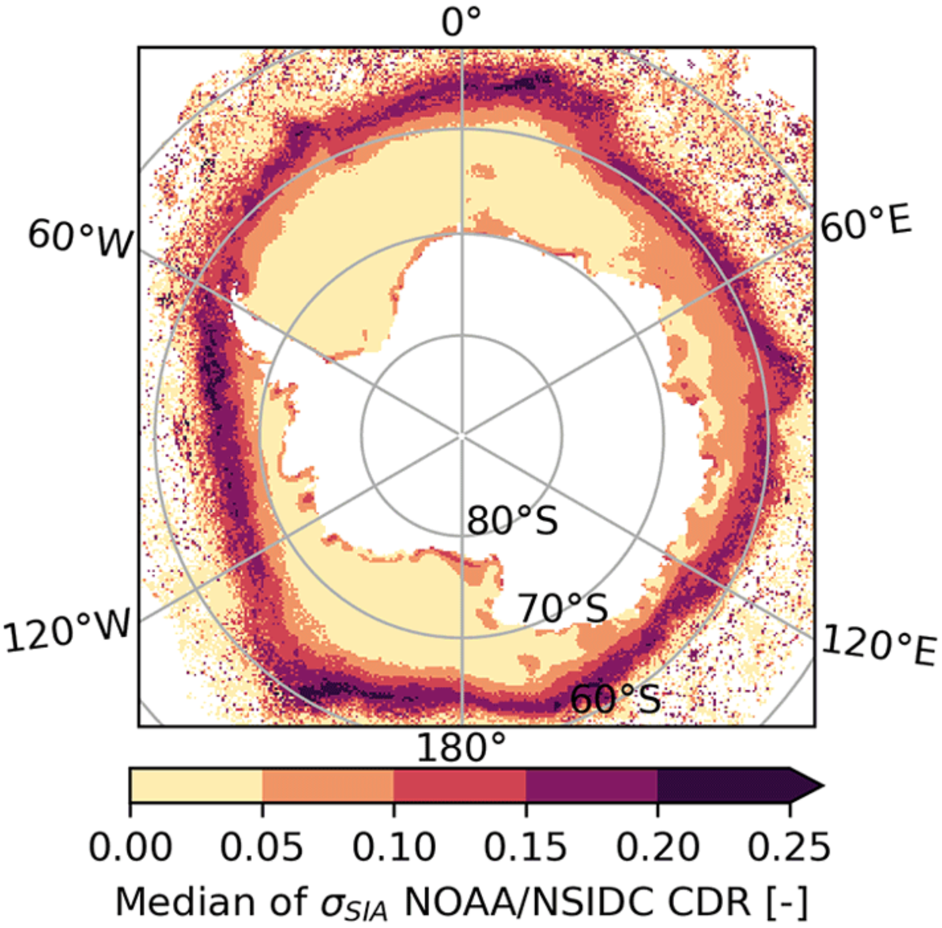

Figure 1.3. Map illustrating the variability of sea ice concentration in the Antarctic region using the median of the indicator (σ_{SIA}) defined by Vichi (2022). σ_{SIA} is used to estimate the chances of encountering variable conditions at each pixel on a monthly climatological timescale. Higher values of the σ_{SIA} median are indicative of larger departures from the long-term conditions (when sea ice is present in the region) and indicate a highly variable region. These highly variable regions are found in the outer part of the sea ice, also known as the Marginal Ice Zone (Vichi, 2022).

While the AMIZ's importance is recognized in the literature, it remains relatively understudied due to the difficulties associated with accessing, navigating, and sampling the region outside of the summer season, a period in which the MIZ is also more difficult to be identified. This has contributed to a bias towards pack ice in existing data, highlighting the need for comprehensive research focusing on the characteristics and dynamics of the sea-ice cover in the AMIZ. Research efforts in the AMIZ have encompassed a wide range of topics, including the physical properties of the consolidated sea-ice cover, the structure of the ice (Lange et al., 1989; Skatulla et al., 2022; Vichi, 2022; Johnson et al., 2023) and to a lesser extent, the biogeochemistry (Tison et al., 2020; Louw et al., 2022).

1.3. Sea ice growth and physical characteristics

Sea ice growth is governed by the exchange of heat, momentum and radiation between the ocean and the atmosphere (Dieckmann & Hellmer, 2003). These exchanges are divided between dynamic (momentum exchanges) and thermodynamic (heat and radiative exchanges). Dynamic sea-ice growth refers to the mechanical processes that alter the ice cover through momentum exchanges between the atmosphere, ice, and ocean. These include wind-driven deformation, oceanic forcing, and interactions between ice floes, which result in processes such as rafting, ridging, and lead formation. Rafting occurs when thin ice floes override one another, thickening the ice without new freezing, while ridging results from the compression of ice floes into pressure ridges composed of broken, piled ice floes (Lange & Eicken, 1991). These dynamic interactions promote the formation of granular and frazil ice, particularly during turbulent conditions, where suspended ice crystals aggregate and consolidate at the surface. The structural complexity introduced by dynamic growth leads to increased heterogeneity in ice thickness, enhanced porosity, and more irregular brine channel networks. Such features can have significant implications for brine drainage, nutrient retention, and biological activity, particularly in young, rapidly evolving ice types commonly found in marginal ice zones.

Thermodynamic growth is a function of the surface heat budget and the oceanic heat flux. The surface heat budget includes the radiative fluxes of solar radiation and incoming and outgoing longwave radiation and the turbulent fluxes of sensible and latent heat plus the heat conduction through the ice. Sea ice growth is a result of the sum of all the surface fluxes - if the sum is negative, the ice cools and grows, if it is positive the ice warms and melts. The radiative terms in the surface heat budget are influenced by albedo (solar radiation), surface temperature (outgoing longwave radiation), and cloud cover (incoming longwave radiation). The turbulent fluxes, sensible and evaporative, are dependent on the wind speed and the difference in temperature and humidity between the surface and the atmosphere. At the ice bottom, the turbulent heat flux from the ocean to the ice and heat conduction through the ice are the only factors that influence sea ice growth. Dynamics of sea ice growth involve the motion of the ice that is typically driven by surface winds (Haas, 2003). The divergence of the ice results in open water and promotes ice formation, while the convergence causes ridging, rafting and increased ice thickness.

As the surface of the ocean loses heat to the atmosphere, sea ice begins to form. In the AMIZ, the dominant mode of ice formation is known as the pancake cycle (Figure 1.4) (Lange et al., 1989). Frazil ice crystals, which are suspended just below the ocean surface, are the first to form. The turbulent waters associated with the Southern Ocean results in these crystals clumping together to form cakes of slush ice that continue to grow by means of accretion. According to the Lange et al. (1989) model, these cakes of ice collide with each other in the ice field, resulting in their edges becoming raised, thus forming pancake ice. These pancakes are only a few centimeters in diameter when first formed.

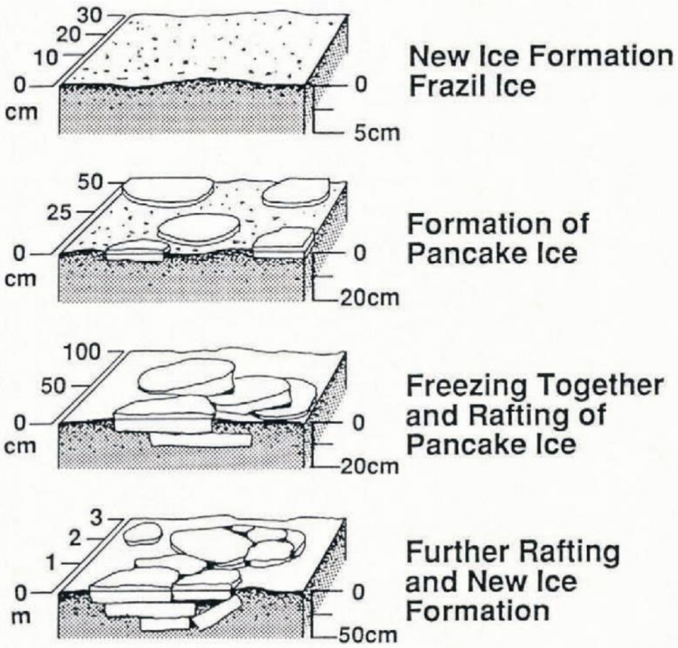

Figure 1.4. The frazil-pancake cycle described by Lange et al. (1989).

According to this conceptual model, as the ice grows, the pancakes are thought to interact with each other, resulting in more collisions. These interactions ultimately appear as rafted features of the pancake ensembles, which influence how the ice field thickens and consolidates (Figure 1.5). Despite the lack of sea-ice formation process-specific work across multiple sectors of the Antarctic sea-ice region, there is a general understanding that ice floes thicker than 0.6 m have been generated by surface deformation processes (Worby et al., 1996).

Figure 1.5. Image of rafted pancake ice floes observed during the SCALE2022 Winter Voyage (Vichi, 2023) aboard the *S.A. Agulhas II*.

Sea ice growth leads to the entrapment of nutrients and biological components in the sea ice within the semi-solid matrix as brine channels. It also promotes the expulsion of concentrated brine, which modifies the underlying water column. Particulate matter can be incorporated into the ice through several physical mechanisms during formation, including nucleation, wave-field pumping, and the harvesting of material by rising frazil crystals, which scavenge particles from the water column as they ascend (Garrison et al., 1989; Spindler, 1994 and references therein). The part of the ice where brine channels are connected and these particles accumulate is the Biologically Active Layer (BAL), where specially adapted microorganisms are able to live, grow and eventually bloom(Golden et al., 1998; Tedesco et al., 2010). This layer forms a dynamic and heterogeneous habitat, structured by the evolving network of brine inclusions that vary with temperature, salinity, and deformation history. Processes like rafting and ridging increase this structural complexity, creating thicker ice layers and distinct internal environments that enhance biological and chemical variability.

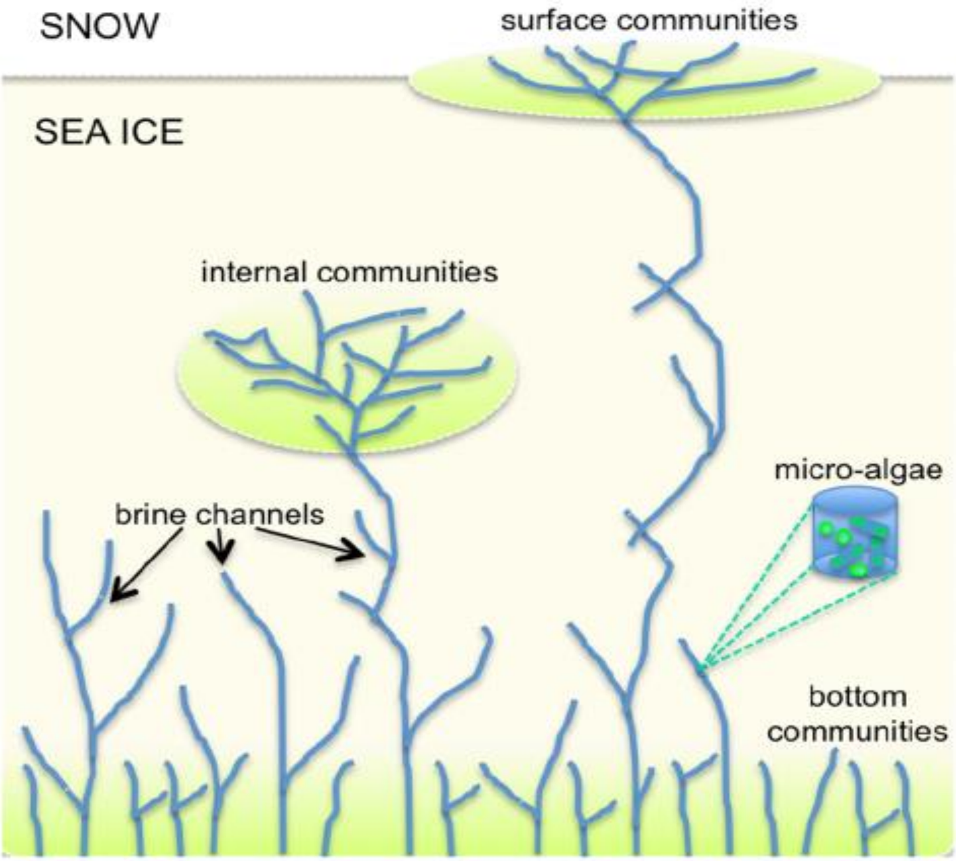

Figure 1.6. Schematic showing the distribution of algal communities in sea ice (Tedesco & Vichi, 2014).

Distinct microbial communities can develop throughout the vertical structure of the ice: bottom communities thrive at the ice–ocean interface where light and nutrient exchange are relatively high; internal communities occupy liquid-filled brine channels within the ice matrix; and surface communities, though often exposed to more extreme conditions, may develop during melt seasons or in features such as melt ponds. These layered microhabitats, while extreme, are crucial for supporting microbial life and facilitating nutrient exchange, and they play a pivotal role in polar biogeochemical cycles and ecosystem functioning (Tedesco & Vichi, 2014).

From a structural perspective, sea ice comprises of various textures such as granular, transitional, and columnar ice. Sea ice structure is influenced by a complex interplay of environmental factors during its formation and growth. As the sea ice grows and the crystal orientation begins to align, the granular ice layer turns into a transitional layer. In this layer, the ice is a mixture of smaller, granular crystals and larger crystals that are beginning to align with columnar ice. The transitional layer is followed by a columnar layer that forms during calmer periods (Figure 1.7) (Petrich & Eicken, 2016). Young ice in the AMIZ typically displays this three-layer structure, with a granular ice layer at the surface, followed by a transitional layer and finally a columnar layer when thermodynamic growth dominates (Figure 1.7) (Weeks & Ackley, 1982; Weeks, 2010). In more dynamic conditions, such as the frequent extratropical cyclones (Vichi et al., 2019), it leads to the breakup and rearranging of the ice pack that ultimately influences the crystal structure. Understanding the internal arrangement of ice crystals provides insights into the prevailing environmental conditions during sea ice growth. The structure of the sea ice influences the distribution of brine channels and air pockets and plays a role in determining its permeability, thermal conductivity, and overall resilience to external forces (Golden et al., 1998).

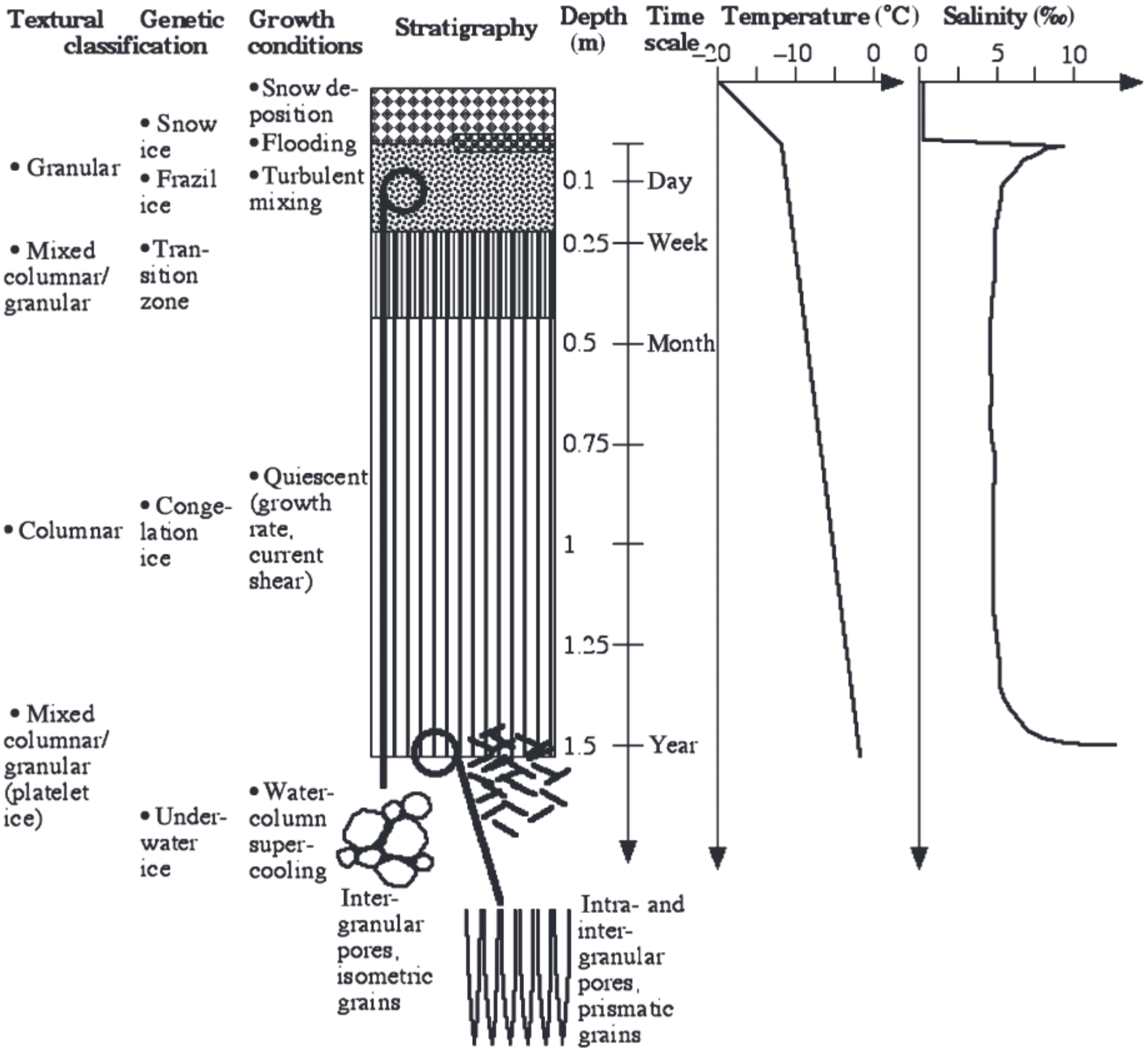

Figure 1.7. Schematic of first year ice properties (Petrich & Eicken, 2016).

Temperature gradients in sea ice are formed during the freezing and thawing processes. Temperature profiles of growing sea ice display on average a linearly increasing trend with the lowest temperature at the top of the ice where the ice is influenced by the overlying atmosphere and the bottom of the ice being closer to the freezing temperature of seawater. An idealised temperature profile of growing first year ice is displayed in Figure 1.7.

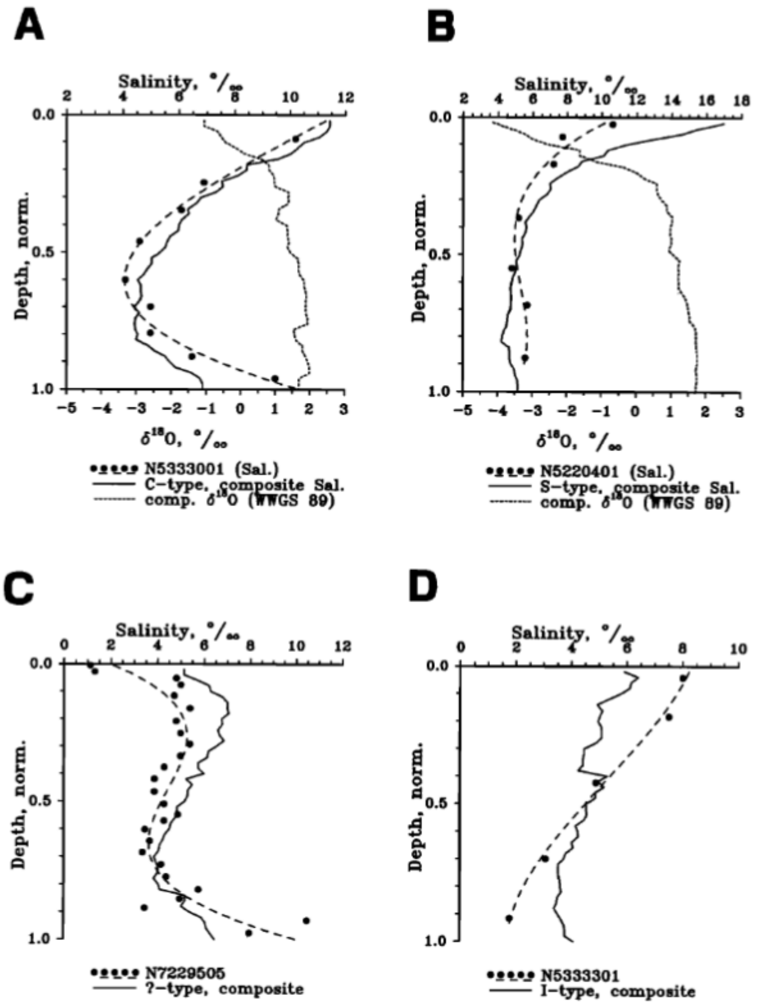

Figure 1.8. Normalised salinity and $\delta^{18}O$ profiles of sea ice (Eicken, 1992).

Salinity profiles from various Antarctic regions and growth conditions were described by Eicken (1992) and are displayed along with $\delta^{18}O$ profiles in Figure 1.8. The salinity profile of young, growing ice is expected to display a C-type curve with higher salinity at the surface, a decrease towards the middle of the ice, followed by an increase at depth. This type of profile is indicative of brine movement through the ice. Slightly older ice, still within the first-year category, may display an S-type salinity curve, with high salinity at the surface and progressively lower salinity toward the bottom. The salinity in first year ice is usually less than the salinity of young growing ice due to desalination processes that act over time. During the onset of the melting season in spring, FYI can exhibit a ?-type curve that has lower surface salinity values as a result of freshwater inputs in the surface ocean lowering the top salinity. Multiyear ice displays an I-type salinity curve that has a decreasing salinity with depth (Eicken, 1992). Tang et al. (2007) showed I-type salinity profiles in undisturbed multiyear ice in their study. While these salinity profile types are useful indicators of ice age and development, they are generalisations, and deviations from these patterns can occur depending on local conditions and ice history.

1.4. Sea ice biogeochemistry

During sea ice growth, the bulk of salts are rejected from the ice, while a fraction is concentrated in narrow channels as liquid brine due to the high salinity. The initial concentration of solutes that make up the sea-ice biogeochemical environment are set by the seawater that the ice grew from and initially behaves conservatively with salinity (Meiners & Michel, 2017) as time passes, the biogeochemical environment evolves within the sea ice and deviates from the salinity trend depending on the utilisation (Gleitz et al., 1996; Meiners & Michel, 2017). The temperature influences the size of brine inclusions in the sea ice, which in turn influences how brines are connected within the ice and subsequently how biological matter is transported, distributed, and exchanged through the ice and with the underlying waters. These channels provide the nutrients and space needed for a biological community to live and grow (Tedesco et al., 2010).

Nutrients in sea ice, such as nitrate, silicate, and phosphate, are necessary for the survival of the internal biological communities. The concentration of these nutrients in sea ice isa function of the concentration of the underlying seawater that is trapped in the ice during formation, brine convection, biological activity, and remineralisation by heterotrophs (Gleitz et al., 1995). The dynamics of these nutrients have been presented in the literature about Antarctic pack ice (Clarke & Ackley, 1984; Gleitz et al., 1995; Becquevort et al., 2009; van der Merwe et al., 2009; Fripiat et al., 2014; Roukaerts et al., 2016; Tison, Schwegmann, et al., 2017), while fewer studies focused on the nutrient status of young, growing ice (Dieckmann et al., 1991; Tison, Schwegmann, et al., 2017; Tison et al., 2020; Louw et al., 2022). This is predominantly due to the difficulty of working in the region during the growth season.

Fripiat et al. (2017) compiled 306 pack ice cores from 19 studies around Antarctica and found spring to be the best represented season, followed by summer, winter and autumn. Their compilation found a bias towards thicker ice, with autumn and early winter being underrepresented. Their study subsequently focused on level ice from late winter to summer - further illustrating the lack of early winter young ice data available for Antarctica (Figure 1.9).

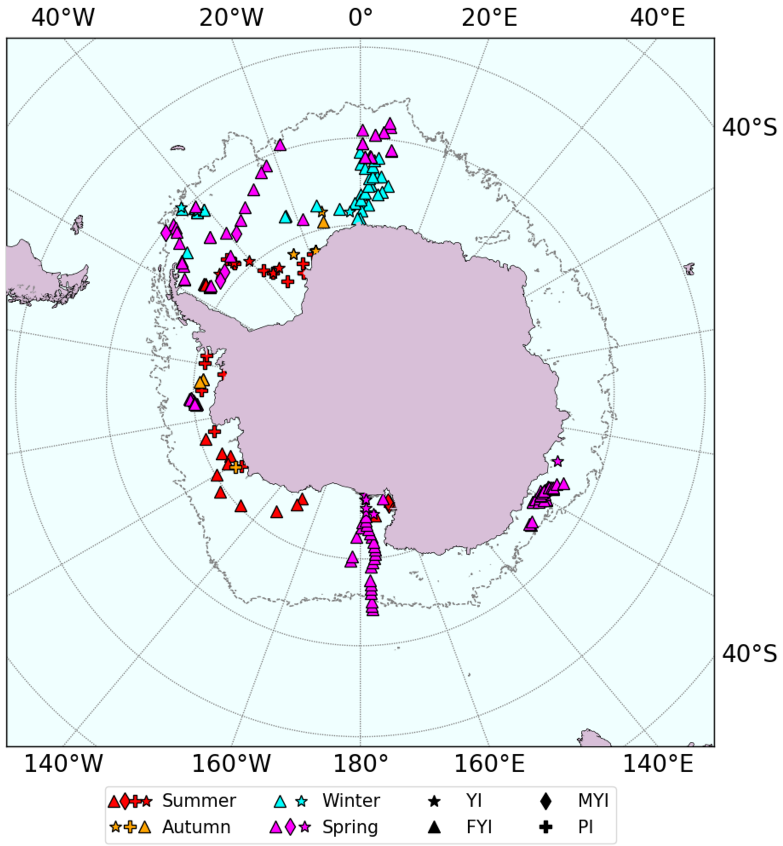

Figure 1.9. Map showing location of existing sea-ice cores analysed for biogeochemical properties compiled by Fripiat et al. (2017). Cores are categorised by season (colour) and ice type (symbol shape).

The vertical distribution of nutrients in sea ice is a result of brine dynamics and biogeochemical activity. Zhou et al. (2013) investigated the link between brine dynamics and ice-ocean exchanges of biogeochemical properties. Their work showed that brine dynamics influence the concentration of nutrients differently at different stages of the ice life - early growth, late growth and melt. During early growth, ice is mainly impermeable and allows for nutrient accumulation during incorporation. There is also bottom convection in the brines that facilitates exchange with the surrounding waters. During late growth, there is full brine convection throughout the ice, leading to increased permeability and exchange with the surrounding waters. This exchange results in decreased bulk nutrient concentrations. The melt stage has a further increase in permeability and an overall slowing of exchange with the surrounding waters.

The concentration of nutrients in sea ice is initially set by the seawater from which the ice grows from. In a fully abiotic system, nutrients are expected to change according to changes in salinity (Meiners & Michel, 2017), however, in many cases, nutrients are observed to deviate from expected concentrations based on conservative behavior. This is often attributed to biological activity. This deviation is best represented by theoretical dilution lines (TDL) that indicate depletion or enrichment of nutrients depending on their position relative to the TDL. There have been several studies that investigated nutrient dynamics of sea ice using TDLs (Dieckmann et al., 1991; Becquevort et al., 2009; van der Merwe et al., 2009; Torstensson et al., 2018).

Nutrient dynamics in sea ice are influenced by the exchange of matter with the surrounding ocean, available space in brine channels and light. C-shaped nutrient profiles have been observed in Antarctic pack ice (Fripiat et al., 2017; Torstensson et al., 2018) while Smith et al. (2011) observed the presence of steep vertical gradients in nutrients through the ice. Clarke and Ackley (1984) found the chlorophyll concentrations in ice reached their peak around 0.2 m from the bottom and credited this enhanced biogeochemical activity to the passive exchange of nutrients with the underlying ocean that replenished nutrients and promoted biological growth. A study by Melnikov (1998) observed the biological dynamics in newly formed and 1 year old pack ice in the western Weddell Sea. Their observations showed that the chlorophyll concentrations produced by ice algae in both ice types were consistently higher than the surrounding seawater.

Clarke and Ackley (1984) contributed to the understanding of nutrient dynamics in sea ice with their study of Weddell Sea pack ice in 1981. They observed nutrient concentrations in ice that were lower than in the surrounding water which was attributed to biological activity. They also observed silicate depletion as a result of diatom growth and concluded that silicate was a limiting nutrient. They also observed low nitrate concentrations that were attributed to diatom utilisation. Their samples had enhanced nitrite concentrations that were hypothesised to be a result of nitrification by bacteria, but their lack of ammonium data made it difficult to confirm. In their study, Clarke and Ackley (1984) also observed large variability in the biogeochemical properties within and between the ice cores taken at the same location. Their study concluded that the ice sampled was a product of several formation processes that occurred at different times in biogeochemically different waters, and that care should be taken even when comparing cores from the same floe.

Dieckmann et al. (1991) analysed sea-ice cores and brine samples from the Weddell Sea ice in winter and found that bulk nutrient concentrations fluctuated widely and did not correlate to salinity. They also found the young ice nutrient content corresponded with the underlying seawater. Nutrient observations in pack ice suggest that the expected trend in winter is that the biogeochemistry is controlled by the underlying seawater with little to no variability (Dieckmann et al., 1991). Fripiat et al. (2017) showed that in winter, sea-ice nutrient concentrations are close to the underlying seawater, which indicates little to no biological activity while in spring, nutrients in sea ice were partially depleted indicating algae growth promoted by the available sunlight. This was challenged by Tison et al. (2017); their study of winter sea ice in the

Weddell Sea suggested that biogeochemical activity in ice is not as dormant during winter as previously thought.

It is important to understand the dynamics of sea ice biogeochemistry to better understand the role sea ice plays in the surface ocean and global system. During sea-ice formation, limiting trace nutrients such as iron are entrained in the ice matrix in the form of brine channels (Lannuzel et al., 2007; van der Merwe et al., 2009; Vancoppenolle et al., 2013). These nutrient loaded brine pockets remain trapped in the ice and are later released into the surface ocean during melting. This stimulates phytoplankton production, resulting in spring blooms and potentially influencing the Southern Ocean's ability to drawdown carbon (Lannuzel et al., 2016). The biogeochemistry of ice-covered oceans is therefore of particular interest because of the extent of the ice cover over the year. However, less is known about the seasonal, growing ice in the AMIZ, which is seasonally advancing and retreating at the edge of this large expanse.

In summary, studies of Antarctic sea ice are limited spatially and temporally, with a bias towards spring and summer seasons due to logistical complexities. Early winter sea ice is typically under-sampled in terms of both physical and biogeochemical properties and data from pancake ice in the Antarctic marginal ice zone are practically non-existent.

1.5. Thermodynamic and biogeochemical modelling of sea ice

Sea ice growth is governed by a complex interplay of thermodynamic processes. The road to understanding thermodynamic processes that influence sea ice has been paved with numerical models dating back to 1891. Sea-ice thermodynamic studies began with the analytical model by Stefan (1891) and progressed to numerical modelling by Maykut and Untersteiner (1971). These models were simplified by Semtner (1976) and were applied to climate studies. More in depth models by Lepparanta (1983) and Cox & Weeks (1988) introduced snow dynamics and the thermal role of brines. These models are based on the concept that sea ice rates of growth and melt depend on how heat is exchanged within the sea ice as well as between the bottom and the top of the ice (Figure 1.10).

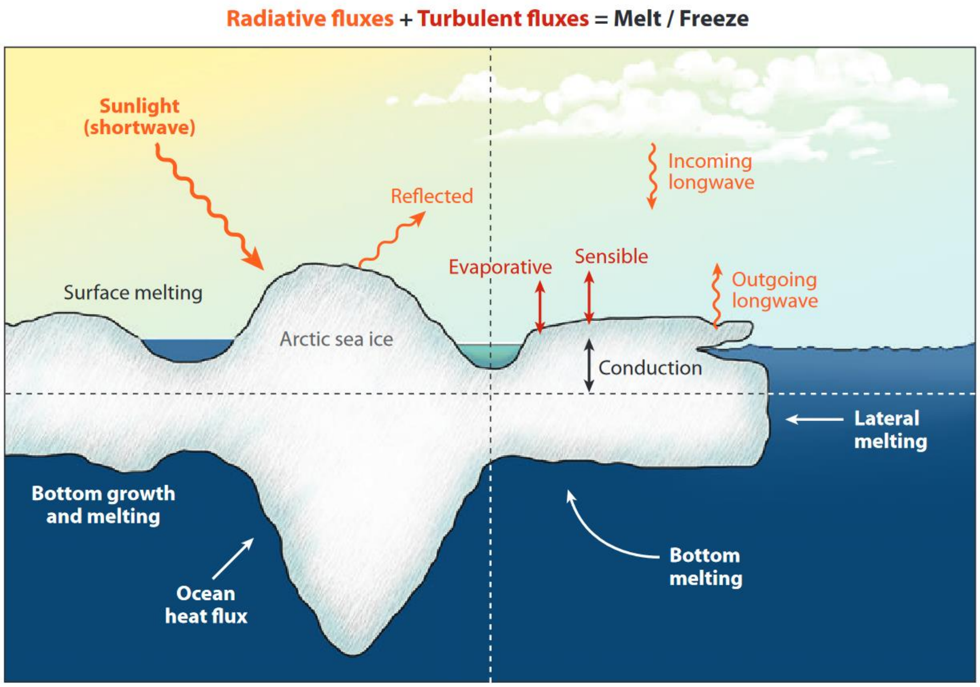

Figure 1.10. Schematic of the sea ice heat budget. Also shown is the equation for the surface heat budget. Radiative fluxes are indicated in orange (net short wave, income longwave, outgoing longwave energy), turbulent fluxes are indicated in red (sensible and evaporative heat) and the conductive energy transfer is indicated in black (Massom & Stammerjohn, 2010).

One of the approaches to modelling sea ice thermodynamics considers a column divided into N-layers of variable thickness, including a snow layer (Figure 1.11). The thickness of each layer is a physical property that can either be prescribed or dynamically simulated by the model. While not solely governed by heat transfer, vertical heat fluxes between the atmosphere, snow, ice, and ocean significantly influence the thermodynamic evolution of these layers through processes such as melting, freezing, and internal temperature redistribution. Accurately resolving these interactions requires careful consideration of the energy balance at the interfaces, which is driven by vertical heat transfer and is described by the following equations:

The net heat budget (F_{net}) describes the sum of the radiative and turbulent heat fluxes at the surface of the sea ice. $F_{net} < 0$ indicates cooling and growth and $F_{net} > 0$ indicates warming and melting and is represented as:

$$F_{net} = (1-\alpha)(1-\beta) \cdot F_{sw} + F_{lw\uparrow} + F_{lw\downarrow} + F_H + F_E + F_Q \tag{1}$$

where α is the surface albedo, β is the fraction of absorbed shortwave radiation that penetrates the ice and escapes at the bottom, F_{sw} is the shortwave radiation, $F_{lw\uparrow}$ is the upward longwave radiation, $F_{lw\downarrow}$ is the downward longwave radiation, F_H is the sensible heat flux, F_E is the latent heat flux and F_Q is the conductive (or sensible) heat flux at the surface of the ice.

The vertical heat transfer in the snow and ice layers is governed by a heat conduction equation that embeds the penetration of solar radiation which depends on the albedo (α) and the extinction coefficient (κ):

$$\rho_i c_i \frac{\partial T_i}{\partial t} = \frac{\partial}{\partial z}\left(k_i \frac{\partial T_i}{\partial z}\right) + (1-\alpha_i) \cdot F_{sw} e^{-\kappa_i z} \tag{2}$$

where the subscript *i* refers to the layer (snow, ice, snow ice etc.), ρ_i is ice density, c_i is the heat capacity, T is the temperature, k_i is the thermal conductivity and F_{sw} is the incoming solar radiation.

The dynamic equation for the ice growth at the ocean-ice interface (i = *ice* in the previous equation) is regulated by the heat balance between the oceanic and conductive fluxes:

$$\rho_{ice} L \frac{\partial H_{ice}}{\partial t} = k_{ice} \frac{\partial T_{ice}}{\partial z} - F_w \tag{3}$$

where ρ_{ice} is the ice density, L is the latent heat of the ice, H_{ice} is the ice thickness, k_{ice} is the thermal conductivity, T_{ice} is the temperature in the layer, and F_w is the oceanic heat flux.

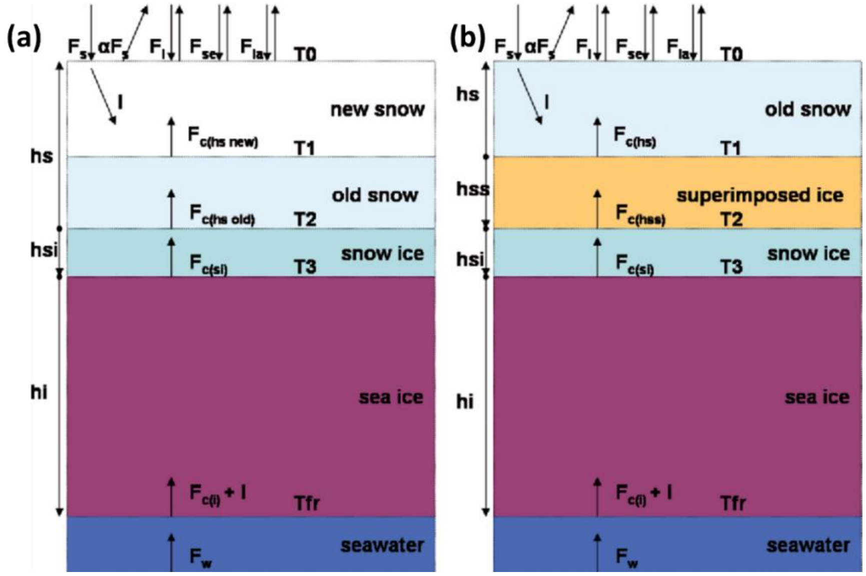

Figure 1.11. General structure of a sea ice model with heat fluxes, temperatures, and various layers indicated during (a) sea ice growth and (b) melt periods (Tedesco et al., 2009).

Incorporating biogeochemistry into sea ice thermodynamic models requires adding equations that represent brine dynamics and biogeochemical processes, along with their interactions with the physical properties of the ice. The coupling between sea ice thermodynamics and biogeochemistry is essential, as factors such as temperature, salinity, and permeability directly influence biogeochemical activity within the ice. Changes in salinity and dissolved constituents in the brine channels over time due to processes like flooding and gravity drainage affect nutrient availability, heat transfer, and microbial habitat within the ice (Vancoppenolle et al., 2010; Vancoppenolle & Tedesco, 2017).

The evolution of salinity in the ice is derived by first assuming that liquid brines are always at their freezing point and in thermal equilibrium with the surrounding ice (e.g., Tedesco et al., 2010; Vancoppenolle et al., 2010). This leads to a linear dependence between the sea-ice temperature T (℃) and the brine salinity

$$T = -\mu S_{br} \tag{4}$$

where $\mu = 0.054$℃ (Assur, 1958). The bulk salinity S_{bk} and brine salinity are linked through the brine volume fraction V_{br},

$$S_{bk} = V_{br} S_{br} \tag{5}$$

which allows us to compute the brine volume as:

$$V_{br} = -\mu \frac{S_{bk}}{T} \tag{6}$$

The evolution of bulk salinity in the ice is then computed by considering the initial entrapment of salt, flushing and gravity drainage:

$$\frac{\partial S_{bk}}{\partial t} = k_{eff} \frac{\partial S_w}{\partial t} - w \frac{\partial S_{br}}{\partial z} + \frac{\partial}{\partial z}\left(\overline{D} \frac{\partial S_{br}}{\partial z}\right) \tag{7}$$

where k_{eff} is the distribution coefficient which is computed empirically as a function of the sea ice growth rate (e.g., Cox & Weeks, 1988), S_w is the seawater salinity, w is the net brine flow due to vertical transport (flushing and flooding) (e.g., Vancoppenolle et al., 2007), S_{br} is the brine salinity and $\overline{D}$ is an effective diffusivity to represent the effect of gravity drainage (e.g., Cox & Weeks, 1988).

The evolution of bulk salinity forms the basis for the transport of biogeochemical constituents in sea ice. By analogy to the ice salinity equations, the physical evolution of the bulk concentration of a nutrient (C_{bk}) can then be represented as:

$$\frac{\partial C_{bk}}{\partial t} = k_{eff} \frac{\partial C_w}{\partial t} - w \frac{\partial C_{br}}{\partial z} + \frac{\partial}{\partial z}\left(\overline{D} \frac{\partial C_{br}}{\partial z}\right) + \left.\frac{\partial C_{bk}}{\partial t}\right|_{bgc} \tag{8}$$

Salinity is a conservative tracer, while biogeochemical components are also affected by the last term in this equation that represents the biogeochemical source and sink terms which will be described in Sec. 2.5.3.

1.6. Field and laboratory techniques for sea ice research in Antarctic

Protocols for the sampling and handling of sea ice have been developed since the early 19th century (Horner, 1989). Field-based observations help to improve our understanding of the ice-covered oceans and the impact changes in this ice cover will have on the global system. Additionally, sea ice field measurements aid in the development and validation of remote sensing techniques and numerical models.

A comprehensive compilation of field techniques for sea ice was published in 2010 (Eicken & Salganek, 2010). Further work done by the Biogeochemical exchanges at Sea Ice Interfaces group (BEPSII) (Miller et al., 2015) completes the existing literature of generally accepted practices for sea-ice biogeochemistry. An important consideration for sea ice field techniques is the recognition that sampling protocols are dictated by the in-situ conditions and available equipment. This leads to field methods varying between research groups and campaigns. Documented methods (Eicken & Salganek, 2010; Miller et al., 2015) are predominantly developed and implemented in the Arctic with on-ice base camps and calm sampling conditions. The Antarctic poses a different set of environmental and sea ice conditions.

Sea ice samples are typically collected for the analysis of physical, mechanical, and biogeochemical properties. Sea ice sampling tends to favour stable, uniform ice for the sake of safety. Sampling strategies aim to sample the entire thickness of the selected sea ice in a random manner, which is done to capture the variability in the snow and sea-ice cover. Generally accepted sampling practices include the coring of sea ice using a rotating cylinder fitted with blades at the base and attached to either a handle for manual driving or a motor. The extraction of the core is followed by temperature measurements along the length of the core. Different protocols are applied to the cores depending on the tests to be performed. Cores are transported horizontally to avoid brine loss and stored for later analyses on ship and land laboratories.

From a biogeochemical perspective, the subsequent processing steps include the cleaning, segmentation and melting of the sea-ice core for further testing. Core segmentation is done along the length of the core using either a handsaw or a bandsaw. The segment sizes vary according to the desired resolution and meltwater volume requirements. Melting techniques include buffer melting and direct melting. The former involves melting the sea-ice segments in prefiltered or artificial seawater (Miller et al., 2015). This is done to reduce the osmotic stress on biology in the ice. The direct melting method involves melting the sea ice slowly to reduce stress on the sample. This method is favoured most often for bulk nutrient analysis. Both methods are conducted in the dark at low temperatures to limit further biological activity (Miller et al., 2015).

The appropriate analysis of sea-ice cores is fundamental to determining its properties. The current practices of sea ice field sampling and laboratory processing vary between research groups and regions depending on available resources, environmental conditions, and time. Most methodologies are not well documented and published, with the majority of accepted practices being developed and implemented in the Arctic. sea-ice core. The field techniques employed during South African cruises for the collection and processing of sea-ice cores were developed and refined in situ, based on the available equipment and environmental conditions, and are further discussed in Chapter 2.

1.7. Thesis aims and objectives

The overarching aim of this thesis is to investigate the seasonal biogeochemical properties of AMIZ sea ice in terms of sea ice algae, nutrients and bacterial processes, and relate them to sea ice conditions and types. This overarching aim is broken up into the following objectives:

1. Adapt existing field and laboratory sampling protocols to the harsh AMIZ conditions, leveraging on available resources, infrastructure, and expertise within the South African research community.
2. Investigate, through an interdisciplinary observational and modelling approach, the magnitude and evolution of winter to spring biological activity in the AMIZ, and its association to sea-ice growth conditions and structure, and environmental factors.
3. Characterize the physical and biogeochemical features of pancake ice compared to brash ice.
4. Collect and process the first data set on nitrogen isotope in AMIZ to assist the interpretation of seasonal variations in biogeochemical properties.

This thesis is divided into six chapters following this introductory chapter:

Chapter 2 provides an overview of the 2019 Southern oCean seAsonaL Experiment (SCALE), and addresses objective 1 by describing the sea ice sampling protocols, sample processing and methods for sea ice modelling that are applied in the following chapters.

Chapter 3 begins to address objective 2 by presenting data from the 2019 winter leg of SCALE and investigates the influence of rafting processes on the biogeochemical properties of winter sea ice.

Chapter 4 continues to address objective 2 by presenting new biogeochemical data from the 2019 spring leg of SCALE and investigates the influence of the prevailing environmental factors during the sea ice lifetime and the resulting physical and biogeochemical properties.

Chapter 5 addresses objective 4 by introducing novel measurements of sea ice biogeochemistry in the form of nitrogen isotope ratios of nitrate and particulate organic nitrogen.

Chapter 6 addresses objective 3 by presenting new biogeochemical data for pancake ice in winter and brash ice in spring 2019 for the AMIZ.

Chapter 7 draws together the results of the previous chapters within the context of the objectives presented above and are discussed in relation to the overarching aim of this thesis. This is followed by a discussion of some of the limitations of the studies conducted. A final section provides recommendations for future research based on the thesis findings and limitations.

Chapter 2

2. Data and Methodology

This chapter discusses the field campaigns conducted in 2019, the field protocols followed and the subsequent laboratory processing of the collected samples. The methods for sea ice modelling are then described along with sensitivity testing and validation.

The methodology work described below has been adapted from work done by the members of the Biogeochemical exchanges at Sea Ice Interfaces group (BEPSII) (Miller et al., 2015) to suit the field and laboratory conditions maintained by the sea ice team at the University of Cape Town. While the field protocols described in this work were applied to all the cores collected during SCALE2019, the analytical protocols focus on the physical and biogeochemical properties of young sea ice in the Antarctic marginal ice zone only. The protocols and methods developed in this thesis have also been applied to other properties investigated during SCALE 2019, such as mechanical and structural features. These are not addressed in this chapter and can be found in Skatulla et al. (2022) and Johnson et al. (2023).

2.1. The Southern oCean seAsonaL Experiment

The Southern oCean seAsonaL Experiment (SCALE, https://www.sapri.ac.za/lto-ocean/scale/) was a multidisciplinary experiment aimed at the establishment and maintenance of long-term and experimental observations of the south-east Atlantic sector of the Southern Ocean. Sea ice samples for this thesis were collected during the 2019 SCALE expeditions (SCALE2019) (Ryan-Keogh & Vichi, 2022) aboard the *S.A. Agulhas II* during the first leg in Winter (18 July 2019 - 12 August 2019) and the second leg in Spring (12 October 2019 - 20 November 2019). Stations were located within a sector ranging from 57°S to 59.5°S and 0°E to 22°E. The samples collected were either from pancakes and unconsolidated floes that were hoisted aboard the vessel or in situ from consolidated floes. A total of 11 individual floes and pancakes were sampled during SCALE2019 (Table 2.1). These stations are hereafter referred to pancake, unconsolidated or consolidated stations after the dominant ice type at the station.

Table 2.1. Table of sea ice stations locations during SCALE2019 including ice type, date of sampling and coordinates.

STATION	ICE TYPE	DATE OF SAMPLING	LATITUDE (°S)	LONGITUDE (°E)
M03	Consolidated Floes	27 July 2019	58.14	0.00
M01	Pancake	28 July 2019	56.80	0.30

SMIZ3	Consolidated Floes	24 October 2019	59.32	00.06
SMIZ2	Consolidated Floes	25 October 2019	58.98	00.01
SMIZ6	Consolidated Floes	29 October 2019	59.36	08.15
SMIZ7	Consolidated Floes	30 October 2019	59.36	10.89
SMIZ8	Unconsolidated Floe	01 November 2019	58.54	17.93
SMIZ9	Unconsolidated Floe	03 November 2019	58.44	21.99

2.1.1. Winter 2019

The SCALE2019 Winter cruise aboard the *S.A. Agulhas II* (VOY-038) departed Cape Town on 18 July 2019 and reached first ice on the 26 July 2019. The cruise had two ice stations where sea-ice cores were collected, one station on consolidated ice and another on pancake ice (Table 2.1). One consolidated floe was sampled overboard and four individual pancake floes were sampled onboard the vessel. At each ice station, a CTD was taken to characterise the underlying water column. The ice station locations are indicated on Figure 2.1.

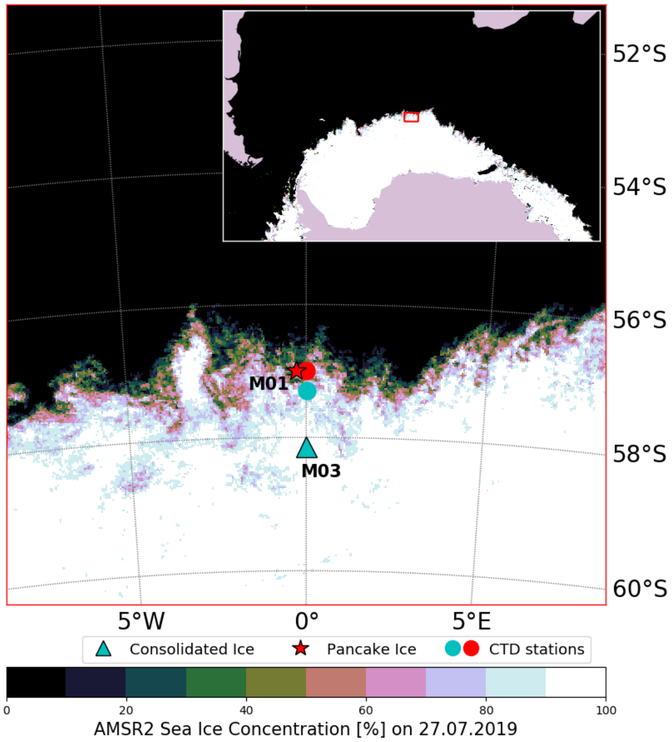

Figure 2.1 Location of the SCALE2019 Winter sea-ice core collection stations and CTD stations. Map is overlaid with sea ice concentration (in percentage) from the AMSR2 satellite product (Spreen et al., 2008).

2.1.2. Spring 2019

The SCALE2019 Spring cruise aboard the SA Agulhas II (VOY-040) departed Cape Town on 12th October 2019 and reached first ice on the 20th October 2019. The cruise had six ice stations where sea-ice cores were collected, four consolidated stations and two open drift stations (Table 2.1). One consolidated floe per station was sampled overboard while three individual ice floes were sampled onboard the vessel at the open drift stations. At each ice station, a CTD was taken to characterise the underlying water column. The ice station locations are indicated on Figure 2.2.

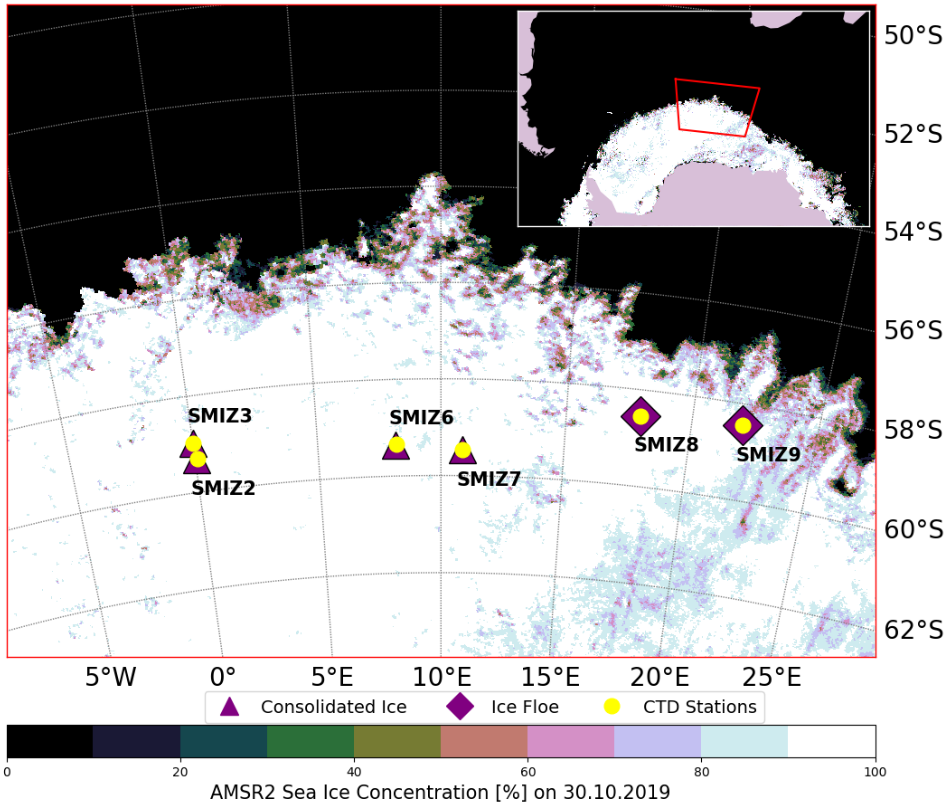

Figure 2.2. Location of the SCALE2019 Spring sea-ice core collection stations and corresponding CTD stations. Map is overlaid with sea ice concentration (in percentage) from the AMSR2 satellite product (Spreen et al., 2008).

2.2. Field sampling

Station locations were adjusted depending on the location of the ice edge and conditions. At the predefined station coordinates, operations were allowed to commence once the captain and crew of the *S.A. Agulhas II* deem the environmental conditions safe. Parameters to be considered for the suitability include ice thickness, ice floe diameter, wind speed, and visibility. The station passed the inspection if the ice was more than 45 cm thick and 100 m in diameter, if wind speed was lower than 25 Kn to allow for crane operations, and weather conditions permitted adequate visibility from the bridge to the ice operations and beyond. Attention was paid to floe topography, as the presence of extended ridge lines, for example, would indicate an area where two floes have collided and joined together, thus creating an area of instability that is prone to cracking and separating from the larger floe.

2.2.1. On-deck ice sampling

During the SCALE2019 expeditions, two types of sea ice from open drift conditions were collected for onboard sampling as described below. Individual pancakes were collected during the SCALE2019 Winter cruise, while broken floes were collected during the SCALE2019 Spring cruise. Both ice types were collected in the same manner and are hereby referred to as pancakes for the purposes of this section. While these ice types were collected in the same manner, they represented two distinct phases of the sea ice life cycle, growth and melt, and were treated as such in the interpretation of results in Chapter 6.

The lifting mechanism used to retrieve pancakes from the ice field was a custom-made net developed by the UCT Polar Engineering group, attached to the ship aft crane (Figure 2.3). The net and crane were able to accommodate a maximum pancake diameter of 3 m, and weight of 1.2 tonnes. Upon arrival at a predetermined station location, the ice field was surveyed for adequately sized pancakes and open water spaces to lower the mechanism into. Once the field was identified, an appropriately sized pancake was selected. The net was lowered via the aft crane into the water surrounding the pancake and dragged underneath the selected pancake (Figure 2.4a). The crew then manoeuvred the net to surround the pancake and raised it out of the water. Care was taken not to drop the net onto the pancake or to pull up the net abruptly. Once lifted, care was taken to maintain the pancake orientation, and it was brought onboard where it was placed on a wooden grid (Figure 2.4b). The purpose of the grid was to keep the pancake elevated above the deck during coring to allow the corer to pass through the pancake without being stopped by the deck below, and to reduce contamination of the samples. Once the pancake was on the grid, the net was lowered to allow for snow depth measurements and sampling. Once complete, the net was carefully removed from under the pancake by the crew. Often, the net removal process resulted in the pancake breaking, this was because the shackles that were used to weigh down the net in the water catch on the bottom of the pancake and have to be pulled free by the crane. Following the net removal, the lifting mechanism was reset and redeployed for the next pancake.

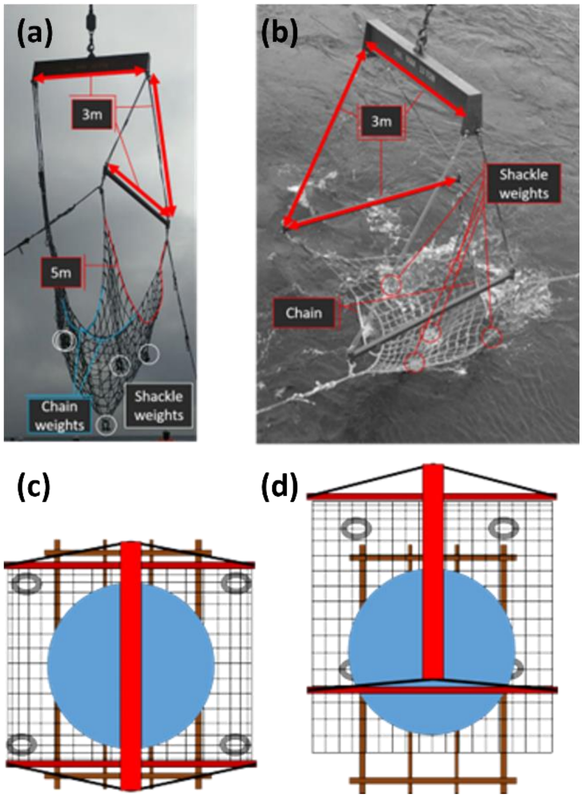

Figure 2.3. Ice lifting net contraption in air (a) and in the water (b). Schematic of the ice when placed on the wooden grid on deck (c) and removed from net (d). (Cr. Mark Hambrock)

After the net was removed, the first cores that were taken were used to measure the temperature profile of the pancake. These cores were extracted across the middle of the pancake (Figure 2.5) and depending on the size of the pancake, a minimum of three physical cores are taken. Following the physical cores were the trace metal clean and biogeochemical cores, then mechanical and structural cores. The order in which these cores were extracted is important because the longer the pancake sits on deck, the more brine was lost due to gravity drainage. The extracted cores were logged, bagged, and stored horizontally until processing.

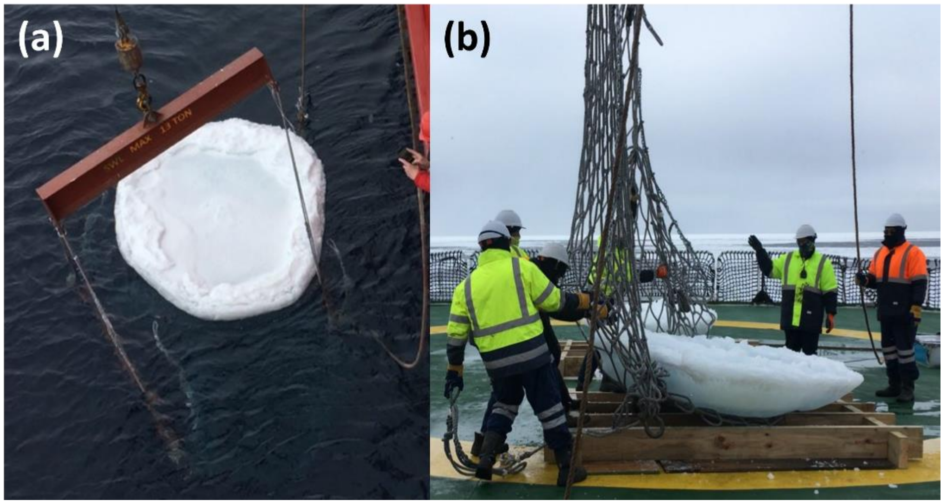

Figure 2.4. (a) Lifting contraption submerged below a pancake. (b) The pancake was placed on the wooden grid by sliding the net out from under it.

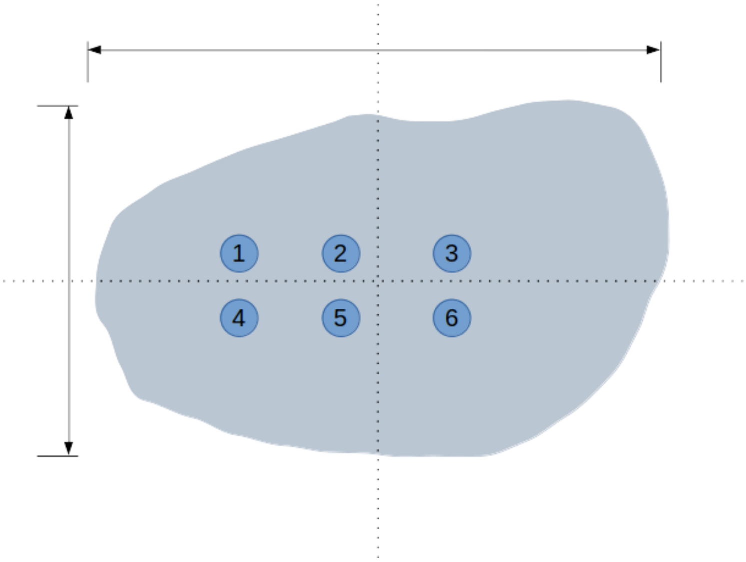

Figure 2.5. Diagram of an on deck pancake coring plan. Cores were taken along the middle of the pancake and clustered towards the centre and away from the edges. Cores were labelled numerically for identification and were placed in appropriately labelled bags during sampling.

2.2.2. Overboard ice sampling

At the predefined station coordinates, the ice field was assessed by the bridge and deck crew. Once the location was cleared, the safety assessment team were briefed by the on-deck crew with regards to safety and ice conditions. If a consolidated floe was found to have cracks and fractures as a result of the vessel, extra caution needed to be taken by the safety assessment team on ice. The team were harnessed, attached to the personnel carrier, and hoisted over the side of the vessel using one of the ships cranes, the choice of crane and subsequently the side of the vessel the team will be deployed on were at the discretion of the ship captain and crew.

Once craned over and before detaching from the hoist, the corer operator assesses the stability of the floe by piercing the snow with a stick until the ice layer below was reached. This assessment is done to determine the snow thickness and aggravate the ice layer to expose cracks along the working area and to ensure the ice below is hard enough to walk on. In the event that the stick was driven through both the snow and ice layer, the station is abandoned, and the team were to return to the ship immediately. Once the stick assessment was complete, the first core was taken while the team were still harnessed to and standing on the personnel carrier. The core was assessed for length, structure and texture. In order to pass the assessment, the core had to be longer than 0.35 m and not crumble when handled. If the test core failed the safety assessment, the operation was terminated, and the team returned to deck immediately. A successful assessment allowed the safety team to step off the personnel carrier and begin the safety assessment of the area. The same steps were followed, and when satisfied with the selected area, sample collection may commence. Drastic variations of thickness along the desired sampling transect may be indicative of an unstable area, and typically, the area would be abandoned, likely biasing the measurements towards floes with more even thicknesses.

Cores were collected along a transect in clusters. A minimum of three clusters were planned per station, if time permitted, more clusters were sampled (Figure 2.6). Once cleared for sampling, a path was assigned along the sampling transect. Teams were instructed to keep on the path when moving between the ship and the clusters, to avoid contaminating the cluster areas or stepping in core cavities. The furthest cluster from the ship was sampled first with the teams moving progressively towards the ship as clusters were completed. A two-meter space between outer cores from each cluster was maintained to avoid contact between clusters, and to achieve a feasible spatial resolution. The order of sample collection was dictated by the requested cores and their corresponding protocols. In the case of SCALE2019 core collection, two corers were used, to allow for the trace metal group to decontaminate the barrel that would be used to collect their samples and not limit sampling prior to trace metal clean core extraction. Assessment cores were allocated to the microplastics team, as these cores and the sampling site would be exposed to contamination factors for a shorter period of time, as opposed to collection once the full team and equipment are present on the ice. The physical and biogeochemical cores were collected last, to maintain in situ conditions for as long as possible.

We acknowledge that the transect and safety assessment goes against the principle of random sampling, but they’re necessary to ensure safety when on ice and since the tests that will be run on the cores cannot be run on one core, the cores need to be related back to each other.

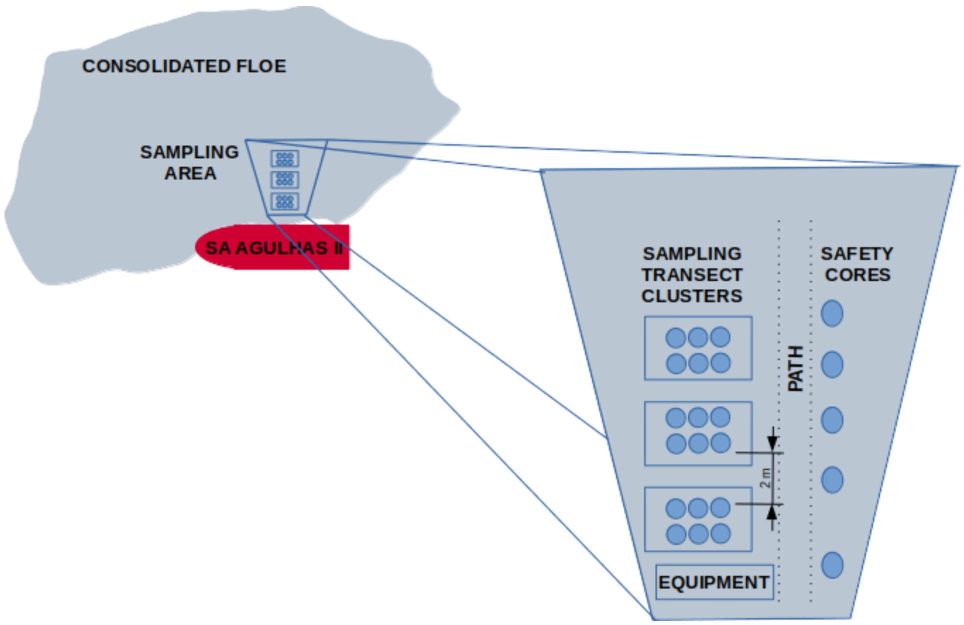

Figure 2.6. Schematic diagram of the sampling transect implemented at a consolidated floe station.

2.2.3. Sea-ice core sampling

Ice cores were extracted using a powered Kovacs Mark II coring system (Figure 2.7). The corer was driven by an electric drill, as opposed to a three-stroke petrol motor, this was done to remove the pollution and contamination effects of the motor. The selected coring area was cleared of the snow layer, the barrel was placed perpendicular to the ice and driven straight down until either the barrel was full (ice thickness > 1 m), or the ocean below was reached (ice thickness is < 1 m). The Mark II coring system retrieves a core that has a diameter of 0.09 m and a maximum length of 1 m. In the case of the sea ice thickness exceeding 1 m, the core was broken at the 1 m point using the barrel and extracted, the core piece was removed from the barrel. The empty barrel was reinserted into the core cavity with an extender attached to it and driven until the barrel was either full or the ocean below is reached. Care was taken when reaching the ice-ocean interface as the possibility of losing either the core or the coring system exists.

Figure 2.7. The Kovacs Mark II sea ice coring system used sea-ice floe during both SCALE2019 cruises. The barrel can retrieve a core up to 1 m long and 9 cm in diameter. Image retrieved from the Kovacs website (https://kovacsicedrillingequipment.com/coring-systems/mark-ii/)

Once extracted, cores were placed in opaque PVC tubing that were pre-marked with top and bottom to indicate the orientation of the core. These bagged cores were stored horizontally at all times, to minimise the loss of material due to brine drainage. Cores were taken either to the UCT Mobile Polar Laboratory (Polar Laboratory; Figure 2.8) for immediate sectioning or to the scientific freezer where they were stored at -21ºC for the journey back to UCT in Cape Town. Cores taken back to UCT were stored horizontally in chest freezers at -21ºC until processing.

Given the sensitive nature of the biogeochemical measurements, any factors that could lead to contamination of the samples collected were taken into consideration and every attempt to mitigate their influence on the samples were taken. The ice corer barrel was cleaned using super-clean, deionised water before the station to remove any substances that may have originated from transportation and storage, and after every coring station to remove remaining salt and protect the barrel from rusting. The barrel was primed by taking a number of cores for non-biogeochemical purposes before taking the biogeochemical cores, thus ensuring a clean corer. Latex gloves were used by team members handling the collected samples.

2.3. Laboratory processing

Of the cores collected, the ones allocated for the physical properties (temperature, salinity) were processed on the ship following collection, while the cores allocated for biogeochemical analysis were stored horizontally at -21ºC in the ship freezers and in chest freezers at -21ºC at UCT until processing. While storage at this temperature is commonly used to preserve sea-ice cores for biogeochemical analysis, studies have shown that long-term freezing can alter certain physical and chemical properties, particularly the distribution of brine, the concentration of nutrients such as ammonium, and microbial community structure (Cox & Weeks, 1986; Miller et al., 2015). Although these effects were not evaluated in the current study, all samples were treated consistently to minimise relative bias. Future work is planned to specifically assess the impacts of long-term storage on both physical and biogeochemical properties of sea ice to inform and improve sample handling protocols. The cores were moved to the Polar Laboratory (Figure 2.8) and sectioned for processing. Cutting of the cores was done at -10ºC to avoid melting during handling.

Figure 2.8. The UCT Mobile Polar laboratory, pictured here installed on the poop deck aboard the *S.A. Agulhas II* for the SCALE2019 cruises.

2.3.1. Physical cores

Immediately following collection, the three cores allocated to physical properties were sampled for temperature by drilling holes along the length of the cores starting from the bottom of the core and moving to top of the core in 0.05 m increments using a battery powered hand drill. A PT-100 temperature probe, with an accuracy of 0.01°C, was inserted into the holes and the temperature was recorded. The cores were then placed in opaque polyethylene tubing and transported horizontally to the mobile polar laboratory to be processed for salinity measurements. The cores were sectioned into 0.05 m segments within an hour of collection using a bandsaw fitted with a Swedish strip steel blade, starting from the bottom of the core. The cut segments were logged and placed in cleaned, prelabeled plastic containers. The segments were allowed to melt at room temperature regardless of light conditions. The meltwater was transferred to amber bottles and stored at room temperature until analysis, this was to ensure the sample temperature was in equilibrium with the salinometer temperature. Samples were read in triplicate using a 8410A Portasal portable salinometer which has a reported accuracy of <0.003 g kg^{-1} (OSIL, 2020).

2.3.2. Biogeochemical cores

The biogeochemical (BGC) sea-ice cores were placed in labelled PVC tubing and sealed with cable ties. These cores were stored horizontally in the dark at -21°C aboard the *S.A. Agulhas II* for the journey back to Cape Town. The cores were moved to a -21°C chest freezer, where they remained in the dark and horizontal in long-term storage until processing. The cores from winter and spring were all processed approximately two years after the winter cruise in 2021 due to a delay in operations owing to the COVID-19 pandemic. The winter spring cores were stored for approximately 5 months less than the winter cores as they were collected last and processed at the same time as the winter cores. The processing of the BGC cores began with the sectioning of the cores in the Polar Laboratory. Initially, the cores were to be sectioned using the bandsaw that was employed for the physical cores, but contamination concerns forced us to alter the cutting methods. The BGC cores were cut using a hand jigsaw fitted with a stainless-steel blade on a wooden rig fitted with plexiglass plates (Figure 2.9). The jigsaw blade was thicker than the bandsaw blade, and as a result, more of the core was shaved off during the cutting process and the cutting scheme had to be altered to avoid further loss of ice. The initial scheme included trimming the outer sections of the core to expose a relatively pristine section, where the outer (discarded) sections would be used for the chlorophyll and salinity analysis and the inner section would be used for the isotope and nutrient analysis (Table A.1). The new scheme divided the 5 cm segment in half, this would allow for chlorophyll analysis and particulate organic nitrogen (PON) analysis while maintaining enough of the core to ensure sufficient meltwater volume (Table A.1). Each half segment was sealed in clean, labelled plastic bags and stored in a chest freezer at -21°C until analysis. Orientation of the core and resulting segments were maintained during cutting to ensure all half segments dedicated to PON or chlorophyll came from the same side of the core.

Figure 2.9. (a) wooden ice core cutting rig with jigsaw, (b) cutting set up in the polar laboratory.

Care needed to be taken to avoid contamination of the sea ice samples as nutrient concentrations are typically very low. Sample care started from the time of the sea-ice core collection and was carried through every step of the analysis procedure. Bulk nutrient concentrations were determined from melted core segments. A variety of melting methods have been applied to sea ice samples collected in both hemispheres. These include direct melting, melting in filtered seawater and melting in concentrated brine (Miller et al., 2015). The latter two methods are employed to reduce the stress and shock associated with large temperature and salinity changes that occur during melting (Miller et al., 2015). This protocol adopts the direct melting method. To mitigate any residual shock and changes in the samples, the ice is melted in the dark in either a fridge or insulated box.

Each half segment was scraped with an ethanol cleaned blade to remove the outer layer of ice (<1 cm) that was in contact with the cutting apparatus and placed in a labelled glass beaker that had been prepared by acid washing in a 10% HCl acid bath, rinsed with DI water and combusted at 500°C for 5 hours. The sample-filled beakers were covered with combusted aluminium foil and placed in a cooler box to melt overnight. Once fully melted, the samples were agitated to mix the meltwater, this removes the stratification that occurs during the melting process. The meltwater from each half segment was filtered through a combusted 25 mm, 0.3 µm Advantec GF/F filter (GF-75s) on a glass filter tower connected to a vacuum pump (Figure 2.10a).

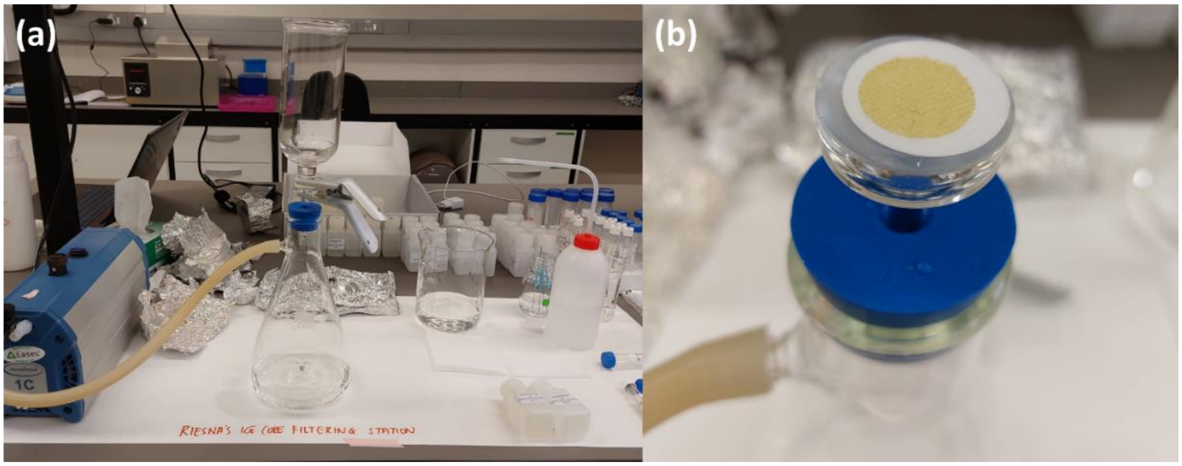

Figure 2.10. (a) Filtration set up with trap flask and funnel connected to a vacuum pump. (b) Filter after a half-segment has been filtered through.

The filters from the PON half segment were placed in combusted aluminium foil envelopes and stored in plastic bags at -80°C until analysis. The filters from the chlorophyll half segments were placed in glass vials and stored at -20°C until analysis (Figure 2.10b). The beakers were weighed with the meltwater and without the meltwater to determine the weight of the sample, this was then used to find the volume of the meltwater that was filtered for the PON and chlorophyll analysis. The filtrate for each half segment was collected in the same trap flask for biogeochemical testing. The filtrate from both halves was homogenized by swirling the trap flask and then aliquoted into duplicate clean 15 ml Falcon tubes for bulk nutrient analyses and high-density polyethylene (HDPE) bottles that had been soaked ("aged") with an ortho-phthalaldehyde (OPA) working reagent for ammonium measurements. Two more HDPE bottles were filled for dissolved organic nitrogen (DON) and nitrate isotope measurements. These aliquots were stored at -20°C immediately following sampling until analysis. Meltwater was stored in glass exetainers in a fridge for oxygen isotope ($\delta^{18}O$) analysis. The volume and sample requirements for each test are summarized in Table A.2.

Bulk nutrient analysis provides insight into the biological activity in the ice and the influence of the ice on the surrounding ocean during ice growth and melt. The bulk concentrations of dissolved phosphorus ($\mathrm{PO_4^{3-}}$), nitrate + nitrite ($\mathrm{NO_3^- + NO_2^-}$), nitrite ($\mathrm{NO_2^-}$) and silicic acid ($Si(\mathrm{OH})_4$) were measured using a SEAL AA500 segmented flow auto-analyser. The detection limit was 0.05 µM, 0.1 µM, 0.05 µM, and 0.2 µM for $\mathrm{PO_4^{3-}}$-, $\mathrm{NO_3^- + NO_2^-}$, $\mathrm{NO_2^-}$ and $\mathrm{Si(OH)_4}$, respectively, while the precision was ±0.06 µM, ±0.2 µM, ±0.05 µM, and ±0.2 µM. Aliquots of 4 certified reference materials (JAMSTEC, lots CE, CC, CH and CG) were included in each run to ensure measurement accuracy. The nitrate-only concentration ($\mathrm{NO_3^-}$) was calculated by subtraction. Hereafter, all references to $\mathrm{NO_3^-}$ are to the $\mathrm{NO_3^-}$ only data. It is known that silicic acid can polymerise upon freezing, and redissolution during thawing is often incomplete, potentially leading to underestimation of its original concentration (Hydes et al., 2010; Miller et al., 2015). To mitigate this effect, samples were thawed and allowed to equilibrate to room temperature before analysis; however, some loss due to incomplete redissolution cannot be ruled out.

The ammonium ($\mathbf{NH_4^+}$) analysis was done manually using the fluorometric method of Holmes et al. (1999). OPA working reagent was added to the frozen samples prior to defrosting them for analysis. The samples were slowly warmed to room temperature in a water bath after OPA was added and incubated in the dark for 4 h once defrosted. Each sample was measured in duplicate using a Turner Designs Trilogy 7500-000 fluorometer equipped with a UV module. The detection limit, calculated as twice the pooled standard deviation (SD) of all standards, was 0.05 µM. Standards and blanks were made daily using Type-1 Milli-Q water. Precision was ± 0.03 µM for replicate samples and standards.

The chlorophyll-a (chl-a) concentrations were determined using the non-acidified fluorometric method (Welschmeyer, 1994). Acetone (90 %) was added to the borosilicate tubes containing the filters and incubated at −20 °C for 24 h. The extracted sample was read using a Turner Designs Trilogy fluorometer that was calibrated with an analytical standard (*Anacystis nidulans*, Sigma-Aldrich®) prior to sampling.

The $\boldsymbol{\delta^{18}O}$ determination involved further filtering of the samples through a 0.2 µm filter and analysed using a Picarro Cavity Ring-Down Spectrometer (CRDS) (Walker et al., 2016). The oxygen isotope composition is given as per mil difference relative to VSMOW (‰, Vienna Standard Mean Ocean Water).

At each sea-ice station, a conductivity–temperature–depth (CTD) cast was conducted for the seawater. Duplicate nutrient samples were collected in 50 mL Falcon tubes from discrete depths to characterise the water column. For the purpose of this work, only the surface samples were used to compare with the in-ice nutrients. The duplicate samples were analysed manually for PO_4^{3-} and NO_2^- (Bendschneider & Robinson, 1952; Murphy & Riley, 1962) using a Thermo Scientific Genesys 30 Visible spectrophotometer. The precision and detection limit were ±0.05 µM and 0.05 µM for NO_2^- and ±0.06 µM and 0.05 µM for PO_4^{3-}. The concentrations of $NO_3^- + NO_2^-$ and $Si(OH)_4$ were determined using a Lachat QuikChem 8500 Series 2 flow injection auto-analyser. Aliquots of certified reference materials (JAMSTEC) were included in each run to ensure measurement accuracy. The detection limit was 0.1 µM and 0.2 µM for $NO_3^- + NO_2^-$ and $Si(OH)_4$ respectively, while the precision was ±0.4 µM and ±0.2 µM. NH_4^+ was analysed manually following the methods of Holmes et al. (1999) in the same manner as the sea-ice samples.

In order to facilitate comparison with the seawater concentrations below the ice, the in-ice nutrients (including NH_4^+) were salinity-normalised using the equation described by Fripiat et al. (2017):

$$C_{norm} = C \cdot \frac{S_w}{S_i} \tag{9}$$

where C_{norm} is the salinity normalised concentration, C is the measured bulk concentration, S_w is the salinity of the seawater, and S_i is the corresponding measured bulk salinity of the ice segment.

2.3.3. Sea-ice texture and stratigraphy

At each station, a dedicated cross-polarisation core was collected. The core was first prepared using the band saw in the mobile polar laboratory and were cut into 0.1 m segments from the top. These were then subsequently cut further down the length of the middle of the segment to create a thick section of 8 mm. Each thick section was processed using a custom-made thermal macrotome cutter that created thin sections of 1 mm thickness, which were subsequently viewed through cross-polarised sheets and photographed. The images were then analysed further to construct stratigraphy diagrams from the identified layering of textures in these images along with the average crystal size. These methods are further discussed in Johnson et al. (2023).

2.3.4. Relative Brine Volume

Brine volume was calculated using the relationship between temperature and salinity described by Frankenstein & Garner (1967):

$$V_b = S_{si}\left(\frac{49.185}{T} + 0.532\right) \tag{10}$$

where V_b is the brine volume fraction, S_{si} is the bulk salinity and T (ºC) is the absolute value of the measured temperature of the section at the time of coring.

For the purposes of this study, a 5% brine volume threshold is used as a first-order approximation of permeability, consistent with (Golden et al., 1998). However, this threshold was derived from columnar sea ice, and its applicability to the frazil-dominated or granular ice of the AMIZ may be limited. Recent studies suggest that granular sea ice may have a higher percolation threshold, possibly around 10%, due to its more disordered crystal structure and reduced brine channel connectivity (Maus et al., 2021; Golden et al., n.d.). Future studies should investigate permeability thresholds specific to frazil and granular ice types to refine our understanding of brine connectivity and biogeochemical exchange in these environments. This limitation should be taken into account when interpreting the results presented in the following chapters.

2.4. Historical sea-ice core data

The database of pack ice nutrient profiles compiled by Fripiat et al. (2017) has been used to compare with our results in Chapter 3. A subset of these cores based on the region (cores within 10° E/W of the 0° meridian), season (cores collected between June and August to represent winter) and length (cores exceeding 1 m were excluded to ensure only first year ice was considered) were compared to our data in Chapter 3. These criteria yielded 28 cores for winter (Figure 2.11) that were used to produce the ranges displayed in Chapter 3. The data were normalised by depth (100*sampling depth / total ice thickness) and binned into 10 % intervals.

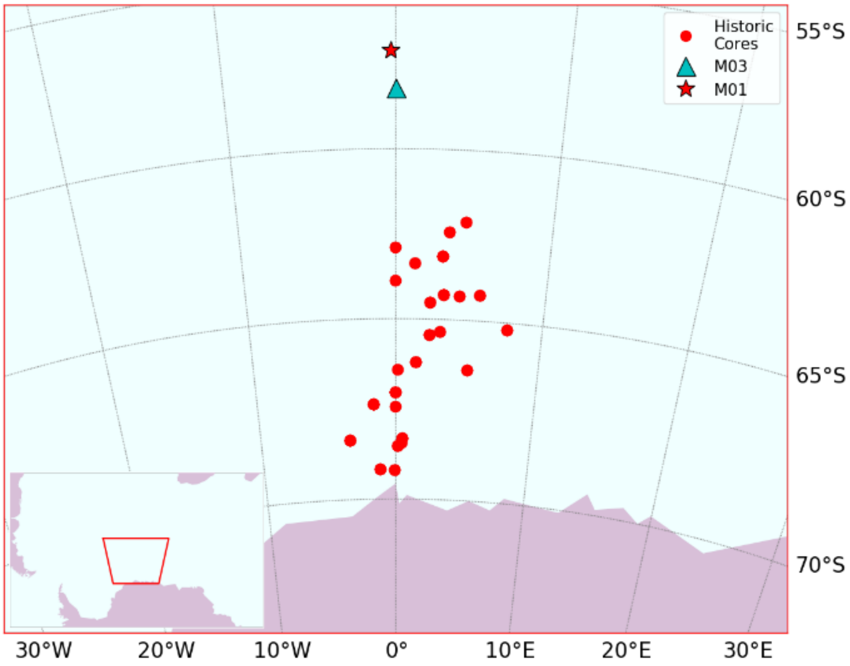

Figure 2.11. Map showing the locations of the ice cores that met our criteria for the historical data comparison for winter in Chapter 3. The red dots represent the historical cores compiled by Fripiat et al. (2017). The locations of our stations per season are also indicated on each map.

2.5. Modelling sea ice

This section describes the methods for model set up and evaluation to identify the appropriate configurations for the simulations presented in Chapter 3 and 4.

2.5.1. Lagrangian backtracking of the sea-ice floes

The coarse resolution sea-ice drift product of the EUMETSAT Ocean and Sea Ice Satellite Application Facility (OSI-SAF) (OSI SAF, 2021) and the OceanParcels Lagrangian tool (Delandmeter & Sebille, 2019) were used to back-track the origin of the sampled sea-ice floes. The satellite product consists of daily drift data that are averaged over two days, with each data point covering an area of 62.5 km by 62.5 km. This dataset was re-gridded into a 0.5 degrees regular geographic grid with a bilinear interpolation and used in the Lagrangian calculation backward from the day of sampling. The backtracking continued until the ice floe could no longer be detected in the satellite product, typically when its concentration dropped below the satellite's detection threshold, or the floe became too small to be resolved. This approach, including its assumptions and limitations, is described and validated in detail by Johnson et al. (2023).

For the winter sampling described in Section 2.1.1, the resolution of the OSI-SAF product initially produced a back trajectory of 11 days for the floe sampled at M03 (red track in Figure 2.12). This short lifetime is unrealistic for thicker FYI, and the trajectory was corrected by considering virtual stations located at the same longitude but shifted of 0.5, 1, and 2 degrees south. The results are shown in Figure 2.12, with the back trajectories relocated to align with the original sampling location. The similarity between trajectories indicates that the floe field drifted coherently within a spatial scale of less than 2 degrees. The sensitivity analysis revealed that the 2-degree offset cannot be used since the drift was very intense in early June 2019, and the sea-ice field moved northward considerably in just a few days, thus decreasing the confidence on the coarse product which is averaged over two days. The back trajectory computed with the offset of 1 degree (purple line in Figure 2.12) was used to extract the environmental variables used in our model simulations.

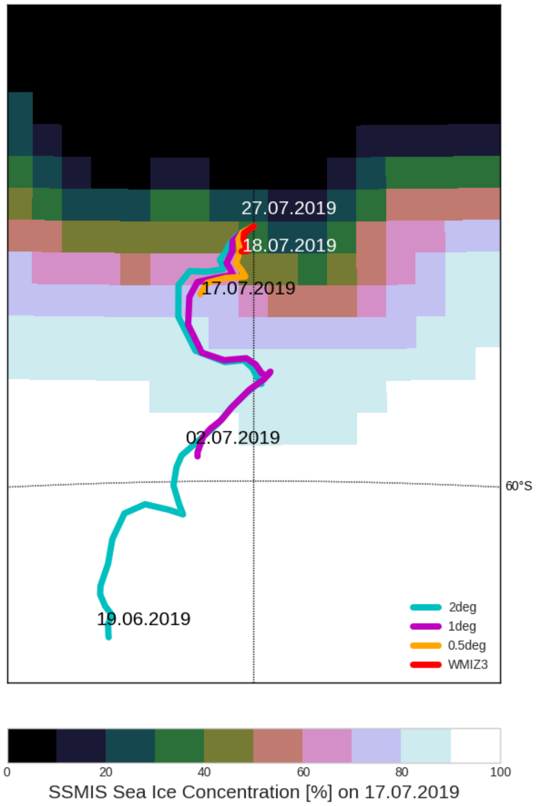

Figure 2.12. Lagrangian trajectories computed for the virtual floes located at 0.5, 1 and 2 degrees south of the M03 station, overlain to the SSMIS SIC on 17.07.2019. The trajectories have been shifted northward of their relative offset to better visualize the difference in the shape. The purple trajectory is the one used for the model simulation displayed.

2.5.2. The Enhanced Sea Ice Model (ESIM)

Work done by Tedesco et al. (2009, 2010) introduced a novel approach to modelling sea ice thermodynamics from a biogeochemical perspective by defining the Biologically Active Layer (BAL) in their thermodynamic sea ice model, the Enhanced Sea Ice Model (ESIM) (Tedesco et al., 2009). The BAL is further discussed in Chapter 3.

The Enhanced Sea Ice Model (ESIM) is a comprehensive 0-D sea ice thermodynamic model, developed by Tedesco et al. (2009) that has two versions, The ESIM1 (Tedesco et al., 2009) and ESIM2 (Tedesco et al., 2010). The ESIM1 was modelled after the Semtner 0-layer model (Section 1.5) and was initially applied to the landfast ice environment of the Baltic and to Arctic fjords. The ESIM2 improves on the thermodynamic components of the ESIM1 by introducing a halodynamic component to simulate the evolution of salinity within the sea ice and the dependence of previously constant physical parameters on salinity. The inclusion of halodynamics allows the model to be treated as a more general sea ice physical model and to calculate the depth of the biologically active layer (BAL) (Tedesco et al., 2010). The aim of the development of ESIM was to model the physical properties of sea ice with the intention of coupling with a biogeochemical model to aid in the study of sea ice biogeochemistry. This work is the first implementation of ESIM to simulate young ice conditions in the AMIZ.

2.5.2.1. Model set up: Atmospheric forcings

The ESIM is forced by atmospheric boundary conditions to determine the balance of the heat fluxes at the ocean-ice, ice-atmosphere and ocean-atmosphere interfaces that are used to compute the surface temperatures. The energy balance is used to determine the growth and melt of ice as briefly introduced in Section 1.5. The model and governing equations are discussed in detail by Tedesco et al. (2010). The ESIM was initially designed and run using the National Centres for Environmental Prediction’s reanalysis (NCEP2) (Kanamitsu et al., 2002) data in the Baltic. In order to run the ESIM with Antarctic conditions, multiple reanalysis data products were compared to assess the influence of spatial resolution on the simulated sea-ice cover in the Antarctic. The chosen products are the ECMWF Re-Analysis 5 (ERA5) (Hersbach et al., 2018), the Japanese 55-year Reanalysis (JRA55) (Kobayashi et al., 2015) and NCEP2. The atmospheric data have been extracted at the location of station M03 during winter 2019 (Figure 2.1) and used to simulate the whole year 2019. The atmospheric forcing file comparison (Figure 2.13) indicates that the three reanalysis products compare well with each other in terms of overall seasonal signal.

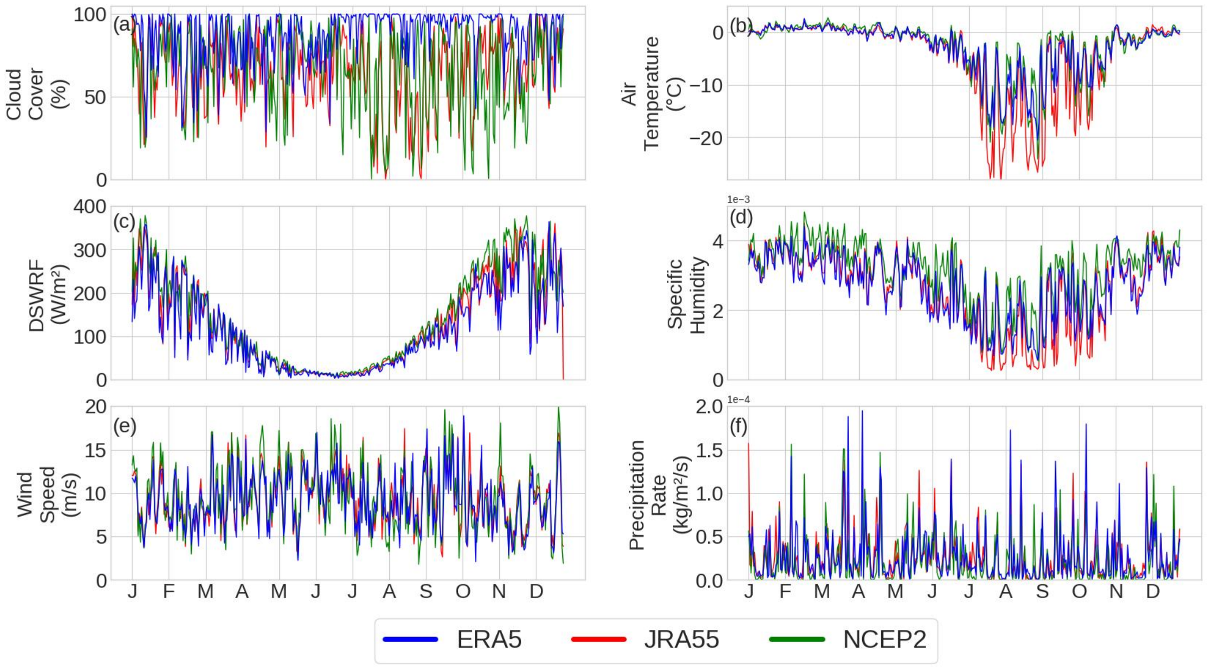

Figure 2.13. Comparison of the atmospheric data at the location of station M03 from the reanalysis products. (a) cloud cover, (b) Air temperature, (c) downward shortwave radiation, (d) specific humidity, (e) wind speed and (f) precipitation rate. Blue lines indicate ERA5, red lines indicate JRA55 and green lines indicate NCEP2.

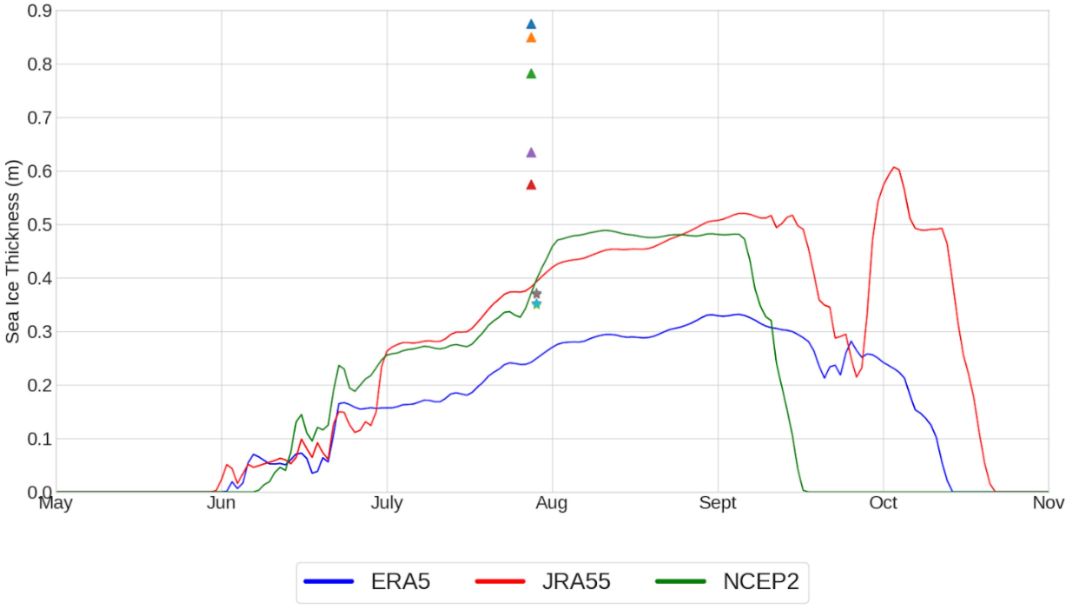

Figure 2.14. Comparison of the sea ice thickness simulated by the ESIM using the different reanalysis products atmospheric forcings. Blue lines indicate ERA5, red lines indicate JRA55 and green lines indicate NCEP2. The coloured symbols indicate the sea ice thickness at M03 (triangles) and M01 (stars).

The sea-ice cover produced by the ESIM is presented in Figure 2.14. The start and end of the ice season is staggered between the three reanalysis products. JRA55 starts the earliest and lasts the longest, followed by ERA5 and finally NCEP2 with the latest initiation and shortest ice season.

Overall, none of the products tested were able to reproduce the sea ice thickness at the station location, this is because ESIM does not include sea-ice dynamics, it simulates the potential thermodynamic growth of sea ice given the atmospheric conditions (see Section 1.3). Given the lack of observations on thickness seasonality at this location, it is not possible to say which product is the best. Based on considerations of freeze up and break-up periods against satellite sea ice concentration data, we chose to use ERA5, which has also been demonstrated to compare well with direct observations in the Southern Ocean (Vichi et al., 2019).

For the simulations in Chapter 3 and 4, the atmospheric data used in the ESIM simulation were not from a fixed location but they were extracted along the floe back trajectory (Figure 2.15). To create a yearlong timeseries, the initial and final position of the floe were fixed for the time before the backtrack period starts and after the sampling day.

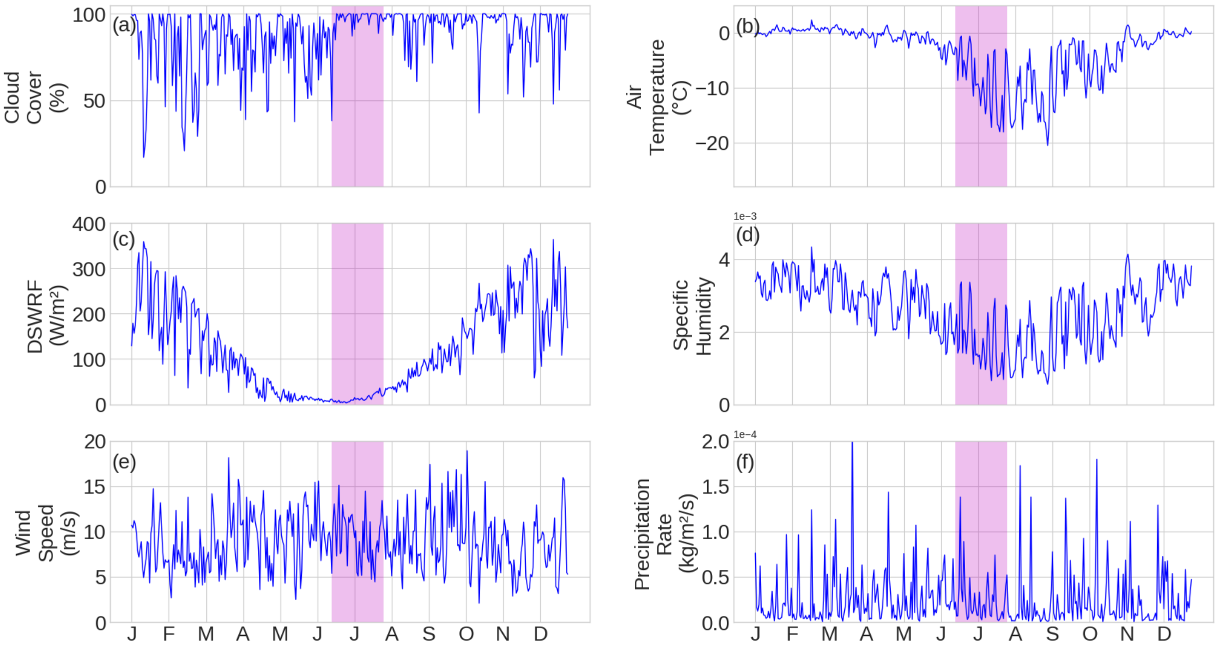

Figure 2.15. Timeseries of ERA5 (Hersbach et al., 2018) atmospheric data extracted along the floe trajectory. (a) cloud cover, (b) Air temperature, (c) downward shortwave radiation, (d) specific humidity, (e) wind speed and (f) precipitation rate. The purple shading indicates the backtrack period. The timeseries for 2019 was created by fixing the initial location of the floe for the time leading up to the backtrack period and the station location for the period following the sampling day.

2.5.2.2. Model set up: Oceanic forcings

One major feature of Antarctic sea ice is the dominance of the oceanic heat flux (OHF) (McPhee et al., 1999). This flux is unknown and can only be measured with dedicated moorings on pack ice or calculated via numerical simulations. The model was perturbed by varying the OHF to study the sensitivity of the simulated sea-ice thickness against observations at M03. The control run used a fixed OHF of 11.72 W/m^2 that was estimated using in-situ ice drift and sea surface temperature data with the formula described by McPhee et al. (1999) and Ackley et al. (2015):

$$OHF = C_H \cdot C_W \cdot v_i \cdot \rho_w \cdot \left(T_{sfc} - T_{fr}\right) \tag{11}$$

where C_H is the turbulent exchange coefficient (estimated as 1.7x10^4 by McPhee et al. (1999) in pack ice conditions), C_W is the specific heat of water, v_i is the sea-ice drift from South African Weather Service buoys deployed during the SCALE Winter 2019 expedition (de Vos et al., 2022), ρ_w is the water density and $\left(T_{sfc} - T_{fr}\right)$ is the temperature elevation computed as the difference between the sea-surface temperature (T_{sfc}) from the CTD and the freezing temperature (T_{fr}). The latter was estimated with the MATLAB GSW package (https://www.teos-10.org/) using the corresponding surface salinity from the CTD.

The control run is compared to two perturbed runs, the first was setting the OHF to 0 $\mathrm{W/m^2}$, effectively 'turning off' the OHF, and the second test introduced an OHF time series that was computed using the equation above which used timeseries data for v_i, T_{sfc} and T_{fr} from the GLORYS ¼ degree resolution product (retrieved from the CMEMS website at https://marine.copernicus.eu/; https://doi.org/10.48670/moi-00018) that was extracted along the computed floe trajectory (Figure 2.16).

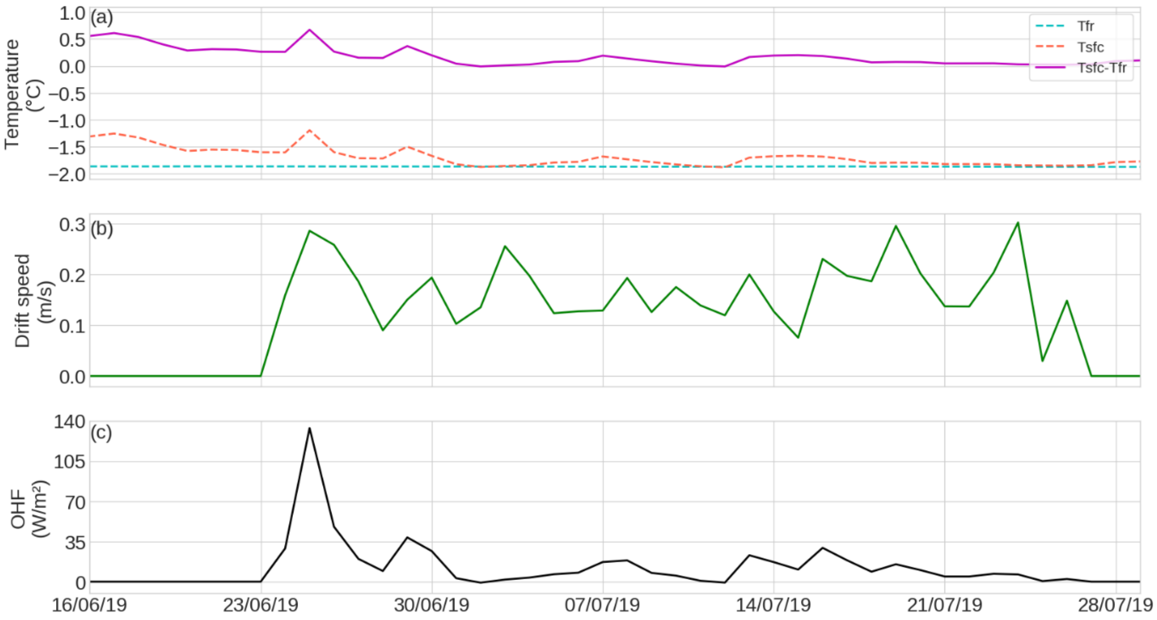

Figure 2.16. (a) Freezing temperature (Tfr; blue dashed line), surface temperature (Tsfc; orange dashed line) and computed temperature elevation (Tsfc – Tfr; solid purple line) and (b) sea ice drift speed extracted for the backtrack period and location from the GLORYS reanalysis product. (c) computed ocean heat flux for the floe trajectory using the equation described by McPhee et al. (1999) and Ackley et al. (2015).

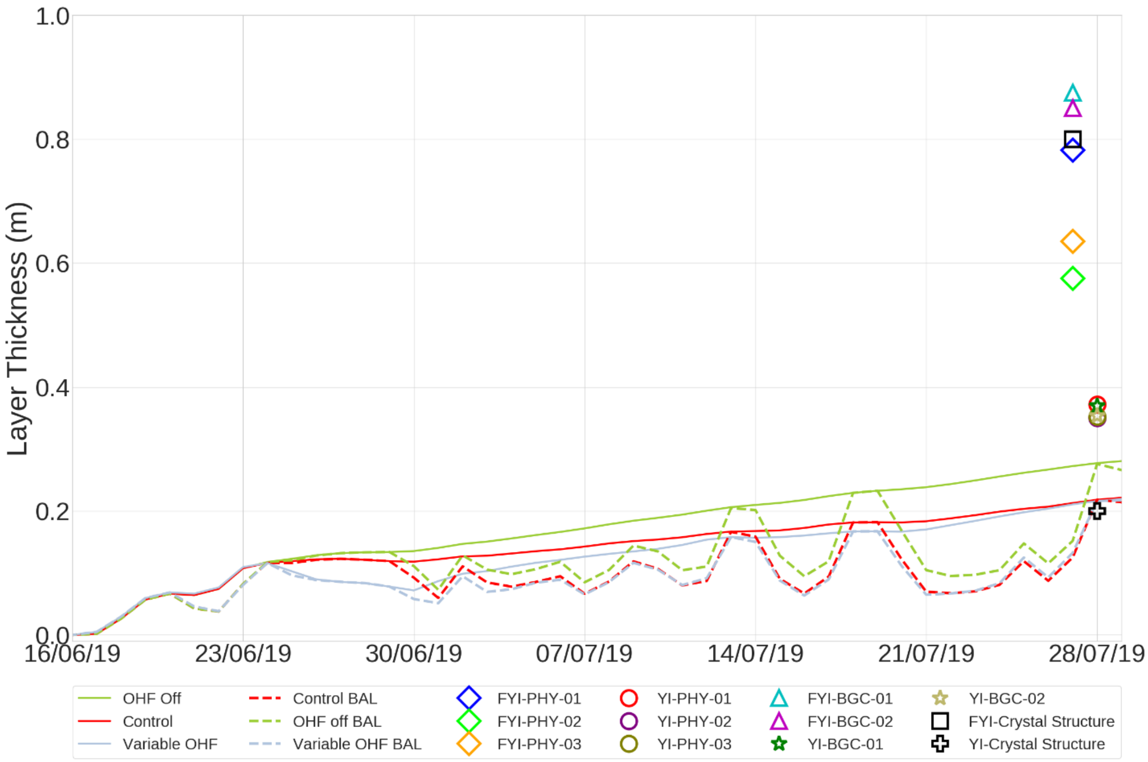

Figure 2.17. Sea ice thickness (solid lines) and biologically active layer thickness (dashed lines) produced by the ESIM for the three OHF sensitivity tests. Red indicates the control run (11.72 W/m^2), green indicates the run with OHF turned off (0 W/m^2) and grey indicates the run with a variable OHF timeseries.

2.5.3. The Biogeochemical Flux Model (BFM-SI)

The properties of the BAL that are simulated by the ESIM are used to initialize the sea ice component of the Biogeochemical Flux Model, the BFM-SI (Tedesco & Vichi, 2010; Vichi et al., 2020; www.bfm-community.eu/). The BFM-SI simulates the entrainment of dissolved constituents from the upper ocean into the sea ice. This flux is parameterized as linearly dependent to the bottom sea-ice growth rate, without explicitly resolving the turbulent fluxes (Tedesco & Vichi, 2010; Duarte et al., 2022). For our purposes, sea-ice biology in the model has been switched off, while the pelagic variables are activated to simulate the concentrations below the sea ice from the time of freeze-up. In addition to the BAL properties from the ESIM (Figure 2.18), the BFM-SI was initialised using the observed nutrient concentrations in the surface ocean below the sea ice at the time of sampling (Table 2.2). These concentrations are assumed to be the background concentrations throughout the winter period, given that the observed mixed layer was more than 150 m deep. It should be noted that a single concentration value was used per variable - to our knowledge, there are no time series of nutrient concentrations from the Southern Ocean since there are no permanent stations. It should also be noted that the nutrient variability between the different samples from the same season is relatively small. The simulations are short enough to assume that the measured winter concentration is representative of the replenished nutrient conditions.

Table 2.2. Table of surface seawater nutrient and chlorophyll concentrations that were used to initialize the BFM-SI for the winter 2019 simulations.

Variable	Concentration
$\mathbf{Si(OH)_4}$	72.1 µM
$\mathbf{PO_4^{3-}}$	2.36 µM
$\mathbf{NO_3^- + NO_2^-}$	28.5 µM
$\mathbf{NH_4^+}$	0.60 µM
Chlorophyll	0.24 µg/L

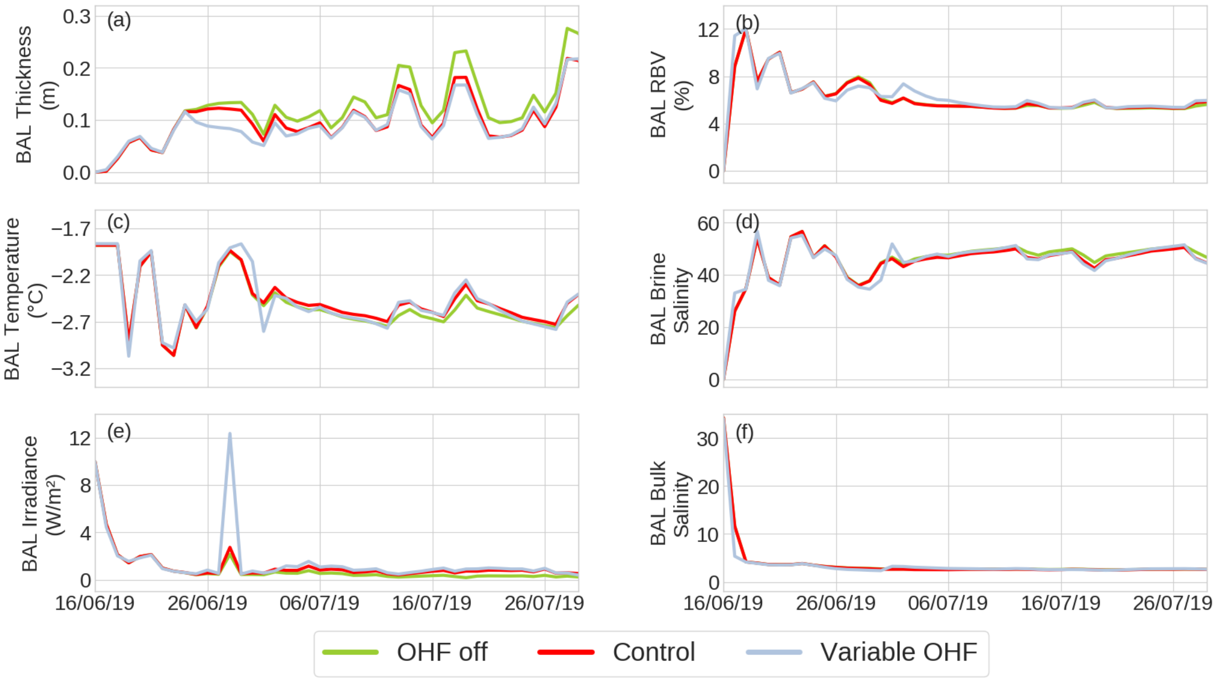

Figure 2.18. ESIM output over the backtrack period that is used to initialize the BFM-SI. (a) BAL thickness, (B) BAL relative brine volume (RBV), (c) BAL temperature, (d) BAL brine salinity, (e) BAL irradiance and (f) BAL bulk salinity. The red line indicates the control run (Control), green line indicates the run with OHF turned off (OHF off) and grey indicates the run with a variable OHF timeseries (Variable OHF).

Chapter 3

3. Rafting of growing Antarctic sea ice enhances in-ice biogeochemical activity in winter[1]

3.1. Introduction

The Antarctic marginal ice zone (AMIZ) is a dynamic region that is dominated by small (< 10 m diameter) floes and frazil ice. The unconsolidated nature of the ice pack leaves it vulnerable to atmospheric forcings, which results in a mobile ice pack. Studies around Antarctica (Jeffries & Weeks, 1993; Worby et al., 1998) have shown that sea ice exceeding 0.5 m thick usually results from deformation-related processes rather than thermodynamic growth. Sea-ice deformation is a result of several processes due to wind, heat fluxes and wave action, which leads to floes being reshaped, flooded and advected on top of surrounding floes (Lange & Eicken, 1991; Worby et al., 1998; Auclair et al., 2022). This process results in irregular crystal structures (Lange & Eicken, 1991; Tison et al., 2020) and the formation of multiple internal biological communities within the sea ice substrate (Spindler, 1990).

Nutrients in sea ice, such as nitrate, silicate, and phosphate, are imperative for the survival of the internal biological communities in sea ice. Studies on nutrients in pack ice have been carried out by (Clarke & Ackley, 1984; Arrigo et al., 1995; Gleitz et al., 1995; Fripiat et al., 2014; Roukaerts et al., 2016; Fripiat et al., 2017; Tison, Schwegmann, et al., 2017). These studies are based on data limited temporally and spatially, with a bias towards spring and summer studies due to the larger number of expeditions that supply the Antarctic bases. Few studies focus on the nutrient status of young, growing ice in the Antarctic marginal ice zone in winter (Dieckmann et al., 1991; Tison et al., 2020; Louw et al., 2022), this is predominantly due to the difficulty of working in the region during the growth season. The concentrations of nutrients change as sea ice forms and consolidates in proportion to the salinity changes. Nutrient observations in pack ice

---

[1] The work in this chapter has been published as Audh, R.R., Fawcett, S.E., Johnson, S., Rampai, T. and Vichi, M., 2023. Rafting of Growing Antarctic Sea Ice Enhances In-Ice Biogeochemical Activity in Winter. Journal of Geophysical Research: Oceans, 128(12), https://doi.org/10.1029/2023JC019925.

suggest that the expected trend in winter is that the biogeochemistry is controlled by the underlying seawater with little to no variability (Dieckmann et al., 1991; Fripiat et al., 2017).

The biogeochemical aspect of thermodynamic modelling had largely been overlooked by early thermodynamic models (e.g., Maykut & Untersteiner, 1971; Semtner, 1976; Lepparanta, 1983; Cox & Weeks, 1988). Work done by Tedesco et al. (2009) and Tedesco and Vichi (2010) introduced a novel approach to modelling sea- ice thermodynamics from a biogeochemical perspective by defining the Biologically Active Layer (BAL) in their thermodynamic sea- ice model, the Enhanced Sea Ice Model (ESIM) (Tedesco et al., 2009). The BAL is the time-varying fraction of sea ice that is connected to the surrounding ocean and interconnected brine channels. This layer allows for the growth and sustenance of biogeochemical activity through interconnected brines and contact with the surrounding ocean. The BAL is characterised by a relative brine volume of over 5% (Golden et al., 1998; Tedesco et al., 2010). While not explored here, there are other methods that are being employed to couple sea ice thermodynamics and biogeochemistry in recent models. The Los Alamos Sea Ice Model (CICE) (Hunke et al., 2015), for example, employs a bio-grid framework that uses a vertical grid to solve the brine height variable and discretize the vertical transport equations of biogeochemical tracers (Jeffery et al., 2016).

In this chapter, we report new biogeochemical measurements for sea-ice samples collected at two stations in the Atlantic AMIZ during winter 2019, representative of young ice (YI) and first year ice (FYI). These terms (i.e., YI and FYI) are used as indicators of sea-ice thickness and sampling location relative to the ice edge, as per the literature (e.g., Thomas, 2016). While previous studies aimed to characterise the spatial variability in sea ice properties by collecting samples across a region and comparing their data to other regions and/or previous studies (Tison, Schwegmann, et al., 2017; Tison et al., 2020), this work is a comparative assessment of the physical and biogeochemical data generated for concurrent YI and FYI fields in the Atlantic sector of the AMIZ. This chapter aims to understand the formation conditions that resulted in complex vertical biogeochemical distributions in the sea ice. The hypothesis is that rafting processes created conditions that enhanced the biogeochemical content (i.e., nutrients, chlorophyll) of the sea ice by conserving the biogeochemical signature of the rafted YI floes. This investigation is supported by the comparison of field data with the output of a reduced-process numerical model that simulates only the thermodynamic growth of sea ice and the passive exchange of nutrients at the ocean-ice interface to demonstrate the biogeochemical impact of mechanical rafting in the wintertime AMIZ.

3.2. Data and Methods

3.2.1. Collection and handling of samples

Sea-ice samples and environmental data were collected during the 2019 SCALE winter expedition (Ryan-Keogh & Vichi, 2022; Section 2.1). For the purpose of this work, only the consolidated station (M03) and one pancake floe (M01-D) will be considered (Figure 3.1a). Station M01 (sampled on 28/07/2019; referred to as the YI station), was characterized by open drift conditions and a combination of pancakes and frazil ice (Figure 3.1b), and station M03 (sampled on 29/07/2019; referred to as the FYI station) was located on a ~200 m-diameter cemented floe (Figure 3.1c). The methods for sample collection and analysis are described in detail in Chapter 2. It should be noted that the ice characteristics described here were determined from multiple cores from the same station. It would have been beneficial to analyse the same core for all properties, biogeochemical, physical, and textural, but the meltwater requirements per segment limited our ability to do so. The physical, biogeochemical, and textural properties described below were derived from cores taken at the same location at each station and related back to each other. All cores were taken approximately 0.1 m from each other at both locations. Surface snow measurements were not reliably recorded during the consolidated station due to the harsh conditions and limited sampling time. The pancake station had snow measurements taken at the time of sampling. Table 3.1 provides information about the winter station details and a breakdown of the cores collected at each station and their designations.

Table 3.1. Station and ice core information for the SCALE2019 winter cruise.

STATION	DATE	LOCATION	SNOW DEPTH (cm)	AVERAGE CORE LENGTH (m)	NO. OF CORES (DESIGNATION)
M03	27/07/2019	58.14°S; 00.00°E	-	0.73 ± 0.092	3 (T/S), 3 (BGC), 1 (CS)
M01	28/07/2019	56.80°S; 00.03°E	3.5	0.32 ± 0.065	3 (T/S), 3 (BGC), 1 (CS)

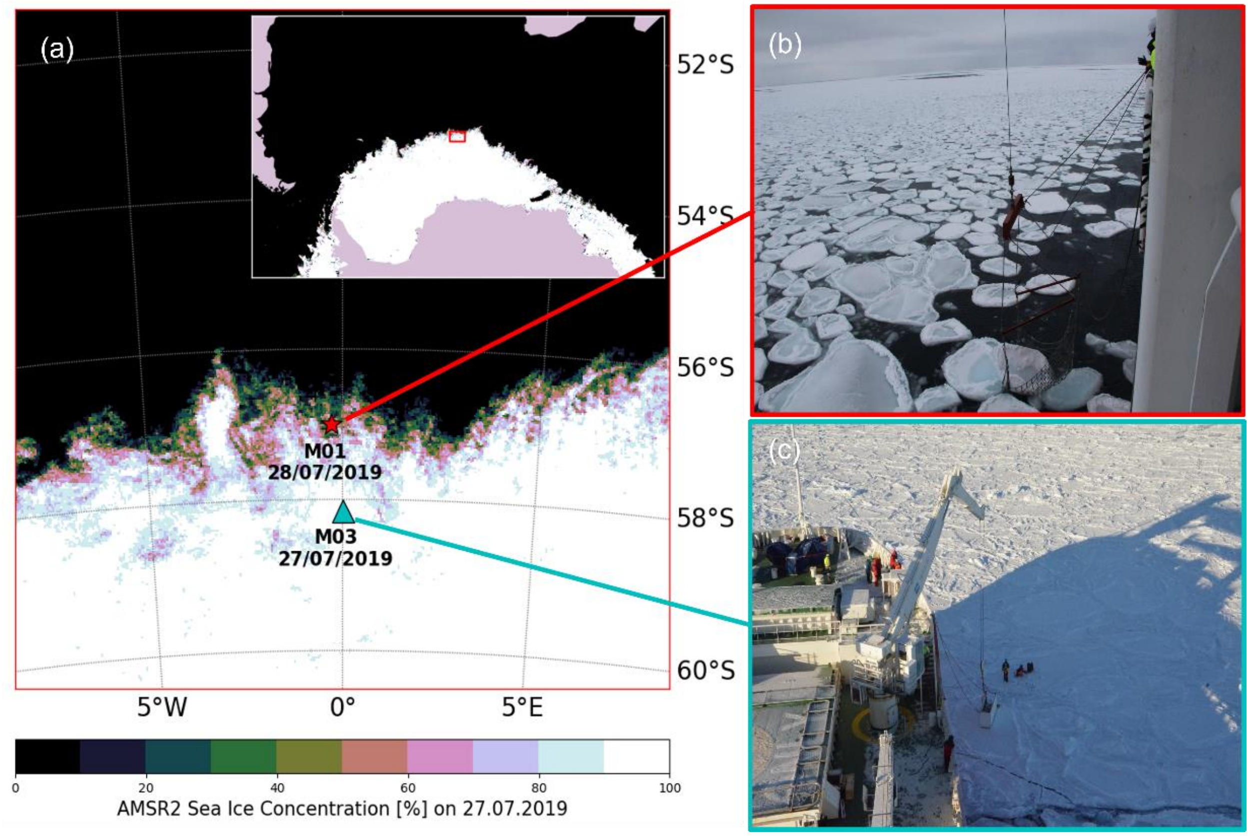

Figure 3.1. (a) Map of the station locations and (b,c) station conditions during the SCALE 2019 winter expedition. The red star indicates station M01 (YI station) and the corresponding image in the red block (b) shows the conditions at the station on the day of sampling. The blue triangle indicates station M03 (FYI station) and the corresponding image in the blue block (c) shows the conditions at the station on the day of sampling. The map (a) is overlaid with the satellite-derived sea ice-concentration for 27/07/2019 taken from the AMSR2 satellite product (Spreen et al., 2008).

3.2.2. Lagrangian backtracking of the sea-ice floes

The origin and trajectory of the ice floe sampled at M03 was determined using the methods described in Section 2.5.1 and presented in Figure 3.2 below.

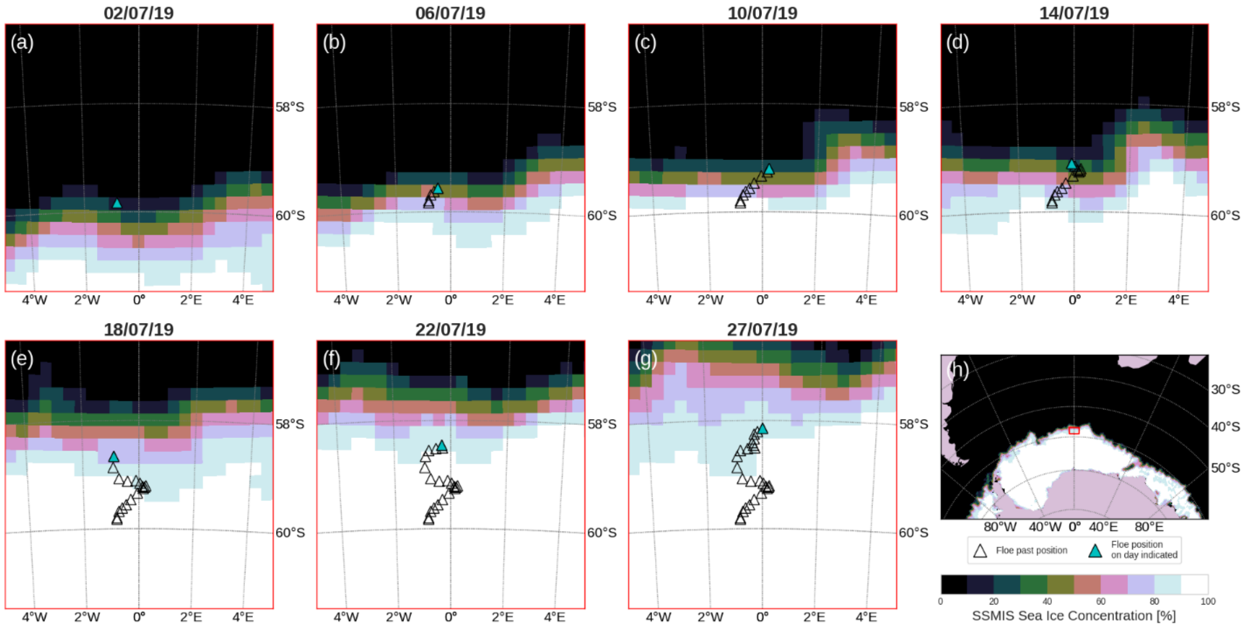

Figure 3.2. Sea ice conditions and back-trajectory of the ice sampled at station M03 during the SCALE2019 winter expedition. The floe trajectory from formation (Panel a, 02/07/2019) to the day of sampling (Panel g, 27/07/2019) is shown by the triangles. The open symbols show the past locations of the floe, and the blue shaded triangle shows its location on the day indicated at the top of each panel. Panel (h) shows the position of the station in a broader context, indicated by the red box. The map color is the daily average sea-ice concentration from the SSMIS satellite product (Maslanik & Stroeve, 1999).

3.2.3. Numerical modelling of sea ice properties

The ESIM was used to simulate the sea-ice growth and properties of the FYI, such as sea ice thickness, snow depth, temperature, and salinity. The output of the ESIM was then used to initialize the BFM-SI which was used to simulate the biogeochemical response of the sea ice. The ESIM and BFM-SI models were run at an hourly time-step during the growth period, starting at the estimated formation location and following the floe back-trajectory presented in Figure 2.12. The methods for the modelling of sea ice properties are described in Section 2.4.

3.3. Results

3.3.1. Ice characteristics

The YI collected at M01 and a diagram showing the positions of the cores collected from it are shown in Figure 3.3. The core lengths and respective analysed properties are displayed in Figure 3.4. The YI cores have a maximum length of 0.37 m and a minimum length of 0.2 m. the ice thickness shows a decrease in length as the cores move closer to the edge of the pancake (Figure 3.3b) with the physical cores being located along the centre of the pancake and the shortest core, the crystal structure core, being located closest to the edge of the pancake. Overall, the core lengths show little variability across the pancake. The FYI cores had a maximum thickness of 1.05 m and a minimum thickness of 0.57 m. The thicknesses show variability throughout the sampled portion of the consolidated floe given that these cores were taken <0.1 m apart.

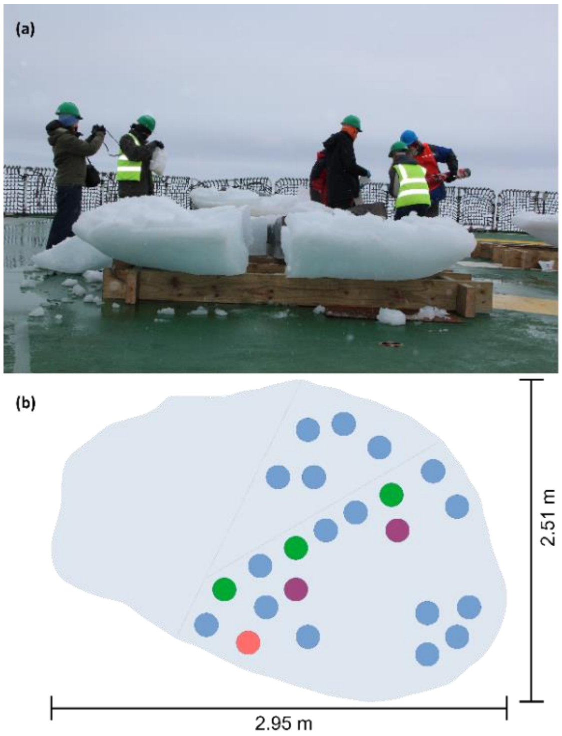

Figure 3.3. (A) Image of the sampled pancake on deck. The pancake broke into 3 pieces when the net was removed. Note that the 3.5 cm snow layer (on average) was not removed to ease the grip of the corer while coring on an uneven surface on deck. (B) Diagram showing the locations of the cores taken from the pancake. The green circles represent the physical cores, purple the isotope cores and orange the crystal structure core. The cores collected for other teams and purposes are also included and are indicated by the blue circles.

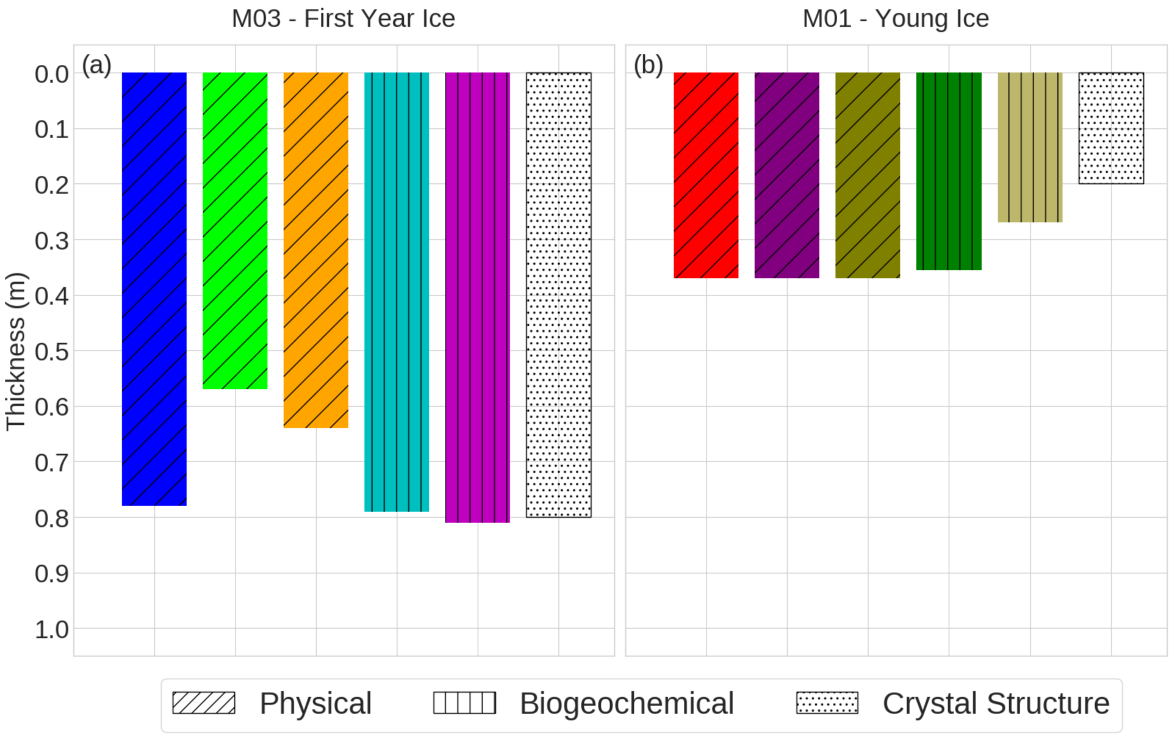

Figure 3.4. Sea-ice core lengths at (a) M03 and (b) M01. Shading corresponds to the core profiles and markings indicate core designations.

3.3.2. Cross polarised images of the cores

Cross polarised images of the cores are displayed in Figure 3.5 and Figure 3.6. The methods used to create these images are discussed in Section 2.3.3.

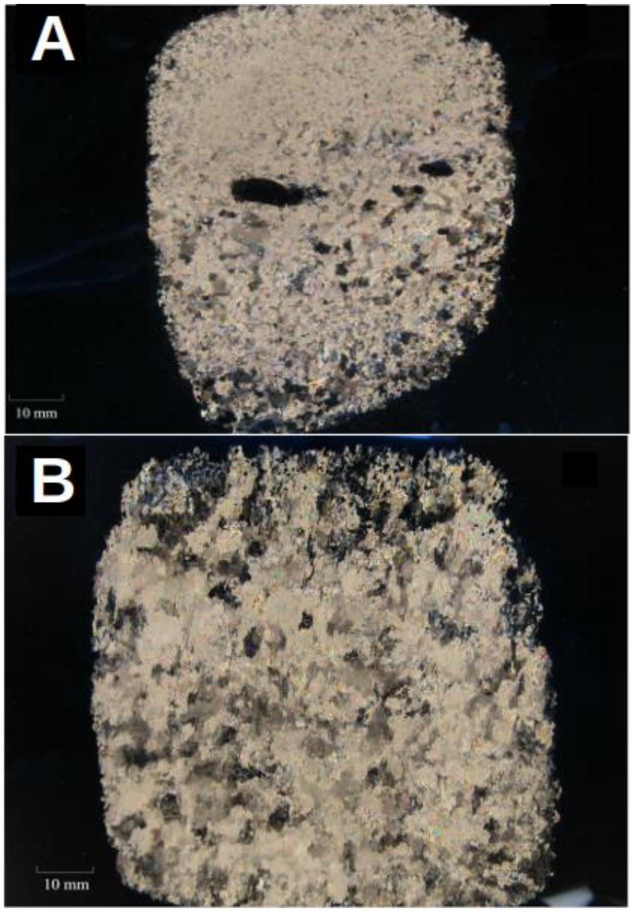

Figure 3.5. Crystal structure images from the dedicated YI core. The images are displayed alphabetically from the top of the core (A) to the bottom of the core (Johnson, Matlakala, et al., 2022).

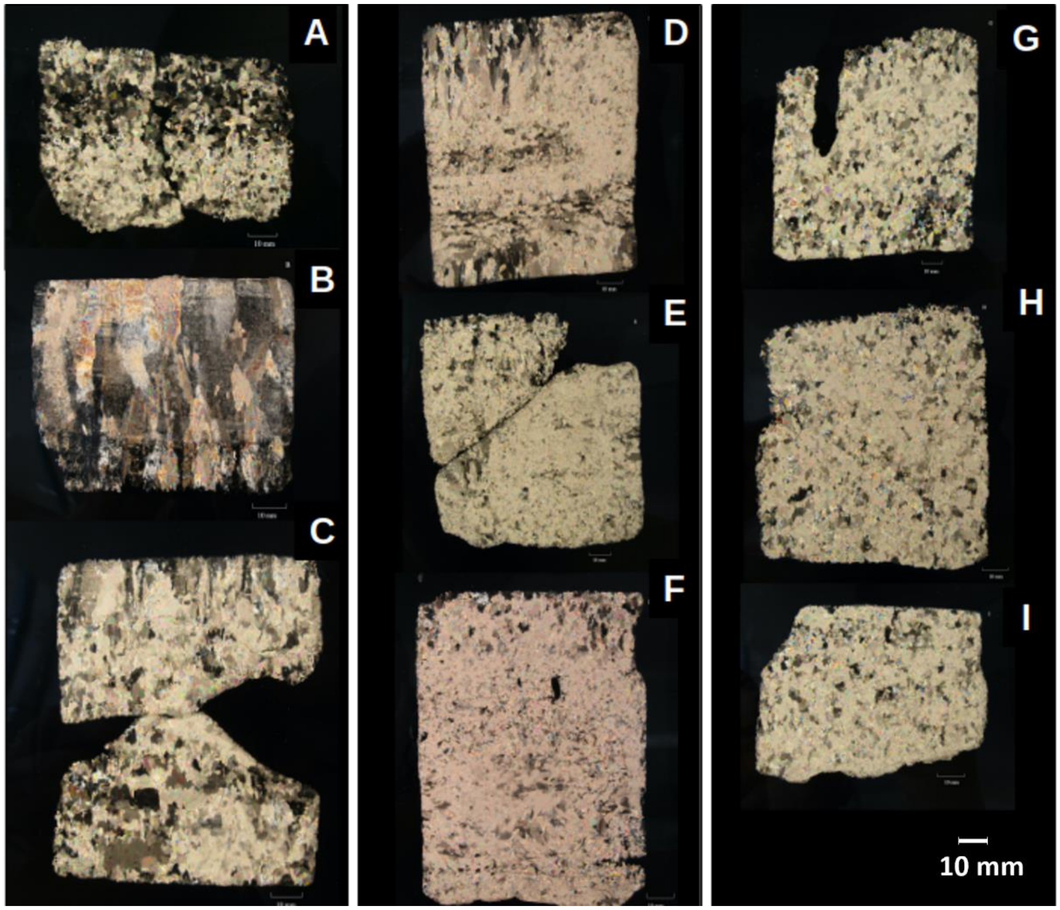

Figure 3.6. Crystal structure images from the dedicated FYI core. The images are displayed alphabetically from the top of the core (A) to the bottom of the core (Johnson, Matlakala, et al., 2022).

3.3.3. Physical properties

The vertical profiles of salinity, temperature, δ^{18}O and stratigraphy are presented in Figure 3.7. The YI Salinity was higher (7.3 to 10.7) at the surface than the bottom (4.5 to 5.9) (Figure 3.7a), while temperature was more homogeneous and was below the freezing temperature at the bottom of the cores (-4.19℃ to -2.54℃), decreasing towards the surface (-6.67℃ to -4.48℃) (Figure 3.7b). Despite being collected within 0.1 m of each other, the salinity profiles of the FYI cores diverged. FYI-PHY-01 and FYI-PHY-02 increased in salinity from minima of 5.1 and 4.4 at the surface to maxima of 8.2 and 8.5 at the bottom, a trend indicative of previous gravity drainage. By contrast, FYI-PHY-03 was characterized by a c-type salinity curve (Eicken, 1992), with lower bottom- and higher surface salinities (5.8 and 7.4, respectively) than in the other cores, comparable to the YI.

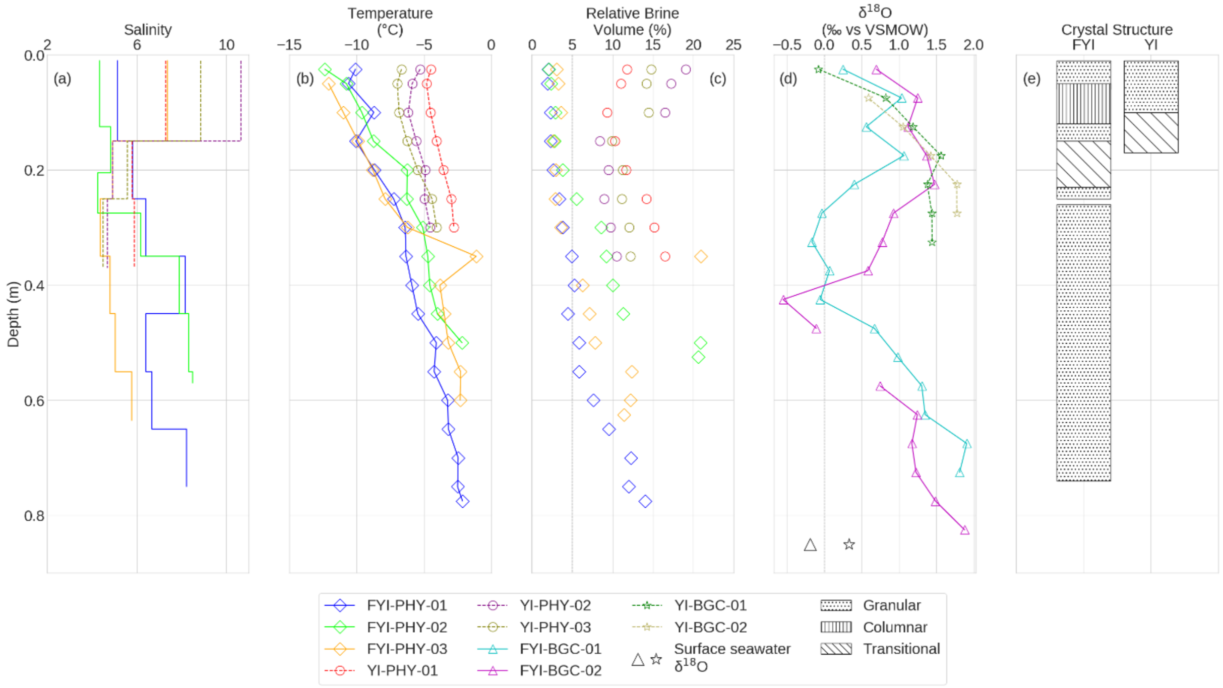

Figure 3.7. Profiles of the physical properties of YI (dashed lines) and FYI (continuous lines), with the cores labelled as follows: ice type-core type-core number (e.g., first year ice physical core 01 is written as FYI-PHY-01). (a) Bulk salinity (0.1 m segments), (b) temperature (0.05 m segments), (c) relative brine volume (RBV) of the physical cores, which is the brine volume as a percentage of the total volume (Frankenstein and Garner, 1967), (d) δ^{18}O (0.05 m segments), and (e) major crystal structure. Because it was measured at coarser resolution, bulk salinity (panel a) is shown without linear interpolation between the centers of adjacent segments. In panel c, the darker vertical line indicates the 5% permeability threshold (Golden et al., 1998). The δ^{18}O (panel d) was analyzed for a different set of cores from those used for temperature and salinity; these data are thus displayed with different colors (see also Figure 3.4) with the different core labels included in the legend. Surface seawater δ^{18}O is shown by the open black symbols below the profiles that correspond to the symbols in the profiles (Ngongo et al., 2022).

The FYI temperature profiles were similar, with bottom maxima of -2.13℃ and -2.20℃ for FYI-PHY-01 and FYI-PHY-02, decreasing to surface minima of -10.08℃ and -12.36℃, while FYI-PHY-03 showed a maximum of -1.11°C at 0.35 m and the lowest surface temperature (-13.11°C). The RBV of the YI cores was >5% (Figure 3.7c), indicating that the ice was completely interconnected and biologically active (Golden et al., 1998; Tedesco et al., 2010). The FYI cores displayed RBVs of <5% in the top 0.2 m, beneath which the RBVs were always >5%.

The $\delta^{18}O$ of the cores revealed a complex structure (Figure 3.7d), described here alongside the ice stratigraphy (Figure 3.7e). Granular ice can be either ice of frazil origin or snow ice. It is difficult to differentiate between the two by means of visual inspection; the $\delta^{18}O$ of the ice is therefore used to make the distinction, with negative $\delta^{18}O$ values indicative of snow ice and positive $\delta^{18}O$ values indicative of frazil ice (Lange et al., 1990). The YI was characterized by a granular layer at the top and a transitional layer at the bottom (Figure 3.5). Surface $\delta^{18}O$ was -0.08‰ and 0.59‰ for YI-BGC-01 and YI-BGC-02, increasing with depth to 1.56‰ and 1.77‰, respectively. For the FYI, the $\delta^{18}O$ of the upper 0.2 m followed that of the YI cores, then decreased strongly to minima of -0.17‰ and -0.55‰ at ~0.4 m, before increasing again to 1.91‰ and 1.88‰ at the bottom of the cores. Since the surface seawater $\delta^{18}O$ was -0.33 ± 0.12‰ (n=2) and -0.19 ± 0.13‰ (n=3) near M01 and M03, the $\delta^{18}O$ of ice formed directly therefrom would be >1‰ (Lange et al., 1990; Eicken, 1992). As such, the mid-depth $\delta^{18}O$ minima hint at snow intrusions (Lange et al., 1990), suggesting that during floe formation, the now-mid-depth layer was at the surface. The FYI core was characterized by a thin granular top section followed by a thicker columnar section, which was partly aligned with the $\delta^{18}O$ maxima. This columnar ice was underlaid by another thin granular section and a transitional section, the latter roughly coincident in depth with start of the $\delta^{18}O$ decline. The thick granular bottom section had similar small crystals of frazil origin at all depths (Figure 3.6). Below and in the discussion, we will refer to the top layer and bottom layer of the FYI core with respect to this discontinuity where the $\delta^{18}O$ minimum was observed.

3.3.4. Biogeochemical properties

The surface seawater nutrient concentrations were similar at M01 and M03, measuring 63.0 µM and 72.1 µM for $\mathrm{Si(OH)_4}$, 2.21 µM and 2.36 µM for $\mathrm{PO_4^{3-}}$, 27.6 µM and 28.5 µM for $\mathrm{NO_3^- + NO_2^-}$ and 0.54 µM and 0.60 µM for $\mathrm{NH_4^+}$. The chlorophyll concentration was 0.10 µg/L at M01 and 0.24 µg/L at M03.

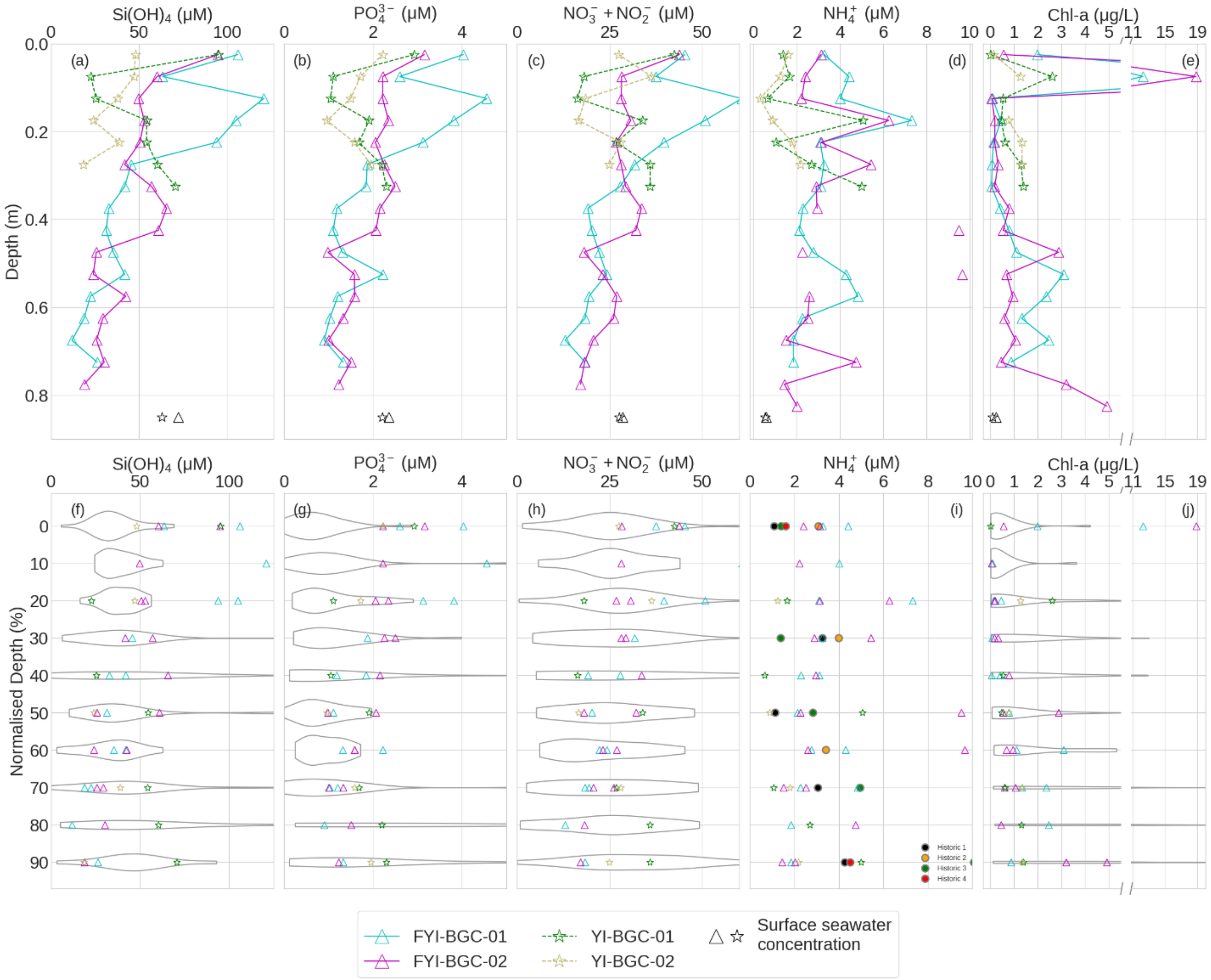

Figure 3.8. Salinity-normalised nutrient (panels a-d) and bulk chlorophyll (chl-a) concentrations (panel e – note the break in the x-axis to accommodate the high values at 0.1 m without losing the definition in the vertical structure for the lower concentrations) for each core collected from the YI (dashed lines and star symbols) and FYI (continuous lines and triangle symbols) floes. The cores are labelled as *ice type-core type-core number* (e.g., first year ice biogeochemical core 01 is written as FYI-BGC-01) and are not the same cores as those presented in Figure 3a-c (with the exception of the $\delta^{18}O$ data shown in Figure 3.7d, which were measured for the BGC cores presented here) (Audh et al., 2023). The black open symbols at the bottom of panels a-e show the surface seawater nutrient- and chl-a concentrations sampled at 5 m using a CTD-niskin rosette. (f-j) Violin plots (which show data density) of historical nutrient and chl-a concentrations binned into 10% depth interval from winter pack-ice cores collated by Fripiat et al. (2017), where n=24 cores for chl-a and n=26 cores for the nutrients, except $\mathrm{NH_4^+}$ for which historical data are available from only four cores; the historical $\mathrm{NH_4^+}$ concentration data are thus displayed alongside our new data as individual concentrations per depth interval rather than as violins. The discrete coloured symbols on the violin plots indicate the depth-normalised concentrations from our YI and FYI cores, binned into the relevant 10% depth intervals.

The salinity-normalised nutrient concentrations and chlorophyll profiles in the ice cores are shown in Figure 3.8a-e. At the top of the YI cores, $\mathrm{Si(OH)_4}$, $\mathrm{PO_4^{3-}}$ and $\mathrm{NO_3^- + NO_2^-}$ were high (95.1 µM, 2.9 µM and 42.4 µM for YI-BGC-01; 47.1 µM, 2.0 µM and 36.3 µM for YI-BGC-02), decreasing to minima near the middle of YI-BGC-01 and bottom of YI-BGC-02 (25.6 µM, 1.0 µM and 16.3 µM; 18.5 µM, 1.0 µM and 16.6 µM) before increasing again towards the bottom of YI-BGC-01 (Figure 3.8a-c). The $\mathrm{NH_4^+}$ concentrations were lowest at the surface of both cores (0.65 µM and 0.89 µM), increasing with depth to a maximum of 5.06 µM in YI-BGC-01 and 2.18 µM in YI-BGC-02 (Figure 3.8d). FYI nutrients were generally higher than in the YI and decreased with depth. FYI-BGC-01 showed concentration maxima at ~0.1 m (120.8 µM, 4.56 µM and 60.6 µM for $\mathrm{Si(OH)_4}$, $\mathrm{PO_4^{3-}}$ and $\mathrm{NO_3^- + NO_2^-}$) while the FYI-BGC-02 concentration maxima occurred at ~0.4 m (94.9 µM, 3.2 µM and 43.8 µM for for $\mathrm{Si(OH)_4}$, $\mathrm{PO_4^{3-}}$ and $\mathrm{NO_3^- + NO_2^-}$), co-located with the $\delta^{18}\mathrm{O}$ minimum (Figure 3.7d). Nutrients decreased to concentrations at the core bottoms that were lower than in the underlying seawater. The FYI $\mathrm{NH_4^+}$ concentrations were less variable with core depth, reaching 7.3 µM (FYI-BGC-01) and 9.6 µM (FYI-BGC-02).

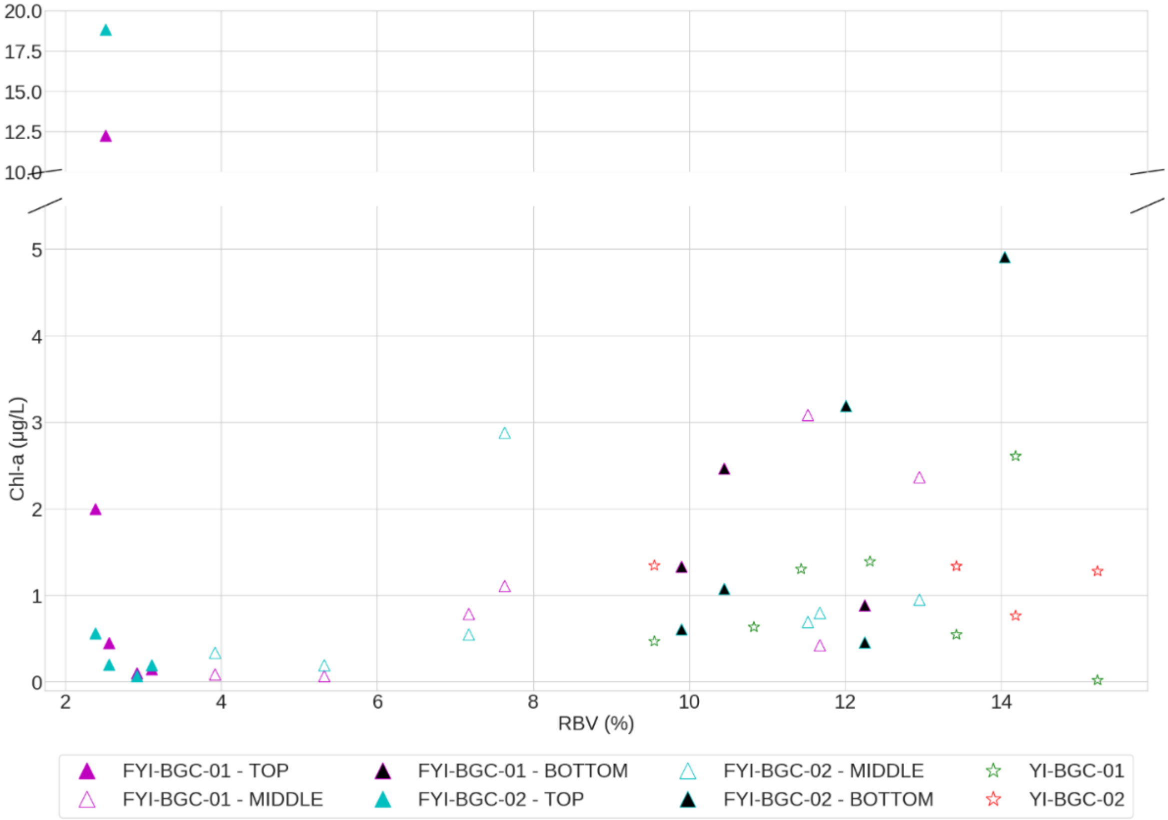

Figure 3.9. Relationship between the chlorophyll (chl-a) concentration and relative brine volume (RBV). Here, "top", "middle" and "bottom" indicate the top 0.2 m, middle 0.4 m and bottom 0.2 m of the FYI cores. Note the break in the y-axis to accommodate the high concentrations.

The chlorophyll concentrations in the YI averaged 1.09 ± 0.57 μg/L (all cores) and were near-constant with depth, except at the surface where chlorophyll was lowest, resembling the seawater concentration (Figure 3.8e). In both FYI cores, chlorophyll varied with depth, peaking at 0.05 m (12.25 μg/L and 18.82 μg/L for FYI-BGC-01 and FYI-BGC-02, respectively) before decreasing to a minimum (0.07 μg/L) near the core centres and then increasing again at the bottom (2.47 μg/L and 4.91 μg/L). These chlorophyll concentrations are up to 10-times those measured in the underlying seawater. The highest chlorophyll concentrations of the FYI cores were observed in the top 0.2 m portion of the sea ice with the lowest permeability, with a RBV < 5% (Figure 3.7c). Additionally, chlorophyll was consistently >1.00 μg/L in both the FYI and YI cores where the RBV was >5%.

The violin plots in Figure 3.8f-j represent the spread of historical wintertime pack-ice nutrient- and chlorophyll concentrations available for the Atlantic sector, as collated by Fripiat et al. (2017). The plots show the data density through the thickness of the violin shape; uniformly low thickness means that the distribution is not well represented due to data sparsity. Our YI measurements largely fall in the thinnest portion of the distribution and even outside the violins for $\mathrm{Si(OH)_4}$ and $\mathrm{PO_4^{3-}}$, and within the higher density range for $\mathrm{NO_3^- + NO_2^-}$. Measurements from the bottom layer of the FYI cores fall within the historical ranges for $\mathrm{Si(OH)_4}$, $\mathrm{PO_4^{3-}}$ and $\mathrm{NO_3^- + NO_2^-}$, while the top-layer concentrations are 2- to 4-times higher than the historical data for $\mathrm{Si(OH)_4}$ and $\mathrm{PO_4^{3-}}$. Sea-ice $\mathrm{NH_4^+}$ measurements are scarce, with the historical winter data deriving from four cores only. Our chlorophyll concentrations fall within the historical range except in the top 0.1 m of the cores where they are 10-times higher. We note that the historical core-bottom chlorophyll distributions indicate a large spread of values with low densities.

Theoretical dilution lines (TDLs) for the sea ice were calculated using the bulk (i.e., not salinity-normalised) seawater nutrient concentrations and bulk sea-ice salinities (Figure 3.10). The TDLs indicate the expected nutrient concentrations in sea ice due only to passive physical entrainment and expulsion of solutes. Bulk nutrient concentrations that fall on the TDLs imply little to no biological activity in the ice, a condition that has been suggested as characteristic of winter (Dieckmann et al., 1991; Fripiat et al., 2017), while deviations from the TDL imply in situ accumulation or depletion of nutrients in the ice. We observed no major difference between the TDLs derived for YI versus FYI. Many of our measurements deviated strongly from the TDLs, with $\mathrm{Si(OH)_4}$ and $\mathrm{PO_4^{3-}}$ largely falling below the TDLs when salinity was ≥6 and on or above the TDLs in lower-salinity sea ice (Figure 3.10a,b). The measured $\mathrm{NO_3^- + NO_2^-}$ concentrations fell closer to the TDL, although many samples were characterized by considerably higher concentrations than expected from dilution alone (Figure 3.10c). All the $\mathrm{NH_4^+}$ concentrations fell above the TDL and were typically 5- to 10-times higher than expected (Figure 3.10d).

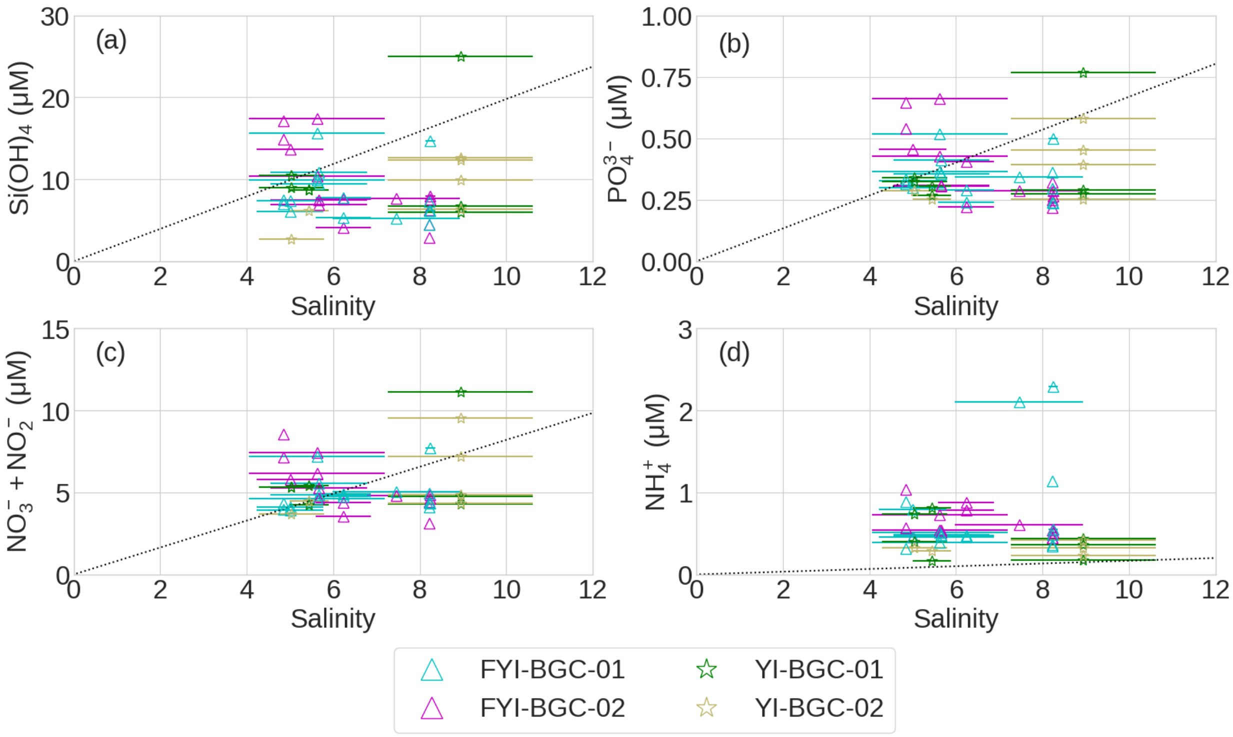

Figure 3.10. Bulk nutrient concentrations (i.e., not salinity-normalised) as a function of salinity in the sea-ice cores (stars indicate YI and triangles show FYI, the colors correspond to the vertical profiles presented in Figure 3.8). The dotted black line indicates the theoretical dilution line (TDL) derived from surface seawater nutrient concentrations and sea-ice salinity measurements. The bulk measured nutrient concentration for each ice section is plotted against the average bulk salinity per depth interval measured for the physical cores (Figure 3.7a), with the error bars representing the standard deviation of the average salinity at each depth corresponding to a nutrient measurement for the three cores analyzed per station.

3.3.5. Numerical modelling of sea ice properties

The ESIM was used to simulate the ice cover's physical properties to assess whether thermodynamic growth alone could create the FYI sea ice thickness seen at M03. The sea ice sampled during winter 2019 had a maximum thickness of 0.85 m at M03 and 0.37 m at M01 (Figure 3.4). Regardless of the choice of OHF, the ESIM-simulated sea ice can only attain the thickness of the YI at M01 (Figure 3.11a) – that is, the simulated sea ice is generally thinner, warmer, and less saline than observed (Figure 3.12). The simulated freeze-up time in mid-June is consistent with the Langrangian back-trajectory reconstruction (Figure 3.2), but the FYI thickness at M03 cannot be simulated by thermodynamic growth in the predicted time frame, even without any OHF (solid green line in Figure 3.11a). We compared the observed sea-ice thicknesses to the simulations produced by the GLORYS ocean reanalysis (https://doi.org/10.48670/moi-00018), which is indicated by the black continuous line in Figure 3.11a. A complete sea-ice model with horizontal dynamics and thermodynamics can reproduce the sea-ice thickness observed at M03. However, the resulting thicker sea ice is not granular nor composed of multiple layers due to the continuum hypothesis implemented in numerical models that results in sea ice being treated as a viscous material.

The dashed lines in Figure 3.11a show the thickness of the simulated BAL, which changes according to the heat balance between the atmospheric reanalysis and the prescribed OHF scenario. This layer passively accumulates the simulated nutrients and is in direct contact with the active pelagic model that was initialized with the observed seawater nutrient- and chlorophyll concentrations. Since granular ice is characterised by elevated porosity, a BAL that extends through the whole thickness of the ice, or changes rapidly, indicates high permeability and younger ice. We tested the hypothesis that the measured sea-ice nutrient concentrations can be attained by passive physical entrainment during ice growth by switching off biological activity in the BFM-SI. Figure 3.11b-e shows the output of the BFM-SI averaged over the month leading up to our sampling (26/06/2019–27/07/2019) for the three OHF scenarios (coloured bars), along with the nutrient concentrations observed in the BAL of the FYI and YI cores (symbols) (see Figure 3.13 for the daily time-series). We evaluated the simulation against a range of measured conditions since the full thickness of the FYI could not be generated by freezing alone and the BFM-SI is a layer model. The BFM-SI output indicates that for all OHF scenarios, physical processes alone can reproduce the observed $\mathrm{PO_4^{3-}}$ and $\mathrm{Si(OH)_4}$ concentrations (Figure 3.11b,c). By contrast, the measured $\mathrm{NO_3^- + NO_2^-}$ concentrations tend to exceed the simulated values, although with overlap at the lower concentration end of the observations (Figure 3.11d), while the measured $\mathrm{NH_4^+}$ concentrations are clearly higher than can be achieved by passive entrainment under any OHF scenario (Figure 3.11e).

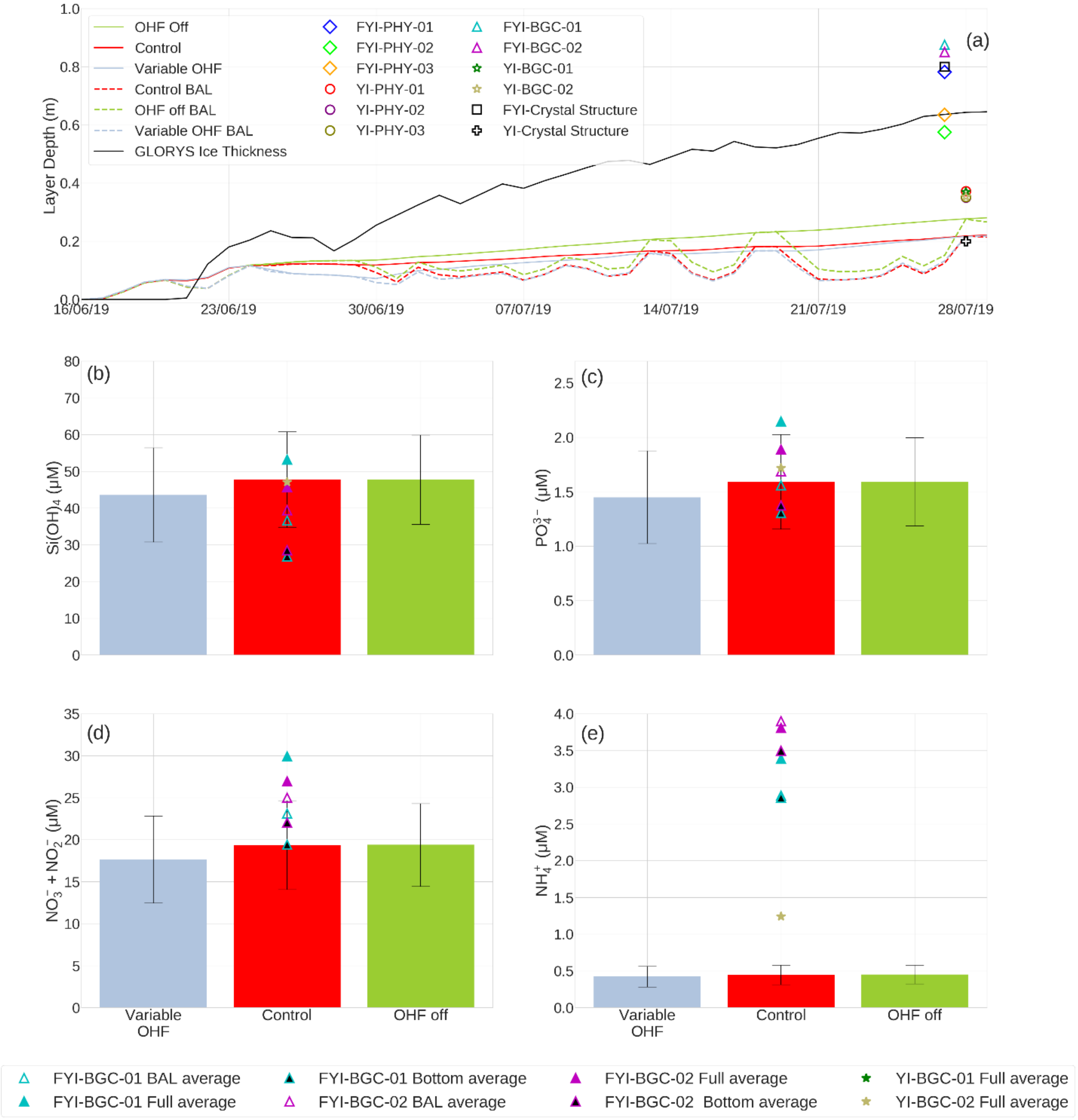

Figure 3.11. (a) Simulated sea-ice thickness from GLORYS reanalysis (continuous black line) and ESIM (continuous colored lines), with the corresponding BAL thickness (dashed lines) for the three OHF scenarios: Variable OHF, fixed OHF (control) and zero OHF. Symbols represent the observed sea-ice thickness for the collected cores – note the overlapped symbols for the YI cores that were the same length. (b-e) Comparison of the BFM-SI model output and the observed nutrient concentrations. The bars indicate the model average and standard deviation (error bar) for the month leading up to our sampling date while symbols indicate the mean salinity-normalised nutrient concentrations measured in the cores. Since the YI cores were characterized by a RBV >5%, the observed BAL nutrient concentrations were averaged over the entire core ("YI Full average"). For the FYI, we tested a range of measured concentrations since the full thickness of the FYI cannot be generated in the model by freezing alone. We used the average nutrient concentration of the bottom 0.3 m of the core ("Bottom average"), the BAL average where RBV was >5% ("BAL average"), and the average for the entire core ("Full average").

Table 3.2. Average nutrient concentrations in FYI cores that were used to evaluate the BFM-SI output. "Bottom average" refers to the average nutrient concentration of the bottom 0.3 m of core, "BAL average" to the BAL average where RBV was >5%, and "Full average" to the average for the entire core.

	$Si(OH)_4$ [μM]		PO_4^{3-} [μM]		$NO_3^- + NO_2^-$ [μM]		NH_4^+ [μM]	
	FYI-BGC-01	***FYI-BGC-02***	***FYI-BGC-01***	***FYI-BGC-02***	***FYI-BGC-01***	***FYI-BGC-02***	***FYI-BGC-01***	***FYI-BGC-02***
BOTTOM AVERAGE	26.83	28.47	1.30	1.37	19.40	22.01	2.86	3.50
BAL AVERAGE	36.53	39.37	1.56	1.69	23.11	24.99	2.88	3.90
FULL AVERAGE	53.13	45.65	2.14	1.89	29.88	26.92	3.38	3.81

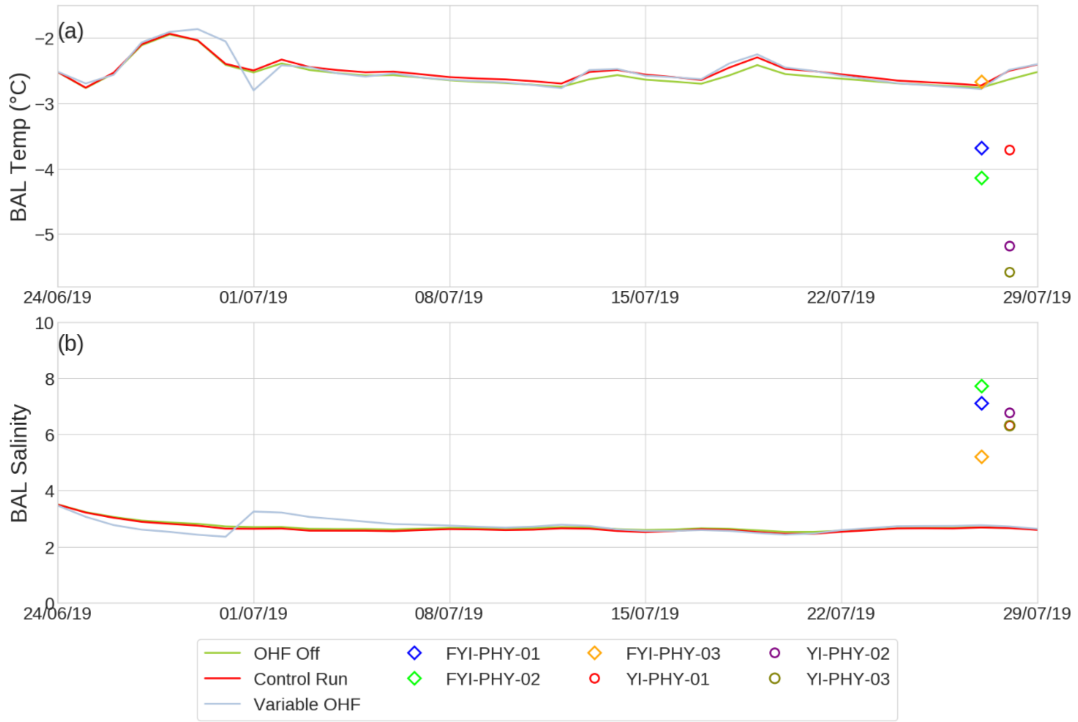

Figure 3.12. ESIM output of the (a) temperature and (b) salinity of the BAL as simulated by the ESIM. The open symbols represent the BAL averages of temperature and salinity of the sampled cores.

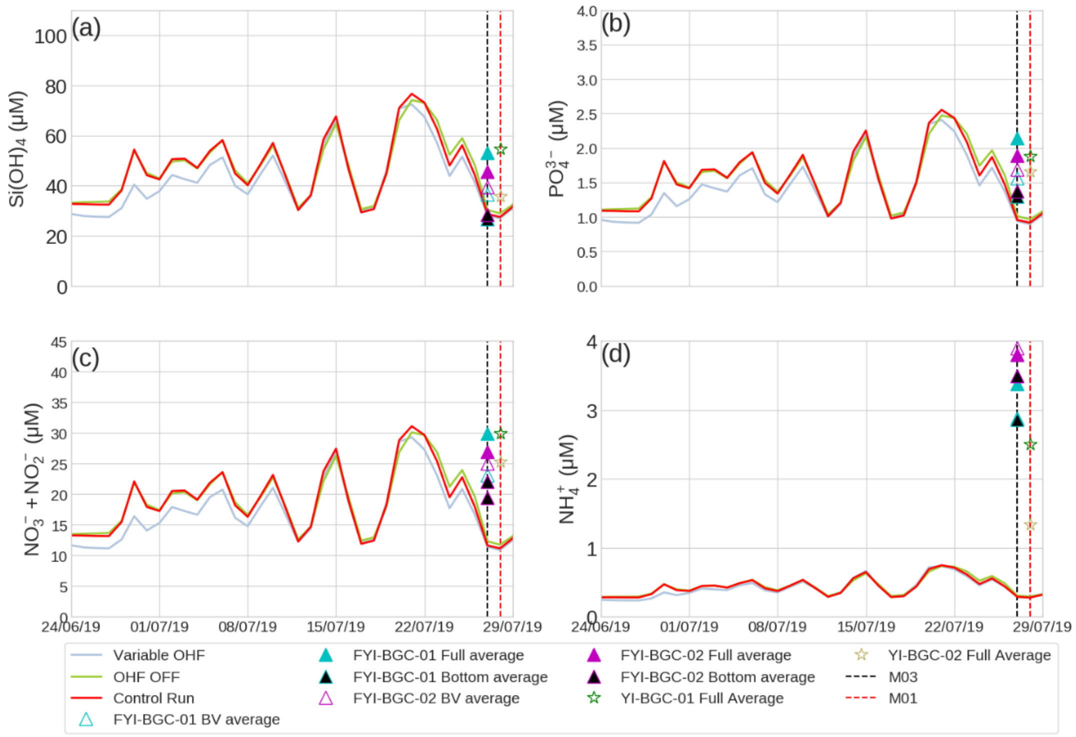

Figure 3.13. Daily timeseries of the BFM-SI outputs over the backtrack period for (a) $\mathrm{Si(OH)_4}$, (b) $\mathrm{PO_4^{3-}}$, (c) $\mathrm{NO_3^- + NO_2^-}$, (d) $\mathrm{NH_4^+}$. Symbols represent the average nutrient concentrations in ice.

3.4. Discussion

The freeze-up and advance of Antarctic sea ice during winter has been considered a quiescent period for sympagic and under-ice pelagic biogeochemical processes, although some historical data and recent observations from expeditions and autonomous devices indicate that biological communities may be active in winter (Melnikov, 1995; Tison, Schwegmann, et al., 2017; Hague & Vichi, 2021; Louw et al., 2022; Mdutyana, Marshall, et al., 2022; Mdutyana, Sun, et al., 2022). Winter sea ice is highly dynamic and continually reshaped by ocean-atmosphere physical drivers (Lange et al., 1989; Dieckmann et al., 1991), with unknown impacts on the distribution and time-evolution of sea-ice biogeochemistry.

3.4.1. Ice type and biogeochemical patterns

We observed complex vertical patterns in the biogeochemistry of growing sea ice, with elevated nutrient- and chlorophyll concentrations in the whole ice column compared to the underlying seawater, although we recognize that our limited dataset makes it difficult to extrapolate our findings to the entire AMIZ. As per our observations, previous studies have reported variability in the biogeochemistry of sea-ice cores collected near each other that displayed similar physical properties (Clarke & Ackley, 1984; Dieckmann et al., 1991; Tison et al., 2020). This variability was attributed to the sampled floe being the product of several formation processes occurring coincidentally and at different rates. We argue that these concurrent processes and the resulting variability in ice properties are a major feature of the AMIZ and should not be disregarded as “biogeochemical noise”. Instead, wintertime variability is just as relevant as that observed during the putative productive period (i.e., spring; Cimoli et al., 2017). The physical properties that we measured have been observed previously in winter (e.g., Lange et al., 1989; Lange & Eicken, 1991; Jeffries et al., 2001). According to these studies, YI is thin, granular and formed from frazil ice while FYI is thicker and more columnar. These structural differences imply that YI should be characterised by higher nutrient concentrations and biomass than FYI, since YI has the potential to retain more brine due to its more disordered crystal structure and reduced brine channel connectivity (Maus et al., 2021; Golden et al., n.d.).. Additionally, processes that typically reduce nutrient concentrations in the sea ice, such as gravity drainage or biological uptake may have had less time to act on the YI compared to the FYI. However, we measured similarly high concentrations of nutrients and chlorophyll in YI and portions of our FYI, which violates the simple thickness-based classification.

Elevated chlorophyll in sea ice has been observed to accompany low nutrient concentrations (Clarke & Ackley, 1984; Torstensson et al., 2018), although co-located high-nutrient and high-chlorophyll concentrations have also been observed to the extent that this condition has been named the “sea-ice nutrient paradox” (Roukaerts et al., 2021 and references therein). The influence of biofilms, as proposed by

Roukaerts et al. (2021), could explain the enhanced nutrients and corresponding high chlorophyll concentrations that we observed in the top (0.2 m) layer of the FYI cores, although we are reluctant to over-interpret so few data.

Our YI nutrient concentrations were generally higher at the top of the cores than in the underlying seawater, while in the rest of the ice they were equal to or lower than the seawater nutrient concentrations. The nutrient concentrations were typically even higher in the top layer of the FYI cores, and only one of the cores (FYI-BGC-02; Figure 3.8e) showed a chlorophyll peak coincident with a nutrient minimum. At both stations, regardless of ice thickness, the chlorophyll concentrations were always higher than those reported for winter pack ice (Meiners et al., 2012; Fripiat et al., 2017). This condition is unlikely the result of surface flooding given the low permeability of the ice in that layer and the fact that the seawater nutrient concentrations were lower than those measured in the surface layer of the ice cores. Additionally, the $\delta^{18}O$ data indicate little evidence of snow ice in the surface layers, which is expected as a result of surface flooding and would manifest as a strong negative $\delta^{18}O$ excursion (Figure 3.7e). Melnikov (1995, 1998) observed high chlorophyll and $Si(OH)_4$ concentrations in the bottom layer of growing YI and an increase in the same variables from the bottom to the top of FYI over 86 days between March and June 1992. The author attributed these high concentrations to infiltration and flooding, although without presenting evidence for a negative freeboard. For our FYI, the snow depth was always <5 cm and the ice was around a month old according to the Lagrangian analysis (Figure 3.2) and the numerical simulation (Figure 3.11a), supporting our assertion that flooding was unlikely.

For both the YI and FYI, our data imply net consumption of nutrients in the bottom half of the cores and accumulation in the top layer, which suggests enhanced in-ice biogeochemical activity compared to in the underlying seawater (Figure 3.8a-d). These conditions are different from the ones described by Roukaerts et al. (2021) for springtime land-fast ice. In the thicker FYI, passive nutrient entrainment through the permeable bottom layer cannot explain the high concentrations at the top of the ice where RBV was <5 % for two out of three cores (Figure 3.7c). The TDL analysis supports this conclusion, with the data above and below the TDL indicating nutrient enrichment and depletion, respectively (Figure 3.10). The numerical experiments further confirm this idea. Assuming permeable granular sea ice of a thickness comparable to the YI at M01, and imposing various OHF scenarios, it is possible to attain the observed $Si(OH)_4$ and PO_4^{3-} concentrations without biological activity (Figure 3.11b,c). However, the concentrations of the nitrogen species, especially NH_4^+, are more difficult to explain via physical entrainment alone (Figure 3.11d,e). The average monthly modelled $NO_3^- + NO_2^-$ concentration is lower than our observations, although the daily simulated values can overlap with our measurements since the modelled BAL fluctuates due to daily atmospheric temperature variability (Figure 3.11a and Figure 3.12a). Such fluctuations have been observed in the field (Melnikov, 1995), but we do not know whether they are realistic without an observational time-series. We thus used the average nutrient concentrations over the month leading up to our sampling as a way to encompass such oscillations of the brine environment.

NH_4^+ stands out as the nutrient whose concentration clearly cannot be explained by passive entrainment. NH_4^+ is known to accumulate in sea ice (Arrigo et al., 1995; Papadimitriou et al., 2007; Zhou et al., 2013, 2014), although the mechanisms resulting in its accumulation are poorly understood. In our cores, NH_4^+ accumulation likely resulted from heterotrophic remineralisation of organic matter. In addition, NH_4^+ may also adsorb onto organic material present in the sea ice matrix, as suggested by Fripiat et al. (2017), further contributing to its retention within the ice. High NH_4^+ availability should in turn favour coincident ammonia oxidation by nitrifiers in the ice (Fripiat et al., 2014), which could explain our elevated (i.e., above the TDL) $NO_3^- + NO_2^-$ concentrations. The numerical model indicates that sea-ice NH_4^+ does not follow the same daily time-series as the other nutrients (Figure 3.13). In our simulation, the low concentration and high turnover rates of NH_4^+ in seawater exert a more active control on ocean-sea-ice exchange than in the case of the other higher-concentration macronutrients. As such, pelagic NH_4^+ is rapidly consumed in the water column and is less available for accumulation in the simulated BAL. We interpret this as a further indication that the source of the elevated in-ice NH_4^+ is most likely remineralisation in the brine channels. The accumulation of this NH_4^+ could be a result of biofilm-facilitated adsorption and spatial separation of consumption versus remineralisation processes, as suggested by Roukaerts et al. (2021). Our study extends the discussion around the role of remineralisation and biofilms in sea ice by presenting data for young, growing sea ice in winter when the system is expected to be in quiescent mode.

3.4.2. Floe rafting as biogeochemical enhancer

The observed nutrient concentrations in the brines of growing YI can be explained by entrainment, while FYI is characterized by the superposition of different nutrient features, which we attribute to the dynamic deformation of rafted or stacked YI floes. This condition cannot be simulated by simple ice-growth models and requires horizontal dynamics. Moreover, it must have occurred earlier in the season since little rafting was observed during the expedition. The daily changes in sea-ice concentration indicate that the ice was very mobile during growth, as is also suggested by the back-trajectories (Figure 3.2). This mobile and unconsolidated ice, typical of the AMIZ (Vichi, 2022), would result in enhanced dynamic interactions among floes. The superposition of columnar and frazil layers in the FYI and the deformed columnar crystals in the middle of the core (Figure 3.6) are consistent with rafting, which is further evidenced by the similarities between the bottom portion of the FYI core and the entire YI core, while the top layer of the FYI core resembles older ice. The YI floe that was too small to be tracked over the back-trajectory window was also frazil ice-dominated, supporting the hypothesis that the bottom section of the FYI formed under turbulent conditions around the same time as the YI. However, the columnar ice in the top layer of the FYI core suggests sea ice growth under calm conditions over a longer period (Eicken, 2003; Petrich & Eicken, 2016). In other words, the top and bottom layers of the FYI formed at different times and may have undergone further transformations via melting and refreezing. Similar conditions were inferred from the stratigraphy of cores collected in spring 2019 by Johnson et al. (2023).

Rafting is thought to be one of the main processes redistributing sea-ice volume in Antarctic sea ice (Worby et al., 1998; Dai et al., 2004), and is physically parameterized in models through viscous-plastic processes that are not suitable for the MIZ (see for instance Herman (2022)). Rafting happens when one floe is pushed onto another, resulting in the scenario illustrated in Figure 8. The details of rafting are unknown, but given the heterogeneous composition of the ice-covered surface, this mechanism is likely to introduce brash and frazil ice into the spaces between the rafted floes, above the floes and below them, resulting in inconsistent stratigraphy akin to that presented for the FYI (Figure 3.7e). Rafting evidenced by the superposition of columnar and frazil layers has been observed under other conditions (e.g., the complex stratigraphy observed in Lytle & Ackley (2001) and van der Merwe et al. (2009) or reported in (Dai et al., 2004). In our case, it is supported by the crystal structure images showing deformed columnar crystals in the middle of the core (Figure 3.6C), which could indicate the cementing zone (Figure 3.14). Additionally, the negative $\delta^{18}O$ excursion in the middle of the FYI implicates snow ice (Lange et al., 1990; Jeffries et al., 2001; Perovich et al., 2004), suggesting that this layer was previously exposed to the surface. This observation supports the hypothesis that the FYI ice is a combination of at least two separate floes that rafted and cemented together, carrying with them their initial sympagic communities (Figure 3.14). The result is a variable biogeochemical environment in the FYI that is independent of thickness-related ice type (i.e., granular).

The enhanced biogeochemical content in the top layer of the FYI cores is inconsistent with a mechanism of visco-plastic ice accretion through volume redistribution in a continuum. Instead, it can only be explained by discrete and successive rafting processes that physically repack the biology. Figure 3.14 provides a schematic visualization of the proposed “enhancement” mechanism. This proposal has implications for the modelling of sea-ice biogeochemistry in growing ice: the continuum visco-plastic mechanism works well for parameterizing the rafting process, but it is unlikely to accumulate biogeochemical constituents throughout the ice core as observed in our data. We also cannot know whether the high in-ice chlorophyll concentrations in the brine pockets at the top of the FYI indicate the presence of an active community during sampling, although Tison et al. (2017) reported an active winter in-ice community in the same region. Nevertheless, the nutrient and biomass reservoirs in the thicker FYI may support microbial processes (e.g., ammonification and nitrification) that are active from winter until melting, a conclusion that is consistent with passive entrainment (i.e., the model) not being able to yield many of the biogeochemical data and distributions that we measured in winter.

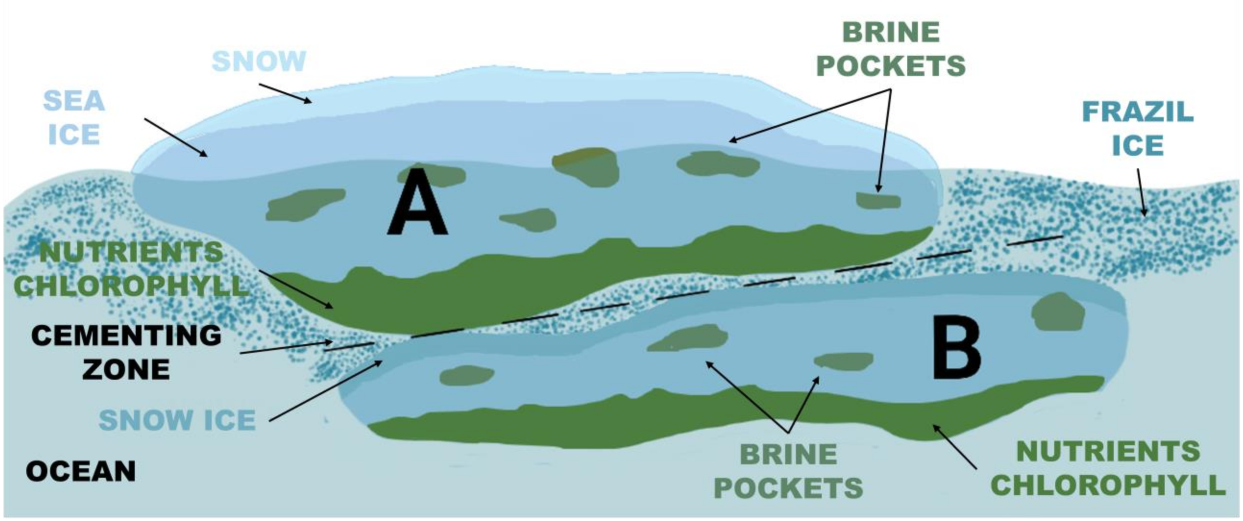

Figure 3.14. Schematic of the proposed rafting mechanism that results in the enhancement of nutrient- and chlorophyll concentrations in first-year winter sea ice.

The nutrients and chlorophyll concentrations measured in the bottom half of our FYI cores fall within the range of historical sea-ice core data available for the region (Figure 3.8f-j; Fripiat et al. 2017). By contrast, the concentrations in the top layer of our FYI cores are higher than the historical values, further supporting our hypothesis of enhanced biogeochemical content due to rafting processes. We acknowledge that our proposed mechanism is based on a limited dataset; however, the data presented here are the only observations collected intentionally from distinct types of sea ice in the AMIZ during winter. Our data contribute to our understanding of the Antarctic sea ice regime by providing insights into and new data for the severely understudied AMIZ. In addition, they reinforce the conclusion of Tison et al. (2020) that larger biogeochemical datasets are required if we are to avoid biases associated with the extrapolation of limited observations. High spatial variability in physical and biogeochemical properties are an inherent feature of Antarctic sea ice, owing to the dynamic formation conditions in the region (Clarke & Ackley, 1984; Dieckmann et al., 1991), and should be accounted for when pooling existing data and developing sea-ice biogeochemical models.

3.5. Conclusion

In this chapter we characterised the physical and biogeochemical properties of young sea ice collected during the 2019 winter leg of the SCALExperiment. The physical properties of the sea ice indicated that the FYI sampled was a product of more than just thermodynamic growth. We investigated this further with the ESIM, that simulated the thermodynamic growth of sea ice at the station location. The ESIM indicated that the maximum sea ice thickness that could be produced by thermodynamics alone was 0.35 m while the sea ice we sampled was in excess of 0.8 m. We hypothesised that the sea ice at the consolidated station was a product of rafting, evidenced further by the crystal structure that indicated frazil dominated sections of ice under older ice with columnar stratigraphy. The implications of this rafting event are seen in the biogeochemical properties that show enhanced biogeochemical properties when compared to the seawater below and to historic cores collected in the region, suggesting that the rafting lead to productive ice being stacked and altering the internal biogeochemistry of the sea ice. The implementation of the BFM-SI indicated that some of the observed nutrient concentrations (particularly $\mathrm{Si(OH)_4}$ and $\mathrm{PO_4^{3-}}$) in the biologically active portions of the ice are reproducible by physical processes. The data presented in this chapter also suggests that the sea ice growth in the AMIZ is more complicated than the traditional pancake cycle described by Lange et al. (1989), this is seen in the variability in properties of the cores from the same station. This suggests that ice growth is not a linear progression of stacking as described in literature, rather a constant rearranging of sea ice with each floe having its own unique developmental history. Further work to support these findings should include analysis of the iron content in the ice and characterization of the biological communities in each section of the rafted ice.

Chapter 4

4. Spatial variability of physical and biogeochemical properties of sea ice in spring 2019[2]

4.1. Introduction

The study conducted by Johnson et al. (2023) in the AMIZ during the SCALE spring 2019 cruise (Section 2.1.2) identified sea ice textures and characterised the growth conditions that were associated with the granular, transitional, and columnar ice types. Their study revealed a complex stratigraphy in the ice sampled, which varied spatially and was dependent on the atmospheric and oceanic conditions experienced by the sea ice from formation to sampling. The dynamic nature of the AMIZ produced an unpredictable stratigraphy in the sea ice sampled, through processes like ridging, rafting and frazil formation.

This chapter presents and discusses complementary biogeochemical data from the expedition. These data are combined with data and interpretation from Johnson et al. (2023) to assess the variability of the biogeochemical properties of sea ice in the spring AMIZ.

4.2. Data and methods

This chapter focuses on the samples collected at SMIZ3 and SMIZ6 (Table 4.1) during the SCALE spring expedition in 2019 (Section 2.1.2). These stations were located along the same latitude and were 463 km apart (Figure 4.1a). These stations were selected for further investigation following the study conducted by Johnson et al. (2023), that found a significant difference in the stratigraphy between SMIZ3 and SMIZ6. A summary of the stations is presented in Table 4.1.

---

[2] Parts of this chapter have been published in Johnson S, Audh RR, de Jager W, et al. Physical and morphological properties of first-year Antarctic sea ice in the spring marginal ice zone of the Atlantic-Indian sector. Journal of Glaciology. 2023;69(277):1351-1364. doi:10.1017/jog.2023.21. I contributed the sea ice temperature, salinity and δ18O data and the formal analysis that is found in the publication. This chapter adds a biogeochemical component to the study conducted and further discusses the temperature, salinity, crystal structure data and part of the δ18O data that were originally published in Johnson et al. (2023).

Table 4.1. Summary of stations presented in this chapter. T/S refers to cores analysed for temperature and salinity, BGC for cores analysed for biogeochemical properties and CS refers to the crystal structure cores.

STATION	DATE	LOCATION	AIR TEMP (°C)	SNOW DEPTH (cm)	AVERAGE CORE LENGTH (m)	NO. OF CORES (DESIGNATION)
SMIZ3	24/10/2019	59.32°S; 00.06°E	-7.40	11	0.57 ± 0.09	4 (T/S), 3 (BGC), 1 (CS)
SMIZ6	29/10/2019	59.36°S; 08.15°E	-9.83	3	0.71 ± 0.14	3 (T/S), 3 (BGC), 1 (CS)

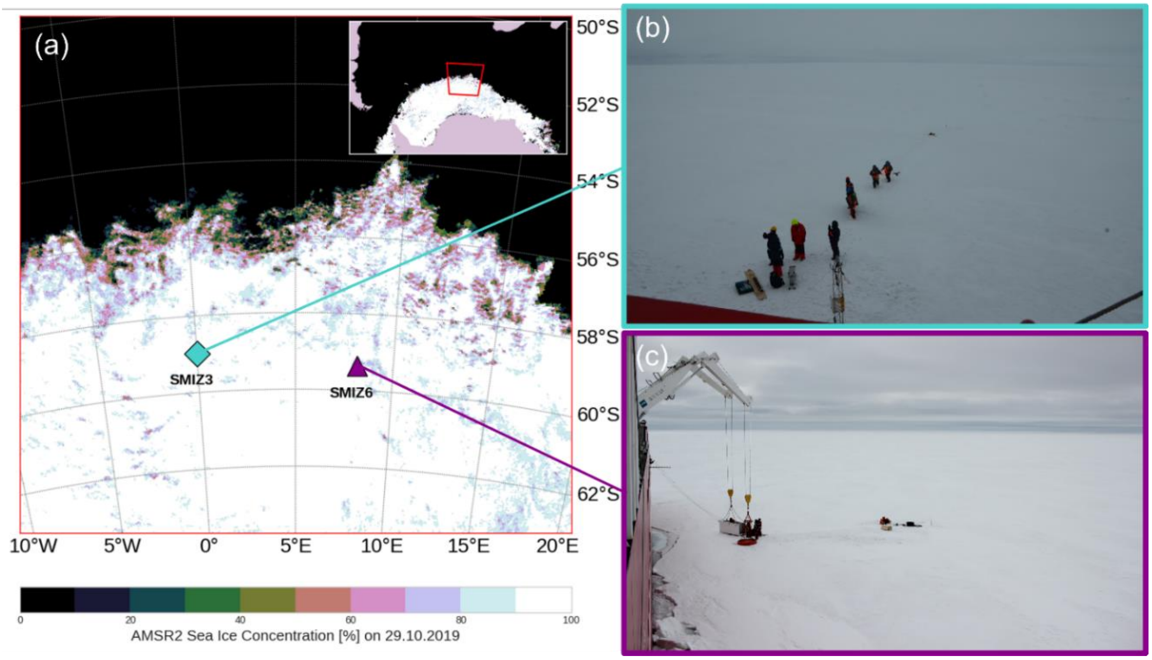

Figure 4.1. (a) Map showing the locations of SMIZ3 and SMIZ6, overlaid with the sea ice concentration derived by the AMSR2 satellite product (Spreen et al., 2008). The environmental conditions during sampling are shown in (b) for SMIZ3 and (c) for SMIZ6.

The sampling of these stations was conducted overboard on cemented first year ice floes following the protocols described in Section 2.2.2. Both stations had level ice and clear conditions (Figure 4.1b,c). The ice at SMIZ3 had a 11 cm thick snow layer, while SMIZ6 had a thinner, 3 cm snow layer (Table 4.1). The physical and biogeochemical profiles of the sea-ice cores collected at both stations were produced using the methods described in Section 2.3. All SCALE2019 cores were treated in the same manner to allow for cross referencing and comparison. The methodology used for the backtracking and model simulations is the same as described in Section 2.5.

4.3. Results

4.3.1. Sea ice characteristics

Eight cores for SMIZ3 and seven cores for SMIZ6 are discussed in this chapter (Figure 4.2). To aid in the interpretation and comparison of the stations, the data from all cores were normalised by depth (i.e. 100*(depth/total core length)). The average core length for SMIZ3 was 0.57 ± 0.09 m and SMIZ6 was 0.71 ± 0.14 m. Both stations show variability in the core thicknesses, with SMIZ6 displaying a slightly larger standard deviation (Table 4.1).

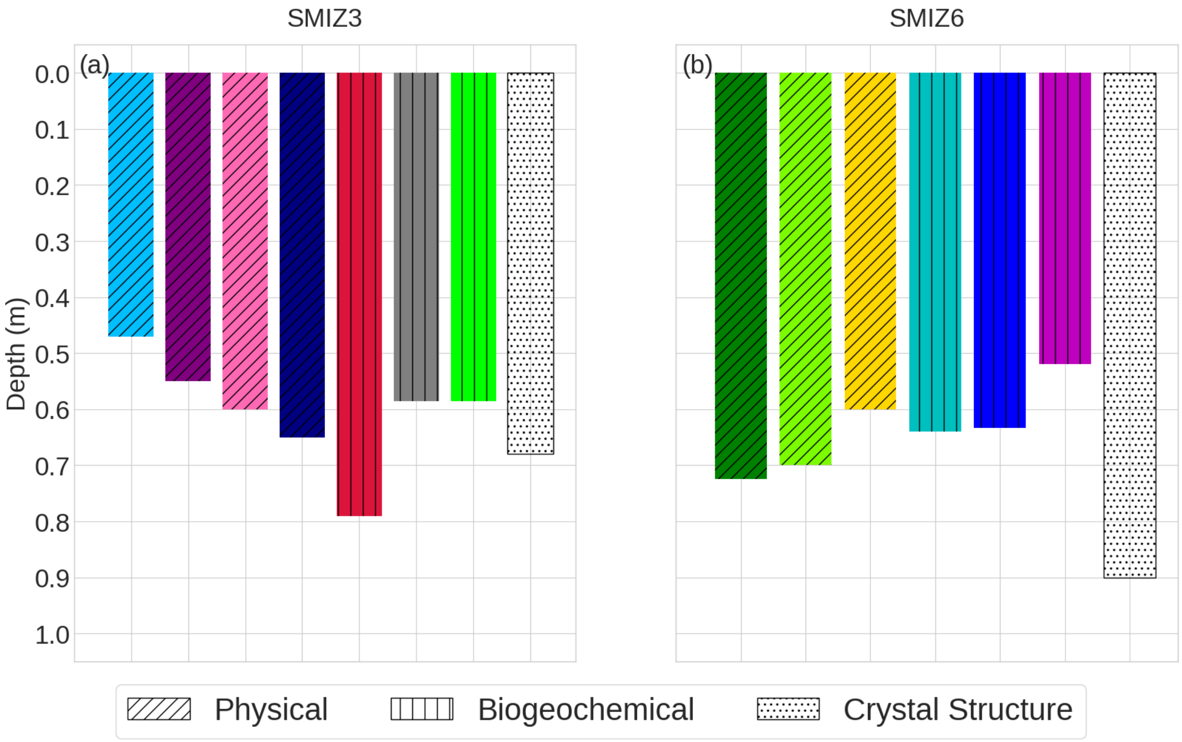

Figure 4.2. Core lengths and designations for (a) SMIZ3 and (b) SMIZ6. Core designations are indicated by the hatches in the bars. Colours correspond to respective core profiles in the following figures.

4.3.2. Sea-ice formation conditions

The reconstructed trajectories of the sea ice sampled at each of the stations are shown in Figure 4.3. The trajectories indicates that the ice originated to the south-west of their respective sampling locations. The ice had an initial northward movement followed by a long eastward trajectory. The floe that became SMIZ3 moved northward from early October while the floe that became SMIZ6 only began to move northward days before sampling occurred. These trajectories were used to extract the atmospheric and oceanic conditions experienced by the floes during their lifetime. The environmental conditions along each floes trajectory contributed to the variability observed in the sea ice properties, these conditions are discussed in detail by Johnson et al. (2023) and are summarised below to help contextualise the resulting biogeochemical properties of the sea ice.

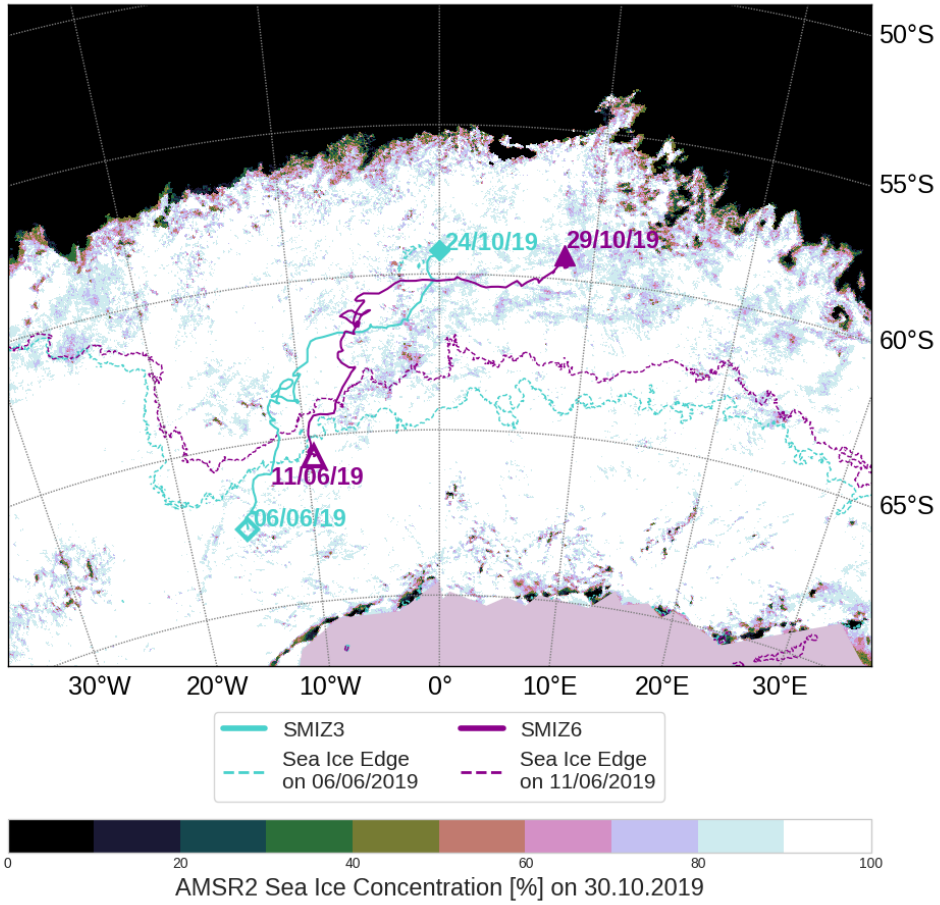

Figure 4.3. Reconstructed trajectories of the sampled sea-ice floes, with the date and location of formation (open symbols) and sampling (closed symbols) indicated. The map is overlaid with the satellite derived sea ice concentration from the AMSR2 product on 30.10.2019 (Spreen et al., 2008). The blue dashed line indicates the location of the sea ice edge on 06/06/2019, which is the estimated date of formation of the first sampled floe (SMIZ3), and the purple dashed line indicates the location of the sea ice edge on 11/06/2019, which is the estimated date of formation of the second sampled floe (SMIZ6).

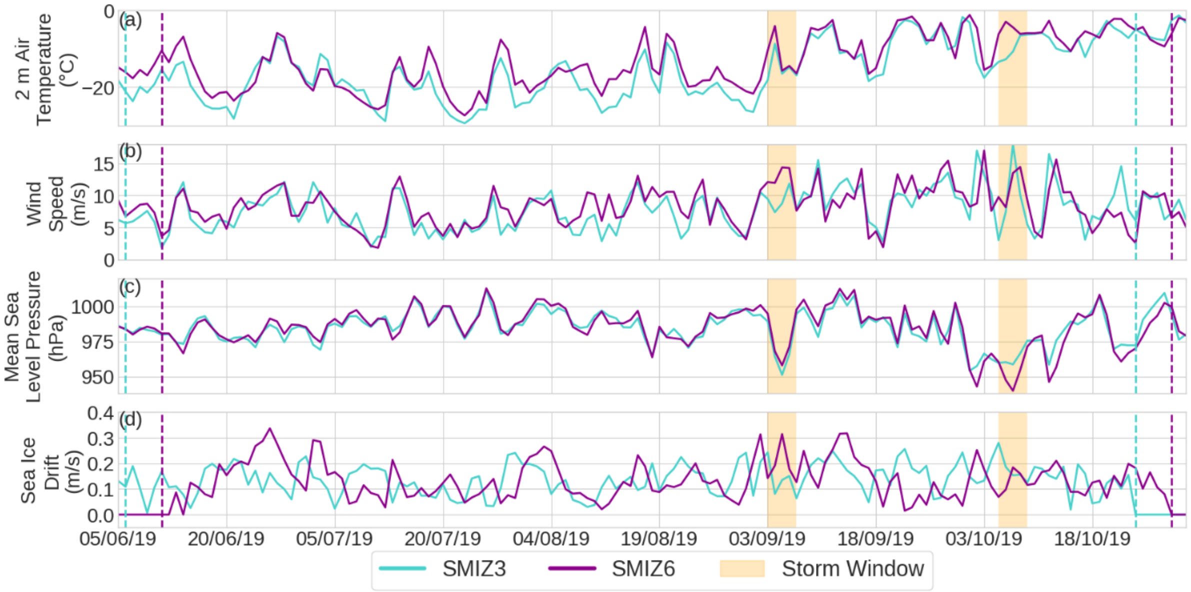

Figure 4.4. (a) 2m air temperature and (b) mean sea level pressure, (c) wind speed and (d) sea ice drift extracted along the trajectories of the sampled ice floe and averaged every 24 hr. Atmospheric variables were obtained from ERA5 (Hersbach et al., 2020) and the sea ice drift data were derived from OSI-SAF (OSI SAF, 2021). Orange shading indicates the storm windows for the storms presented in Figure 4.5. The vertical dashed lines indicate the start of the backtrack window (i.e. date of floe formation) and the end of the back trajectory (i.e. day of sampling).

The atmospheric conditions and sea ice drift along the floe's reconstructed trajectories are displayed in Figure 4.4. The 2 m air temperature data (Figure 4.4a), indicates that both floes experienced similar temperature fluctuations over their trajectories, with a clear seasonal increase from July to October, and an overall warming trend that starts at the onset of spring in September. A notable difference between the floes occurred in mid- to late August, where SMIZ3 experienced colder temperatures, while SMIZ6 experienced an increase in atmospheric temperature during this period (Figure 4.4a). The wind speed data (Figure 4.4c) indicates that both floes experienced similar conditions, with an overall increase as the floes move northward into the westerly winds. Deviations between the stations occurred in late July, where SMIZ3 experienced a drop in wind speeds and then in early September, when SMIZ6 underwent a sudden surge in wind speeds. Following these deviations, both floes experienced a decrease in wind speeds in mid-September. The presence of polar cyclones influence the environmental conditions in AMIZ and subsequently the sea-ice cover (Vichi et al., 2019). The largest storms that passed over the region of interest were identified by a significant drop in MSLP below 970 hPa and are indicated by the shading in Figure 4.4. The polar cyclones are further marked by rapid decreases in sea ice concentration and increases in windspeed (Figure 4.4c). The decrease in wind speed experienced by both floes in mid-September may be attributed to the passing of a large storm. The presence of a storm also influences the ice field. Sea ice concentration analysis by Johnson et al. (2023) revealed differences between the stations over their respective trajectories. While both stations initially experienced similar conditions, the onset of the cyclone period in late August was the start of frequent fluctuations in sea ice concentration for SMIZ6, while SMIZ3 remained relatively constant at a high concentration (around 90-95%). A lower and frequently changing sea ice concentration, as experienced by SMIZ6, is indicative of an unconsolidated and mobile ice pack. This is further supported by the sea ice drift data (Figure 4.4d), i.e. the larger the drift, the more mobile the ice pack was, which would make deformation events more likely to occur. SMIZ6 experienced overall higher drift speeds compared to the SMIZ3 and more frequent periods of increased drift speeds that suggest periods of break up and increased motion in the ice field. The storm signal is also evident in the drift data, with both stations experiencing an increase in drift speeds during the storm windows, and SMIZ6 experiencing this increase more intensely than SMIZ3.

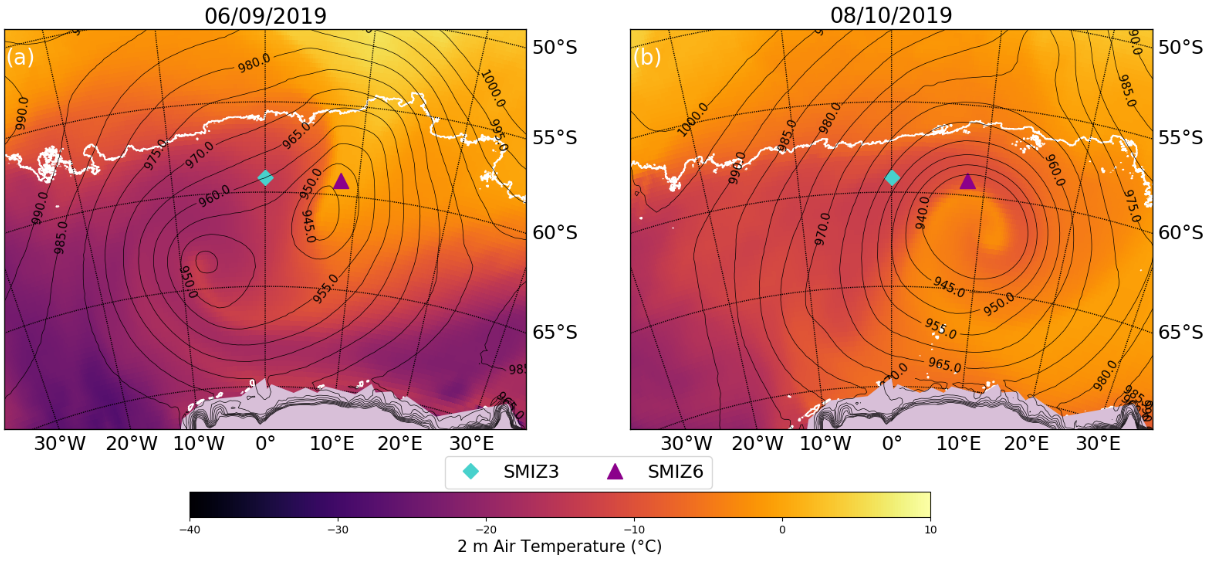

Figure 4.5. Synoptic maps showing the 2 m air temperature (colour map) and the mean sea level pressure (contours) from ERA5 (Hersbach et al., 2020) for the two large polar cyclones over the stations on (a) 06/09/2019 and (b) 08/10/2019. Closed symbols indicate the location of each station. The sea ice edge is indicated by the white contour.

The polar cyclones of interest were identified by a surface pressure below 970 hPa and are shown in Figure 4.5. They both present the advection of warmer maritime air at two different stages of development, and the air mass entrapment within the core of the cyclone (Vichi et al., 2019). The storm shown in Figure 4.5b can be classified as an extreme polar cyclone with a surface pressure of 940 hPa (Wei & Qin, 2016). The influence of these storms can be seen in the atmospheric and sea ice conditions (Figure 4.4) with increases in temperature, drops in surface pressure, increased wind speeds and sea ice drift speeds. SMIZ6 seems to have experienced both storms more intensely than the SMIZ3, given its proximity to the eye of the storm in both cases. A drift divergence analysis was conducted by Johnson et al. (2023) and further supports this. Their analysis revealed an overall highly variable divergence field over the region and while both stations displayed a similar drift divergence trend, the magnitude of the divergence field over the storm periods differed significantly between SMIZ3 and SMIZ6. Both stations displayed negative divergence values during the storm periods (which indicates convergence), with the SMIZ3 field experiencing lower convergence values than SMIZ6 for the storm indicated in Figure 4.5a. The extreme polar cyclone in October (Figure 4.5b) resulted in a convergence between 0.02 and 0.04 day^{-1} for SMIZ3, while SMIZ6 experienced a comparatively severe convergence of 0.12 day^{-1} (Johnson et al., 2023).

There is clear evidence that the sea-ice floes that became SMIZ3 and SMIZ6 experienced a distinct difference in growth conditions owing to variations in the atmospheric and oceanic conditions over their respective trajectories from initial growth to sampling. The most extreme differences in these conditions were attributed to polar cyclones that influenced the atmosphere, ocean and resulting sea ice field. The ice floe that became SMIZ3 experienced relatively calmer conditions over its lifetime from growth to sampling, while SMIZ6 in comparison experienced a more turbulent lifetime, with increased dynamic processes and deformation events. This difference has ultimately resulted in each floe developing and displaying distinct physical and biogeochemical sea ice properties.

4.3.3. Physical properties

The physical properties of the ice at both stations are presented in Figure 4.6, these data were first published with an in-depth interpretation by Johnson et al. (2023) and are presented here along with a summary of their interpretation and the addition of the $\delta^{18}O$ data for SMIZ3 to contextualise the resulting biogeochemical properties of the sea ice sampled at both stations. The data presented here represents the average sea ice profiles and corresponding standard deviations for each station that were produced by first normalising the ice depth and averaging the corresponding data points per 10% depth interval. The data are presented this way to characterise overall similarities and differences between the stations opposed to features from individual cores from each station. For individual ice core profiles per station that are true to depth, see Figure B.1 and Figure B.2 in Appendix B.

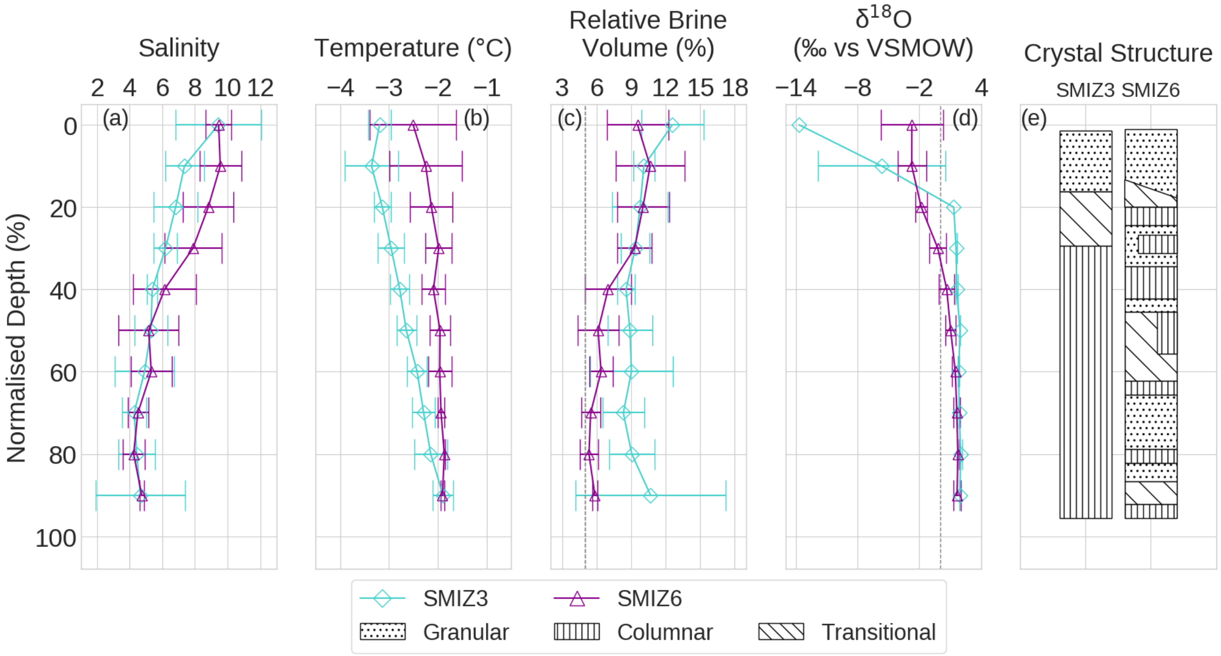

Figure 4.6. Vertical profiles of the average (a) salinity, (b) temperature, (c) relative brine volume, (d) $\delta^{18}O$ and (e) crystal structure from the cores collected at SMIZ3 (blue profile) and SMIZ6 (purple profile). The data for each core per station were depth normalised (i.e. 100*(depth/total core length)) and binned into 10% depth intervals, the averages (represented by the open symbols in each profile) and standard deviation (represented by the error bars) per depth interval were then computed for each station. Note: in the case of SMIZ3 in (d), the dataset was incomplete at the time of writing, hence the lack of error bars for some depth intervals (Audh et al., 2022).

The salinity profiles (Figure 4.6a) for both stations have similar surface values, followed by a decrease with depth in SMIZ3, and a slight increase in depth for SMIZ6. The profiles then converge in the bottom half of the ice. The temperature profiles (Figure 4.6b) indicate overall colder sea ice at SMIZ3 compared to SMIZ6. The ice at SMIZ3 displays a clear increase in temperature with depth throughout the ice while the ice from SMIZ6 displays a more constant temperature with depth following an initial increase in temperature in the top 40% of the ice. The temperature profiles for both stations converge at the bottom of the ice. The RBV (Figure 4.6c) of both stations are over the 5% permeability threshold (Golden et al., 1998), suggesting that the ice at both stations were capable of sustaining biogeochemical activity throughout the thickness. The RBV profiles display a higher surface value for SMIZ3 followed by a convergence through to the middle of the ice and finally a divergence with SMIZ3 displaying the higher RBV in the bottom 60% of the ice.

The cross polarised images of the sea-ice cores (Figure 4.7) reveal that the ice from both stations displayed the same three ice textures: granular, transitional and columnar. The granular texture was identified by small, randomly orientated crystals, which suggested rapid formation under turbulent conditions. The crystals then increase in size for the transitional texture, which displays a mix of small and larger crystals in the initial stage of arrangement. The columnar texture is identified by the largest crystals with a uniform arrangement. While the ice from both stations displayed the same types of ice textures, the actual structure of the ice was significantly different between stations. Here we look at the $\delta^{18}O$ (Figure 4.6d) alongside the crystal structure (Figure 4.6e) to better differentiate between the ice textures. The ice from SMIZ3 displayed a typical stratigraphy (Weeks, 2010), with granular ice at the surface followed by a short transitional layer and finally a longer columnar ice portion. The granular layer at the surface of the ice corresponds to the δ^{18}O minimum, which suggests snow ice (Lytle & Ackley, 2001; Arndt et al., 2021), the transitional layer corresponds to the steady increase of the $\delta^{18}O$ with depth, followed by the positive $\delta^{18}O$ that corresponds with the columnar section. This stratigraphy suggests that the ice formed under relatively calm conditions. In contrast, SMIZ6 displayed a more complex structure, composed of several unusual layering of textures. The surface granular layer corresponded with the negative $\delta^{18}O$, suggesting the presence of snow ice. The transition from granular to transitional ice textures is slanted, suggesting potential rafting of floes, but the exact origin of observed layers remains unclear. Below the transitional layer, the influence of dynamic disturbances during sea-ice growth is evident. The ice displays intrusions of columnar crystals and variations in crystal textures indicating multiple deformation-related activities. A distinct change in sea-ice texture from columnar to granular crystals deeper in the ice suggests either rafting or deposition of granular frazil sea ice, since the $\delta^{18}O$ of the corresponding deeper granular layers in the ice suggests ice of frazil origin.

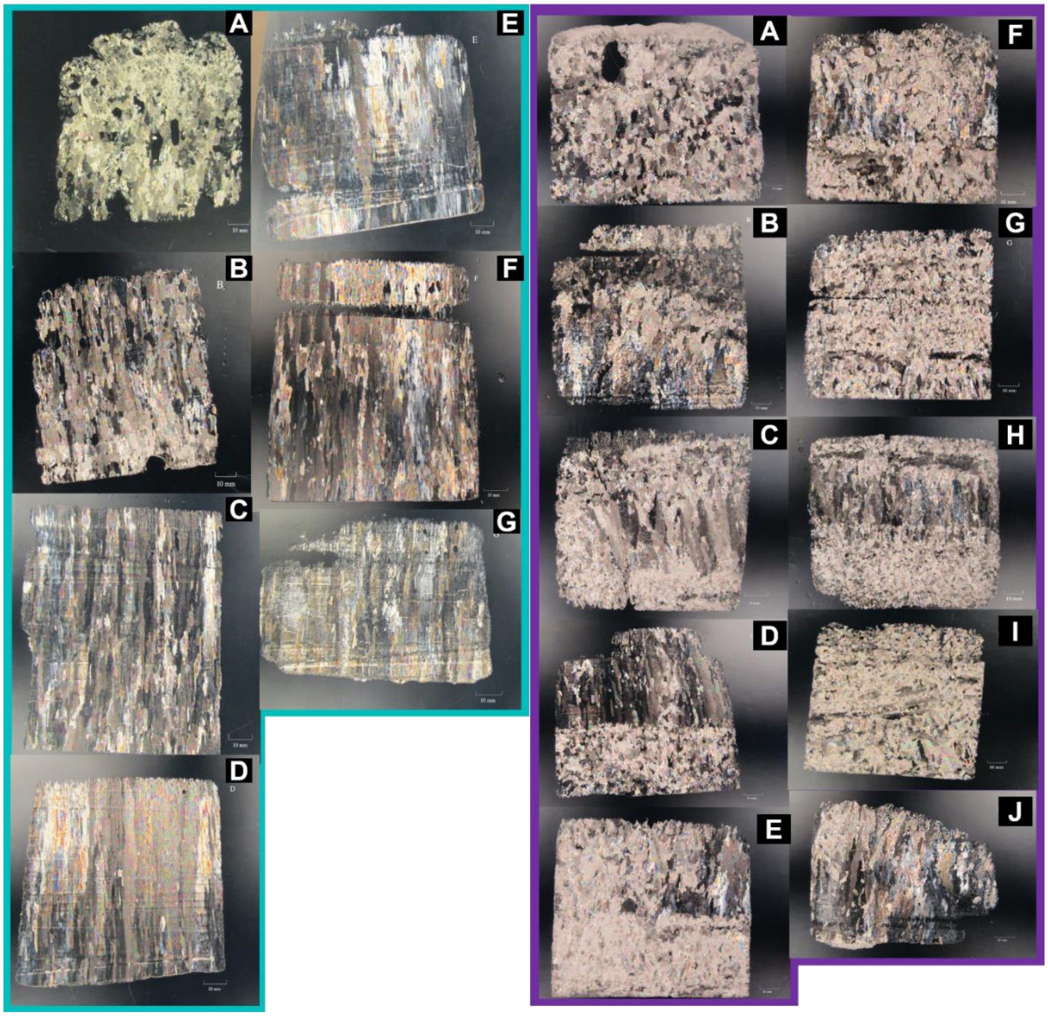

Figure 4.7. Crystal structure images of the cores taken from SMIZ3 (blue box) and SMIZ6 (purple box). The images are displayed alphabetically from the top of the core (A) to the bottom of the core. See Figure 4.2 for the lengths of the cores (Johnson, Khoboko, et al., 2022).

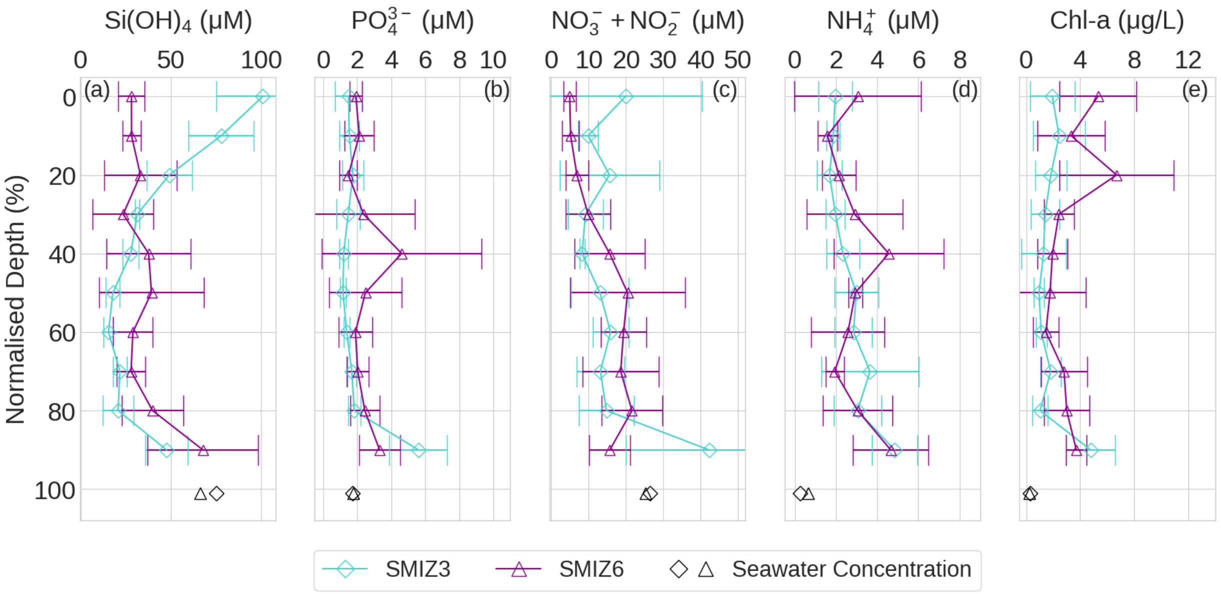

Figure 4.8. Vertical profiles of the average (a-d) salinity normalised nutrient- and (e) chlorophyll (chl-a) concentrations from the cores collected at SMIZ3 (blue profile) and SMIZ6 (purple profile). The concentration data for each core per station were depth normalised (i.e. 100*(depth/total core length)) and binned into 10% depth intervals, the average concentration (represented by the open symbols in each profile) and standard deviation (represented by the error bars) per depth interval was then computed for each station. The open black symbols below the profiles represent the seawater concentrations for each station with the symbol shape corresponding to the station profile.

4.3.4. Biogeochemical properties

The average salinity normalised nutrient and chlorophyll concentration profiles at each station are displayed in Figure 4.8. The profiles from SMIZ3 all display a maximum concentration at the bottom of the ice while SMIZ6 displays maximum concentrations in the ice interior and at the bottom. The seawater $\mathrm{Si(OH)_4}$ concentrations were 75.24 and 66.35 µM for SMIZ3 and SMIZ6 respectively. The ice from SMIZ3 displayed elevated $\mathrm{Si(OH)_4}$ in the top 0.2 m, followed by depleted $\mathrm{Si(OH)_4}$ with respect to seawater in the bottom portion of the ice. SMIZ6 displayed depleted $\mathrm{Si(OH)_4}$ throughout the ice, with the exception of the maximum concentration at the bottom of the ice that was slightly elevated (67.77 ± 30.63 µM). The ice $\mathrm{PO_4^{3-}}$ at SMIZ3 was elevated compared to the seawater (1.74 µM) in the bottom of the ice, but equal to or less than the seawater in the rest of the sea ice. The sea ice at SMIZ6 displayed $\mathrm{PO_4^{3-}}$ maximum of 4.62 ± 4.70 µM in the middle of the ice, and overall elevated $\mathrm{PO_4^{3-}}$ concentrations throughout the ice compared to the seawater (1.75 µM). The sea ice at both SMIZ3 and SMIZ6 displayed depleted $\mathrm{NO_3^- + NO_2^-}$ compared to the seawater (26.45 and 25.33 µM respectively) throughout the ice, except for the bottom of the SMIZ3 ice, where the maximum concentration (42.25 ± 22.24 µM) was elevated compared to the seawater. The ice $\mathrm{NH_4^+}$ for both stations displayed a general increase from low surface values to bottom maxima and overall elevated concentrations throughout the ice compared to the seawater (0.25 and 0.64 µM for SMIZ3 and

SMIZ6 respectively). The seawater chlorophyll concentrations for SMIZ3 and SMIZ6 were 0.30 and 0.23 µM respectively and were consistently lower than the sea ice concentrations for both stations. These elevated concentrations relative to the seawater suggests biological activity in the ice, with SMIZ6 displaying overall higher chlorophyll throughout the ice compared to SMIZ3.

Table 4.2. Average and standard deviation of the ice nutrient- and chlorophyll (chl-a) concentration for SMIZ3 and SMIZ6. The average and standard deviations were computed over three cores per station.

STATION	$\mathbf{Si(OH)_4}$ **(µM)**	$\mathbf{PO_4^{3-}}$ **(µM)**	$\mathbf{NO_3^- + NO_2^-}$ **(µM)**	$\mathbf{NH_4^+}$ **(µM)**	**Chl-a (µg/L)**
SMIZ3	41.08 ± 28.49	1.91 ± 1.31	16.18 ± 9.82	2.72 ± 0.98	1.87 ± 1.13
SMIZ6	35.47 ± 12.62	2.47 ± 0.90	13.81 ± 6.53	2.94 ± 1.01	3.25 ± 1.65

Overall, SMIZ6 showed higher variability between cores taken across the floe, this can be seen in the larger standard deviations per depth interval in the average concentration profiles in Figure 4.8 and further in the individual core profiles (Figures Figure B.1 and Figure B.2), compared to the ice from SMIZ3 which displayed smaller standard deviations. As an overall summary (Table 4.2), the ice from SMIZ3 displayed a higher average content of $\mathrm{Si(OH)_4}$ and $\mathrm{NO_3^- + NO_2^-}$ compared to SMIZ6, while the ice from SMIZ6 displayed higher $\mathrm{PO_4^{3-}}$, $\mathrm{NH_4^+}$ and chlorophyll.

4.3.5. Numerical modelling of sea ice properties

As done for the winter case in Chapter 3, the ESIM (Section 2.5.2) was used to simulate the thermodynamic growth of the sea ice along the computed floe trajectory for both stations (Figure 4.3). For the purpose of this chapter, a variable OHF was used (see Section 2.5.2.2 for methods on the timeseries computation). The results of these simulations are presented in Figure 4.9. The ESIM simulation produced sea ice before the estimated date of formation from the computed trajectory (Figure 4.9). A discrepancy is expected due to the resolution of the satellite drift product that was used, since the floe trajectory was computed from the first date that ice drift can be estimated from passive microwave data. According to the atmospheric data that were used to force the ESIM, the conditions at the same location were conducive to sea ice growth up to one month earlier.

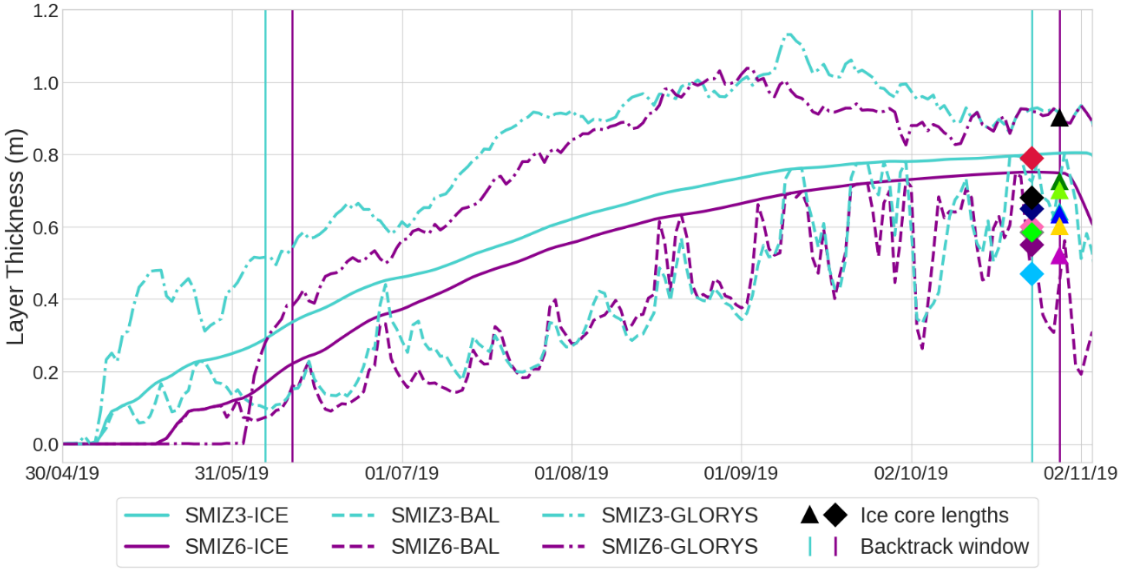

Figure 4.9. Simulated sea-ice thickness from GLORYS reanalysis (dash-dot line) and ESIM (continuous solid lines), with the corresponding BAL thickness (dashed lines) for SMIZ3 (blue lines) and SMIZ6 (purple lines). Symbols represent the observed sea-ice thickness for the collected cores at each station (colours correspond to the cores indicated in Figure 4.2). The vertical lines indicate the start of the backtrack window (i.e. estimated date of floe formation) and the end of the back trajectory (i.e. day of sampling).

The maximum ice thicknesses sampled at the stations were 0.78 m at SMIZ3 and 0.90 m at SMIZ6 (Table 4.1 and Figure 4.2). In contrast with the winter simulation presented in Section 3.3.5, the ESIM was able to simulate the maximum observed sea ice thickness at SMIZ3, while at SMIZ6 simulated ice was thicker than all cores except the longest one, which was used for the crystal structure analysis only (Figure 4.2b). The ESIM sea ice thickness was also compared to the GLORYS ocean reanalysis (https://doi.org/10.48670/moi-00018). GLORYS simulated thicker sea ice throughout the winter for both stations and converges towards the thermodynamic only model in spring. For SMIZ6, the GLORYS sea ice thickness matched the longest core from that station. Coincidentally, the longest core was used for the crystal structure analysis, which showed evidence of deformation (Figure 4.7). The similarity between that core and GLORYS, which is a dynamic model, supports the hypothesis that the ice at SMIZ6 grew thicker via dynamic processes.

We compare the simulated temperature and bulk salinity of the BAL in Figure 4.10. Given that the ice at both stations had a RBV > 5% throughout the ice (Figure 4.6c), the data for the BAL of the ice is taken as the average of the full ice profile. ESIM simulated warmer ice for SMIZ6 compared to SMIZ3, a feature that was also seen in the ice core data (see also Figure 4.6b). When compared to the ice data, the simulated ice for SMIZ3 was slightly warmer than the observed ice in all except one ice core, while SMIZ6 had the opposite, with the simulated ice being generally colder than the observed ice in all cores except one (Figure 4.10a). The major discrepancy was found in the simulated bulk salinity (Figure 4.10a). The observed bulk salinity of 5-7 was only simulated at the ice formation, with a very steep decline due to gravity drainage, and a minor salinity increase much lower than the spring observations could only be simulated in SMIZ6.

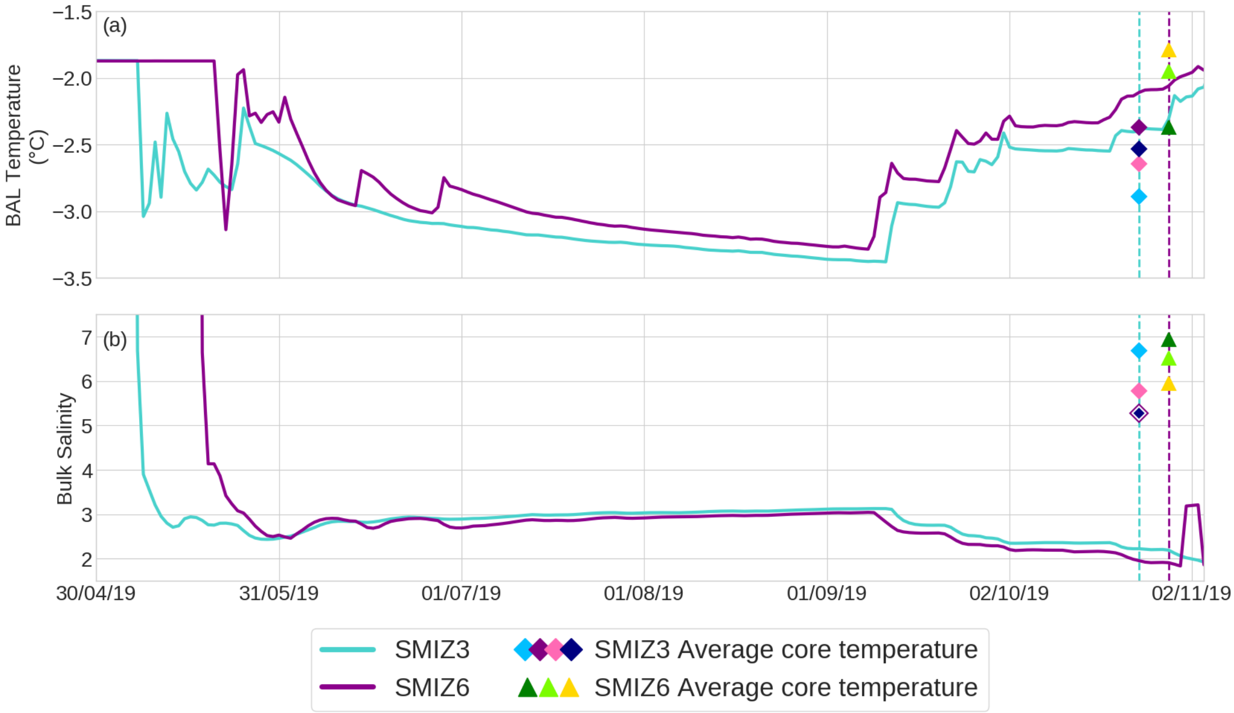

Figure 4.10. (a) BAL temperature and (b) Bulk Salinity simulated by the ESIM over the backtrack period for SMIZ3 (blue) and SMIZ6 (purple). Vertical dashed lines indicate the day of sampling for the respective stations. Symbols indicate the average core data for each station and the colours correspond to the cores indicated in Figure 4.2.

4.4. Discussion

4.4.1. Spatial variability of physical and biogeochemical properties in spring 2019

The sea ice conditions in the AMIZ during spring 2019were variable across sectors and influenced by dynamic growth conditions. Johnson et al. (2023) provided an initial analysis of the physical properties of the sea ice at SMIZ3 and SMIZ6 and supported their findings with atmospheric and oceanic data that described the environment that the ice grew in and the factors that led to the physical properties observed in the sea ice. The sea ice at SMIZ3 displayed a more typical stratigraphy with granular ice followed by columnar ice, while SMIZ6 displayed a structure more affected by sea ice dynamical processes with multiple layers.

It is evident from the environmental conditions and physical properties of the ice described in detail by Johnson et al. (2023) and summarized in the previous section, that there was a distinct difference in the growth conditions and resulting sea ice between the stations throughout their respective lifetimes. The model simulations provided further insight into the formation conditions at both stations (Figure 4.9), indicating that observed sea ice thickness at both stations could be reproduced thermodynamically during the growing season.

For the sea ice from SMIZ3, the presence of an 11 cm snow layer (Table 4.1) and the strong negative $\delta^{18}O$ at the surface suggests a snow ice layer that formed as a result of surface flooding of seawater and eventual refreezing. Further evidence of this flooding signal can be seen in the higher salinity values (Figure 4.6a) and the similarity between the in-ice nutrient concentrations and the underlying sea water (Figure 4.8). Columnar ice tends to reject nutrients from the ice matrix as it grows (Clarke & Ackley, 1984), resulting in lower concentrations of nutrients in the ice compared to the surrounding seawater. This can be seen in the SMIZ3 profiles (Figure 4.8), where the lower nutrients correspond to the columnar layer in the ice (Figure 4.6e). Algal nutrient consumption cannot be entirely ruled out at this station, although the bottom increase in chlorophyll corresponds to the observed maxima in nutrients. The increase in nutrient concentrations at the bottom of the ice could be a result of increased exchange with the underlying ocean, promoted by warming of the bottom layer (Figure 4.6b) and the increase in the RBV of the ice (Figure 4.6c).

The ice at SMIZ6 displays an irregular crystal structure, typical of deformed ice (Lange & Eicken, 1991; Jeffries & Weeks, 1993). The influence of the complex structure of the ice is evident in the variability of nutrient concentrations with depth throughout the ice as well as the variability between ice cores (Figure B.2). This spatial variability further suggests the concept discussed in Section 3.4.2, that is, multiple cycles of breaking and rafting of floes with different formation histories contribute to the biogeochemical content. This is consistent with the few previous studies, which also attributed the complex vertical structure to several formation processes occurring at different rates (Clarke & Ackley, 1984; Dieckmann et al., 1991). The lower RBV (Figure 4.6c) in the bottom half of the core corresponds to the irregular layering of the ice textures and indicates low permeability. This would influence the distribution of nutrients throughout the sea ice and exchange with the ocean below and could explain the slight spike in nutrient concentrations in the middle of the ice (Figure 4.8).

The ESIM was able to simulate a sea ice thickness that was similar to the observed sea ice for both stations (Figure 4.9), indicating that sea ice can grow thermodynamically as columnar ice to the observed spring thickness and even above. Given the nature of the model, the simulated ice column is however composed of uniform ice, while the dynamic nature of the AMIZ and the resulting sea ice structure demonstrates evidence of the sea ice growth being interrupted by multiple instances of breaking, rearranging and rafting events. This difference is evident in the salinity simulation; the model simulated very low bulk salinity (Figure 4.10b), which is indicative of rapid and continuous brine drainage characteristic of columnar ice. The comparison with the winter simulations and data (Figure 3.12) indicates that AMIZ ice may be overall more saline throughout the winter and spring seasons, and this may be due to the multiple stages of layering discussed in Chapter 3, which ultimately retain ice floes with different brine contents. The fact that, despite the different vertical structures, both floes had high bulk salinity indicates that AMIZ ice has reduced gravity drainage, and it is more often affected by seawater flooding. The model simulates bulk salinity only, and not the vertical distribution, which, according to the observations (Figure 4.6) is characterised by high salinity at the top and minimum salinity at the bottom that is nevertheless higher than the modelled mean. This further demonstrates that sea ice models consider sea ice as a single, homogenous layer, in line with typical columnar ice found in the Arctic.

While the sea-ice biogeochemical environment relies on the permeability and stratigraphy of the sea ice that influences the exchange of nutrients and gases both within the sea ice and with the underlying ocean, we must also acknowledge the influence of the prevailing conditions during sampling. As discussed above, the sea ice at SMIZ3 displayed signs of surface flooding promoted by an 11 cm thick snow layer (Table 4.1). The snow layer also insulated the ice against the atmosphere, leading to colder ice (Figure 4.6b). In contrast, the snow layer at SMIZ6 was 3 cm thick (Table 4.1), this suggests that the floe was not properly insulated from the atmosphere. The lack of insulation resulted in warmer ice temperatures (Figure 4.6b) and promoted biological activity through the availability and penetration of solar radiation. The latter is seen in the overall higher chlorophyll throughout the SMIZ6 sea ice compared to SMIZ3, with chlorophyll maxima closer to the surface layer (Figure 4.8e). The high chlorophyll also corresponds to low nutrient concentrations in the SMIZ6 sea ice.

The BFM was not used to simulate the sea ice biogeochemistry during spring as done in winter due to the complexities involved with simulating relatively older sea ice and an active biogeochemical environment. The BFM requires further refinement to include these intricacies for the Antarctic, which exceeded the scope of this thesis.

4.4.2. Evolution of sea ice properties from winter to spring

Figure 4.11 compares the winter data from Section 3.3 with the spring samples. The evolution of the sea ice physical and biogeochemical properties from winter to spring displays a warming of the ice, accompanied by the decrease in bottom salinity as the relative brine volume increases. Increased surface salinity in the spring cores is evidence of surface flooding of seawater, which is further corroborated by corresponding negative $\delta^{18}O$ values at the surface of the ice typical of snow ice. Depleted $NO_3^- + NO_2^-$ in the spring sea ice suggests sea ice primary production, although this depletion is not found in the other nutrients. In particular, $Si(OH)_4$ concentrations in the winter station are as high as the westernmost spring station SMIZ3. The spring sea ice displays higher chlorophyll concentrations throughout the ice compared to winter, indicating increased production from winter to spring. The fact that there is a direct inverse relationship between macronutrient concentrations and chlorophyll is indicative of the need to consider additional variables, such as nutrient isotopes both in the inorganic and organic components, as will be presented in Chapter 5.

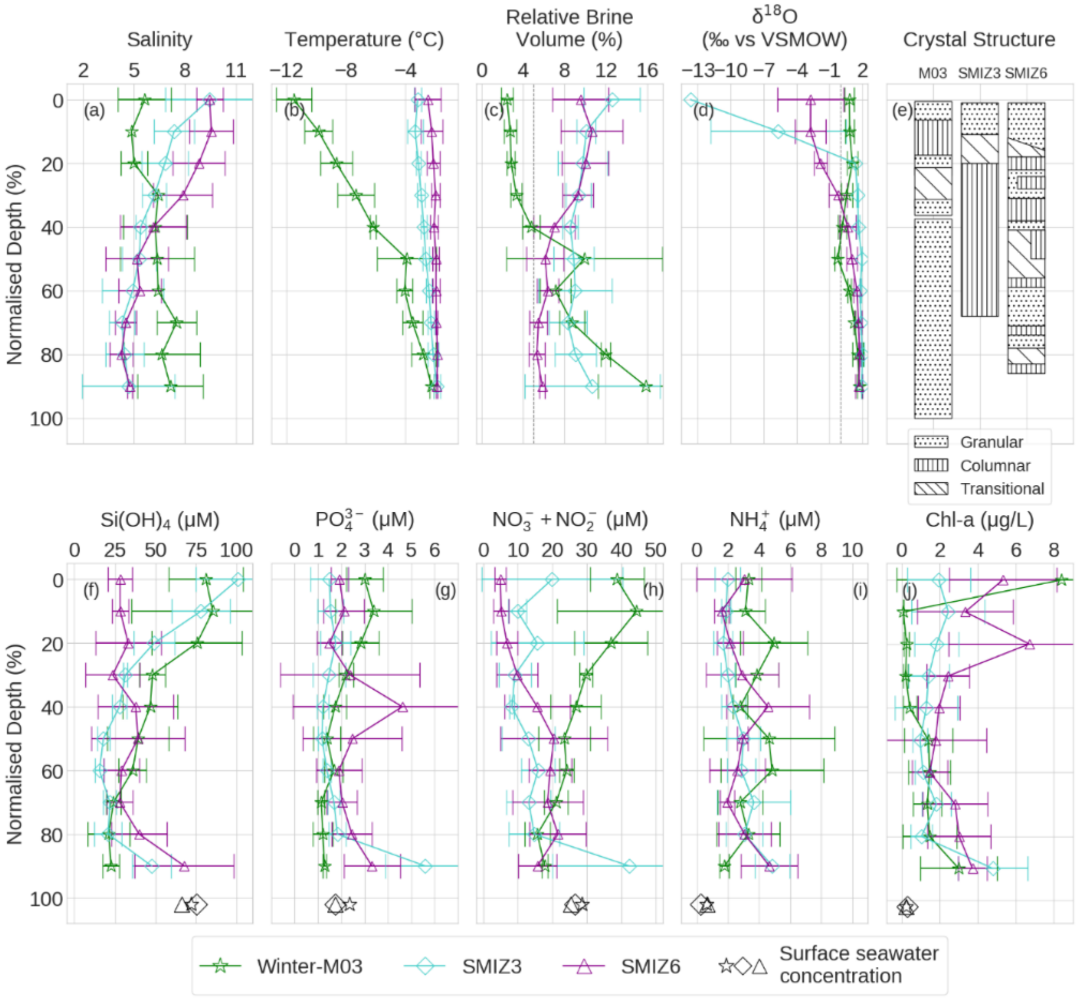

Figure 4.11. Average profiles of (a) Salinity, (b) temperature, (c) relative brine volume, (d) $\delta^{18}O$, (e) crystal structure, (f-i) salinity normalised nutrients and (j) chlorophyll data for the winter sea ice (M03) (star symbols, green profiles), SMIZ3 (diamond symbols, blue profiles) and SMIZ6 (triangle symbols, purple profiles). Open symbols at the bottom of plots f-j correspond to the profiles and indicate the surface seawater concentrations. Profiles are depth normalised (i.e. 100*(depth/total core length)) to aid in comparison.

4.5. Conclusion

This chapter focused on the study of the biogeochemical components from the same samples described in terms of their physical properties by Johnson et al. (2023). We analysed two stations that displayed distinctly different physical properties that arose from the ice at both stations experiencing different atmospheric conditions over their respective lifetimes. Upon investigation of the stratigraphy of the ice, we observed the ice from the westernmost sampling station, SMIZ3, displayed first-year ice characteristics with a prevalence of columnar ice which suggested growth was dominated by thermodynamic processes alone in calmer ocean conditions. This contrasted to the easternmost station, SMIZ6, which displayed disrupted stratigraphy that suggested thickening via dynamic processes and/or multiple freeze-melt-refreeze cycles. The biogeochemical data reflects the influence of the sea ice structure, both vertically through the ice, where SMIZ3 shows less vertical variability than SMIZ6 and horizontally across the sampled floe, where the multiple cores from SMIZ6 led to larger standard deviations than SMIZ3. The data presented indicated that the observed biogeochemical environment was ultimately dominated by the prevailing conditions observed during sampling, i.e. surface flooding and snow insulation. The SMIZ3 sea-ice biogeochemical environment was similar to the underlying seawater. This paired with the elevated surface salinity and presence of a thick snow layer and snow ice indicated that surface flooding around the time of sampling influenced the biogeochemical environment in the sea ice. The relatively thin snow layer on the SMIZ6 sea ice allowed for light penetration that promoted primary productivity in the surface layers of the SMIZ6 sea ice, which displayed elevated chlorophyll- and depleted nutrient concentrations in the upper layers. The data presented here emphasizes the importance of considering dynamic growth conditions and environmental factors when considering sea ice biogeochemical distributions and further supports the need to adapt existing sea ice models to better simulate the Antarctic sea ice environment by including dynamic processes and considering sea ice as more than a single, homogenous, columnar layer, as in the Arctic. The comparison between winter and spring sea-ice core data indicates the transition from winter to spring displays an overall warming of the ice, evidence of increased brine drainage and surface flooding and an increase in biological activity that was indicated by elevated chlorophyll concentrations. The transition from winter to spring and the resulting biogeochemical dynamics will be discussed further in Chapter 5.

Chapter 5

5. Seasonal comparison of sea-ice nitrogen isotope ratios

5.1. Introduction

Nitrogen (N) is one of the essential nutrients required by organisms to grow, and its cycling in the Antarctic sea ice environment is vital to the biogeochemical processes occurring under extreme conditions. Within the sea ice, N exists in various pools, primarily as nitrate ($\mathrm{NO_3^-}$), ammonium ($\mathrm{NH_4^+}$), and particulate and dissolved organic N (PON and DON, respectively). Each of these pools plays a distinct role in the N cycle and reflects different aspects of biological and chemical processes in the ice. $\mathrm{NO_3^-}$ is a key N source for primary producers, particularly phytoplankton, and its concentration and isotopic composition are widely used to infer rates of biological uptake and recycling. $\mathrm{NH_4^+}$, generated through the remineralisation of organic matter, is both a substrate for nitrification and a source of N to primary producers, while PON consists of N incorporated into biomass and detritus, serving as an indicator of biological productivity and organic matter cycling within the ice (Fripiat et al., 2014, 2015).

The isotopic composition of N (δ^{15}N) in these pools can provide valuable insights into the processes controlling N cycling. Nitrogen has two stable isotopes, ^{14}N and ^{15}N, with the former being by far the more abundant of the two (i.e., 99.63% of all the N on Earth). The δ^{15}N is the per mille (‰) deviation of the $^{15}\mathrm{N}/^{14}\mathrm{N}$ ratio in a sample from the $^{15}\mathrm{N}/^{14}\mathrm{N}$ ratio in the universal reference standard, N_2 in air:

$$\delta^{15}N\ (\text{‰ vs Air}) = \left(\frac{\left(\frac{^{15}N}{^{14}N}\right)_{sample}}{\left(\frac{^{15}N}{^{14}N}\right)_{standard}} - 1 \right) \times 1000 \qquad (12)$$

The isotopic composition of a pool of N can be used to identify the dominant processes that add or remove N with a characteristic pattern of isotopic discrimination, as well as various potential sources of the N. These include biological processes like N_2 fixation, N assimilation, nitrification, organic matter remineralisation, denitrification (Mariotti et al., 1981; Sigman et al., 1999; Montoya, 2008; Casciotti et al., 2011; Smart et al., 2015; Henley et al., 2017; Sigman & Fripiat, 2019). The δ^{15}N of an N pool varies as a result of isotopic fractionation during chemical, physical and biological processes that favour the reaction of one isotope over the other because of the difference in their masses. The degree of fractionation during a unidirectional reaction is given by the kinetic isotope effect (ε), which is quantified as the ratio of rates at which the two isotopes are converted from one form to another:

$$\varepsilon\ (‰)\ =\left(\left(\frac{{}^{15}k}{{}^{14}k}\right)-1\right)\times 1000 \tag{13}$$

where ${}^{n}k$ is the rate coefficient for the ^{n}N-containing reactant (Mariotti et al., 1981; Sigman et al., 1999). These principles have been well-documented in open ocean systems, where N isotope studies have elucidated the links between the degree of NO_3^- utilization and its isotopic composition (Sigman et al., 1999, 2000; Rafter et al., 2013 and references therein). More recently, these approaches have been applied to sea ice environments to shed light on *in situ* biogeochemical dynamics (Fripiat et al., 2014, 2015; Henley et al., 2017, 2023). The $\delta^{15}N$ of nitrate ($\delta^{15}N_{NO_3^-}$) is a powerful tool for tracing N transformations within sea ice as it reflects the balance of isotopic fractionation during co-occurring biological and physical processes. For instance, during NO_3^- assimilation by phytoplankton, the lighter ${}^{14}N$ isotope is preferentially taken up, causing the remaining NO_3^- pool to become enriched in ${}^{15}N$, resulting in higher $\delta^{15}N_{NO_3^-}$ values (Sigman et al., 1999). This process has been observed to be significant during periods of active biological growth in sea ice, especially in the spring when light availability increases (Fripiat et al., 2014).

Other N cycle processes also influence $\delta^{15}N_{NO_3^-}$. N_2 fixation, for instance, introduces low-$\delta^{15}N$ PON into a system, which, upon remineralisation and subsequent nitrification, will lower the $\delta^{15}N_{NO_3^-}$ values (Sigman et al., 1999; Rafter et al., 2013). N_2 fixation, however, is highly unlikely to occur in sea ice due to the extreme cold, lack of light, and oxygen-rich conditions within the sea ice matrix, all of which inhibit the activity of the nitrogenase enzyme required for N_2 fixation (Knapp, 2012). While a recent study has found evidence of N_2 fixation under coastal Antarctic sea ice in summer (Shiozaki et al., 2020); studies on N cycling in Antarctic environments have found no evidence for N_2 fixation in sea ice (Fripiat et al., 2014) or in Antarctic Marginal Ice Zone (AMIZ) surface waters (Smart et al., 2015). Nitrification is the microbial conversion of NH_4^+ via NO_2^- to NO_3^- and occurs with a large isotope effect, meaning that the conversion of NH_4^+ to NO_3^- strongly favours the transfer of the lighter isotope (${}^{14}N$), thus introducing low-$\delta^{15}N_{NO_3^-}$ into the system (Casciotti et al., 2003). That said, the effect of nitrification on $\delta^{15}N_{NO_3^-}$ depends largely on the completeness of the process (Sigman et al., 2009; Smart et al., 2015). If nitrification is complete and provided that it competes with no other process (e.g., NH_4^+ uptake by phytoplankton), the $\delta^{15}N$ of the newly formed NO_3^- will resemble the $\delta^{15}N$ of the original organic matter and NH_4^+ being remineralised. However, when nitrification is incomplete, its substantial isotope effect will be expressed (Casciotti et al., 2003), resulting in low $\delta^{15}N_{NO3}$ values for newly nitrified NO_3^- (DiFiore et al., 2009; Smart et al., 2015). Thus, the

$\delta^{15}N$ of NO_3^- produced through nitrification is influenced by both the $\delta^{15}N$ of the organic matter and NH_4^+ precursors and the extent to which those substrates are converted to NO_3^- (Casciotti et al., 2003; Rafter et al., 2013; Fripiat et al., 2015). Nitrification may be especially important for the $\delta^{15}N_{NO_3^-}$ in winter sea ice, where light-limited conditions reduce phytoplankton growth, yet microbial processes remain active (as demonstrated in Chapter 3 and by Tison et al. (2017)). Evidence of nitrification has been observed in landfast ice (Priscu et al., 1990) and was suggested in Chapter 3 by the elevated concentrations of NH_4^+ and NO_3^- in our winter sea-ice cores. Denitrification is the microbial reduction of NO_3^- to N_2 gas, which, as in the case of NO_3^- assimilation by phytoplankton, preferentially removes ^{14}N from the NO_3^- pool, enriching the remaining NO_3^- in ^{15}N and raising its $\delta^{15}N$ (Granger et al., 2008; Sigman et al., 2009). Denitrification only occurs under conditions of (near-)zero oxygen. The interconnected brine channels within the sea ice facilitate gas exchange, which typically prevents the development of anoxic conditions, making denitrification unlikely (Golden et al., 1998; Tison, Delille, et al., 2017). Additionally, studies investigating N cycling in Antarctic sea ice have not found significant evidence of denitrification and instead attribute elevated $\delta^{15}N_{NO_3^-}$ values to other processes, such as nitrate assimilation (Fripiat et al., 2015). However, several studies in Arctic and Baltic sea ice have reported isotopic signals consistent with denitrification, suggesting that this process may occur under specific conditions in those regions (Kaartokallio, 2001; Rysgaard & Glud, 2004; Clark et al., 2020)

Along with $\delta^{15}N_{NO_3^-}$, the bulk PON concentration and corresponding N isotopic composition ($\delta^{15}N_{PON}$) can contribute to our understanding of the biogeochemical processes occurring in sea ice. The concentration of PON ([PON]) provides an indication of biomass in the ice and the $\delta^{15}N_{PON}$ records both the dominant N sources fueling autotrophic growth and evidence of heterotrophic breakdown of the PON biomass (Fripiat et al., 2014). For example, biomass fueled by NO_3^- is usually high in $\delta^{15}N_{PON}$ relative to growth supported by regenerated N sources like NH_4^+ (Lourey et al., 2003; Fawcett et al., 2011, 2014). At the same time, heterotrophic bacteria preferentially consume ^{14}N-bearing organic matter, causing the $\delta^{15}N_{PON}$ to rise during remineralisation (Lehmann et al., 2002; Möbius, 2013). As such, the $\delta^{15}N_{PON}$ can be used to help identify the dominant process or processes contributing to biomass growth and removal in the sea ice (Rau et al., 1991; Fripiat et al., 2014).

Physical processes affecting the sea ice can also play a significant role in setting the $\delta^{15}N$ of the NO_3^- pool. For instance, brine rejection during sea-ice formation can concentrate NO_3^- and elevate $\delta^{15}N_{NO_3^-}$ values in the brine channels, while the infiltration of low-$\delta^{15}N$ seawater during melting and flooding events can dilute the isotopically enriched NO_3^- pool in the ice, lowering the overall sea-ice $\delta^{15}N_{NO_3^-}$ (Fripiat et al., 2014). Taken together, the interplay between biological processes such as N assimilation and nitrification, and physical processes like brine rejection and flooding, all contribute to the variability in the δ^{15}N of the NO_3^- pool in Antarctic sea ice. Understanding these dynamics is essential for interpreting N cycling in polar regions, particularly as they relate to the broader Southern Ocean ecosystem. Despite this, studies of the N-isotopic composition of Antarctic sea ice remain limited. Most of the existing research has focused on spring and summer pack ice (Rau et al., 1991; Fripiat et al., 2014) and landfast ice (Cozzi & Cantoni, 2010; Fripiat et al., 2015). Of these studies, only two have provided co-collected data on the concentration and isotopic composition of both NO_3^- and PON (Fripiat et al., 2014, 2015). There is thus a notable lack of data for first year ice (FYI), which limits our understanding of N cycling in the AMIZ. This chapter aims to address this gap by presenting the first data on NO_3^- and PON concentration and isotopic composition in FYI during winter and spring in the Atlantic sector of the AMIZ, with the aim of contributing to a more complete understanding of the biogeochemical processes occurring in Antarctic sea ice.

5.2. Data and methods

The data presented in this chapter are from the SCALE2019 winter and spring expeditions (Section 2.1), specifically the winter MIZ3 station, sampled on 27 June 2019, and spring SMIZ3 station, sampled on 24 October 2019. These stations were selected because they are in the same region and thus provide the best case-study for a common location in the AMIZ in two different seasons (Figure 5.1). The data presented here were generated for the same cores presented in Chapters 3 and 4. The processing of the ice cores in preparation for the analysis described in this section is documented in Section 2.3.2. The N isotope data were produced in the Marine Biogeochemistry Laboratory at the University of Cape Town using the "denitrifier method" developed by Sigman et al. (2001) and an isotope-ratio mass spectrometer (IRMS) with custom-built in-line N_2O concentration and purification system (Weigand et al., 2016). The method is detailed below.

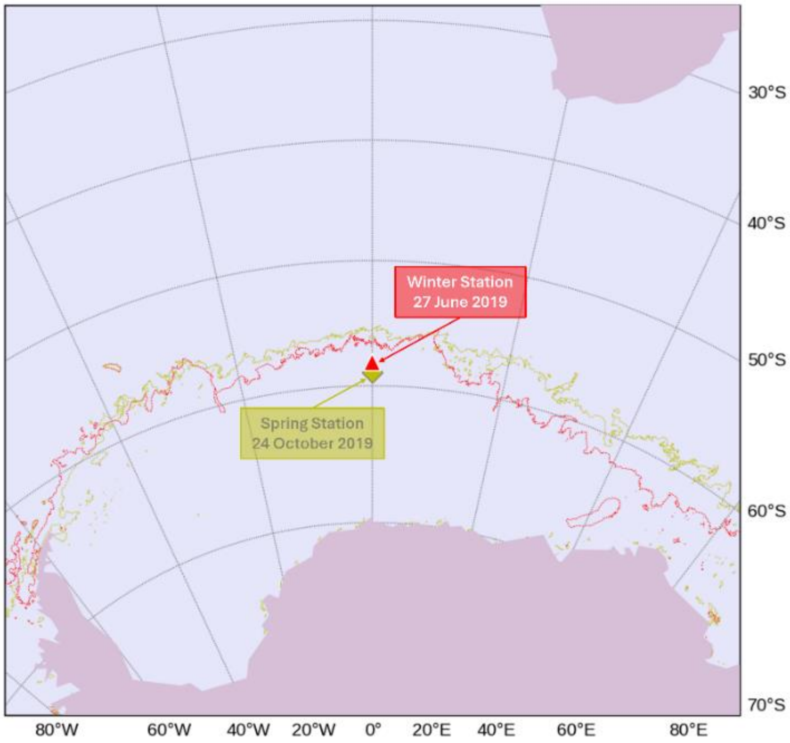

Figure 5.1. Station locations in the Antarctic Polar region overlaid with the location of the AMIZ for winter (red line) and spring (green line). The ice overlay is from the AMSR2 satellite product (Spreen et al., 2008).

5.2.1. Harvesting the bacteria

The denitrifying bacteria, *Pseudomonas aureofaciens* (P. aur), were first inoculated in CAS Phos media (two 250 mL bottles per harvest, Weigand et al., 2016). After 8-10 days, when the NO_3^-/NO_2^- concentration in the media had declined to undetectable levels, the culture was ready for harvesting. This involved centrifuging the media in 50 mL Falcon tubes to concentrate the P. aur. cells and remove them from the spent growth media. The concentrated P. aur pellets were then resuspended in NO_3^- free media using a vortex mixer. 2 mL of this solution was added to 20 mL borosilicate headspace vials that were sealed using butyl septa and aluminium crimp caps. These vials were then fitted with a venting needle (23-gauge, 1.5”) and placed on the flushing rig to be degassed with N_2 gas to remove any contaminant N_2O and generate anoxic conditions. After 4 hours, a bacterial blank was tested. This involved removing a vial from the flushing rig and after 30 min, killing the bacteria in that vial using a few drops of 10 M NaOH. Antifoam was then added, and the vial was measured by the IRMS. The purpose of testing the bacterial blank is to determine whether the level of N_2O in the vials (i.e., the “bacterial blank”) is low enough to proceed with the harvest. This condition is met by a IRMS peak area (which is linearly related to the quantity of N_2O in the sample) of <2% of the sample area. If this condition is not met, another vial is taken off every hour until the bacterial blank is low enough to proceed. Once the bacterial blank is low enough, all the vials are removed from the flushing rig and stored septa-down to prevent leakage.

5.2.2. Injecting standards and samples

Prior to injecting, samples and standards were defrosted and shaken to homogenise the contents of the bottles. The volume injected into each bacterial vial depends on the concentration of $\mathrm{NO_3^-}$ in the samples and standards, and was calculated as follows:

$$Injection\ volume = \frac{X\ nmol}{[NO_3^-]} \tag{14}$$

where *X nmol* refers to the desired N content for the IRMS run, which can be 5 nmol, 10 nmol or 20 nmol, and is determined by the $\mathrm{NO_3^-}$ concentration range of the samples – in other words, for relatively high concentration samples, 20 nmol of N will be injected into the bacterial vials, while for low concentration samples, fewer nmols of N are analysed in order to prevent the injection volumes from becoming too large. $[NO_3^-]$ refers to the bulk concentration of $\mathrm{NO_3^-}$ in the samples or standards. The standard concentrations should align with the sample concentrations. The standards are certified $\mathrm{NO_3^-}$ reference materials prepared in high purity Milli-Q water that are used to calibrate the sample isotope ratios after IRMS analysis. The standards used were IAEA-$\mathrm{NO_3^-}$, potassium nitrate with a $\delta^{15}\mathrm{N}$ of 4.7 ± 0.2‰ vs. $\mathrm{N_2}$ air (Gonfiantini, 1984), and USGS34, potassium nitrate with a $\delta^{15}\mathrm{N}$ of -1.8 ± 0.1‰ vs. $\mathrm{N_2}$ air (Böhlke et al., 2003). A set of standards were injected at the beginning of each batch run and then after every nine samples. The pooled standard deviation of the standards from all runs was 0.30‰ for IAEA-$\mathrm{NO_3^-}$ and 0.24 ‰ for USGS34.

Once the injection volumes were determined, an appropriately sized gas-tight syringe fitted with a needle (26-gauge, ½” or ⅝”) was used to inject the samples and standards into the prepared vials. The needle and syringe were rinsed three times between samples with Type 1 Milli-Q, followed by a rinse with the new sample. The needle was also replaced after every eight samples. Following injection, the vials were stored septa-down in the dark and allowed to denitrify for an hour and a half. After that time, a few drops of 10 M NaOH was injected into the vials to kill the bacteria, followed by a few drops of antifoam. Typically, a harvest is analysed the following day on the IRMS, so the vials were kept septa-down in the dark until then. If the samples were to be analysed more than a day after the harvest, they were frozen septa-down.

5.2.3. Isotope analysis using the IRMS

The analysis using the IRMS follows the methods outlined in Weigand et al. (2016). The prepared vials were loaded into the IRMS autosampler rack. A 22-gauge needle extracted the $\mathrm{N_2O}$ gas from each vial with helium as the carrier gas. The system was purged with helium between each sample extraction and $\mathrm{N_2O}$ in helium standards were passed through the system before the first sample was run and after every eight samples. The concentration of the N_2O standards was dependent on the concentration of the samples in each run. The measured mass ratios of N_2O, $45/44$ and $46/44$ were used to calculate the isotope ratios, $^{15}N/^{14}N$ and $^{18}O/^{16}O$. The contribution of ^{17}O to mass 45 (which requires knowledge of $46/44$) was corrected for prior to the calibration of the $\delta^{15}N$ values to N_2 in air.

5.2.4. Bulk PON concentration and $\delta^{15}N$

The PON filters (Section 2.3.2) were prepared by first drying for 24 hours at 40°C and then cut in half using stainless steel scissors that were cleaned prior to each use with ethanol. One half of the filter was placed in a combusted (500°C for 6 hours) 4 mL borosilicate Wheaton vial while the other half was refrozen. The persulfate oxidation method (Knapp et al., 2005; Fawcett et al., 2011; Van Oostende et al., 2017) was used to convert the PON on the filters to NO_3^-. Briefly, 2 mL of persulfate oxidizing reagent (POR) was added to the vials with the filter halves and to vials containing blank combusted filters plus varying amounts of two L-glutamic acid isotope standards, USGS40 ($\delta^{15}N$ = -4.5 ± 0.1‰) and USGS41a ($\delta^{15}N$ = 47.6 ± 0.1‰) (Qi et al., 2003). The latter was done to quantify the N content and $\delta^{15}N$ of the procedural blank. The POR was made by dissolving 2 g of NaOH and 2 g of five-times recrystallized, methanol-rinsed potassium persulfate in 100 mL of high purity Milli-Q water. The vials were autoclaved at 121°C for 55 min on a slow vent setting following the addition of the POR. Sample pH was lowered to 5-8. The vials were then centrifuged to separate the residual filter (GF-75) from the liquid sample and the liquid was transferred to a fresh, combusted 4 mL borosilicate Wheaton vial. The concentration of the oxidized NO_3^- was measured via chemiluminescent analysis (Garside, 1982; Braman & Hendrix, 1989) using a NO_x analyser (Teledyne T200) with a custom-built front end. The $\delta^{15}N$ of the oxidized NO_3^- was then analysed following the methods described above.

To correct the sample measurements for the POR+GF-75 blank, a two-end member mixing model was used:

$$\delta^{15}N_{PON} = \frac{(\delta^{15}N_{measured} \times PON_{measured}) - (\delta^{15}N_{blank} \times PON_{blank})}{PON_{measured} - PON_{blank}} \tag{15}$$

where $\delta^{15}N_{PON}$ is the corrected value, the $\delta^{15}N_{measured}$ is the $\delta^{15}N$ of each sample plus blank measured by the IRMS, $\delta^{15}N_{blank}$ is the $\delta^{15}N$ of the POR+GF-75 blank that is estimated using the vials containing blank filters plus varying amounts of glutamic acid standard (i.e. blank+standard) following Montoya (2008). PON_{blank} is the PON concentration of the POR+GF-75 blank and $PON_{measured}$ is the PON concentration of the sample plus blank, both measured using the NO_x analyzer.

5.2.5. Concentration-weighted average calculation for $\delta^{15}\mathrm{N}_{\mathrm{NO_3^-}}$ and $\delta^{15}\mathrm{N}_{\mathrm{PON}}$

The concentration-weighted averages for the N pools in the winter- and spring sea ice were calculated to reflect the overall isotopic signature in the sampled sea ice, considering the varying $[\mathrm{NO_3^-}]$ and [PON] in each core. This method accounts for the fact that layers with higher $[\mathrm{NO_3^-}]$ or [PON] should have a proportionally greater influence on the average δ^{15}N value, providing a more representative isotopic profile for the entire core. The concentration-weighted average across all cores per season, $\bar{x}$, was calculated using the following formula:

$$\bar{x} = \frac{\sum_{i=1}^{N} w_i x_i}{\sum_{i=1}^{N} w_i} \tag{16}$$

where *N* is the number of samples, w_i represents the $[\mathrm{NO_3^-}]$ or [PON] for a given sample and x_i represents the δ^{15}N of the sample.

5.2.6. Concentration-weighted standard deviation calculation for $\delta^{15}\mathrm{N}_{\mathrm{NO_3^-}}$ and $\delta^{15}\mathrm{N}_{\mathrm{PON}}$

The concentration-weighted standard deviation captures the variability in δ^{15}N across the layers, accounting for the differences in $[\mathrm{NO_3^-}]$ and [PON], which helps in assessing the consistency of the isotopic signature throughout the sea ice and improves the accuracy of comparisons. The concentration-weighted standard deviation across all cores per season, σ, was calculated using the following formula:

$$\sigma = \sqrt{\frac{\sum_{i=1}^{N} w_i (x_i - \bar{x})^2}{\frac{(N-1)}{N} \sum_{i=1}^{N} w_i}} \tag{17}$$

where *N* is the number of non-zero $[\mathrm{NO_3^-}]$ or [PON] samples, w_i represents the $[\mathrm{NO_3^-}]$ or [PON] for a given sample, x_i represents the δ^{15}N value of the sample and $\bar{x}$ represents the calculated concentration-weighted average.

5.3. Results

The depth normalised vertical profiles of salinity-normalised $NO_3^- + NO_2^-$ and PON and the corresponding $\delta^{15}N_{NO_3^-}$ and $\delta^{15}N_{PON}$ for the sea-ice cores from both seasons are presented in Figure 5.2. The nutrient concentrations are replotted from Figure 3.8c and Figure B.1h; the corresponding core information can be found in Section 3.3.1 for the winter ice cores and Section 4.3.1 for the spring ice cores. The seawater values are displayed below the corresponding profiles in Figure 5.2 and in Table 5.1. For true (i.e., not normalised) depth profiles, see Figure C.1.

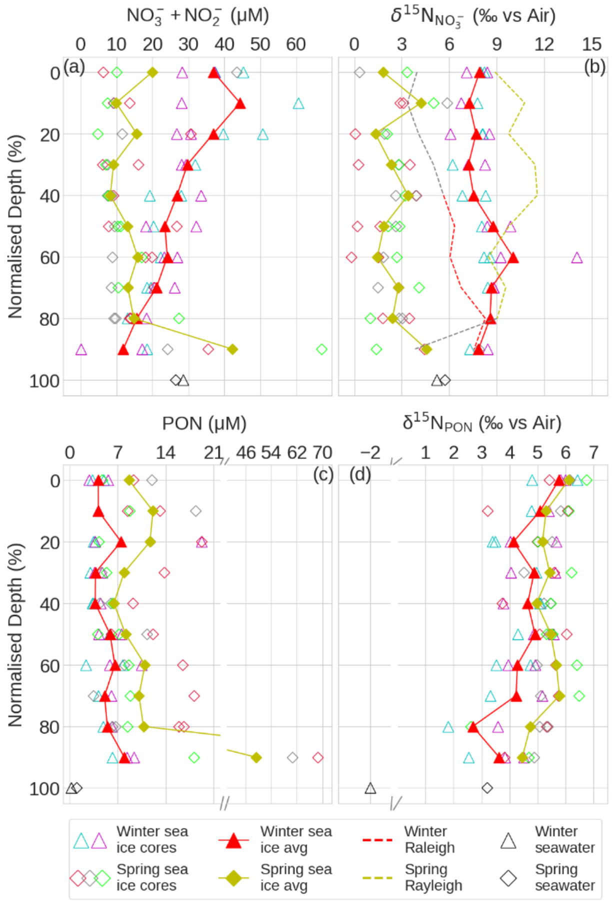

Figure 5.2. Vertical profiles of (a) salinity-normalised $NO_3^- + NO_2^-$ (data previously presented in Figure 3.8c and Figure B.1h) and corresponding (b) $\delta^{15}N_{NO_3^-}$; (c) salinity-normalised PON (note the break in the x-axis to accommodate higher concentrations) and corresponding (d) $\delta^{15}N_{PON}$ (note the break in the x-axis to accommodate to lower seawater concentration) from winter 2019 (triangle symbols) and spring 2019 (diamond symbols). The open-coloured symbols represent individual core data and the connected filled symbols represent the averaged values for the sea ice for winter (red) and spring (yellow). The open black symbols below the profiles indicate the respective surface seawater values (symbols correspond to the profiles). Panel (b) also includes the Rayleigh model output for each season as dashed lines, with the portions of the ice that do not follow the Rayleigh model ($[NO_3^-]_{ice} > [NO_3^-]_{sw(source)}$) indicated by grey shading – the model is further described in the following section (section 5.4). All profiles are depth normalised (i.e. 100*(depth/total core length)) to aid in comparison.

Table 5.1. Table of seawater concentrations of $NO_3^- + NO_2^-$ and PON and the corresponding $\delta^{15}N$ values for winter and spring.

SEASON	$NO_3^- + NO_2^-$ (μM)	$\delta^{15}N_{NO_3^-}$ (‰)	PON (μM)	$\delta^{15}N_{PON}$ (‰)
WINTER	28.50	5.2 ± 0.02	0.2 ± 0.2	-2.0 ± 0.5
SPRING	26.45	5.7 ± 0.5	1.0 ± 0.3	3.2 ± 1.2

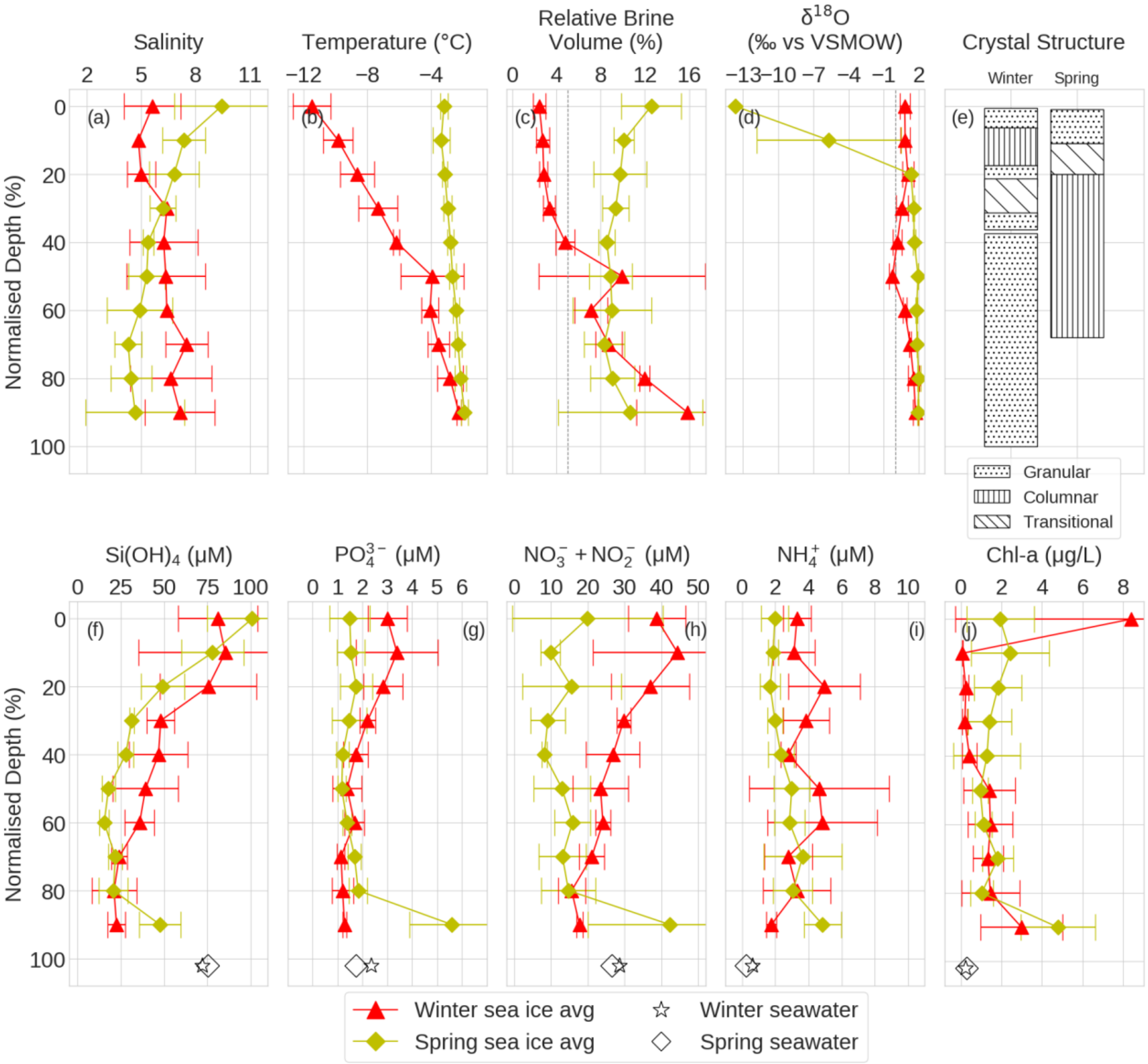

Figure 5.3. Average profiles of (a) salinity, (b) temperature, (c) relative brine volume, (d) sea-ice $\delta^{18}O$, (e) crystal structure, (f-i) salinity-normalised nutrients and (j) chlorophyll (chl-a) data for the winter sea ice (triangle symbols, red profiles) and the spring sea ice (diamond symbols, yellow profiles). Open symbols at the bottom of plots f-j correspond to the profiles and indicate the surface seawater concentrations. Profiles are depth normalised (i.e. 100*(depth/total core length)) to aid in comparison.

The winter sea ice exhibited $NO_3^- + NO_2^-$ depletion in the bottom half of the ice and accumulation in the top half of the ice compared to the underlying seawater (see also Section 3.3.4), with an overall decreasing trend from the surface of the ice to the bottom (Figure 5.2a). The spring sea ice, in comparison, exhibited overall $\mathrm{NO_3^-} + \mathrm{NO_2^-}$ depletion throughout the ice (see also Section 4.3.4), except at the bottom of the core where the highest concentrations were found (42.3 ± 22.2 µM, relative to the seawater value of 26.5 µM). As discussed in section 4.4.2, the $[\mathrm{NO_3^-} + \mathrm{NO_2^-}]$ could be indicative of an increase in primary production that would accompany and increase in solar radiation when the season shifts from winter to spring. The elevated concentrations at the bottom of the spring cores can be attributed to input from the underlying seawater as the permeability at the bottom of the ice increases when it starts to melt.

The winter sea-ice core $\delta^{15}\mathrm{N_{NO_3^-}}$ profiles were relatively invariant with depth and the concentration-weighted average for all cores, 7.5 ± 2.6‰, was higher than the underlying seawater value of 5.2 ± 0.02‰ (Table 5.1). In contrast, the spring cores displayed lower concentration-weighted average $\delta^{15}\mathrm{N_{NO_3^-}}$, 2.2 ± 1.9‰, compared to both the winter sea-ice values and the underlying seawater value of 5.7 ± 0.05‰. Core 2 deviated from the other two cores by displaying higher $\delta^{15}\mathrm{N_{NO_3^-}}$ just below the surface, 7.9‰, and again at the bottom of the core, 5.9‰ (Figure C.1). The $\delta^{15}\mathrm{N_{NO_3^-}}$ data show a clear difference between the winter and spring sea ice, with winter sea ice characterised by a far higher $\delta^{15}\mathrm{N_{NO_3^-}}$ than the spring sea ice, and neither converging on the $\delta^{15}\mathrm{N_{NO_3^-}}$ of the underlying seawater.

The winter and spring sea-ice [PON], averaging 5.44 ± 1.97 µM and 13.61 ± 7.08 µM, respectively, were both elevated throughout the ice compared to the underlying seawater, 0.2 ± 0.2 µM in winter and 1.0 ± 0.3 µM in spring (Table 5.1), and the winter sea-ice [PON] were generally lower than the spring concentrations.

In both seasons, the $\delta^{15}\mathrm{N_{PON}}$ in the sea ice exhibited an overall decreasing trend with depth, although all cores were characterized by vertical variability in $\delta^{15}\mathrm{N_{PON}}$. The winter ice had a concentration-weighted average $\delta^{15}\mathrm{N_{PON}}$ of 4.4 ± 1.0‰, which was higher than the seawater value, -2.0 ± 0.5‰. The spring sea ice displayed a concentration-weighted average $\delta^{15}\mathrm{N_{PON}}$, 5.1 ± 0.9‰, that was higher than both the underlying seawater, 3.2 ± 1.2‰, and the winter sea-ice average $\delta^{15}\mathrm{N_{PON}}$.

5.4. Discussion

Throughout this section, while the figures presented refer to the actual measured values as $NO_3^- + NO_2^-$ to accurately represent the data, we will be using NO_3^- for consistency in the text. The winter sea ice exhibits depleted $[NO_3^-]$ in the bottom 70% of the ice accompanied by elevated $\delta^{15}N_{NO_3^-}$ values relative to the underlying seawater (Figure 5.2a,b). This pattern is suggestive of active NO_3^- assimilation by ice-associated biology, particularly phytoplankton (Sigman et al., 1999; Fripiat et al., 2014; Henley et al., 2017). During NO_3^- assimilation, phytoplankton preferentially take up the lighter isotope (^{14}N) over the heavier isotope (^{15}N), causing the residual NO_3^- pool to become enriched in ^{15}N, which can explain the elevated $\delta^{15}N_{NO_3^-}$ values observed in the sea ice (Figure 5.2b) (Mariotti et al., 1981; Sigman et al., 1999; Sigman & Fripiat, 2019). This process of isotopic fractionation results in progressively higher $\delta^{15}N_{NO_3^-}$ values in the sea ice as NO_3^- is consumed (Fripiat et al., 2014). The PON data support a case for active NO_3^- assimilation within the sea ice, showing elevated [PON] and $\delta^{15}N_{PON}$ values relative to seawater (Figure 5.2c,d). As NO_3^- assimilation proceeds, the PON produced will be lower in $\delta^{15}N$ than the NO_3^- by the amount of the isotope effect. As the NO_3^- becomes depleted and its $\delta^{15}N_{NO_3^-}$ rises, the newly produced PON reflects this, resulting in higher $\delta^{15}N_{PON}$ values, although still lower than the $\delta^{15}N_{NO_3^-}$ of the NO_3^- being consumed (Fripiat et al., 2015). The relatively high $\delta^{15}N_{PON}$ measured in sea-ice cores presented here therefore likely reflects the consumption of NO_3^- within the sea ice environment. The depleted $[Si(OH)_4]$ and elevated [chlorophyll] observed in the sea ice compared to underlying the seawater suggest diatom growth within the ice (Figure 5.3f,j). Diatoms are known to thrive in sea ice environments, where they actively assimilate nutrients and contribute to PON formation (Arrigo, 2003; Riaux-Gobin et al., 2005; Fripiat et al., 2014). Given that the concentration of organic matter entrained from seawater during ice formation is too low to explain the observed in-ice [PON], these findings strongly suggest that phytoplankton, particularly diatoms, are growing within the sea ice, consuming the NO_3^- entrained into the ice from seawater.

During NO_3^- assimilation by phytoplankton, the relationship between $\delta^{15}N_{NO_3^-}$ and $[NO_3^-]$ can be described by the Rayleigh model (Mariotti et al., 1981). This simple model characterises the expected relationship between $\delta^{15}N_{NO_3^-}$ and $[NO_3^-]$ in a closed system, where under a constant isotope effect, the NO_3^- source is taken up (i.e., assimilated) with no resupply or loss (Sigman et al., 1999). This relationship is described by the Rayleigh reactant equation as follows:

$$\delta^{15}N_{reactant} = \delta^{15}N_{initial} - \varepsilon \cdot \{\ln(f)\}$$

where $\delta^{15}N_{initial}$ refers to the starting $\delta^{15}N_{NO_3^-}$ of the NO_3^- source, in this case assumed to be represented by the surface seawater, ε is the kinetic isotope effect associated with NO_3^- assimilation that is set as constant at 5‰ for this model (Mariotti et al., 1981; Sigman et al., 1999; Cozzi & Cantoni, 2010; Fripiat et al., 2014), and f is the fraction of residual NO_3^- supply remaining, computed as:

$$f = \frac{NO_3^-}{NO_{3-initial}^-}$$

where NO_3^- refers to the measured concentration in sea ice and $NO_{3-initial}^-$ refers to the measured seawater concentration.

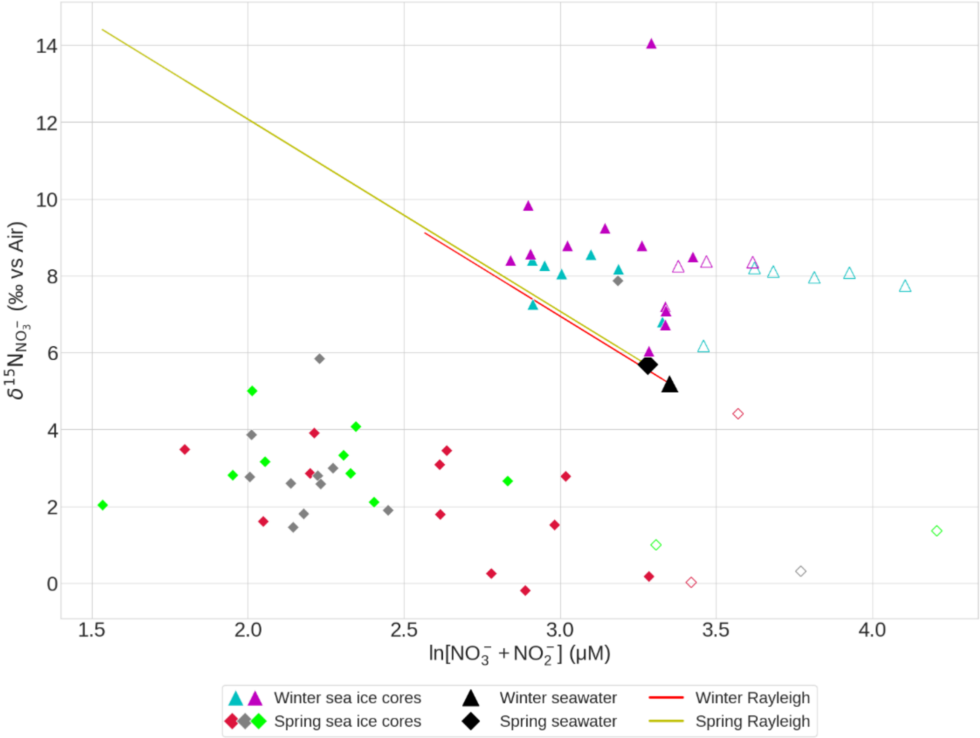

Figure 5.4. Measured $\delta^{15}N_{NO_3^-}$ vs $\ln([NO_3^- + NO_2^-])$ in all cores from both seasons. The computed relationship per core according to the Rayleigh reactant equation (Mariotti et al., 1981) using initial values of $[NO_3^- + NO_2^-]_{sw}$ of 28.50 μM for winter and 26.45 μM for spring and $\delta^{15}N_{NO_3^- -initial}$ of 5.20‰ and 5.70‰ for winter and spring and a constant isotope effect of 5‰ (Mariotti et al., 1981; Sigman et al., 1999; Cozzi & Cantoni, 2010; Fripiat et al., 2014) is represented by the solid red line for winter and yellow line for spring. The samples where f >1 (i.e., $\ln([NO_3^- + NO_2^-]) > \ln([NO_3^- + NO_2^-]_{initial})$ are indicated by the open symbols for each season.

Adherence to this model (i.e., a coupled decrease in $[NO_3^-]$ and increase in $\delta^{15}N_{NO_3^-}$ that follows the relationship determined by the prescribed isotope effect) would indicate that the sea ice approximates a closed system following seawater NO_3^- entrainment during sea ice growth (i.e., N is neither lost from nor gained by the ice following the initial entrainment of seawater NO_3^-). The resulting photosynthetic NO_3^- assimilation in the sea ice would then be the only process acting on the NO_3^- pool (i.e., nitrification, for example, is negligible), with this relationship described by a constant isotope effect, typically around 5‰, as demonstrated in previous field and culture studies (Sigman et al., 1999; Granger et al., 2004; Fripiat et al., 2014, 2019) . Figure 5.4 shows the ice core data from winter and spring plotted in $\delta^{15}N_{NO_3^-}$ vs ln$[NO_3^- + NO_2^-]$ space along with the relationship implied by the Rayleigh reactant equation and an isotope effect of 5‰ for NO_3^- assimilation (e.g., Mariotti et al., 1981; Cozzi & Cantoni, 2010; Fripiat et al., 2014). The majority of the winter data adhere relatively well to the Rayleigh model in the cases where the in-ice $[NO_3^-]$ ≤ seawater $[NO_3^-]$ – that is, there is a general increase in $\delta^{15}N_{NO_3^-}$ coincident with a decline in $[NO_3^-]$, although the data do not evolve from the underlying (i.e., initial) seawater values. This trend strongly suggests active assimilation of NO_3^- within the ice. The open symbols in Figure 5.4 correspond to samples from the top 30% of the winter sea ice where the $[NO_3^-]$ is elevated relative to the seawater concentration (Figure 5.2). At the same time, the $\delta^{15}N_{NO_3^-}$ is also higher than the seawater value. These data suggest that the upper 30% of the sea ice was influenced by more than just NO_3^- assimilation.

A possible explanation for the deviation observed in the upper layers of the winter sea ice is the overwashing of seawater onto the sea-ice surface. This process introduces high-$[NO_3^-]$ seawater into the ice through infiltration and could account for the elevated $[NO_3^-]$ observed in the upper layers of the sea ice relative to the seawater (Figure 5.2a). However, while overwashing might explain the elevated $[NO_3^-]$, it does not fully explain the elevated $\delta^{15}N_{NO_3^-}$. If overwashing were solely responsible for the deviation from expectations, the observed $\delta^{15}N_{NO_3^-}$ would be expected to be closer to the (lower-$\delta^{15}N_{NO_3^-}$) seawater value, rather than being enriched (Figure 5.2c). However, NO_3^- in the upper layer of the sea ice, as in the rest of the core, may have been partially assimilated, and thus elevated in $\delta^{15}N_{NO_3^-}$, prior to the introduction of new NO_3^- by overwashing. This confluence of processes could result in a measured NO_3^- mixture (i.e., partially assimilated + overwashed) that is high in both $[NO_3^-]$ and $\delta^{15}N_{NO_3^-}$. Regardless, the $\delta^{15}N$ data from the winter sea ice challenge the traditional notion that sea ice is biogeochemically dormant during the colder months (Dieckmann et al., 1991; Fripiat et al., 2017). Instead, they suggest a more dynamic system with active microbial processes. If the sea ice environment were truly dormant, we would expect the [PON] and $\delta^{15}N_{PON}$ data to mirror the underlying seawater, reflecting passive entrainment during sea-ice formation. While entrainment could elevate the [PON], it is a non-fractionating process and thus could not account for the observed $\delta^{15}N_{PON}$values. Instead, the elevated [PON] and corresponding $\delta^{15}N_{PON}$ signatures point to active biological processes, such as NO_3^- assimilation, continuing within the sea ice during winter. Additionally, the accumulation of both NH_4^+ and NO_3^- strongly suggests that nitrification is also occurring within the ice. This process would tend to decrease the $\delta^{15}N_{NO_3^-}$ (Casciotti et al., 2003; Smart et al., 2015), in apparent contrast to the observations. However, that the $\delta^{15}N_{NO_3^-}$ is relatively high does not rule out nitrification but instead underscores the dominant influence of isotopic fractionation during NO_3^- assimilation on the $\delta^{15}N_{NO_3^-}$ of the measured in-ice NO_3^- pool.

As the season transitions from winter to spring, conditions become more favourable for primary production in sea ice, with increased light availability and warmer ice temperatures (Figure 5.3b). The spring $\mathrm{NO_3^-}$ data show clear signs of primary productivity, with depleted $[\mathrm{NO_3^-} + \mathrm{NO_2^-}]$ and elevated [PON] (Figure 5.2a,c) and [chlorophyll] (Figure 5.3j) relative to the underlying seawater. One might expect that under these favourable conditions, continued $\mathrm{NO_3^-}$ assimilation by phytoplankton in the ice would further raise the $\delta^{15}\mathrm{N}_{\mathrm{NO_3^-}}$ relative to that observed in the winter. However, the data show lower $\delta^{15}\mathrm{N}_{\mathrm{NO_3^-}}$ values than were measured in both the underlying seawater in spring and the winter sea ice (Figure 5.2b). They also deviate significantly from the modelled Rayleigh relationship expected for $\mathrm{NO_3^-}$ assimilation alone (Figure 5.4), assuming that either the underlying seawater or the winter sea ice $\mathrm{NO_3^-}$ pool reflects the initial springtime conditions. This is notable because while assimilation is evidenced by the low $[\mathrm{NO_3^-}]$ in the sea ice relative to the underlying seawater, the corresponding low $\delta^{15}\mathrm{N}_{\mathrm{NO_3^-}}$ implicates another process that offsets the isotopic enrichment from assimilation and drives down the $\delta^{15}\mathrm{N}_{\mathrm{NO_3^-}}$.

Physical processes like flooding and brine convection can lead to the high $\delta^{15}\mathrm{N}_{\mathrm{NO_3^-}}$ of the winter being lost and replaced with relatively low $\delta^{15}\mathrm{N}_{\mathrm{NO_3^-}}$ seawater (Fripiat et al., 2014). Flooding occurs when the overlying snow layer is thick enough to depress the ice surface below sea level. Seawater can then flood the surface of the ice and if the sea ice is permeable enough, can infiltrate the sea ice from the surface into the ice interior. The infiltrated seawater can then move through the ice via interconnected brine channels, resulting in the down-washing of relatively low $\delta^{15}\mathrm{N}_{\mathrm{NO_3^-}}$ seawater into the sea ice, and the loss of residual higher $\delta^{15}\mathrm{N}_{\mathrm{NO_3^-}}$ (i.e., from earlier partial $\mathrm{NO_3^-}$ assimilation in the ice) at the ice-ocean interface (Figure 5.5). Such an infiltration is evidenced by the extremely negative $\delta^{18}\mathrm{O}$ values in the surface of the spring ice, which indicate the freezing of a mixture of meteoric (i.e., snow-derived) ice, seawater, and brine (Tison et al., 2008; Fripiat et al., 2014). In conjunction, an RBV >5% would allow for the movement of seawater through the ice from surface to the bottom (Golden et al., 1998). Both these properties (i.e., a negative $\delta^{18}\mathrm{O}$ and a RBV >5%) were observed in the spring cores (Chapter 4; Figure 4.6c,d), indicating that conditions may have favoured the penetration of seawater $\mathrm{NO_3^-}$ into the spring sea ice, thus explaining the observed low $\delta^{15}\mathrm{N}_{\mathrm{NO_3^-}}$ in the sea ice.

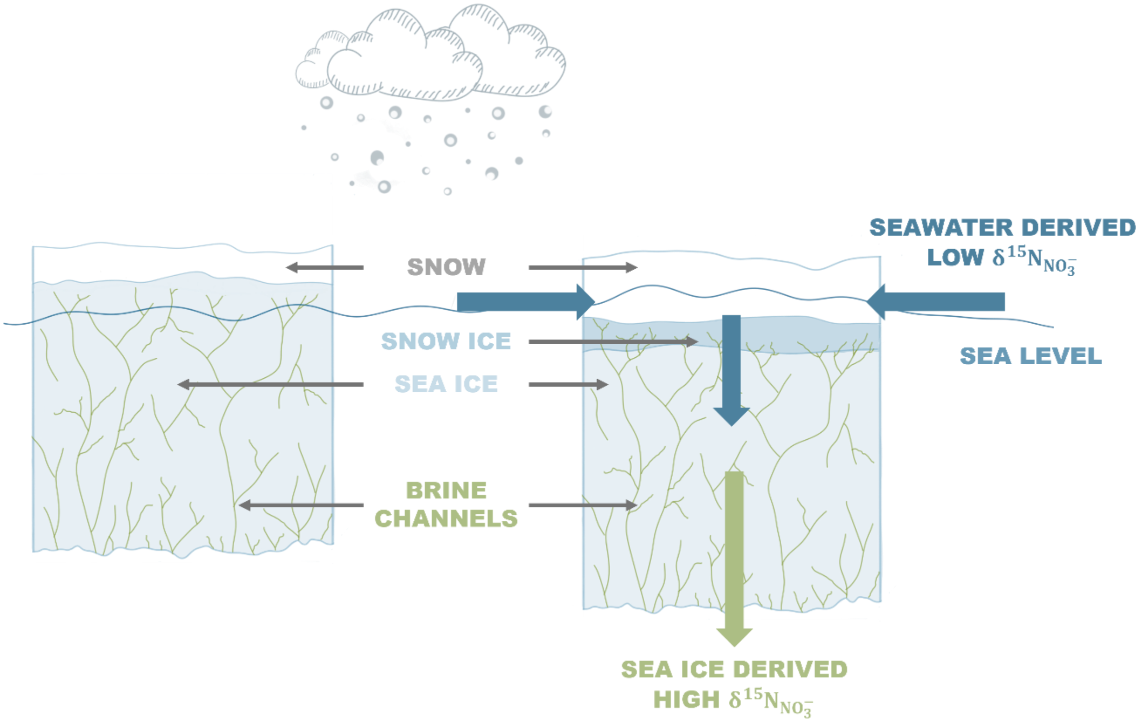

Figure 5.5. Schematic illustrating the process of seawater infiltration and brine convection that arises from snow-loading at the surface of the ice, which results in the ice being pushed below sea level, thus allowing seawater infiltration at the surface. This infiltration produces snow ice as the depressed snow layer melts and refreezes and also allows for seawater to infiltrate the sea ice. Seawater infiltration introduces low-$\delta^{15}N_{NO_3^-}$ to the ice and potentially expels partially assimilated, high-$\delta^{15}N_{NO_3^-}$ through the brine channels.

However, alteration of the in-ice $\delta^{15}N_{NO_3^-}$ by seawater infiltration was unlikely the only process occurring during the spring. The presence of elevated [NH_4^+] in the spring sea ice (Figure 5.3i) suggests that NH_4^+ is being actively remineralised from PON and is subsequently available for nitrification. If nitrification is incomplete, as suggested by the elevated [NH_4^+], then the $\delta^{15}N$ of the NO_3^- produced will be much lower than would be expected for NO_3^- assimilation (Sigman et al., 1999; Casciotti et al., 2003; Smart et al., 2015). This process would weaken the isotopic enrichment from NO_3^- assimilation, possibly even erasing it entirely, and result in the observed (depleted) isotopic composition of NO_3^- in the sea ice. Mdutyana et al. (2020; 2022) have shown evidence of the presence of active nitrifiers in the upper water column of the AMIZ that, if entrained into the ice, would likely catalyze nitrification in the ice. Evidence of nitrification in sea ice has been observed, albeit mainly in landfast sea ice. For example, Priscu et al. (1990) directly measured the first step of nitrification (i.e. the oxidation of NH_4^+ to NO_2^-) and other studies have documented the accumulation of both NO_3^- and NO_2^- in landfast ice (Arrigo et al., 1995; Cozzi & Cantoni, 2010) and the accumulation of NH_4^+ and NO_2^- in sea ice (Riaux-Gobin et al., 2005). Additionally, in Chapter 3, we alluded to the role of biofilms to explain the accumulation of nutrients in the sea ice. These biofilms would also provide a favourable environment for nitrification since nitrifiers tend to excrete extracellular polymeric substances (EPS) and embed in biofilms (Hagopian & Riley, 1998; Fripiat et al., 2014; Flemming et al., 2016; Roukaerts et al., 2021). The ongoing remineralisation of PON in the sea, inferred from the accumulation of NH_4^+, produces low-$\delta^{15}N_{NH_4^+}$ (Möbius, 2013; Smart et al., 2015) that ultimately yields low-$\delta^{15}N_{NO_3^-}$ when nitrified. We thus propose that the NO_3^- pool in the ice is being constantly replenished with isotopically light NO_3^- derived from PON remineralization and incomplete nitrification. This process counteracts the isotopic enrichment that would otherwise occur from NO_3^- assimilation, leading to lower $\delta^{15}N_{NO_3^-}$ values than expected from the $[NO_3^-]$ data.

Our findings mimic those of Fripiat et al. (2014) presented in their Figure 2, but with the various processes occurring earlier in the season. Specifically, our winter ice was characterized by PON accumulation, similar to what Fripiat et al. (2014) observed in early spring. Their study suggested that the accumulated organic N originated from earlier periods of NO_3^- assimilation while we invoke active NO_3^- (and other N-form) assimilation in the winter ice. Our spring ice exhibited low-$\delta^{15}N_{NO_3^-}$ relative to seawater, comparable to the late spring data reported in the Fripiat et al. (2014) study. They attributed this low-$\delta^{15}N_{NO_3^-}$ to the coupling of incomplete NO_3^- assimilation and the subsequent loss of high-$\delta^{15}N_{NO_3^-}$ through brine convection, which would yield lower $\delta^{15}N$ values in the ice relative to the underlying seawater. Their study also suggested that nitrification contributed significantly to the NO_3^- being assimilated within the ice, leading to a shift from dominantly new to dominantly regenerated production from early to late spring. Our data indicate a similar temporal evolution, but occurring between winter and early spring. The parallels between the present study and the work of Fripiat et al. (2014) suggest that the N dynamics observed by Fripiat et al. (2014) are not only characteristic of Antarctic pack ice but also occur in FYI in the AMIZ. Furthermore, the temporal alignment of our winter and spring data with their early and late spring data implies that FYI in the AMIZ exhibits a temporally advanced seasonal cycle compared to pack ice.

Overall, our new data suggest that the sea ice in the AMIZ is influenced by multiple biological and physical processes that are ongoing to a greater or lesser extent year-round (Figure 5.6). Following initial entrainment of NO_3^- during sea ice growth, we propose that the biological process that are ongoing in the sea ice include NO_3^- assimilation, which raises both $\delta^{15}N_{NO_3^-}$ and $\delta^{15}N_{PON}$, PON remineralization, which raises the $\delta^{15}N_{PON}$ and produces NH_4^+ that has a low-$\delta^{15}N_{NH_4^+}$, NH_4^+ assimilation, which produces PON with a $\delta^{15}N_{PON}$ that is similar to the $\delta^{15}N_{NH_4^+}$ of the NH_4^+ being assimilated, and finally nitrification, which, if incomplete and/or occurring coincident with a process of N assimilation, can increase the $\delta^{15}N_{NH_4^+}$ and lower the $\delta^{15}N_{NO_3^-}$. At the same time, proposed physical processes include surface flooding of seawater that introduces relatively low-$\delta^{15}N_{NO_3^-}$ into the sea ice and the removal of high-$\delta^{15}N_{NO_3^-}$ through brine convection and gravity drainage. These processes ultimately lowers the $\delta^{15}N_{NO_3^-}$ in the sea ice. The overlapping processes outlined above complicate interpretation of the sea-ice N isotope data and suggest that the sea-ice N cycle is more dynamic and active than previously understood, particularly in the winter.

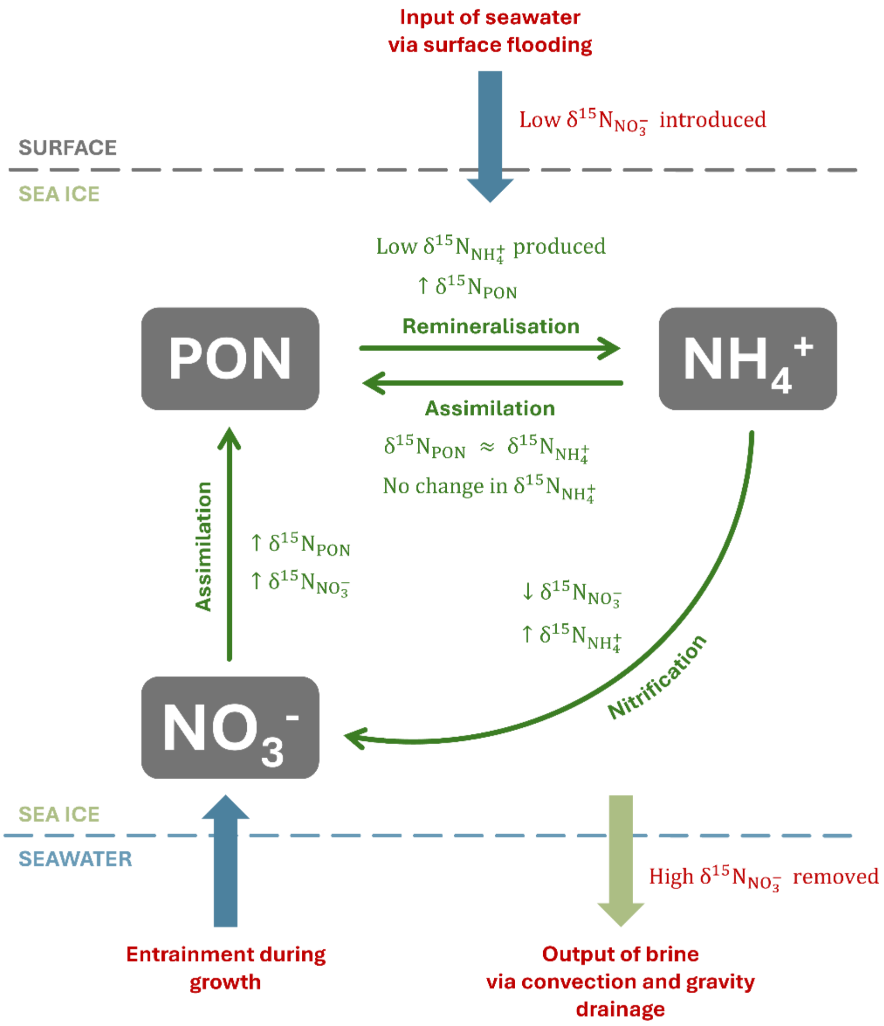

Figure 5.6. Schematic of the overlapping processes potentially acting on the various pools in sea ice and the resulting influence on the isotopic ratios. Biological processes are indicated in dark green and physical processes are indicated in red. Interfaces between the sea ice and seawater (surface) are indicated by blue (grey) dashed lines.

5.5. Conclusion

In summary, our data clearly show that NO_3^- assimilation occurs in the sea ice early in its growth season (winter), such that by the time we sampled, there was no indication of a dormant biogeochemical environment in the sea ice. The observed isotopic patterns provide compelling evidence for ongoing microbial activity in sea ice during winter, challenging the traditional view of sea ice being a relatively inactive environment in colder months and supporting the findings outlined in Chapter 3. Additionally, multiple co-occurring processes continue to influence the isotopic composition of the sea ice environment as the season transitions from winter to spring, suggesting that the biogeochemical environment within the ice is dynamically influenced by overlapping biogeochemical and physical processes. This negates the possibility of sea ice being a closed system. Our data also suggests that the sea ice environment in the AMIZ is temporally advanced relative to pack ice, displaying similar patterns in winter that have previously been observed in pack ice in spring.

To further strengthen our understanding of the N cycle in sea ice, incorporating measurements of DON (concentration and $\delta^{15}N$) and $\delta^{15}N_{NH_4^+}$, and investigating the relationship between nitrate $\delta^{15}N$ and $\delta^{18}O$, the latter of which is sensitive to organic matter remineralisation and can track the modification of NO_3^- (Sigman et al., 2009; Rafter et al., 2013), would be beneficial. These findings highlight the need for more comprehensive data to elucidate the complex biogeochemical dynamics of FYI in the AMIZ.

Chapter 6

6. Biogeochemical characteristics of pancake ice and brash ice in the AMIZ

6.1. Introduction

The SCALE2019 expeditions (Section 2.1) provided a unique opportunity to sample ice in the growing phase as pancake ice during the winter expedition and ice in the melting stage as brash ice during the spring expedition. Here we present the data from each sea ice type, compare their respective physical and biogeochemical properties and explore the relationship between these ice types and the surface ocean in their respective seasons. The data presented in this chapter represents the first biogeochemical measurements of pancake ice and brash ice for the Atlantic marginal ice zone for both winter and spring in the Southern Ocean.

6.2. Data and methods

The collection and handling of samples from floes taken on board the research vessel and sampled on deck have been detailed earlier in Section 2.2.1. The date of sampling and location of each station and their positions relative to each other are presented in Figure 6.1. Details of the stations and the sampling conditions are given in Table 6.1. The pancake ice (PI) was collected from station M01 in winter and the brash ice (BI) was collected from station SMIZ9 in spring. For ease of interpretation and differently from the previous chapters, the season and ice type will be referred to in the text and figures as opposed to the station name and core IDs.

Table 6.1. Table of station details and ice properties for M01 and SMIZ9.

STATION/ ICE TYPE	DATE	STATION LOCATION	AIR TEMP (°C)	SNOW DEPTH (cm)	ICE THICKNESS (m)	AVERAGE CORE LENGTH (m)
M01/ PANCAKE	28/07/2019	56.80°S; 00.03°E	-8.0	3.5	0.37	0.32 ± 0.065
SMIZ9/ BRASH	03/11/2019	58.44°S; 21.99°E	-3.5	5.5	0.50	0.49 ± 0.009

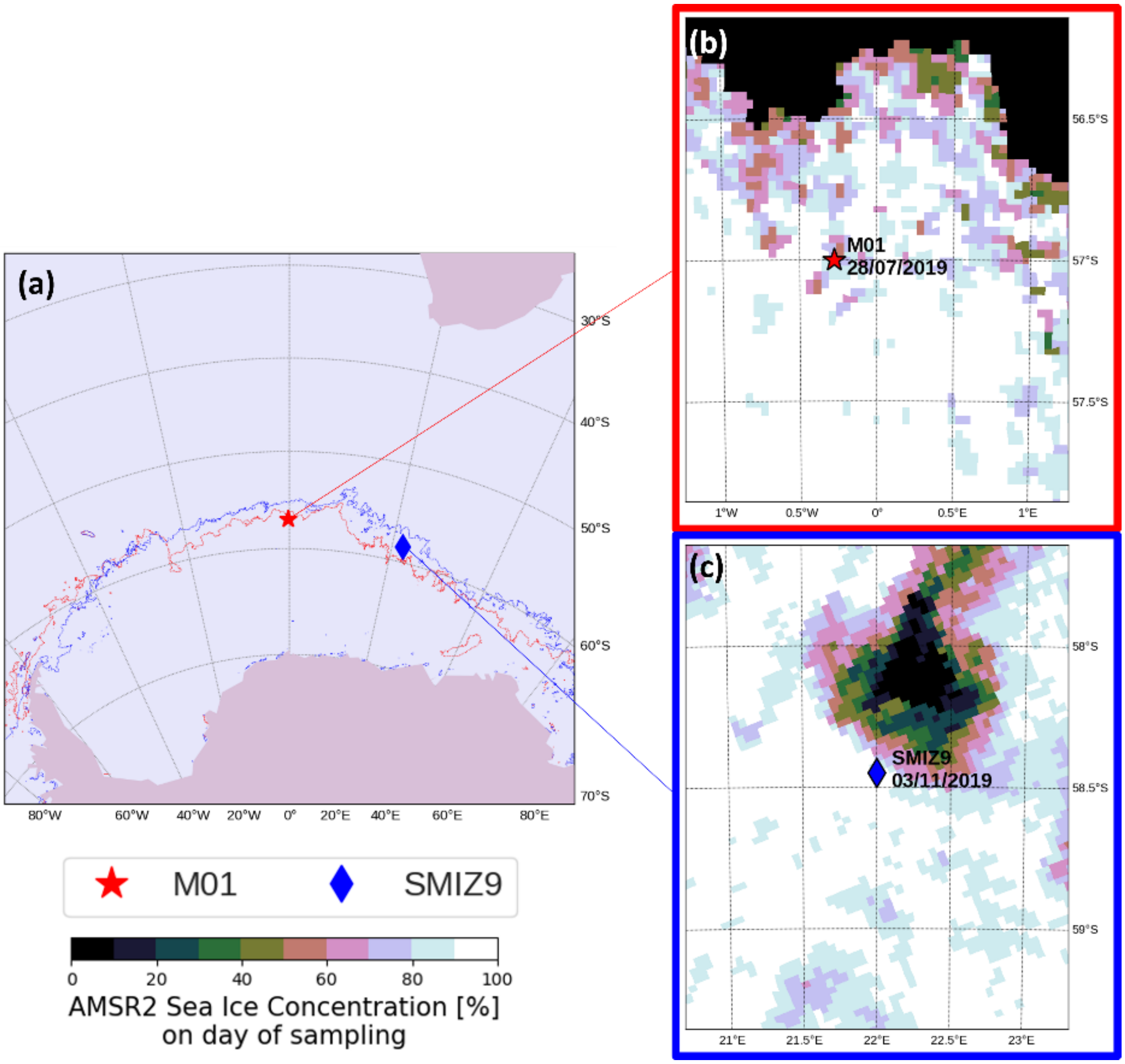

Figure 6.1. (a) Station locations in the Antarctic Polar region overlaid with the location of the AMIZ for winter (red line) and spring (blue line), (b-c) sea ice concentration maps for (a) M01 and (b) SMIZ9. The ice overlay is from the AMSR2 satellite product (Spreen et al., 2008).

6.3. Results and discussion

6.3.1. Environmental and sea ice conditions

Both stations were in unconsolidated, open drift conditions at the time of sampling (Figure 6.2b). This can be seen in the lower sea ice concentration around the stations in Figure 5.1b, c. The sea ice sampled at each station was at different stages in the ice growth cycle; the ice at M01 was classified as pancake ice, given the season (winter) and the ice at SMIZ9 was classified as brash ice from the season (spring) and visual clues from the ice field including broken floes and brash ice (Figure 6.2b).

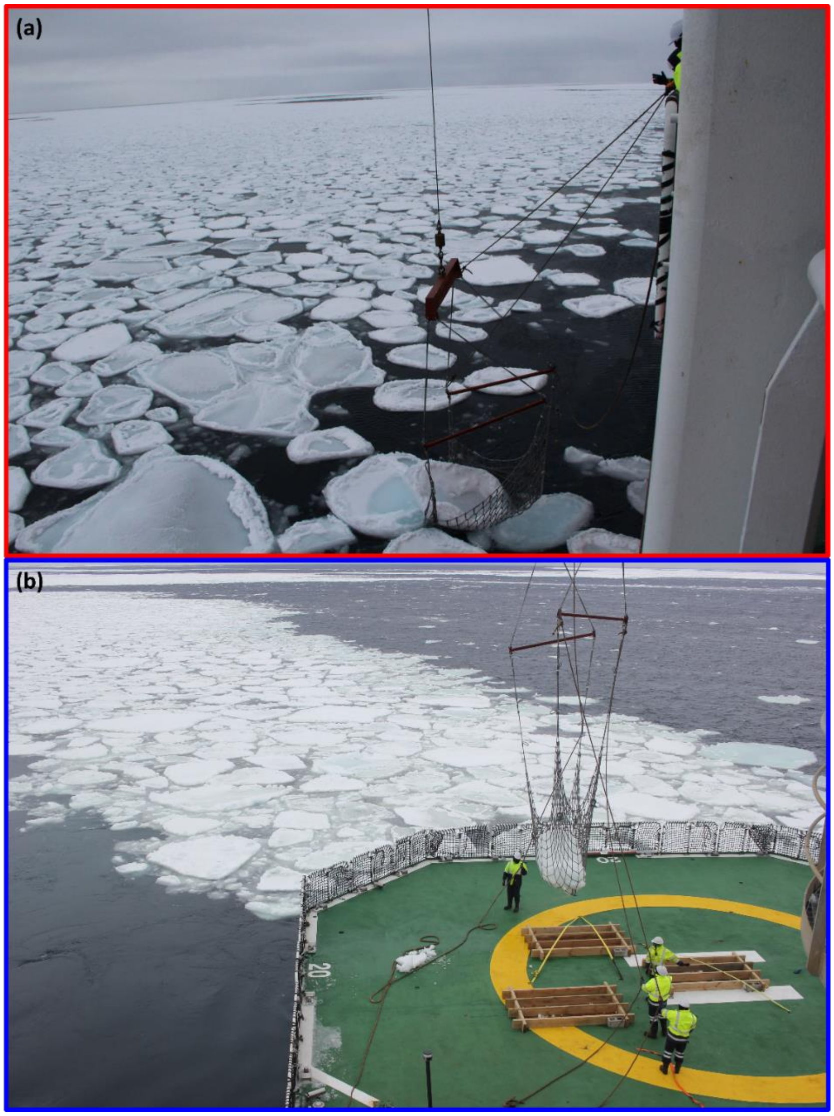

Figure 6.2. Images of the station conditions at (a) M01 and (b) SMIZ9. The ice field at M01 was comprised of pancake ice with relatively small portions of open water. The ice field at SMIZ9 was comprised of a combination of broken floes, brash ice and large open water spaces.

The PI had soft, rounded edges and a 3.5 cm thick snow layer (Figure 6.3a), while the BI had rough, irregular edges, with signs of melting and a 5.5 cm thick snow layer (Figure 6.3b). The PI had a maximum core thickness of 0.37 m and the cores collected indicate a uniform thickness that reduces as the cores move towards the edge of the pancake (as seen in Figure 6.4a and the corresponding locations of the cores in Figure 6.3c). In contrast, the BI had a maximum core thickness of 0.6 m and displayed variability in the thickness of cores throughout the floe (as seen in Figure 6.4b and the corresponding locations of the cores in Figure 6.3d). The irregular thickness and rough underside of the BI can be attributed to the influence of melting processes causing the brine channels to expand as well as mechanical processes within the ice pack (e.g., interactions between floes within the ice field).

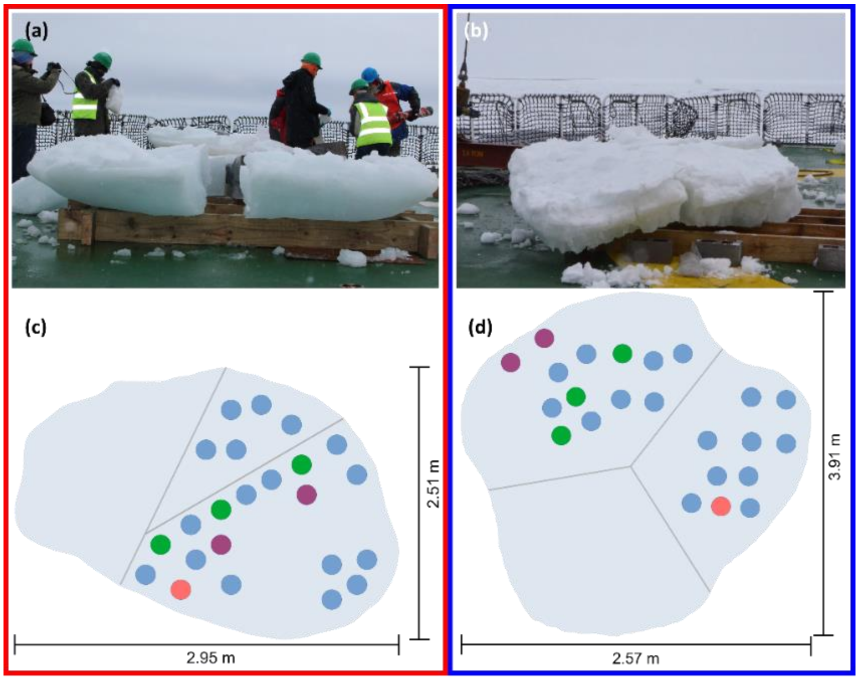

Figure 6.3. Images (a-b) of the sea ice sampled and location of the cores taken (c-d) from the pancake (red box) and the brash ice (blue box). Purple circles indicate BGC cores, green indicates physical cores and orange indicates crystal structure cores. The cores collected for other teams and purposes are also included and are indicated by the blue circles.

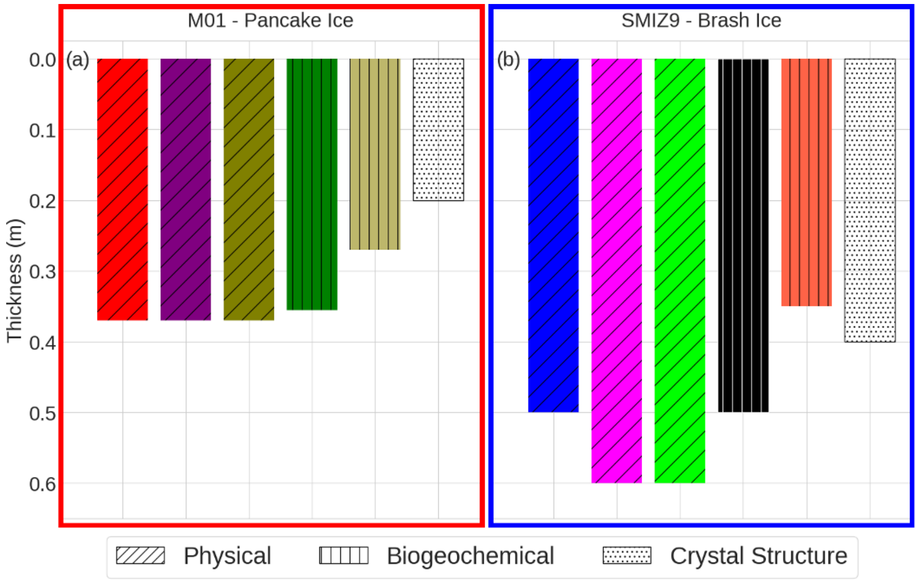

Figure 6.4. Core lengths and designations for the pancake ice (a) and the brash ice (b). Core designations are indicated by the hatches in the bars and shading corresponds to the respective core profiles in the following figures.

6.3.2. Relationship between pancake ice, brash ice, and the surface ocean properties

The comparison begins with the analysis of relationships between sea ice and the surface ocean, which is of relevance due to the nature of smaller floes typically found in open drift or semi-closed conditions. The CTD profiles for the upper 200 m of the water column and corresponding nutrient concentrations are displayed in Figure 6.5.

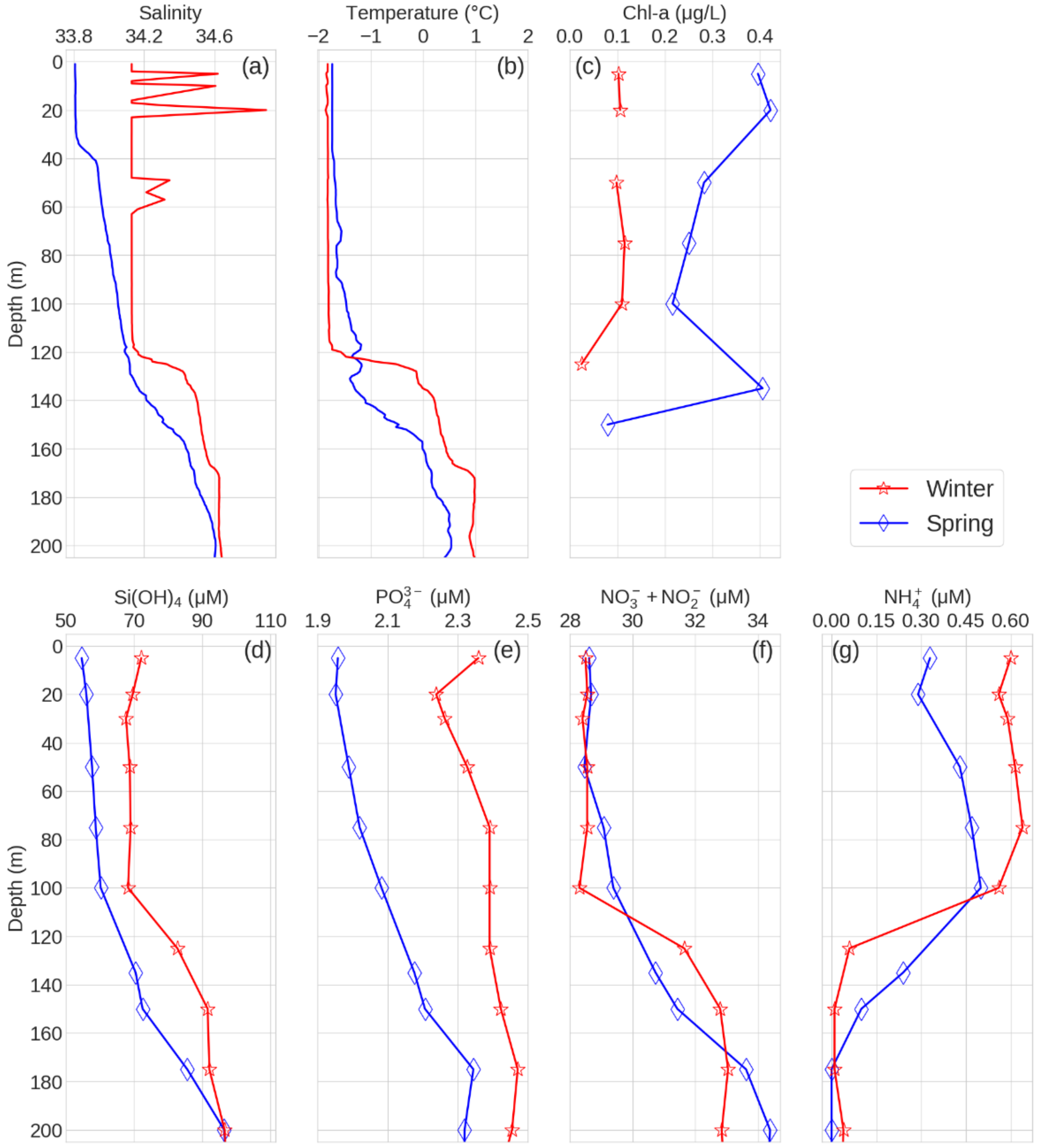

Figure 6.5. (a) Salinity and (b) temperature profiles from the CTD and corresponding (c) chlorophyll (chl-a) and (d-g) nutrient profiles for the upper 200 m of the water column at M03 in winter (red line) and SMIZ9 in spring (blue line). Each symbol in panels c-g indicates the depth at which a seawater sample was taken.

The difference between the seasons and the influence of the dominant sea ice process, either growth or melt, can be seen at the surface ocean. Surface ocean salinity (Figure 6.5a) is higher and more vertically variable in winter, when brine rejection during sea ice growth is occurring. In contrast, the surface ocean in spring has a lower salinity owing to the melting of sea ice causing a dilution effect with the input of low-salinity water at the surface. The surface temperature (Figure 6.5b) is not significantly different between the two stations, but winter does display the lower surface temperature between the stations. From a biogeochemical perspective, the surface ocean in winter displays lower chlorophyll concentrations and higher nutrient concentrations. This can be attributed to the lower solar radiation in winter and slowing down of primary productivity as sea ice grows. The surface ocean in spring shows relatively higher chlorophyll concentrations and an overall reduction in nutrient concentrations relative to winter as a result of increased productivity as the available light increases and sea ice begins to retreat.

6.3.3. Physical properties

The physical properties for all cores collected from both ice types are presented in Figure 6.6a-e. To aid in comparison, the profiles are presented with normalised depths, for true depth profiles see Appendix D. The PI had an overall higher salinity than the BI, which is interpreted as the PI being younger than the BI and still in the initial incorporation phase. Brine drainage had not yet progressed in the PI, while the BI had been experiencing gravity drainage for longer and further brine losses due to melting processes.

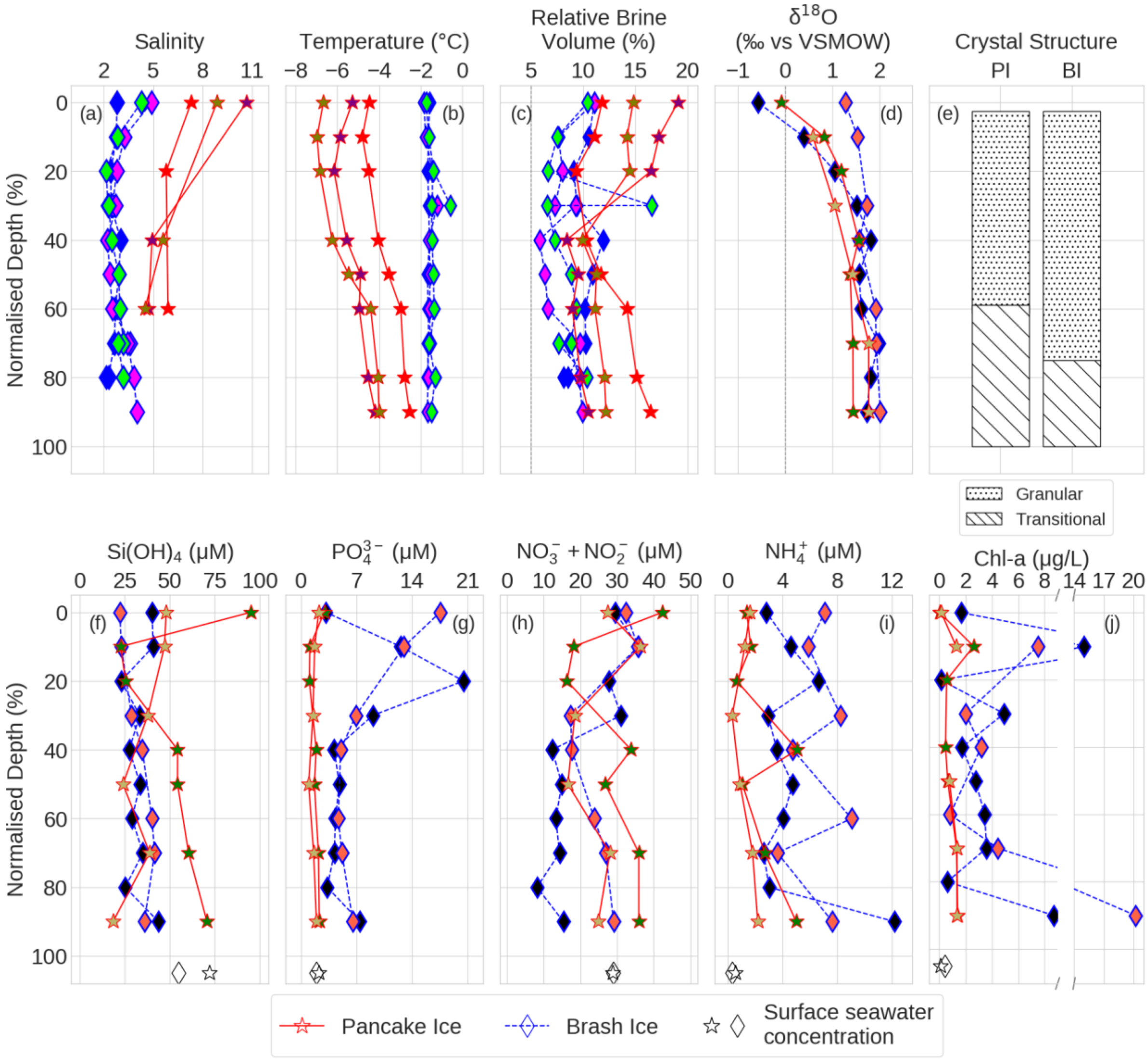

Figure 6.6. (a) Salinity, (b) temperature, (c) relative brine volume, (d) $\delta^{18}O$, (e) crystal structure, (f-i) salinity normalised nutrients and (j) chlorophyll (chl-a) data for the sea-ice cores from pancake ice (star symbols, red profiles) and brash ice (diamond symbols, blue profiles). Open symbols at the bottom of plots f-j correspond to the profiles and indicate the surface seawater concentrations. Profiles are depth normalised (i.e. 100*(depth/total core length)) to aid in comparison. Symbol inner shading corresponds to the cores displayed in Figure 6.4.

The temperature of the ice was also distinctly different between the ice types (Figure 6.6b). The PI displayed colder temperatures, above the freezing point for sea water (-1.8°C) throughout. The BI was warmer than the PI, this can be attributed to the increased solar radiation in spring compared to winter and the accompanying increase in atmospheric (Table 6.1) and sea surface temperature. The relative brine volume (RBV) of both ice types (Figure 6.6c) fell above the 5% permeability threshold throughout all cores. This suggests that both ice types were permeable and capable of supporting biological activity through brine convection and nutrient exchange.

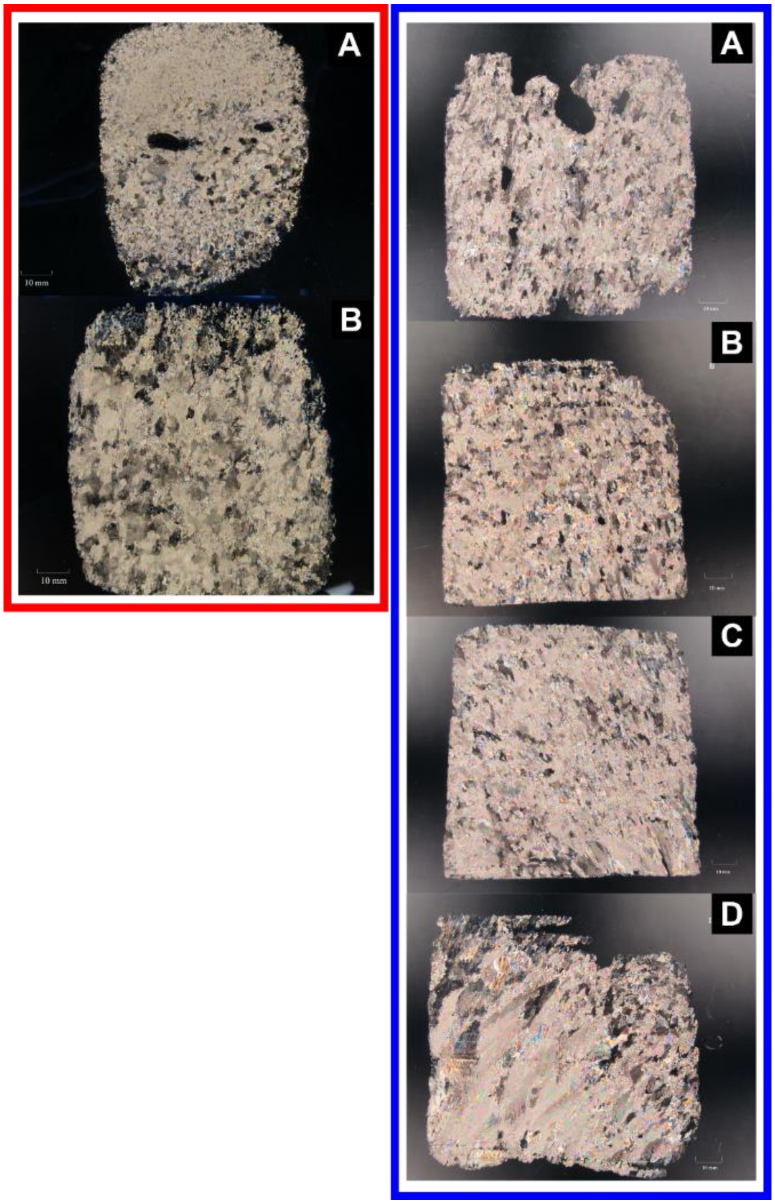

Figure 6.7. Crystal structure images of the cores taken from M01 (red box) and SMIZ9 (blue box). The images are displayed alphabetically from the top of the core (A) to the bottom of the core (Johnson, Khoboko, et al., 2022; Johnson, Matlakala, et al., 2022).

Ice texture images for both ice types are displayed in Figure 6.7. The methods for producing the images are discussed in Section 2.3.3. Note that crystal structure images could be used to identify signs of active melting in the sea ice, however, our use of a thermal macrotome to produce the thin sections (Johnson et al., 2023) effectively melts the ice while cutting, which resulted in our inability to distinguish between signs of in-situ melting of the ice and melting caused by the wire. The corresponding crystal structure diagrams are displayed in Figure 6.6e. Two ice textures were identified in both ice types, granular ice and transitional ice. The distinction between the origin of the granular ice (snow ice, superimposed ice, or frazil ice) is difficult to determine by visual inspection alone, and thus the analysis of the $\delta^{18}\mathrm{O}$ was performed (Figure 6.6d) and is discussed in conjunction with the ice texture data. The top of the PI core (Panel A in the red box of Figure 6.7) was made up of very small granular crystals (1.38 ± 0.44 cm) which is indicative of very rapid freezing conditions; typical in the formation process of PI. These small granular crystals increase in size with depth, demonstrating the gradual deceleration in the formation of individual crystals thus allowing them to grow larger and eventually longer. The $\delta^{18}\mathrm{O}$ profiles for the PI were nearly identical and constant throughout the ice. The surface layer $\delta^{18}\mathrm{O}$ was slightly negative, which corresponded to the thin (3.5 cm) snow layer that was present (Table 6.1), the remainder of the PI displayed positive $\delta^{18}\mathrm{O}$ values with little variability with depth, indicating granular ice of frazil origin. While also being composed of granular and transitional textures, the BI was composed of, on average, larger granular crystals than the PI (2.99 ± 1.03 cm) and a more defined $\delta^{18}\mathrm{O}$ minimum at the surface for one of the cores, which suggests snow ice (Lytle & Ackley, 2001; Arndt et al., 2021) and did correspond to the snow layer that was present (Table 6.1). The difference between the cores from the BI in the surface layer $\delta^{18}\mathrm{O}$ values suggests horizontal variability across the floe. The BI transitional crystals can be seen to be close to forming columnar textures (Panel D in the blue box of Figure 6.7) and correspond to the positive $\delta^{18}\mathrm{O}$ values. These large transitional crystals (9.63 ± 3.48 cm) allude to previous consolidated or partially consolidated conditions that would allow such large crystals to form undisturbed. Since brash ice is a fragment of larger, consolidated floes, it is possible that at some time in the BI life, it formed part of a closed ice pack that allowed for undisturbed formation of these large crystals.

6.3.4. Biogeochemical properties

The biogeochemical profiles of both ice types are presented in Figure 6.6f-j. The nutrient concentrations for the seawater underlying the PI were 72.10, 2.36, 28.5, and 0.60 µM for $\mathrm{Si(OH)_4}$, $\mathrm{PO_4^{3-}}$, $\mathrm{NO_3^- + NO_2^-}$ and $\mathrm{NH_4^+}$ respectively and 54.75, 1.96, 28.95 and 0.33 µM respectively for the seawater underlying the BI. These concentrations are also indicated below the ice profiles in Figure 6.6f-j. The PI displayed depleted $\mathrm{Si(OH)_4}$ relative to seawater throughout both cores, except for the top and bottom layers of one of the cores. The PI $\mathrm{PO_4^{3-}}$ was depleted throughout the ice while the $\mathrm{NH_4^+}$ was elevated throughout the ice. The $\mathrm{NO_3^-} +$

NO_2^- varied throughout the ice among both cores, with portions either elevated or depleted in the ice, with no correlation between the cores from the PI. The PI chlorophyll was elevated throughout the ice with an average concentration of 0.99 ± 0.71 µg/L but, if compared with the BI chlorophyll, not significantly higher than the seawater (0.10 µg/L).

The BI displayed depleted $Si(OH)_4$ and elevated PO_4^{3-} and NH_4^+ throughout the ice compared to the seawater. The BI displayed elevated $NO_3^- + NO_2^-$ in the top 30% of the ice and depleted concentrations in the bottom portion of the ice. The BI displayed significantly elevated chlorophyll concentrations throughout the ice of 5.04 ± 5.51 µg/L, much higher than the seawater (0.40 µg/L). The chlorophyll concentrations in both the BI samples have two maximums, one just below the surface of the ice and the second at the ice-ocean interface.

Table 6.2. Table of mean concentration and standard deviation of biogeochemical parameters of pancake ice (M01-BGC), brash ice (SMIZ9-BGC) and the underlying seawater.

SAMPLE TYPE	$Si(OH)_4$ (µM)	PO_4^{3-} (µM)	$NO_3^- + NO_2^-$ (µM)	NH_4^+ (µM)	Chl-a (µg/L)
M01-BGC-01	54.76 ± 25.15	1.88 ± 0.67	29.89 ± 9.81	2.50 ± 1.84	1.00 ± 0.86
M01-BGC-02	35.73 ± 12.06	1.66 ± 0.43	25.28 ± 7.17	1.34 ± 0.67	0.97 ± 0.53
SMIZ9-BGC-01	33.17 ± 6.98	7.36 ± 5.51	20.25 ± 9.70	4.71 ± 2.90	4.26 ± 4.51
SMIZ9-BGC-02	32.39 ± 7.80	8.41 ± 4.94	26.12 ± 7.01	6.61 ± 1.95	6.35 ± 7.16

Using theoretical dilution lines (TDLs; Figure 6.8), we are able to evaluate the nutrient dynamics within the sea ice and the influence of biological activity through deviations from the TDLs. During sea ice growth stages, nutrients concentrations in ice are expected to reflect the concentrations of the underlying seawater and cluster on or around the TDL. The PI follows this trend, with concentrations of $Si(OH)_4$, PO_4^{3-} and $NO_3^- + NO_2^-$ clustering around the TDL, with no significant deviations that would imply active biogeochemical activity. The BI $Si(OH)_4$ concentrations fell below the TDL for all depths, while the PO_4^{3-} and NH_4^+ concentrations fell above the TDL for all depths, indicating accumulation. The $NO_3^- + NO_2^-$ concentrations were distributed close to the TDL for some depths, but majority fell below the TDL. Nomura et al. (2023) observed similar trends in their brash ice from the Indian sector of the Southern Ocean of depleted $Si(OH)_4$, $NO_3^- + NO_2^-$ and accumulation of PO_4^{3-} and NH_4^+. The accumulation of PO_4^{3-} has been observed in previous studies (Fripiat et al., 2017; Nomura et al., 2023) and attributed to the preferential release of PO_4^{3-} during decomposition. The elevated nutrients in the brash ice can also be attributed to the enhanced seawater intrusions as a result of the melting of the ice and opening of the brine channels. The accumulation of NH_4^+ was common to both ice types. NH_4^+ is known to accumulate in sea ice and has also been observed in previous studies (Arrigo et al., 1995; Papadimitriou et al., 2007; Zhou et al., 2013, 2014; Ugalde et al., 2016; Fripiat et al., 2017; Nomura et al., 2023).

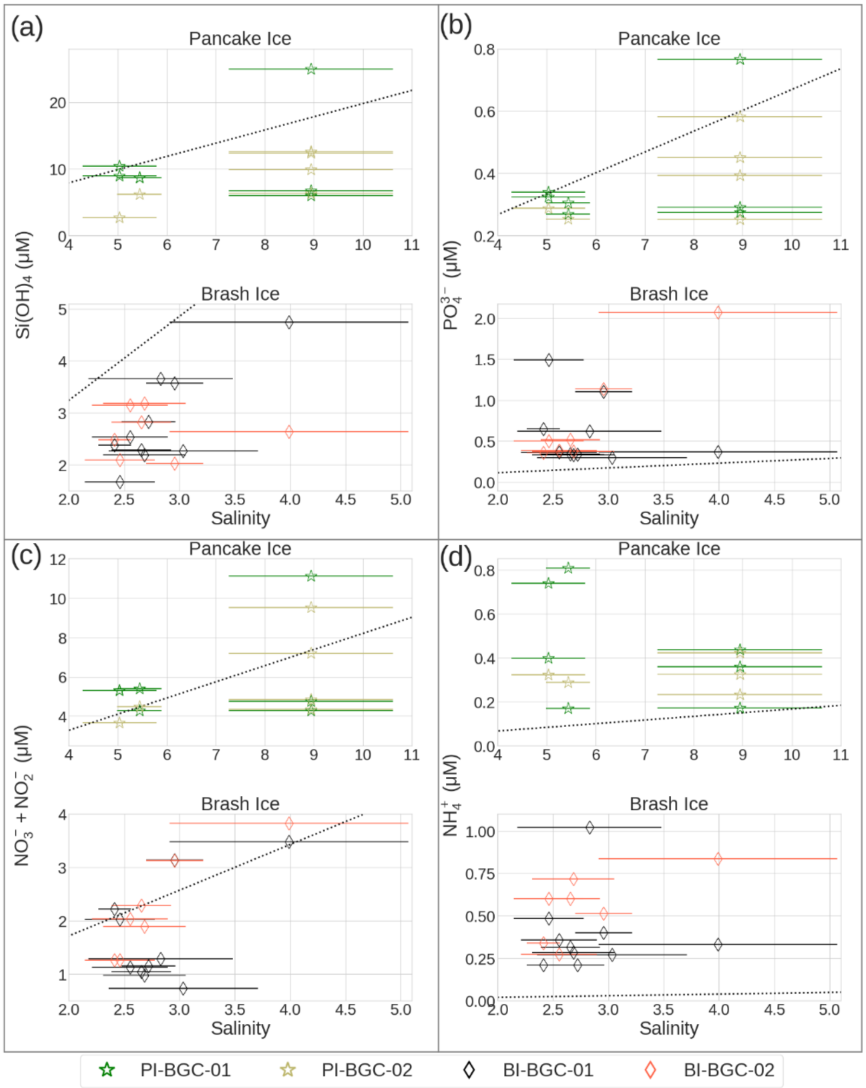

Figure 6.8. Bulk nutrient concentrations in the cores as a function of salinity in all samples from both ice types. Dotted lines indicates the theoretical dilution line (TDL) based on the concentration of nutrients in and salinity of the surface water.

Overall, the PI was saltier and colder than the BI (Figure 6.6a,b), which is indicative of the season and growth stage of the ice types. The higher chlorophyll concentration in the BI relative to the PI is the only biogeochemical variable that clearly indicated enhanced biological activity in the BI, and could be attributed to the increase in available solar radiation in spring. All the other variables do not clearly allow us to separate winter from spring conditions in these types of sea ice. The BI displayed more vertical and horizontal variability in the thickness and nutrient concentrations between cores compared to PI. This variability suggests that the PI was more consistent across the sampled floe compared to the BI, where the in-ice biogeochemical environment was likely influenced by the dynamic processes and fragmentation experienced by the ice pack over its longer lifetime. This variability across the ice floe and throughout the depth of the ice was seen in the other stations from spring (Chapter 4) and further demonstrates that the sea ice biogeochemistry in the AMIZ is shaped by the multiple cycles of breaking, rafting and rearranging as the ice pack transitions from young ice to first year ice, as suggested in Chapter 3.

The high accumulation of $\mathrm{PO_4^{3-}}$ in the BI is difficult to explain considering the higher algal biomass and lower background concentration of the underlying seawater. This accumulation was also seen in $\mathrm{NH_4^+}$, which is the other remineralized nutrient. This is another example of the “sea-ice nutrient paradox” (e.g. Roukaerts et al., 2021) that has been discussed earlier in Section 3.4.1. PI also presented accumulation of remineralised nutrients, in line with the observations of the consolidated station from the winter sampling (Section 3.3.4). However, it is interesting to note that $\mathrm{PO_4^{3-}}$ measured at the consolidated ice floes in spring did not show major signs of accumulation (Figure 4.8b). As remarked in Section 3.4.2, multiple observations from different conditions are needed to disentangle the complex balance between consumption, remineralisation, and accumulation in the brine environment. One possible explanation for the unexpectedly low $\mathrm{PO_4^{3-}}$ concentrations could be the precipitation or co-precipitation of $\mathrm{PO_4^{3-}}$ with calcium carbonate in the form of ikaite ($\mathrm{CaCO_3 \cdot 6H_2O}$) (Hu & Wang, 2020). Ikaite formation has been documented in both Antarctic and Arctic sea ice (Dieckmann et al., 2008, 2010), and laboratory studies have shown that $\mathrm{PO_4^{3-}}$ can be strongly co-precipitated with ikaite under cold, high-alkalinity conditions (Hu et al., 2014). In fact, elevated $\mathrm{PO_4^{3-}}$ concentrations have been proposed as a precondition for ikaite formation in sea ice (Dieckmann et al., 2010), making this process a plausible and potentially important sink for $\mathrm{PO_4^{3-}}$ in the brine environment. Further investigation is needed to better understand the extent to which $\mathrm{PO_4^{3-}}$ precipitation or co-precipitation with ikaite influences nutrient distributions in sea ice.

6.4. Conclusion

This chapter focused on the analysis of physical and biogeochemical data from sea-ice cores taken from pancake ice (PI) and brash ice (BI) in the Atlantic sector of the AMIZ. These ice types are under-sampled due to the complexities of in-situ sampling. In this chapter, we compared the characteristics of each ice type and conclude that the age of the sea ice, and to some extent the season in which it was sampled, primarily determined the observed biogeochemical dynamics in each type. The biogeochemical signature of the pancake ice closely resembled the surface ocean. This similarity suggests that the sampled pancake was in the earlier stages of growth, where active incorporation of surface seawater dominates. This paired with the relatively low chlorophyll concentrations suggested reduced biogeochemical activity, which is typical of winter conditions (i.e., reduced solar radiation). It is important to clarify that this observed signature does not contradict the enhanced biogeochemical activity described in Chapter 3. Rather, the pancake ice represents an earlier developmental stage, prior to the transition into first-year ice (FYI), where biogeochemical enhancement was observed. In this sense, the pancake ice provides a reference for the classical or baseline winter sea ice biogeochemistry, before the onset of biogeochemical enhancement. By contrast, the brash ice displayed characteristics of an active biogeochemical system (i.e., elevated chlorophyll and depleted nutrients relative to seawater), as a result of increased primary production promoted by the availability of solar radiation in spring. Additionally, the brash ice biogeochemistry was more variable between cores and with depth compared to the PI. This variability is reminiscent of the consolidated sea ice sampled in spring (Chapter 4) that had undergone dynamic growth conditions and multiple processes of breaking, rearranging and rafting. Since brash ice is a fragment of larger floes, it has likely experienced these same processes. The surface ocean also displayed characteristics that were indicative of the season and prevailing sea ice growth stage. In winter, the surface ocean was colder and saltier, due to the production of sea ice and resulting brine rejection, and nutrient rich due to more intense mixing and reduced primary production in the surface ocean. In contrast, the surface ocean in spring was relatively warmer, fresher due to the increase in solar radiation. This resulted in the warming of the surface ocean and melting of the sea ice, which caused an input of fresh water into the surface ocean. The spring surface data indicated an overall increase in primary production from winter to spring, with all nutrients, apart from NO_3^- , being depleted relative to the winter concentrations and elevated chlorophyll concentrations. The characterization of the biogeochemistry of these sea ice types expands our understanding of the relationship between sea ice and the surface ocean, as well as the influence of the season and environmental factors on the biogeochemical dynamics of the sea ice system.

Chapter 7

7. Conclusions and Outlook

Each data chapter (Chapters 3-6) of this thesis included a conclusions section pertaining to the research presented therein. To avoid repetition, the conclusions provided in chapters 3-6 will not be restated here. Instead, this chapter offers a summary of the broad contributions made by the entirety of the work detailed in this thesis, comments on the remaining knowledge gaps, and recommendations for future directions that could aid in bridging these gaps. As a reminder, this thesis aimed to address multiple key objectives, with the overarching goal of advancing our understanding of seasonal sea ice biogeochemistry in the Atlantic sector of the Antarctic Marginal Ice Zone (AMIZ). These objectives included:

1. the development and implementation of field and laboratory sampling protocols for Antarctic sea ice collected under AMIZ conditions that could be utilized by South African researchers,
2. employing existing sea ice models to simulate the growth of young ice during the SCALE2019 expedition, and
3. contributing new data and insights to enhance the available information on biogeochemical properties of seasonal Antarctic sea ice in the AMIZ.

This thesis presented novel physical and biogeochemical data from three understudied sea ice types found often concurrently in the AMIZ: pancake ice, first year ice (FYI) and brash ice. These data are the product of several days spent in the field and laboratory developing new and adapting existing protocols to leverage the resources and infrastructure available to South African researchers. The protocols presented in **Chapter 2** represent a pivotal component of my research and postgraduate journey and contributed to the development of South African field research in the AMIZ. This thesis employed a multidisciplinary approach to broaden our understanding of the physical and biogeochemical characteristics of seasonal sea ice in the AMIZ, by collaborating across engineering and oceanographic disciplines. Techniques employed included cross polarisation of sea-ice cores, biogeochemical analysis of sea ice meltwater, use of numerical models, remote sensing data and sea ice tethered buoys.

7.1. New insights into sea ice growth and biogeochemistry in the AMIZ

The Antarctic Marginal Ice Zone (AMIZ) is a dynamic region at the boundary between the open ocean and sea-ice covered ocean. It experiences significant seasonal and spatial variability in ice cover, influenced by ocean currents, wind, and temperature fluctuations (Vichi, 2022). The biogeochemistry of the AMIZ is complex due to the frequent formation and melting of sea ice, which creates a highly variable environment for physical and biogeochemical processes (Swadling et al., 2023). Understanding this region and how sea ice grows and the evolution of the resulting biogeochemical system from growth and incorporation in winter to melt in spring and summer holds particular significance as it would provide insight into the biogeochemical cycling of nutrients in the wider Southern Ocean. While significant progress has been made in understanding Antarctic sea ice dynamics, gaps remain, particularly in data availability for constraining pancake ice properties and the transition from young ice (YI) to first-year ice (FYI) in the AMIZ. This data gap is a result of the harsh conditions that persist in the AMIZ, particularly during the winter growth period, and the difficulties associated with sampling such a dynamic region. As a result, the **physical characteristics** of growing Antarctic sea ice have thus far been understood by combining field data from different regions of the pack ice and AMIZ, and by considering the conceptual "pancake ice cycle" (Lange et al., 1989) as the baseline process. This model assumes a linear, monotonic transition from YI to FYI as ice thickness increases. The authors described a much more complex sea ice environment observed during these pioneering cruises in the winter AMIZ, and we argue that the subsequent extrapolation and uptake of their model in the literature was much more simplified. In particular, the interpretation of this model gave rise to the categorization of ice type by thickness alone, a method widely employed by satellite analysis and numerical models. Satellite derived sea ice types are produced by classifying ice types based on measured thickness (i.e. thinner ice would be identified as YI and thicker ice would be FYI or older). This classification treats sea-ice formation in the AMIZ as a monotonic, possibly linear process, which likely oversimplifies sea ice growth in this dynamic region. Rafting of pancakes is thus seen as a process equivalent to thermodynamic columnar ice growth. By investigating concurrent ice fields in the winter AMIZ, we showed that the complex physical transition from YI to FYI has implications for the resulting biogeochemical properties. Our findings in **Chapter 3** demonstrate that sea-ice formation is not a simple linear progression of thermodynamic thickening. FYI is indeed a rafted combination of YI as described by Lange et al. (1989), but we expand on this concept, suggesting that its complex structure is likely set by multiple processes of breaking and rearranging of successive pancake cycles and the resulting biogeochemical environment is influenced and enhanced by these processes.

Our findings in **Chapter 4** further demonstrate that sea ice biogeochemistry continues to undergo complex and dynamic changes beyond the initial growth period in winter and into spring that are influenced by factors such as wind, storms, ocean currents, and atmospheric temperature fluctuations. While thickness is one indicator of ice type, it does not capture the full variability of the physical properties nor the formation history of the ice and the resulting biogeochemical environment. The comparison between different sectors and their formation conditions in **Chapter 4** also demonstrates how different processes can produce sea ice of similar thickness but with very different layering structures and biogeochemical properties, making thickness alone an incomplete metric for classification.

From a biogeochemical perspective, Antarctic sea ice has **historically** been viewed as a relatively dormant environment during the winter months, with limited biogeochemical activity. This perspective has been shaped by studies such as Dieckmann et al. (1991) and Fripiat et al. (2017), which suggested that the sea ice biogeochemistry in winter is set by the underlying seawater and that the cold, harsh conditions and reduced light availability in winter result in **minimal biogeochemical processes** within the sea ice. However, emerging research presented in the introduction and our data from **Chapter 3**, provide compelling evidence that contradicts this notion. Our findings reveal **that sea ice in the AMIZ experiences significant biogeochemical activity during the winter months**. Elevated concentrations of chlorophyll, a marker of phytoplankton biomass, alongside evidence of active microbial processes, suggest that biological production continues within the sea ice despite limited light conditions. This microbial activity is critical in driving processes such as nutrient cycling. The novel N isotope ratios presented in **Chapter 5** further solidify the argument that winter sea ice is biogeochemically active. These data reveal that **processes such as nitrate assimilation and nitrification are ongoing during winter**. The elevated δ^{15}N values observed in winter sea ice indicate significant microbial uptake of the lighter N isotope (^{14}N), a hallmark of biological activity, including phytoplankton nitrate utilization. Additionally, comparison between our N isotope data and those of Fripiat et al. (2014) in **Chapter 5** indicates that **the AMIZ is more advanced temporally compared to the biogeochemistry in pack ice**. This means that the nutrient cycling and microbial processes typically observed in spring pack ice are already well underway earlier in the growth season in the AMIZ. This advanced state suggests a temporal shift in biogeochemical processes in the AMIZ, likely driven and enhanced by dynamically intermittent environmental factors such as rafting, as suggested in **Chapter 3**. The AMIZ thus demonstrates a more accelerated onset of biogeochemical activity, contributing to an earlier and more vigorous nutrient cycling regime than previously recognized in Antarctic sea ice. These findings expand on the traditional view of Antarctic sea ice as dormant during winter and reveal that significant biogeochemical processes are already in motion, laying the groundwork for a more productive ecosystem as the growth season progresses.

Chapter 6 presents the first direct comparison of pancake ice and brash ice in the AMIZ. The key differences between these ice types were revealed to be a direct result of the season they grew in. Our data demonstrated that the **pancake ice**, which represented the initial stage of sea ice growth and incorporation in winter, displayed biogeochemical profiles that were more closely aligned with the underlying seawater. This indicated minimal in-ice biological activity during the initial formation and incorporation periods, prior to the enhancement that occurs during the transition to FYI that was proposed in **Chapter 3**. In contrast, the **brash ice** in spring showed greater variability in both physical and biogeochemical characteristics. The influence of increased solar radiation in spring was evident in elevated chlorophyll concentrations and nutrient dynamics within the brash ice, indicative of a more productive biogeochemical environment. **Chapter 6** also highlights the importance of considering the interaction between sea ice and the surface ocean. In winter, incorporation of surface water into the sea ice dominates the system, with lower primary production as a result of reduced solar radiation. In comparison, spring surface waters displayed clear modification of surface ocean properties that were driven by the onset of sea ice melting, i.e. warmer, fresher, and nutrient-depleted due to ice melting and increased productivity. The data presented in **Chapter 6** expands our knowledge of the sea ice–surface ocean interaction, highlighting how environmental factors and seasonality shape the biogeochemical dynamics of the sea ice system.

7.2. Limitations of the study

While the work presented here contributes valuable insights into the biogeochemical properties of Antarctic sea ice in the AMIZ, several limitations should be acknowledged. One key limitation was the use of multiple sea-ice cores to characterise the properties of an ice floe and relating the resultant data to each other as if they were from the same core. This approach was employed due to the sampling requirements for the targeted variables; for example, the biogeochemical tests were destructive and required large volumes of meltwater compared to the crystal structure analysis that required portions of the cores to remain intact. While this approach provided a broad view of the sea ice properties, it introduced a degree of uncertainty to the characterisation of the sea ice. Analysing a single core for multiple, related variables (i.e. temperature, salinity and biogeochemical parameters) would likely increase the accuracy of the results. This approach will be explored in future research and methodological development. Another limitation was that only a portion of a larger, consolidated sea-ice floe was sampled per station, which may not have captured the full range of spatial variability within the floe. The spatial variability of the sea ice properties was already evident in the cores we sampled from a small portion of the floe, so we can assume it would be more pronounced across the entire floe. Additionally, the growth phase of Antarctic sea ice is spatially extensive and diverse, which prevents us from generalizing our findings to the extended AMIZ.

Delays between sampling and analysis of the sea-ice cores due to logistical constraints is common in ice field techniques. In this particular case, the global COVID-19 pandemic may have further impacted the preservation and integrity of sensitive variables like chlorophyll and some nutrient concentrations. That said, nitrate preserves well, both in terms of concentration and isotopic ratio.

Lastly, the study relied on published sea ice models to simulate sea ice growth and biogeochemical properties. While these models provided valuable insights, they are not appropriately configured to capture the complexities of the dynamic sea ice environment of the AMIZ, particularly with regard to dynamic growth processes such as rafting.

These limitations underscore the need for further refinement of sampling protocols and methodologies, particularly for studies in the dynamic and remote environment of the AMIZ. Future work should focus on improving these protocols to enhance the accuracy and consistency of the data collected. Despite these limitations, the data presented still contribute significantly to the understanding of sea ice biogeochemistry in the AMIZ and serve as a foundation for future studies in this field.

7.3. Implications for Antarctic sea ice modelling

Sea ice numerical models used in simulations of Arctic and Antarctic polar systems share the same underlying thermodynamics and dynamics equations. This is justifiable from the viewpoint of sea ice as a physico-chemical material. However, significant regional differences in Antarctic environmental conditions, sea-ice formation processes, biogeochemistry, and ultimately the limited skills of these models in reproducing regional trends and variability, indicate the need to adapt and refine the models by incorporating Antarctic-specific data and processes. The insights gained from this thesis highlight several key areas where existing sea ice models need to be updated to better reflect the nature of Antarctic sea ice. For example, Antarctic sea ice experiences more frequent formation of frazil ice and dynamic processes like rafting and ridging due to turbulent environmental conditions that persist during sea ice growth and ultimately influence the thickness of the ice produced. These processes and their influence on the sea ice environment are widely acknowledged, but are not adequately represented in existing models, as demonstrated in **Chapters 3 and 4**. Traditional models have often portrayed the growth of sea ice as a linear progression of thermodynamic thickening, simplifying the dynamic and complex nature of ice formation and reformation. Our simulations in **Chapters 3 and 4** further demonstrate the influence of dynamic processes in sea ice growth and the inability of models based on the continuum approximation to simulate the vertical distribution of biogeochemical properties in the AMIZ. Sea ice biogeochemistry models will never simulate the biomass accumulation we observed by means of local growth processes only. Our data advocate for the need to incorporate horizontal dynamics involving multiple sea ice layers to account for the influence of dynamic processes such as rafting, flushing, overwashing, and drainage on sea ice biogeochemistry and the surface ocean. Additionally, the novel N isotope data presented in **Chapter 5** provide definitive evidence of an active biogeochemical environment in winter sea ice. Models should therefore consider the sea ice matrix in the AMIZ as more permeable and granular, thus allowing an active biogeochemical environment throughout the year, rather than only during the spring and summer months.

7.4. Reflections and future research avenues

Throughout my postgraduate journey, I have had the unique privilege of witnessing and contributing to the early stages of Antarctic Marginal Ice Zone and sea ice research in South Africa. Being at the forefront of biogeochemical studies of sea ice in the AMIZ has been both challenging and rewarding. The lack of specific resources and infrastructure for sea ice research meant that I had to adapt, innovate, and develop methodologies while conducting my research and expanding my knowledge about the field. This experience not only deepened my understanding of the AMIZ but also sharpened my skills and intuition, particularly when in the field. While I thrived in the practical aspects of my research—fieldwork, developing sampling protocols, sample analysis, data processing, and mentoring new students—I often felt out of place within the more traditional "academic" side of research. This discomfort persisted throughout much of my studies and impacted how I approached my research.

This experience has definitely underscored the importance of mental health care and the vital role of support systems throughout the postgraduate journey. The encouragement from my mentors, peers, and loved ones has been invaluable in navigating the highs and lows of this journey. I feel incredibly privileged to have had the opportunity to participate in this research, to experience the majesty of sea ice and the Antarctic first-hand, and to contribute to our understanding of this critical region. These experiences have not only enriched my scientific knowledge but have also shaped me into a more resilient and reflective individual. As I near the completion of my thesis, I am beginning to discover the type of researcher I want to be and how I fit into the broader academic community. I find myself with a renewed enthusiasm for my research and a strong desire to continue exploring the mysteries of sea ice and the AMIZ. There is so much more to learn, and I am eager to contribute to South Africa's research efforts in the Antarctic. My goal is to carve out a space for myself in this field, not only as a researcher but also as a mentor, supporting the next generation of scientists in their Antarctic endeavours.

From a research perspective, I intend to continue to focus on characterising the physical and biogeochemical properties of sea ice in the Antarctic, with a particular emphasis on the AMIZ. My work has emphasised the importance of in-situ observations for the development and validation of sea ice models and remote sensing products. A significant aspect of my research will be the ongoing development and refinement of protocols for sea ice studies, both in the field and in the laboratory. The unpredictable nature of in-situ research presents challenges, especially when it comes to the storage of sea-ice core samples for extended periods. Maintaining the "clean" conditions necessary for accurate biogeochemical analysis is crucial but often difficult to achieve while at sea. I intend to explore how storage time and conditions influence the integrity of sea ice properties, with the goal of establishing best practices for long-term sample preservation. I will also be expanding on the research done in this thesis to prepare the work for publication. I plan to make all data generated by my research publicly accessible through the South African Polar Research Infrastructure's Open Data Platform (SAPRI ODP, https://www.sapri.ac.za/data-products-society/data/). While I strongly believe that hoarding data hinders progress, it's important to note that not all sea ice data are currently available in public repositories. Additionally, there is a lack of dedicated metadata standards or focused efforts to ensure that this type of data adheres to FAIR (**F**indability, **A**ccessibility, **I**nteroperability, and **R**eusability) principles. Making data openly accessible is essential for fostering collaboration and driving scientific advancements.

In addition to traditional methods, I plan to incorporate newer technologies into my research. The Polar ARGO program (https://argo.ucsd.edu/expansion/polar-argo/), which deploys autonomous floats under ice, offers a novel way to collect data from the polar regions that are otherwise inaccessible due to the sea-ice cover and the BGC-ARGO program (https://biogeochemical-argo.org/) that has developed biogeochemical sensors that are deployed on ARGO floats, enabling the remote collection of oceanic biogeochemical data. In addition, remote sensing techniques, such as satellite-based observations, will also be integrated to enhance the spatial and temporal resolution of sea ice monitoring. These technologies have the potential to revolutionize our understanding of sea ice processes and the influence of sea ice on the surface ocean, and I am eager to support their development and apply them to my future research. By combining innovative, multidisciplinary approaches with a deepened understanding of sea ice physical and biogeochemical properties, I hope to contribute to South Africa's Antarctic research efforts. My long-term goal is to help establish a comprehensive framework for sea ice research that not only advances scientific knowledge but also supports the development of future researchers in this field. This thesis is the first step in achieving that goal.

7.5. Summary and broad suggestions for future sea ice research in the AMIZ

In summary, this thesis has contributed significantly to advancing our understanding of the physical and biogeochemical properties of seasonal sea ice in the AMIZ. Our findings challenge existing assumptions about sea ice in the Antarctic by demonstrating that the **growth of sea ice is not a linear progression of thermodynamic thickening over time, but is instead a product of multiple processes of breaking and rearranging** promoted by the dynamic environmental conditions that persist in the AMIZ. Additionally, the resulting sea-ice biogeochemical environment is influenced and enhanced by these dynamic growth conditions. The sea ice in the AMIZ revealed that **significant biological processes are taking place during the winter growth season, indicating that sea ice serves as a dynamic biogeochemical reservoir in winter, well before the traditionally recognized productive period in spring**. These findings underscore the **complexity and interconnectedness** of physical and biogeochemical processes in the AMIZ, emphasizing the need for updated and integrated modelling approaches to better represent Antarctic sea ice. Additionally, the dataset presented here includes the **first biogeochemical measurements for pancake, brash and first year ice in the region**, including novel measurements **of sea-ice N isotope ratios**. The work presented here underscores the dynamic and complex nature of sea ice in the AMIZ and highlights the importance of integrating physical, biogeochemical, and modelling approaches to fully comprehend its behaviour and implications. The data presented here contributes to the relatively sparse collection of historical data for the Antarctic. This, combined with the insights gained here, provides a foundation for future studies and underscores the need for continued exploration and adaptation of sea ice methodologies and models to better characterise and simulate the Antarctic environment.

As a general note, continued research is essential to further unravel the intricacies of sea ice growth and biogeochemistry in the AMIZ and its implications for polar ecosystem dynamics and global biogeochemical cycles. As demonstrated by the work presented in this thesis, in order to comprehensively characterize the biogeochemical properties of sea ice within the AMIZ, we need to acknowledge the interconnectedness of the various processes influencing sea-ice formation and evolution at the seasonally expanding and receding interface of Antarctic sea ice with the Southern Ocean. For example, the conditions occurring during sea ice growth in a turbulent environment influence the internal structure of the ice, which in turn influences how the brine channels develop and incorporate brines, which ultimately influences how the biogeochemical constituents are distributed. Frequent storms then further reshape the AMIZ system and its biogeochemical content. An approach like the *whole-of-system research* would be beneficial in the context of AMIZ research. This approach seeks to understand the interconnectedness of various components within a complex system by examining their interactions holistically as opposed to in isolation. This method is appropriate, given the dynamic and multifaceted nature of the sea ice environment. The AMIZ represents a critical interface where ocean, sea ice, atmosphere, and biological processes converge. A whole-of-system approach would allow researchers to investigate how these components influence one another by integrating across scales and disciplines, thereby creating a more comprehensive understanding of the AMIZ. Future research in the AMIZ should acknowledge the interconnectedness of the AMIZ characteristics and prioritize the whole-of-system approach through multidisciplinary and collaborative research efforts. This approach is essential for accurately characterising the region and improving the predictive capacity of models that aim to simulate the region and address climate change impacts on the AMIZ and the global system as a whole – ultimately informing better conservation strategies and enhancing the global understanding of polar systems under changing environmental conditions.

From a South African perspective, the National Research Foundation (NRF) through the South African National Antarctic Program (SANAP) has provided funding to enable South African researchers to study the Southern Ocean and Antarctica, with recently funded projects focusing on the AMIZ. The recent establishment of the South African Polar Research Infrastructure (SAPRI) will enable South African research in the AMIZ to expand through the provisioning of infrastructure, equipment and skills development to both established researchers and new and emerging researchers who wish to enter the Antarctic research field but have previously lacked the resources or skills to do so. Part of the SAPRI that will enable sea ice research is the Polar Lab Integrated Facility (IF), which includes fixed and mobile laboratories that are equipped to simulate the Antarctic environment. The Polar Lab IF will enable researchers to conduct experiments under controlled conditions, process temperature sensitive samples in sub-zero laboratories and train students and researchers in field techniques while in South Africa. The goal of SAPRI and the Polar Lab IF is to make sea ice research more accessible and inclusive and allow us to nurture a new generation of researchers and foster national and international collaboration. The latter would allow local researchers to connect with more established researchers in the field and by sharing our science internationally, we will be able to access a wider range of funding, resources, expertise, and data, thereby enhancing the scope and quality of our research.

References

Ackley, S.F., Xie, H. & Tichenor, E.A. 2015. Ocean heat flux under Antarctic sea ice in the Bellingshausen and Amundsen Seas: two case studies. *Annals of Glaciology*. 56(69):200–210. DOI: 10.3189/2015AOG69A890.

Arndt, S., Haas, C., Meyer, H., Peeken, I. & Krumpen, T. 2021. Recent observations of superimposed ice and snow ice on sea ice in the northwestern Weddell Sea. *Cryosphere*. 15(9):4165–4178. DOI: 10.5194/TC-15-4165-2021.

Arrigo, K.R. 2003. Primary Production in Sea Ice. In *Sea Ice*. John Wiley & Sons, Ltd. 143–183. DOI: 10.1002/9780470757161.ch5.

Arrigo, K.R. 2014. Sea Ice Ecosystems. *https://doi.org/10.1146/annurev-marine-010213-135103*. 6:439–467. DOI: 10.1146/ANNUREV-MARINE-010213-135103.

Arrigo, K.R., Dieckmann, G., Gosselin, M., Robinson, D.H., Fritsen, C.H. & Sullivan, C.W. 1995. High resolution study of the platelet ice ecosystem in McMurdo Sound, Antarctica: biomass, nutrient, and production profiles within a dense microalgal bloom. *Marine Ecology Progress Series*. 127(1–3):255–268. DOI: 10.3354/MEPS127255.

Assur, A. 1958. Composition of Sea Ice and Its Tensile Strength. In *Arctic Sea Ice*. U.S. Army Snow, Ice and Permafrost Research Establishment. 106–138.

Auclair, J.P., Dumont, D., Lemieux, J.F. & Ritchie, H. 2022. A model study of convergent dynamics in the marginal ice zone. *Philosophical Transactions of the Royal Society A*. 380(2235). DOI: 10.1098/RSTA.2021.0261.

Audh, R.R., Johnson, S., Hambrock, M., Marquart, R., Pead, J., Rampai, T., Skatulla, S. & Vichi, M. 2022. Sea ice core temperature and salinity data collected during the 2019 SCALE Spring Cruise. DOI: 10.5281/ZENODO.6997631.

Audh, R.R., Johnson, S., Hambrock, M., Little, H., Mirkin, J., Omatuku, E., Hall, B., Rampai, T., et al. 2023. Sea ice core biogeochemical data collected during the 2019 SCALE Winter Cruise. DOI: 10.5281/ZENODO.7821287.

Becquevort, S., Dumont, I., Tison, J.L., Lannuzel, D., Sauvée, M.L., Chou, L. & Schoemann, V. 2009. Biogeochemistry and microbial community composition in sea ice and underlying seawater off east

Antarctica during early spring. *Polar Biology*. 32(6):879–895. DOI: 10.1007/S00300-009-0589-2/FIGURES/7.

Bendschneider, K. & Robinson, R.J. 1952. A New Spectrophotometric Method for the Determination of Nitrite in Sea Water.

Böhlke, J.K., Mroczkowski, S.J. & Coplen, T.B. 2003. Oxygen isotopes in nitrate: new reference materials for 18O:17O:16O measurements and observations on nitrate-water equilibration. *Rapid Communications in Mass Spectrometry*. 17(16):1835–1846. DOI: 10.1002/RCM.1123.

Braman, R.S. & Hendrix, S.A. 1989. Nanogram Nitrite and Nitrate Determination in Environmental and Biological Materials by Vanadium(III) Reduction with Chemiluminescence Detection. 61:2715–2718.

Casciotti, K.L., Sigman, D.M. & Ward, B.B. 2003. Linking Diversity and Stable Isotope Fractionation in Ammonia-Oxidizing Bacteria. *Geomicrobiology Journal*. 20(4):335–353. DOI: 10.1080/01490450303895.

Casciotti, K.L., Buchwald, C., Santoro, A.E. & Frame, C. 2011. Assessment of Nitrogen and Oxygen Isotopic Fractionation During Nitrification and Its Expression in the Marine Environment. *Methods in Enzymology*. 486(C):253–280. DOI: 10.1016/B978-0-12-381294-0.00011-0.

Cimoli, E., Meiners, K.M., Lund-Hansen, L.C. & Lucieer, V. 2017. Spatial variability in sea-ice algal biomass: an under-ice remote sensing perspective. *Adv Polar Sci*. 28(4):268–296. DOI: 10.13679/j.advps.2017.4.00268.

Clark, S.C., Granger, J., Mastorakis, A., Aguilar-Islas, A. & Hastings, M.G. (in press). An Investigation Into the Origin of Nitrate in Arctic Sea Ice. *Global Biogeochemical Cycles*. 34(2):e2019GB006279. DOI: 10.1029/2019GB006279.

Clarke, D.B. & Ackley, S.F. 1984. Sea ice structure and biological activity in the Antarctic marginal ice zone. *Journal of Geophysical Research*. 89(C2):2087–2095. DOI: 10.1029/JC089IC02P02087.

Cox, G.F.N. & Weeks, W.F. 1986. Changes in the Salinity and Porosity of Sea-Ice Samples During Shipping and Storage. *Journal of Glaciology*. 32(112):371–375. DOI: 10.3189/S0022143000012065.

Cox, G.F.N. & Weeks, W.F. 1988. Numerical simulations of the profile properties of undeformed first-year sea ice during the growth season. *Journal of Geophysical Research: Oceans*. 93(C10):12449–12460. DOI: 10.1029/JC093IC10P12449.

Cozzi, S. & Cantoni, C. 2010. Stable isotope (δ13C and δ15N) composition of particulate organic matter, nutrients and dissolved organic matter during spring ice retreat at Terra Nova Bay. *Antarctic Science*. 23(1):43–56. DOI: 10.1017/S0954102010000611.

Dai, M., Shen, H.H., Hopkins, M.A., Ackley, S.F., Dai, M., Shen, H.H., Hopkins, M.A. & Ackley, S.F. 2004. Wave rafting and the equilibrium pancake ice cover thickness. *Journal of Geophysical Research: Oceans*. 109(C7):7023. DOI: 10.1029/2003JC002192.

De Vries, T. 2022. The Ocean Carbon Cycle. *Annual Review of Environment and Resources*. 47(Volume 47, 2022):317–341. DOI: 10.1146/annurev-environ-120920-111307.

Delandmeter, P. & Sebille, E.V. 2019. The Parcels v2.0 Lagrangian framework: New field interpolation schemes. *Geoscientific Model Development*. 12(8):3571–3584. DOI: 10.5194/GMD-12-3571-2019.

Dieckmann, G.S. & Hellmer, H.H. 2003. The Importance of Sea Ice: An Overview. In *Sea Ice*. John Wiley & Sons, Ltd. 1–21. DOI: 10.1002/9780470757161.ch1.

Dieckmann, G.S., Lange, M.A., Ackley, S.F. & Jennings, J.C. 1991. The nutrient status in sea ice of the Weddell Sea during winter: effects of sea ice texture and algae. *Polar Biology*. 11(7):449–456. DOI: 10.1007/BF00233080/METRICS.

Dieckmann, G.S., Nehrke, G., Papadimitriou, S., Göttlicher, J., Steininger, R., Kennedy, H., Wolf-Gladrow, D. & Thomas, D.N. 2008. Calcium carbonate as ikaite crystals in Antarctic sea ice. *Geophysical Research Letters*. 35(8). DOI: 10.1029/2008GL033540.

Dieckmann, G.S., Nehrke, G., Uhlig, C., Göttlicher, J., Gerland, S., Granskog, M.A. & Thomas, D.N. 2010. Brief Communication: Ikaite ($CaCO_3$·$6H_2O$) discovered in Arctic sea ice. *The Cryosphere*. 4(2):227–230. DOI: 10.5194/tc-4-227-2010.

DiFiore, P.J., Sigman, D.M. & Dunbar, R.B. 2009. Upper ocean nitrogen fluxes in the Polar Antarctic Zone: Constraints from the nitrogen and oxygen isotopes of nitrate. *Geochemistry, Geophysics, Geosystems*. 10(11). DOI: 10.1029/2009GC002468.

Duarte, P., Assmy, P., Campbell, K. & Sundfjord, A. 2022. The importance of turbulent ocean-sea ice nutrient exchanges for simulation of ice algal biomass and production with CICE6.1 and Icepack 1.2. *Geoscientific Model Development*. 15(2):841–857. DOI: 10.5194/GMD-15-841-2022.

Eicken, H. 1992. Salinity profiles of Antarctic sea ice: Field data and model results. *Journal of Geophysical Research: Oceans*. 97(C10):15545–15557. DOI: 10.1029/92JC01588.

Eicken, H. 2003. From the Microscopic, to the Macroscopic, to the Regional Scale: Growth, Microstructure and Properties of Sea Ice. In *Sea Ice*. John Wiley & Sons, Ltd. 22–81. DOI: 10.1002/9780470757161.ch2.

Eicken, H. & Salganek, M. 2010. *Field Techniques for Sea-Ice Research*. University of Alaska Press.

Fawcett, S.E., Lomas, M.W., Casey, J.R., Ward, B.B. & Sigman, D.M. 2011. Assimilation of upwelled nitrate by small eukaryotes in the Sargasso Sea. *Nature Geoscience*. 4(10):717–722. DOI: 10.1038/ngeo1265.

Fawcett, S.E., Lomas, M.W., Ward, B.B. & Sigman, D.M. 2014. The counterintuitive effect of summer-to-fall mixed layer deepening on eukaryotic new production in the Sargasso Sea. *Global Biogeochemical Cycles*. 28(2):86–102. DOI: 10.1002/2013GB004579.

Flemming, H.C., Wingender, J., Szewzyk, U., Steinberg, P., Rice, S.A. & Kjelleberg, S. 2016. Biofilms: an emergent form of bacterial life. *Nature Reviews Microbiology 2016 14:9*. 14(9):563–575. DOI: 10.1038/nrmicro.2016.94.

Frankenstein, G. & Garner, R. 1967. Equations for Determining the Brine Volume of Sea Ice from −0.5° to −22.9°C. *Journal of Glaciology*. 6(48):943–944. DOI: 10.3189/S0022143000020244.

Fripiat, F., Sigman, D.M., Fawcett, S.E., Rafter, P.A., Weigand, M.A. & Tison, J.L. 2014. New insights into sea ice nitrogen biogeochemical dynamics from the nitrogen isotopes. *Global Biogeochemical Cycles*. 28(2):115–130. DOI: 10.1002/2013GB004729.

Fripiat, F., Sigman, D.M., Massé, G. & Tison, J.L. 2015. High turnover rates indicated by changes in the fixed N forms and their stable isotopes in Antarctic landfast sea ice. *Journal of Geophysical Research: Oceans*. 120(4):3079–3097. DOI: 10.1002/2014JC010583.

Fripiat, F., Meiners, K.M., Vancoppenolle, M., Papadimitriou, S., Thomas, D.N., Ackley, S.F., Arrigo, K.R., Carnat, G., et al. 2017. Macro-nutrient concentrations in Antarctic pack ice: Overall patterns and overlooked processes. *Elementa*. 5. DOI: 10.1525/ELEMENTA.217/112432.

Fripiat, F., Martínez-García, A., Fawcett, S.E., Kemeny, P.C., Studer, A.S., Smart, S.M., Rubach, F., Oleynik, S., et al. 2019. The isotope effect of nitrate assimilation in the Antarctic Zone: Improved estimates and paleoceanographic implications. *Geochimica et Cosmochimica Acta*. 247:261–279. DOI: 10.1016/j.gca.2018.12.003.

Garrison, D.L., Close, A.R. & Reimnitz, E. 1989. Algae concentrated by frazil ice: evidence from laboratory experiments and field measurements. *Antarctic Science*. 1(4):313–316. DOI: 10.1017/S0954102089000477.

Garside, C. 1982. A chemiluminescent technique for the determination of nanomolar concentrations of nitrate and nitrite in seawater. *Marine Chemistry*. 11(2):159–167. DOI: 10.1016/0304-4203(82)90039-1.

Gleitz, M., Loeff, M. vd, Thomas, D.N., Chemistry, G.D.-M. & undefined 1995. 1995. Comparison of summer and winter inorganic carbon, oxygen and nutrient concentrations in Antarctic sea ice brine. *Elsevier*. Available: https://www.sciencedirect.com/science/article/pii/030442039500053T.

Gleitz, M., Kukert, H., Riebesell, U. & Dieckmann, G.S. 1996. Carbon acquisition and growth of Antarctic sea ice diatoms in closed bottle incubations. *Marine Ecology Progress Series*. 135(1–3):169–177. DOI: 10.3354/MEPS135169.

Golden, K.M., Ackley, S.F. & Lytle, V.I. 1998. The percolation phase transition in sea ice. *Science*. 282(5397):2238–2241. DOI: 10.1126/SCIENCE.282.5397.2238/ASSET/911D480C-BC9B-4AA7-B8E7-881BB6C68B15/ASSETS/GRAPHIC/SE5087087004.JPEG.

Golden, K.M., Gully, A., Sampson, C. & Lubbers, D. n.d. Critical Threshold Behavior of Fluid Transport in Granular Antarctic Sea Ice. Available: http://www.math.utah.edu/~css/Publications/Goldengranperm_et_al_2021.pdf.

Gonfiantini, R. 1984. Stable isotope reference samples for geochemical and hydrological investigations. *Int. J. Appl. Radiat. Isot.; (United Kingdom)*. 35:5(5):426. DOI: 10.1016/0020-708X(84)90059-0.

Granger, J., Sigman, D.M., Needoba, J.A. & Harrison, P.J. 2004. Coupled nitrogen and oxygen isotope fractionation of nitrate during assimilation by cultures of marine phytoplankton. *Limnology and Oceanography*. 49(5):1763–1773. DOI: 10.4319/lo.2004.49.5.1763.

Granger, J., Sigman, D.M., Lehmann, M.F. & Tortell, P.D. 2008. Nitrogen and oxygen isotope fractionation during dissimilatory nitrate reduction by denitrifying bacteria. *Limnology and Oceanography*. 53(6):2533–2545. DOI: 10.4319/lo.2008.53.6.2533.

Haas, C. 2003. Dynamics versus Thermodynamics: The Sea Ice Thickness Distribution. In *Sea Ice*. John Wiley & Sons, Ltd. 82–111. DOI: 10.1002/9780470757161.ch3.

Hagopian, D.S. & Riley, J.G. 1998. A closer look at the bacteriology of nitrification. *Aquacultural Engineering*. 18(4):223–244. DOI: 10.1016/S0144-8609(98)00032-6.

Hague, M. & Vichi, M. 2021. Southern ocean biogeochemical argo detect under-ice phytoplankton growth before sea ice retreat. *Biogeosciences*. 18(1):25–38. DOI: 10.5194/BG-18-25-2021.

Henley, S.F., Tuerena, R.E., Annett, A.L., Fallick, A.E., Meredith, M.P., Venables, H.J., Clarke, A. & Ganeshram, R.S. 2017. Macronutrient supply, uptake and recycling in the coastal ocean of the west Antarctic Peninsula. *Deep Sea Research Part II: Topical Studies in Oceanography*. 139:58–76. DOI: 10.1016/J.DSR2.2016.10.003.

Henley, S.F., Cozzi, S., Fripiat, F., Lannuzel, D., Nomura, D., Thomas, D.N., Meiners, K.M., Vancoppenolle, M., et al. 2023. Macronutrient biogeochemistry in Antarctic land-fast sea ice: Insights from a circumpolar data compilation. *Marine Chemistry*. 257:104324. DOI: 10.1016/J.MARCHEM.2023.104324.

Herman, A. 2022. Granular effects in sea ice rheology in the marginal ice zone. *Philosophical Transactions of the Royal Society A*. 380(2235). DOI: 10.1098/RSTA.2021.0260.

Hersbach, H., Bell, B., Berrisford, P., Biavati, G., Horányi, A., Sabater, J.M., Nicolas, J., Peubey, C., et al. 2018. *ERA5 hourly data on single levels from 1979 to present. Copernicus Climate Change Service (C3S) Climate Data Store (CDS), 10.*

Hersbach, H., Bell, B., Berrisford, P., Hirahara, S., Horányi, A., Muñoz-Sabater, J., Nicolas, J., Peubey, C., et al. 2020. The ERA5 global reanalysis. *Quarterly Journal of the Royal Meteorological Society*. 146(730):1999–2049. DOI: 10.1002/QJ.3803.

Holmes, R.M., Aminot, A., Kérouel, R., Hooker, B.A. & Peterson, B.J. 1999. A simple and precise method for measuring ammonium in marine and freshwater ecosystems. *Canadian Journal of Fisheries and Aquatic Sciences*. 56(10):1801–1808. DOI: 10.1139/F99-128.

Horner, R.A. 1989. Arctic Sea-Ice Biota. In *The Arctic Seas: Climatology, Oceanography, Geology, and Biology*. Y. Herman, Ed. Boston, MA: Springer US. 123–146. DOI: 10.1007/978-1-4613-0677-1_5.

Hu, Y.-B. & Wang, F. 2020. Effect of ikaite precipitation on phosphate removal in sea ice. *Polar Research*. (July, 8). DOI: 10.33265/polar.v39.3413.

Hu, Y.-B., Dieckmann, G.S., Wolf-Gladrow, D.A. & Nehrke, G. 2014. Laboratory study on coprecipitation of phosphate with ikaite in sea ice. *Journal of Geophysical Research: Oceans*. 119(10):7007–7015. DOI: 10.1002/2014JC010079.

Hunke, E.C., Lipscomb, W.H., Turner, A.K., Jeffery, N. & Elliott, S. 2015. CICE: The Los Alamos Sea ice model documentation and software user's manual version 5.1 LA-CC-06-012. *T-3 Fluid Dynamics Group, Los Alamos National Laboratory*. 675:15.

Hydes, D., Aoyama, M., Aminot, A., Bakker, K., Becker, S., Coverly, S., Daniel, A., Dickson, A., et al. 2010. Determination of dissolved nutrients (N, P, Si) in seawater with high precision and inter-comparability using gas-segmented continuous flow analysers. (June, 1). Available: https://archimer.ifremer.fr/doc/00020/13141/ [2025, May 01].

Jeffery, N., Elliott, S.M., Hunke, E.C., Lipscomb, W.H. & Turner, A.K. 2016. *Biogeochemistry of CICE: the Los Alamos Sea Ice Model Documentation and Software User's Manual zbgc_colpkg modifications to Version 5*. Los Alamos National Laboratory (LANL), Los Alamos, NM (United States). Available: https://www.osti.gov/servlets/purl/1329842 [2025, April 29].

Jeffries & Weeks. 1993. Structural characteristics and development of sea ice in the western Ross Sea. *Antarctic Science*. 5(1):63–75. DOI: 10.1017/S0954102093000094.

Jeffries, M.O., Krouse, H.R., Hurst-Cushing, B. & Maksym, T. 2001. Snow-ice accretion and snow-cover depletion on Antarctic first-year sea-ice floes. *Annals of Glaciology*. 33:51–60. DOI: 10.3189/172756401781818266.

Johnson, S., Matlakala, B., Vichi, M. & Rampai, T. 2022. Crystal size and texture data of sea ice from the Antarctic Marginal Ice Zone collected in Winter 2019. DOI: 10.5281/ZENODO.6977589.

Johnson, S., Khoboko, T., Matlakala, B., Vichi, M. & Rampai, T. 2022. Crystal size and texture data of sea ice from the Antarctic Marginal Ice Zone collected in Spring 2019. DOI: 10.5281/ZENODO.6966958.

Johnson, S., Audh, R.R., Jager, W. de, Matlakala, B., Vichi, M., Womack, A. & Rampai, T. 2023. Physical and morphological properties of first-year Antarctic sea ice in the spring marginal ice zone of the Atlantic-Indian sector. *Journal of Glaciology*. (April):1–14. DOI: 10.1017/JOG.2023.21.

Kaartokallio, H. 2001. Evidence for active microbial nitrogen transformations in sea ice (Gulf of Bothnia, Baltic Sea) in midwinter. *Polar Biology*. 24(1):21–28. DOI: 10.1007/s003000000169.

Kanamitsu, M., Ebisuzaki, W., Woollen, J., Yang, S.K., Hnilo, J.J., Fiorino, M. & Potter, G.L. 2002. NCEP–DOE AMIP-II Reanalysis (R-2). *Bulletin of the American Meteorological Society*. 83(11):1631–1644. DOI: 10.1175/BAMS-83-11-1631.

Knapp, A. 2012. The sensitivity of marine N2 fixation to dissolved inorganic nitrogen. *Frontiers in Microbiology*. 3. DOI: 10.3389/fmicb.2012.00374.

Knapp, A.N., Sigman, D.M. & Lipschultz, F. 2005. N isotopic composition of dissolved organic nitrogen and nitrate at the Bermuda Atlantic Time-series study site. *Global Biogeochemical Cycles*. 19(1):1–15. DOI: 10.1029/2004GB002320.

Kobayashi, S., Ota, Y., Harada, Y., Ebita, A., Moriya, M., Onoda, H., Onogi, K., Kamahori, H., et al. 2015. The JRA-55 Reanalysis: General Specifications and Basic Characteristics. *Journal of the Meteorological Society of Japan. Ser. II*. 93(1):5–48. DOI: 10.2151/JMSJ.2015-001.

Lange, M.A. & Eicken, H. 1991. The sea ice thickness distribution in the northwestern Weddell Sea. *Journal of Geophysical Research: Oceans*. 96(C3):4821–4837. DOI: 10.1029/90JC02441.

Lange, Ackley, S.F., Wadhams, P., Dieckmann, G.S. & Eicken, H. 1989. Development of Sea Ice in the Weddell Sea. *Annals of Glaciology*. 12:92–96. DOI: 10.3189/S0260305500007023.

Lange, M.A., Schlosser, P., Ackley, S.F., Wadhams, P. & Dieckmann, G.S. 1990. 18O concentrations in sea ice of the Weddell Sea, Antarctica. *Journal of Glaciology*. 36(124):315–323. DOI: 10.3189/002214390793701291.

Lannuzel, D., Schoemann, V., Jong, J. de, Tison, J.L. & Chou, L. 2007. Distribution and biogeochemical behaviour of iron in the East Antarctic sea ice. *Marine Chemistry*. 106(1–2):18–32. DOI: 10.1016/J.MARCHEM.2006.06.010.

Lannuzel, D., Vancoppenolle, M., Merwe, P.V.D., Jong, J.D., Meiners, K.M., Grotti, M., Nishioka, J. & Schoemann, V. 2016. Iron in sea ice: Review & new insights. *Elementa*. 4. DOI: 10.12952/JOURNAL.ELEMENTA.000130/112863.

Lehmann, M.F., Bernasconi, S.M., Barbieri, A. & McKenzie, J.A. 2002. Preservation of organic matter and alteration of its carbon and nitrogen isotope composition during simulated and in situ early sedimentary diagenesis. *Geochimica et Cosmochimica Acta*. 66(20):3573–3584. DOI: 10.1016/S0016-7037(02)00968-7.

Lepparanta, M. 1983. A Growth Model for Black Ice, Snow Ice and Snow Thickness in Subarctic Basins. *Hydrology Research*. 14(2):59–70. DOI: 10.2166/NH.1983.0006.

Lourey, M.J., Trull, T.W. & Sigman, D.M. 2003. Sensitivity of δ15N of nitrate, surface suspended and deep sinking particulate nitrogen to seasonal nitrate depletion in the Southern Ocean. *Global Biogeochemical Cycles*. 17(3). DOI: 10.1029/2002GB001973.

Louw, S.D.V., Walker, D.R. & Fawcett, S.E. 2022. Factors influencing sea-ice algae abundance, community composition, and distribution in the marginal ice zone of the Southern Ocean during winter. *Deep Sea Research Part I: Oceanographic Research Papers*. 185:103805. DOI: 10.1016/J.DSR.2022.103805.

Lytle, V.I. & Ackley, S.F. 2001. Snow-ice growth: a fresh-water flux inhibiting deep convection in the Weddell Sea, Antarctica. *Annals of Glaciology*. 33:45–50. DOI: 10.3189/172756401781818752.

Mariotti, A., Germon, J.C., Hubert, P., Kaiser, P., Letolle, R., Tardieux, A. & Tardieux, P. 1981. Experimental determination of nitrogen kinetic isotope fractionation: Some principles; illustration for the denitrification and nitrification processes. *Plant and Soil*. 62(3):413–430. DOI: 10.1007/BF02374138/METRICS.

Maslanik, J. & Stroeve, J. 1999. *Near-Real-Time DMSP SSMIS Daily Polar Gridded Sea Ice Concentrations, Version 1 - AmeriGEOSS Community Platform DataHub. (BETA)*. Available: https://data.amerigeoss.org/dataset/near-real-time-dmsp-ssmis-daily-polar-gridded-sea-ice-concentrations-version-1 [2024, September 15].

Massom, R.A. & Stammerjohn, S.E. 2010. Antarctic sea ice change and variability – Physical and ecological implications. *Polar Science*. 4(2):149–186. DOI: 10.1016/j.polar.2010.05.001.

Maus, S., Schneebeli, M. & Wiegmann, A. 2021. An X-ray micro-tomographic study of the pore space, permeability and percolation threshold of young sea ice. *The Cryosphere*. 15(8):4047–4072. DOI: 10.5194/tc-15-4047-2021.

Maykut, G.A. & Untersteiner, N. 1971. Some results from a time-dependent thermodynamic model of sea ice. *Journal of Geophysical Research*. 76(6):1550–1575. DOI: 10.1029/JC076I006P01550.

McPhee, M.G., Kottmeier, C. & Morison, J.H. 1999. Ocean Heat Flux in the Central Weddell Sea during Winter. *Journal of Physical Oceanography*. 29(6):1166–1179. DOI: 10.1175/1520-0485(1999)029.

Mdutyana, M., Thomalla, S.J., Philibert, R., Ward, B.B. & Fawcett, S.E. 2020. The Seasonal Cycle of Nitrogen Uptake and Nitrification in the Atlantic Sector of the Southern Ocean. *Global Biogeochemical Cycles*. 34(7). DOI: 10.1029/2019GB006363.

Mdutyana, M., Marshall, T., Sun, X., Burger, J.M., Thomalla, S.J., Ward, B.B. & Fawcett, S.E. 2022. Controls on nitrite oxidation in the upper Southern Ocean: insights from winter kinetics experiments in the Indian sector. *Biogeosciences*. 19(14):3425–3444. DOI: 10.5194/BG-19-3425-2022.

Mdutyana, M., Sun, X., Burger, J.M., Flynn, R.F., Smith, S., Horsten, N.R.V., Roychoudhury, A.N., Planquette, H., et al. 2022. The kinetics of ammonium uptake and oxidation across the Southern Ocean. *Wiley Online Library*. 67(4):973–991. DOI: 10.1002/lno.12050.

Meiners, K.M. & Michel, C. 2017. Dynamics of nutrients, dissolved organic matter and exopolymers in sea ice. In *Sea Ice*. John Wiley & Sons, Ltd. 415–432. DOI: 10.1002/9781118778371.ch17.

Meiners, K.M., Vancoppenolle, M., Thanassekos, S., Dieckmann, G.S., Thomas, D.N., Tison, J.L., Arrigo, K.R., Garrison, D.L., et al. 2012. Chlorophyll a in Antarctic sea ice from historical ice core data. *Geophysical Research Letters*. 39(21). DOI: 10.1029/2012GL053478.

Melnikov. 1995. An in situ experimental study of young sea ice formation on an Antarctic lead. *Journal of Geophysical Research: Oceans*. 100(C3):4673–4680. DOI: 10.1029/94JC02354.

Melnikov. 1998. Winter production of sea ice algae in the western Weddell Sea. *Journal of Marine Systems*. 17(1–4):195–205. DOI: 10.1016/S0924-7963(98)00038-4.

van der Merwe, P., Lannuzel, D., Nichols, C.A.M., Meiners, K., Heil, P., Norman, L., Thomas, D.N. & Bowie, A.R. 2009. Biogeochemical observations during the winter–spring transition in East Antarctic sea ice: Evidence of iron and exopolysaccharide controls. *Marine Chemistry*. 115(3–4):163–175. DOI: 10.1016/J.MARCHEM.2009.08.001.

Miller, L.A., Fripiat, F., Else, B.G.T., Bowman, J.S., Brown, K.A., Collins, R.E., Ewert, M., Fransson, A., et al. 2015. Methods for biogeochemical studies of sea ice: The state of the art, caveats, and recommendations. *Elementa*. 3:38. DOI: 10.12952/JOURNAL.ELEMENTA.000038/112717.

Möbius, J. 2013. Isotope fractionation during nitrogen remineralization (ammonification): Implications for nitrogen isotope biogeochemistry. *Geochimica et Cosmochimica Acta*. 105:422–432. DOI: 10.1016/j.gca.2012.11.048.

Montoya, J.P. 2008. Nitrogen Stable Isotopes in Marine Environments. *Nitrogen in the Marine Environment*. (January):1277–1302. DOI: 10.1016/B978-0-12-372522-6.00029-3.

Muench, R.D. 1989. *The sea ice margin: a summary of physical phenomena*.

Murphy, J. & Riley, J.P. 1962. A modified single solution method for the determination of phosphate in natural waters. *Analytica Chimica Acta*. 27(C):31–36. DOI: 10.1016/S0003-2670(00)88444-5.

Ngongo, E.O., Audh, R.R., Hall, B., Skatulla, S., MacHutchon, K., Rampai, T. & Vichi, M. 2022. Sea ice core temperature and salinity data collected during the 2019 SCALE Winter Cruise. DOI: 10.5281/ZENODO.6997449.

Nomura, D., Sahashi, R., Takahashi, K.D., Makabe, R., Ito, M., Tozawa, M., Wongpan, P., Matsuda, R., et al. 2023. Biogeochemical characteristics of brash sea ice and icebergs during summer and autumn in the Indian sector of the Southern Ocean. *Progress in Oceanography*. 214:103023. DOI: 10.1016/J.POCEAN.2023.103023.

OSI SAF. 2021. DOI: 10.15770/EUM_SAF_OSI_NRT_2007.

OSIL. 2020. *Guideline Portasal Salinometer*. (Report). Available: https://osil.com/product/portasal-salinometer-8410a/.

Papadimitriou, S., Thomas, D.N., Kennedy, H., Haas, C., Kuosa, H., Krell, A. & Dieckmann, G.S. 2007. Biogeochemical composition of natural sea ice brines from the Weddell Sea during early austral summer. *Wiley Online Library*. 52(5):1809–1823. DOI: 10.4319/lo.2007.52.5.1809.

Perovich, D.K., Elder, B.C., Claffey, K.J., Stammerjohn, S., Smith, R., Ackley, S.F., Krouse, H.R. & Gow, A.J. 2004. Winter sea-ice properties in Marguerite Bay, Antarctica. *Deep Sea Research Part II: Topical Studies in Oceanography*. 51(17–19):2023–2039. DOI: 10.1016/J.DSR2.2004.07.024.

Petrich, C. & Eicken, H. 2016. Overview of sea ice growth and properties. *Sea Ice: Third Edition*. (November):1–41. DOI: 10.1002/9781118778371.CH1.

Priscu, J.C., Downes, M.T., Priscu, L.R., Palmisano, A.C. & Sullivan, C.W. 1990. Dynamics of ammonium oxidizer activity and nitrous oxide (N2O) within and beneath Antarctic sea ice. *Marine ecology progress series*. 62:37–46.

Qi, H., Coplen, T.B., Geilmann, H., Brand, W.A. & Böhlke, J.K. 2003. Two new organic reference materials for δ13C and δ15N measurements and a new value for the δ13C of NBS 22 oil. *Rapid Communications in Mass Spectrometry*. 17(22):2483–2487. DOI: 10.1002/RCM.1219.

Rafter, P.A., Difiore, P.J. & Sigman, D.M. 2013. Coupled nitrate nitrogen and oxygen isotopes and organic matter remineralization in the Southern and Pacific Oceans. *Journal of Geophysical Research: Oceans*. 118(10):4781–4794. DOI: 10.1002/JGRC.20316.

Rau, G.H., Sullivan, C.W. & Gordon, L.I. 1991. δ13C and δ15N variations in Weddell Sea particulate organic matter. *Marine Chemistry*. 35(1–4):355–369. DOI: 10.1016/S0304-4203(09)90028-7.

Riaux-Gobin, C., Tréguer, P., Dieckmann, G., Maria, E., Vétion, G. & Poulin, M. 2005. Land-fast ice off Adélie Land (Antarctica): short-term variations in nutrients and chlorophyll just before ice break-up. *Journal of Marine Systems*. 55(3–4):235–248. DOI: 10.1016/J.JMARSYS.2004.08.003.

Roukaerts, A., Cavagna, A.J., Fripiat, F., Lannuzel, D., Meiners, K.M. & Dehairs, F. 2016. Sea-ice algal primary production and nitrogen uptake rates off East Antarctica. *Deep Sea Research Part II: Topical Studies in Oceanography*. 131:140–149. DOI: 10.1016/J.DSR2.2015.08.007.

Roukaerts, A., Deman, F., Van der Linden, F., Carnat, G., Bratkic, A., Moreau, S., Lannuzel, D., Dehairs, F., et al. 2021. The biogeochemical role of a microbial biofilm in sea ice: Antarctic landfast sea ice as a case study. *Elementa: Science of the Anthropocene*. 9(1):00134. DOI: 10.1525/elementa.2020.00134.

Ryan-Keogh, T. & Vichi, M. 2022. *SCALE-WIN19 & SCALE-SPR19 Cruise Report*. University of Cape Town.

Rysgaard, S. & Glud, R.N. 2004. Anaerobic N2 production in Arctic sea ice. *Limnology and Oceanography*. 49(1):86–94. DOI: 10.4319/lo.2004.49.1.0086.

Semtner, A.J. 1976. A Model for the Thermodynamic Growth of Sea Ice in Numerical Investigations of Climate in: Journal of Physical Oceanography Volume 6 Issue 3 (1976). *Journal of Physical Oceanography*. 6(3):379–389.

Shepherd, A., Fricker, H.A. & Farrell, S.L. 2018. Trends and connections across the Antarctic cryosphere. *Nature 2018 558:7709*. 558(7709):223–232. DOI: 10.1038/s41586-018-0171-6.

Shiozaki, T., Fujiwara, A., Inomura, K., Hirose, Y., Hashihama, F. & Harada, N. 2020. Biological nitrogen fixation detected under Antarctic sea ice. *Nature Geoscience*. 13(11):729–732. DOI: 10.1038/s41561-020-00651-7.

Sigman, D.M. & Fripiat, F. 2019. Nitrogen Isotopes in the Ocean. *Encyclopedia of Ocean Sciences, Third Edition: Volume 1-5*. 1–5:263–278. DOI: 10.1016/B978-0-12-409548-9.11605-7.

Sigman, D.M., Altabet, M.A., Mccorkle, D.C., Francois, • R. & Fischer, G. 2000. The d15N of nitrate in the Southern Ocean: Nitrogen cycling and circulation in the ocean interior. *JOURNAL OF GEOPHYSICAL RESEARCH*. 105(C8):599–618. DOI: 10.1029/2000JC000265.

Sigman, D.M., Casciotti, K.L., Andreani, M., Barford, C., Galanter, M. & Böhlke, J.K. 2001. A bacterial method for the nitrogen isotopic analysis of nitrate in seawater and freshwater. *Analytical Chemistry*. 73(17):4145–4153. DOI: 10.1021/AC010088E/ASSET/IMAGES/LARGE/AC010088EF00006.JPEG.

Sigman, D.M., DiFiore, P.J., Hain, M.P., Deutsch, C., Wang, Y., Karl, D.M., Knapp, A.N., Lehmann, M.F., et al. 2009. The dual isotopes of deep nitrate as a constraint on the cycle and budget of oceanic fixed nitrogen. *Deep Sea Research Part I: Oceanographic Research Papers*. 56(9):1419–1439. DOI: 10.1016/j.dsr.2009.04.007.

Sigman, O.M., Altabet, M.A., McCorkle, D.C., Francois, R. & Fischer, G. 1999. The δ15N of nitrate in the southern ocean: Consumption of nitrate in surface waters. *Global Biogeochemical Cycles*. 13(4):1149–1166. DOI: 10.1029/1999GB900038.

Skatulla, S., Audh, R.R., Cook, A., Hepworth, E., Johnson, S., Lupascu, D.C., MacHutchon, K., Marquart, R., et al. 2022. Physical and mechanical properties of winter first-year ice in the Antarctic marginal ice zone along the Good Hope Line. *Cryosphere*. 16(7):2899–2925. DOI: 10.5194/TC-16-2899-2022.

Smart, S.M., Fawcett, S.E., Thomalla, S.J., Weigand, M.A., Reason, C.J.C. & Sigman, D.M. 2015. Isotopic evidence for nitrification in the Antarctic winter mixed layer. *Global Biogeochemical Cycles*. 29(4):427–445. DOI: 10.1002/2014GB005013.

Smith, R.E.H., Harrison, W.G., Harris, L.R. & Herman, A.W. 2011. Vertical Fine Structure of Particulate Matter and Nutrients in Sea Ice of the High Arctic. *https://doi.org/10.1139/f90-154*. 47(7):1348–1355. DOI: 10.1139/F90-154.

Spindler, M. 1990. A comparison of Arctic and Antarctic sea ice and the effects of different properties on sea ice biota. *Geological history of the polar oceans: Arctic versus Antarctic*. 173–186. DOI: 10.1007/978-94-009-2029-3_10/COVER.

Spindler, M. 1994. Notes on the biology of sea ice in the Arctic and Antarctic. *Polar Biology*. 14(5):319–324. DOI: 10.1007/BF00238447.

Spreen, G., Kaleschke, L. & Heygster, G. 2008. Sea ice remote sensing using AMSR-E 89-GHz channels. *Journal of Geophysical Research: Oceans*. 113(C2):2–03. DOI: 10.1029/2005JC003384.

Stefan, J. 1891. Ober die Theorie der Eisbildung.

Swadling, K.M., Constable, A.J., Fraser, A.D., Massom, R.A., Borup, M.D., Ghigliotti, L., Granata, A., Guglielmo, L., et al. 2023. Biological responses to change in Antarctic sea ice habitats. *Frontiers in Ecology and Evolution*. 10:1073823. DOI: 10.3389/FEVO.2022.1073823/BIBTEX.

Tang, S., Qin, D., Ren, J., Kang, J. & Li, Z. 2007. Structure, salinity and isotopic composition of multi-year landfast sea ice in Nella Fjord, Antarctica. *Cold Regions Science and Technology*. 49(2):170–177. DOI: 10.1016/j.coldregions.2007.03.005.

Tedesco, L. & Vichi, M. 2010. DOI: 10.2139/ssrn.1633366.

Tedesco, L. & Vichi, M. 2014. Sea Ice Biogeochemistry: A Guide for Modellers. *PLOS ONE*. 9(2):e89217. DOI: 10.1371/journal.pone.0089217.

Tedesco, L., Vichi, M., Haapala, J. & Stipa, T. 2009. An enhanced sea-ice thermodynamic model applied to the Baltic Sea. Available: https://helda.helsinki.fi/bitstream/handle/10138/233258/ber14-1-068.pdf?sequence=1.

Tedesco, L., Vichi, M., Haapala, J. & Stipa, T. 2010. A dynamic Biologically Active Layer for numerical studies of the sea ice ecosystem. *Ocean Modelling*. 35(1–2):89–104. DOI: 10.1016/J.OCEMOD.2010.06.008.

Thomas, D.N. 2016. Sea Ice: Third Edition. *Sea Ice: Third Edition*. (November):1–652. DOI: 10.1002/9781118778371.

Tison, J.-L., Worby, A., Delille, B., Brabant, F., Papadimitriou, S., Thomas, D., de Jong, J., Lannuzel, D., et al. 2008. Temporal evolution of decaying summer first-year sea ice in the Western Weddell Sea, Antarctica. *Deep Sea Research Part II: Topical Studies in Oceanography*. 55(8):975–987. DOI: 10.1016/j.dsr2.2007.12.021.

Tison, J.L., Schwegmann, S., Dieckmann, G., Rintala, J.M., Meyer, H., Moreau, S., Vancoppenolle, M., Nomura, D., et al. 2017. Biogeochemical Impact of Snow Cover and Cyclonic Intrusions on the Winter Weddell Sea Ice Pack. *Journal of Geophysical Research: Oceans*. 122(12):9548–9571. DOI: 10.1002/2017JC013288.

Tison, J.-L., Delille, B. & Papadimitriou, S. 2017. Gases in sea ice. In *Sea Ice*. John Wiley & Sons, Ltd. 433–471. DOI: 10.1002/9781118778371.ch18.

Tison, J.L., Maksym, T., Fraser, A.D., of … M.C.-A. & undefined 2020. 2020. Physical and biological properties of early winter Antarctic sea ice in the Ross Sea. *cambridge.org*. DOI: 10.1017/aog.2020.43.

Torstensson, A., Fransson, A., Currie, K., Wulff, A. & Chierici, M. 2018. Microalgal photophysiology and macronutrient distribution in summer sea ice in the Amundsen and Ross Seas, Antarctica. *PLoS ONE*. 13(4). DOI: 10.1371/JOURNAL.PONE.0195587.

Toyota, T., Haas, C. & Tamura, T. 2011. Size distribution and shape properties of relatively small sea-ice floes in the Antarctic marginal ice zone in late winter. *Deep Sea Research Part II: Topical Studies in Oceanography*. 58(9–10):1182–1193. DOI: 10.1016/J.DSR2.2010.10.034.

Ugalde, S.C., Westwood, K.J., Enden, R. van den, McMinn, A. & Meiners, K.M. 2016. Characteristics and primary productivity of East Antarctic pack ice during the winter-spring transition. *Deep Sea Research Part II: Topical Studies in Oceanography*. 131:123–139. DOI: 10.1016/J.DSR2.2015.12.013.

Van Oostende, N., Fawcett, S.E., Marconi, D., Lueders-Dumont, J., Sabadel, A.J.M., Woodward, E.M.S., Jönsson, B.F., Sigman, D.M., et al. 2017. Variation of summer phytoplankton community composition and its relationship to nitrate and regenerated nitrogen assimilation across the North Atlantic Ocean. *Deep Sea Research Part I: Oceanographic Research Papers*. 121:79–94. DOI: 10.1016/J.DSR.2016.12.012.

Vancoppenolle, M. & Tedesco, L. 2017. Numerical models of sea ice biogeochemistry. In *Sea Ice*. John Wiley & Sons, Ltd. 492–515. DOI: 10.1002/9781118778371.ch20.

Vancoppenolle, M., Bitz, C.M. & Fichefet, T. 2007. Summer landfast sea ice desalination at Point Barrow, Alaska: Modeling and observations. *Journal of Geophysical Research: Oceans*. 112(C4). DOI: 10.1029/2006JC003493.

Vancoppenolle, M., Goosse, H., Montety, A.D., Fichefet, T., Tremblay, B. & Tison, J.L. 2010. Modeling brine and nutrient dynamics in Antarctic sea ice: The case of dissolved silica. *Journal of Geophysical Research: Oceans*. 115(C2):2005. DOI: 10.1029/2009JC005369.

Vancoppenolle, M., Meiners, K.M., Michel, C., Bopp, L., Brabant, F., Carnat, G., Delille, B., Lannuzel, D., et al. 2013. Role of sea ice in global biogeochemical cycles: emerging views and challenges. *Quaternary Science Reviews*. 79:207–230. DOI: 10.1016/J.QUASCIREV.2013.04.011.

Vichi, M. 2022. An indicator of sea ice variability for the Antarctic marginal ice zone. *tc.copernicus.org*. Available: https://tc.copernicus.org/preprints/tc-2021-307/.

Vichi, M. 2023. *SCALE-WIN22 Cruise Report*. Zenodo. DOI: 10.5281/zenodo.7902557.

Vichi, M., Eayrs, C., Alberello, A., Bekker, A., Bennetts, L., Holland, D., Jong, E. de, Joubert, W., et al. 2019. Effects of an Explosive Polar Cyclone Crossing the Antarctic Marginal Ice Zone. *Geophysical Research Letters*. 46(11):5948–5958. DOI: 10.1029/2019GL082457.

Vichi, M., Lovato, T., Butenschön, M., Tedesco, L., Lazzari, P., Cossarini, G., Masina, S., Pinardi, N., et al. 2020. *The Biogeochemical Flux Model (BFM): Equation Description and User Manual. BFM version 5.2. BFM Report series N. 1, Release 1.2, June 2020*.

de Vos, M., Barnes, M., Biddle, L.C., Swart, S., Ramjukadh, C.L. & Vichi, M. 2022. Evaluating numerical and free-drift forecasts of sea ice drift during a Southern Ocean research expedition: An operational perspective. *Journal of Operational Oceanography*. 15(3):187–203. DOI: 10.1080/1755876X.2021.1883293.

Walker, S.A., Azetsu-Scott, K., Normandeau, C., Kelley, D.E., Friedrich, R., Newton, R., Schlosser, P., Mckay, J.L., et al. 2016. Oxygen isotope measurements of seawater (18O/ 16O): A comparison of cavity ring-down spectroscopy (CRDS) and isotope ratio mass spectrometry (IRMS). *Limnology and Oceanography: Methods*. 14(1):31–38. DOI: 10.1002/LOM3.10067.

Weeks, W.F. 2010. *On Sea Ice*. University of Alaska Press. Available: https://books.google.co.za/books?hl=en&lr=&id=9S55O6WzuL8C&oi=fnd&pg=PR5&dq=weeks+2010+

on+sea+ice&ots=6VI9SCHb7O&sig=HokvCxiEDmoR40Ek1ZcKxv4K8hE&redir_esc=y#v=onepage&q=weeks%202010%20on%20sea%20ice&f=false.

Weeks, W.F. & Ackley, S.F. 1982. Growth, Structure, and Properties of Sea Ice. *CRREL Monograph (US Army Cold Regions Research and Engineering Laboratory)*. 9–164. DOI: 10.1007/978-1-4899-5352-0_2/COVER.

Wei, L. & Qin, T. 2016. Characteristics of cyclone climatology and variability in the Southern Ocean. *Acta Oceanologica Sinica*. 35(7):59–67. DOI: 10.1007/s13131-016-0913-y.

Weigand, M.A., Foriel, J., Barnett, B., Oleynik, S. & Sigman, D.M. 2016. Updates to instrumentation and protocols for isotopic analysis of nitrate by the denitrifier method. *Rapid Communications in Mass Spectrometry*. 30(12):1365–1383. DOI: 10.1002/RCM.7570.

Welschmeyer, N.A. 1994. Fluorometric analysis of chlorophyll a in the presence of chlorophyll b and pheopigments. *Wiley Online Library*. 39(8):1985–1992. DOI: 10.4319/lo.1994.39.8.1985.

Worby, A.P., Jeffries, M.O., Weeks, W.F., Morris, K. & Jaña, R. 1996. The thickness distribution of sea ice and snow cover during late winter in the Bellingshausen and Amundsen Seas, Antarctica. *Journal of Geophysical Research: Oceans*. 101(C12):28441–28455. DOI: 10.1029/96JC02737.

Worby, A.P., Massom, R.A., Allison, I., Lytle, V.I. & Heil, P. 1998. East Antarctic Sea Ice: A Review of Its Structure, Properties and Drift. (March):41–67. DOI: 10.1029/AR074P0041.

Zhou, J., Delille, B., Eicken, H., Vancoppenolle, M., Brabant, F.E.E., Carnat, G., Geilfus, N.-X., Papakyriakou, T., et al. 2013. Physical and biogeochemical properties in landfast sea ice (Barrow, Alaska): Insights on brine and gas dynamics across seasons. *Wiley Online Library*. 118(6):3172–3189. DOI: 10.1002/jgrc.20232.

Zhou, J., Delille, B., Kaartokallio, H., Kattner, G., Kuosa, H., Tison, J.-L., Autio, R., Dieckmann, G.S., et al. 2014. Physical and bacterial controls on inorganic nutrients and dissolved organic carbon during a sea ice growth and decay experiment. *Marine Chemistry*. 166:59–69. DOI: 10.1016/j.marchem.2014.09.013.

Appendix A. Chapter 2

Table A.1. Table of sea-ice core cutting trials using a bandsaw and jigsaw and resulting approximate meltwater volumes.

CUT TYPE	DIAGRAM	APPROXIMATE MELTWATER VOLUME (mL)
	BANDSAW	
Full 5 cm segment	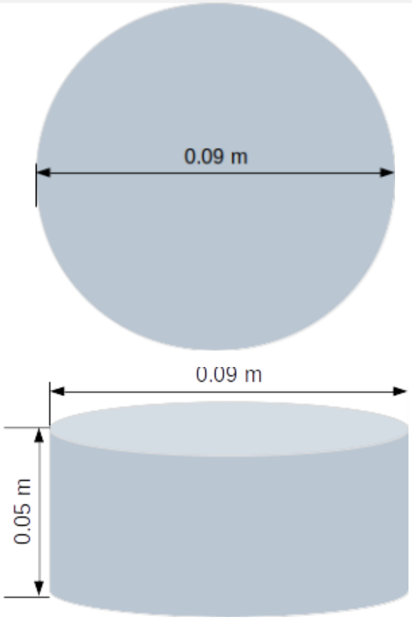	264
Sides only		79

CUT TYPE	DIAGRAM	APPROXIMATE MELTWATER VOLUME (mL)
Inner section	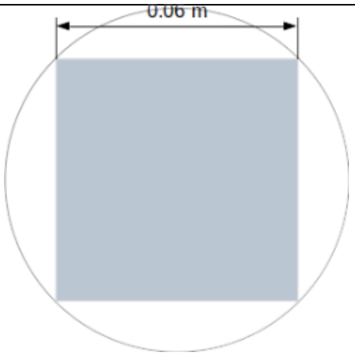	171
	JIGSAW	
Full 5 cm segment	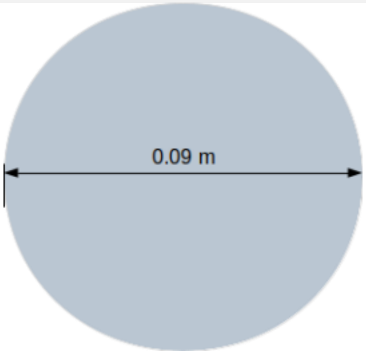 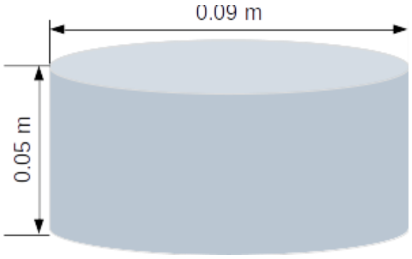	250
Chosen cut: **Split for PON and chlorophyll filtering**	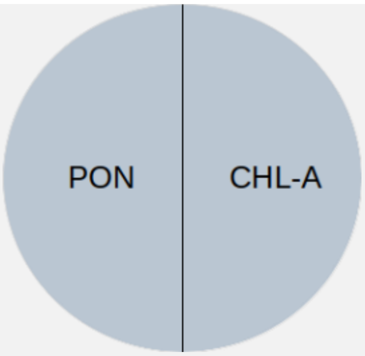	120 per half segment

Table A.2. Table of sea ice meltwater volume requirements for intended biogeochemical analysis.

Test	Volume required (ml)	Sample requirements
Chlorophyll	- Filter corresponding segment and collect filtrate for other tests. - Volume calculated by weight of beaker.	0.3 µm combusted GF/F filters
PON	- Filter corresponding segment and collect filtrate for other tests. - Volume calculated by weight of beaker	0.3 µm combusted GF/F filters
Nutrients (excluding $\mathbf{NH_4^+}$)	30	Duplicate nutrients 2x 15 mL tubes by autoanalyser
$\mathbf{NH_4^+}$	40	Duplicate NH_4^+ in aged HDPE bottles - 20 mL each
Nitrate isotopes	45	1 HDPE bottle
DON	45	1 HDPE bottle
Oxygen isotopes	20	1 glass exetainer vial
Total volume required (mL)	180	Remainder used for rinsing

Appendix B. Chapter 4

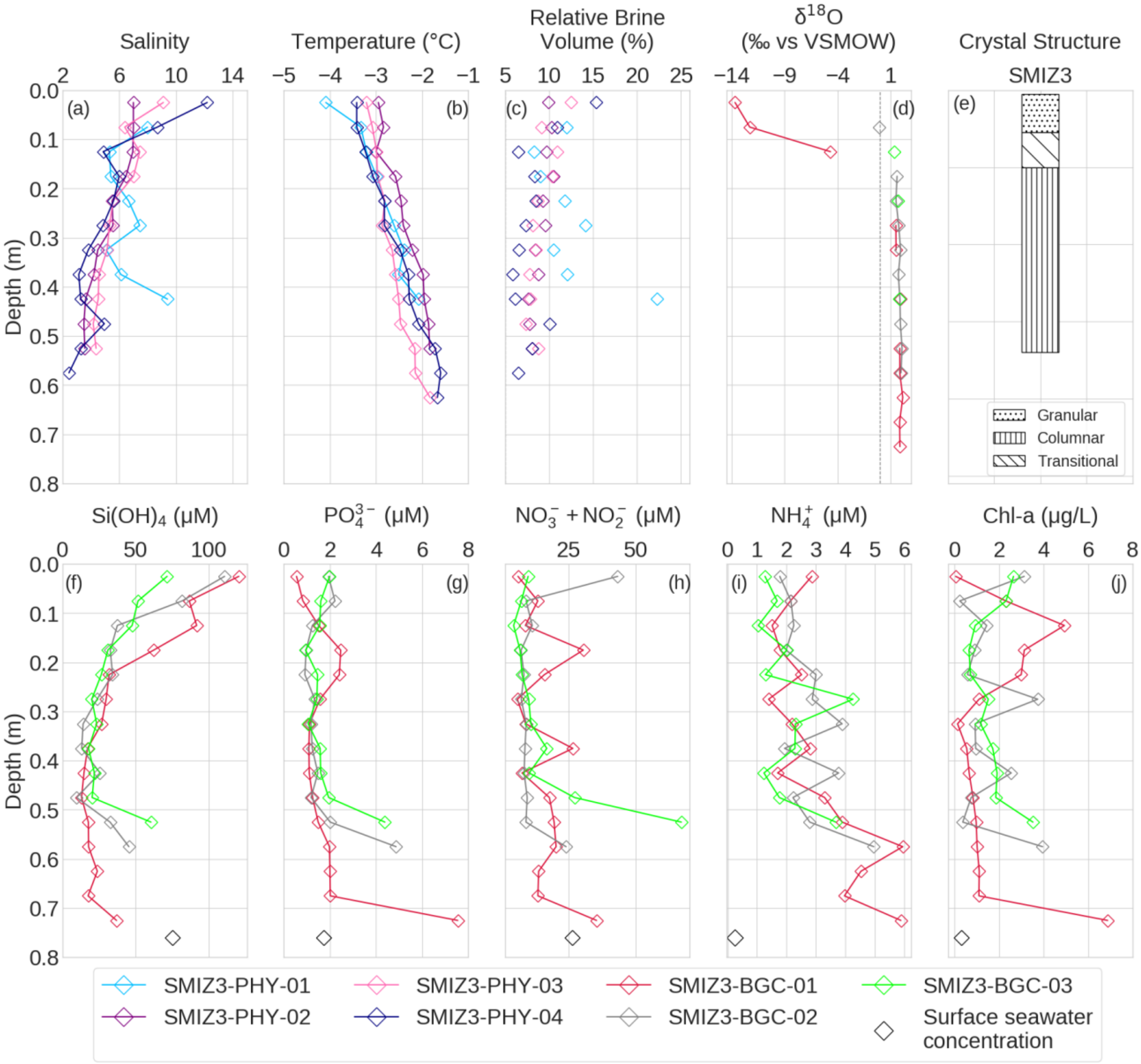

Figure B.1. (a) salinity, (b) temperature, (c) δ^{18}O (incomplete dataset), (d) crystal structure, (e-h) salinity normalised nutrients, (i) chlorophyll data for the sea-ice cores from SMIZ3. Open symbols at the bottom of plots e-i indicate the surface seawater concentrations.

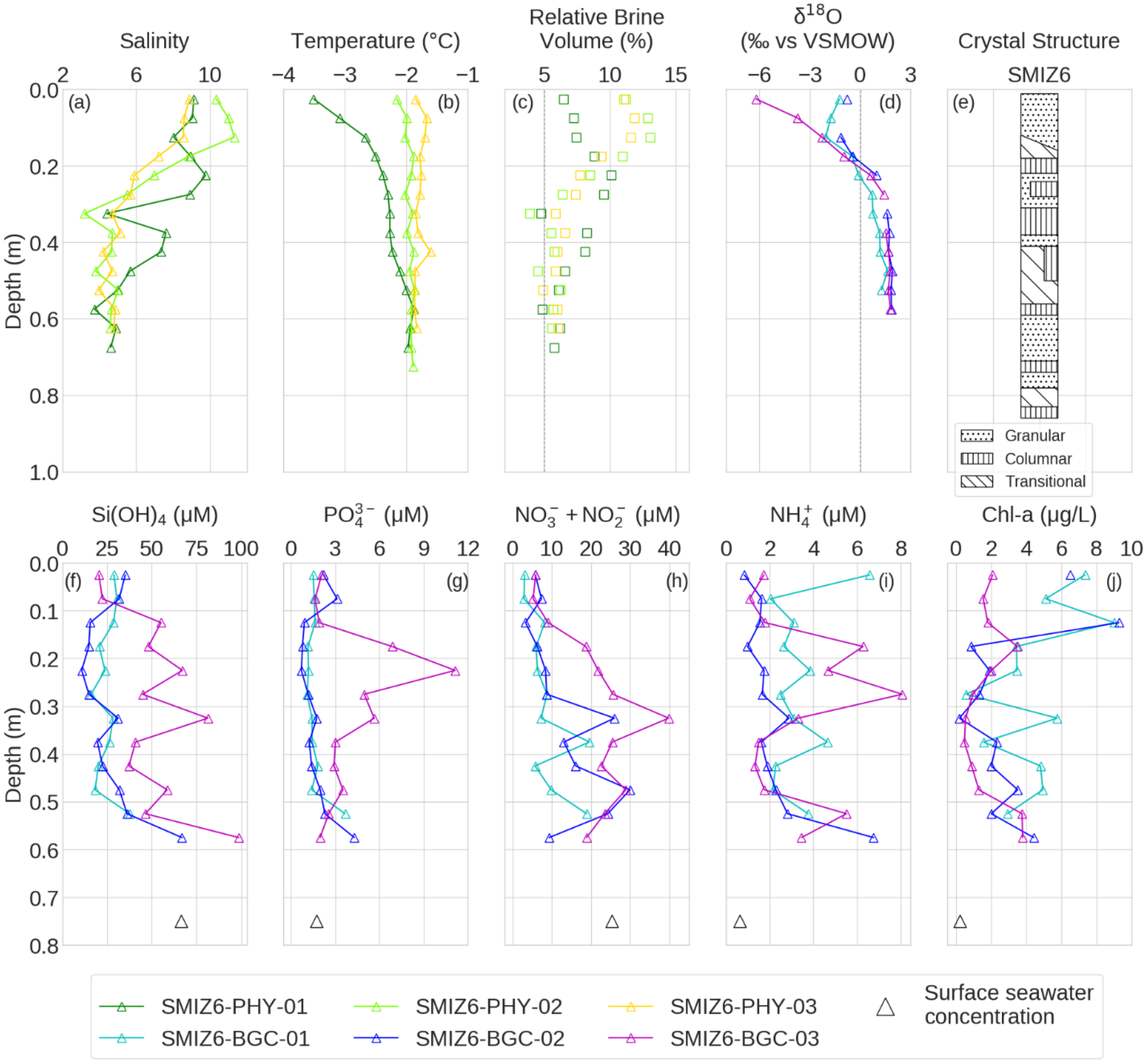

Figure B.2. (a) salinity, (b) temperature, (c) δ^{18}O (incomplete dataset), (d) crystal structure, (e-h) salinity normalised nutrients, (i) chlorophyll data for the sea-ice cores from SMIZ6. Open symbols at the bottom of plots e-i indicate the surface seawater concentrations.

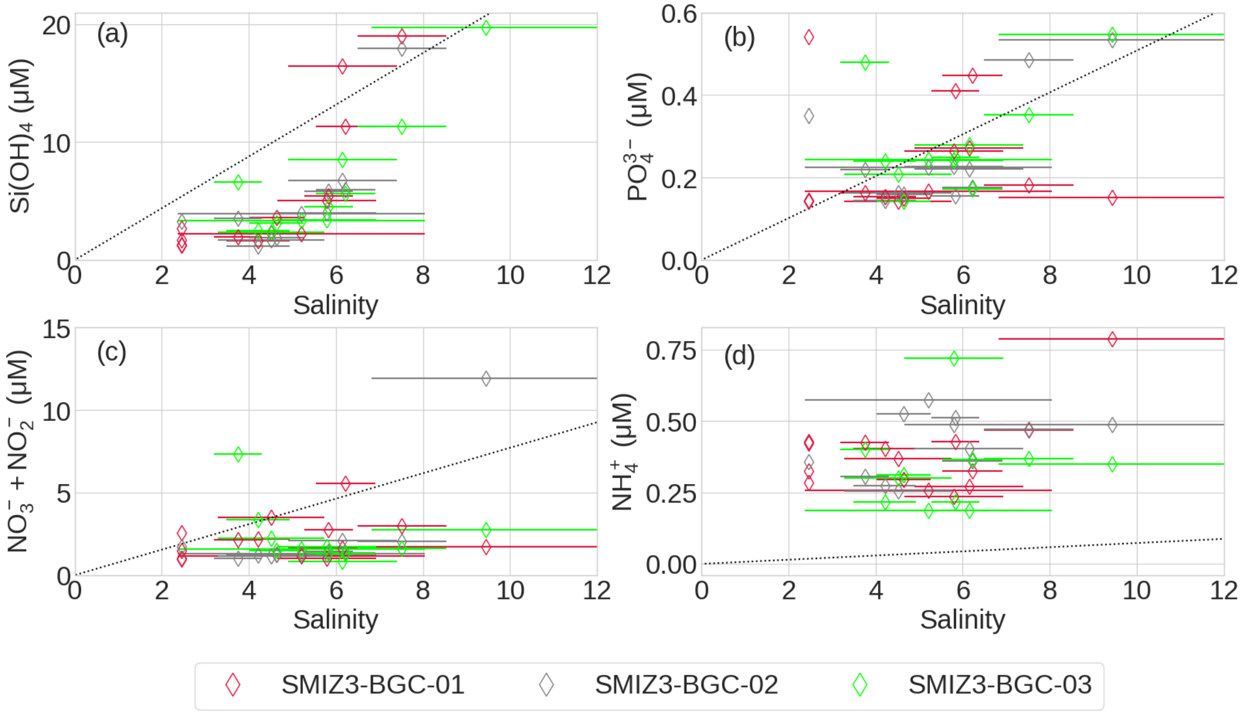

Figure B.3. Bulk nutrient concentrations (i.e., not salinity-normalised) as a function of salinity in the sea-ice cores from SMIZ3 (the colors correspond to the vertical profiles presented in Figure B.1). The dotted black line indicates the theoretical dilution line (TDL) derived from surface seawater nutrient concentrations and sea-ice salinity measurements. The bulk measured nutrient concentration for each ice section is plotted against the average bulk salinity per depth interval measured for the physical cores (Figure B.1a), with the error bars representing the standard deviation of the average salinity at each depth corresponding to a nutrient measurement for the three cores analyzed per station.

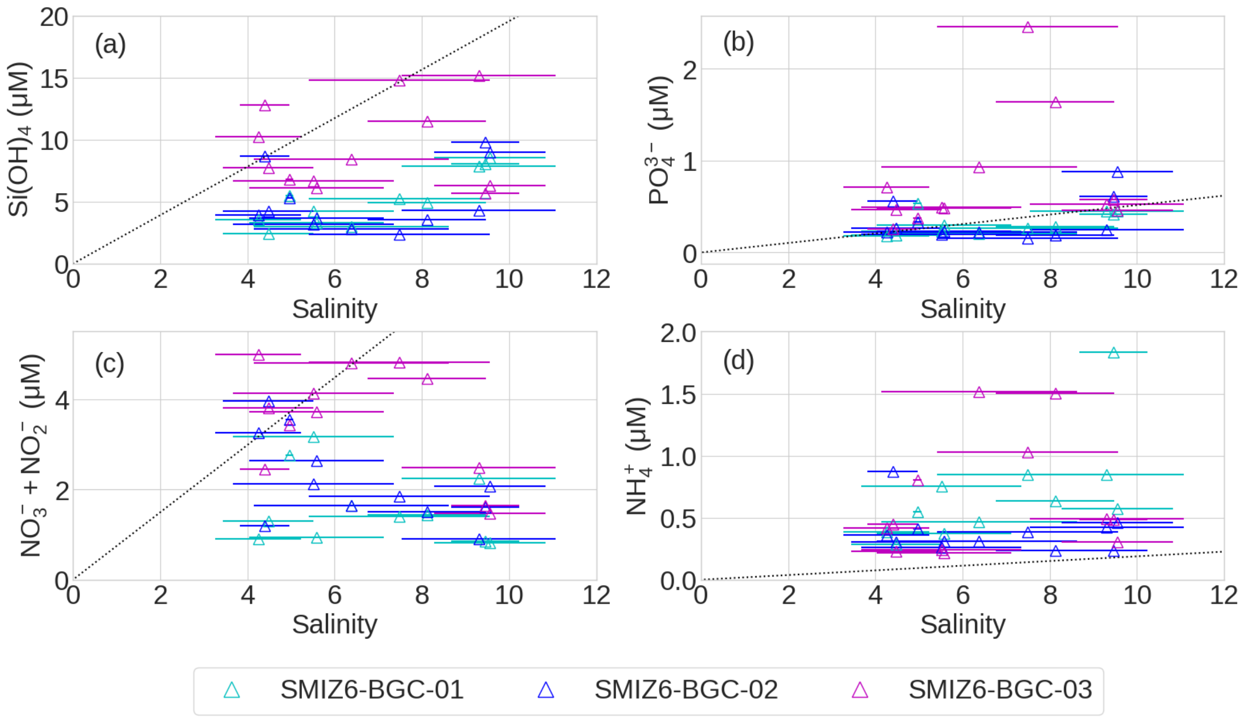

Figure B.4. Bulk nutrient concentrations (i.e., not salinity-normalised) as a function of salinity in the sea-ice cores from SMIZ6 (the colors correspond to the vertical profiles presented in Figure B.2). The dotted black line indicates the theoretical dilution line (TDL) derived from surface seawater nutrient concentrations and sea-ice salinity measurements. The bulk measured nutrient concentration for each ice section is plotted against the average bulk salinity per depth interval measured for the physical cores (Figure B.2a), with the error bars representing the standard deviation of the average salinity at each depth corresponding to a nutrient measurement for the three cores analyzed per station.

Appendix C.Chapter 5

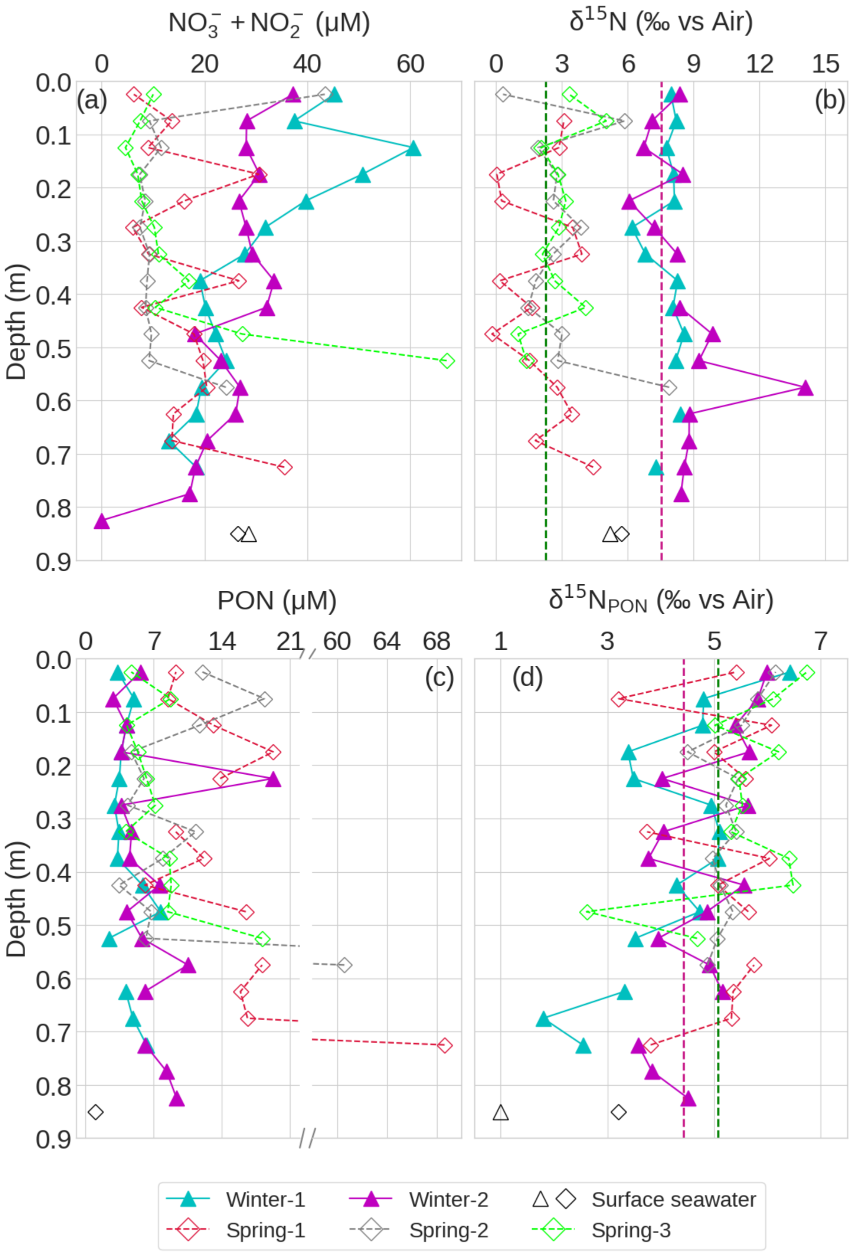

Figure C.1. Vertical profiles of (a) salinity normalised $NO_3^- + NO_2^-$ and corresponding (b) $\delta^{15}N_{NO_3^-}$; (c) salinity normalised PON (note the break in the x-axis to accommodate higher concentrations) and corresponding (d) $\delta^{15}N_{PON}$ from winter 2019 (triangle symbols) and spring 2019 (diamond symbols). The open black symbols below the profiles indicate the respective surface seawater values (symbols correspond to the profiles). Note the discontinuous profiles in (b) which resulted from a delay in sample analysis. Vertical dashed lines in (b) and (d) indicate the average $\delta^{15}N$ values for the winter sea ice (red line) and spring sea ice (green line).

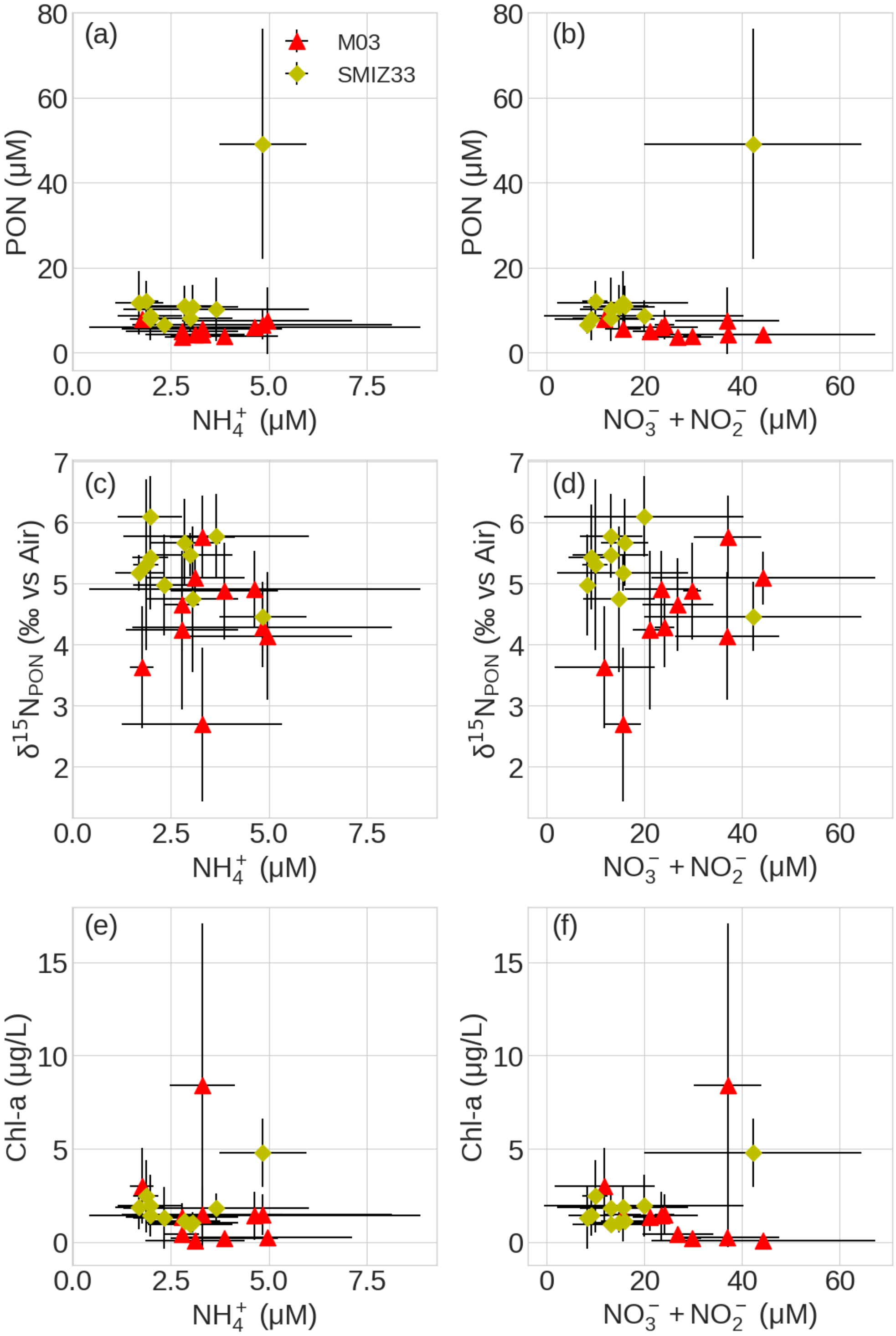

Figure C.2. Average salinity normalised [NH_4^+] vs (a) [PON], (c) $\delta^{15}N_{PON}$, (e) [chlorophyll] and $NO_3^- + NO_2^-$ vs (b) [PON], (d) $\delta^{15}N_{PON}$, (f) [chlorophyll] for the winter sea ice (red triangles) and spring sea ice (green diamonds). Error bars for both variables per panel correspond to the standard deviation in the average for the sea ice data per depth bin.

Appendix D.Chapter 6

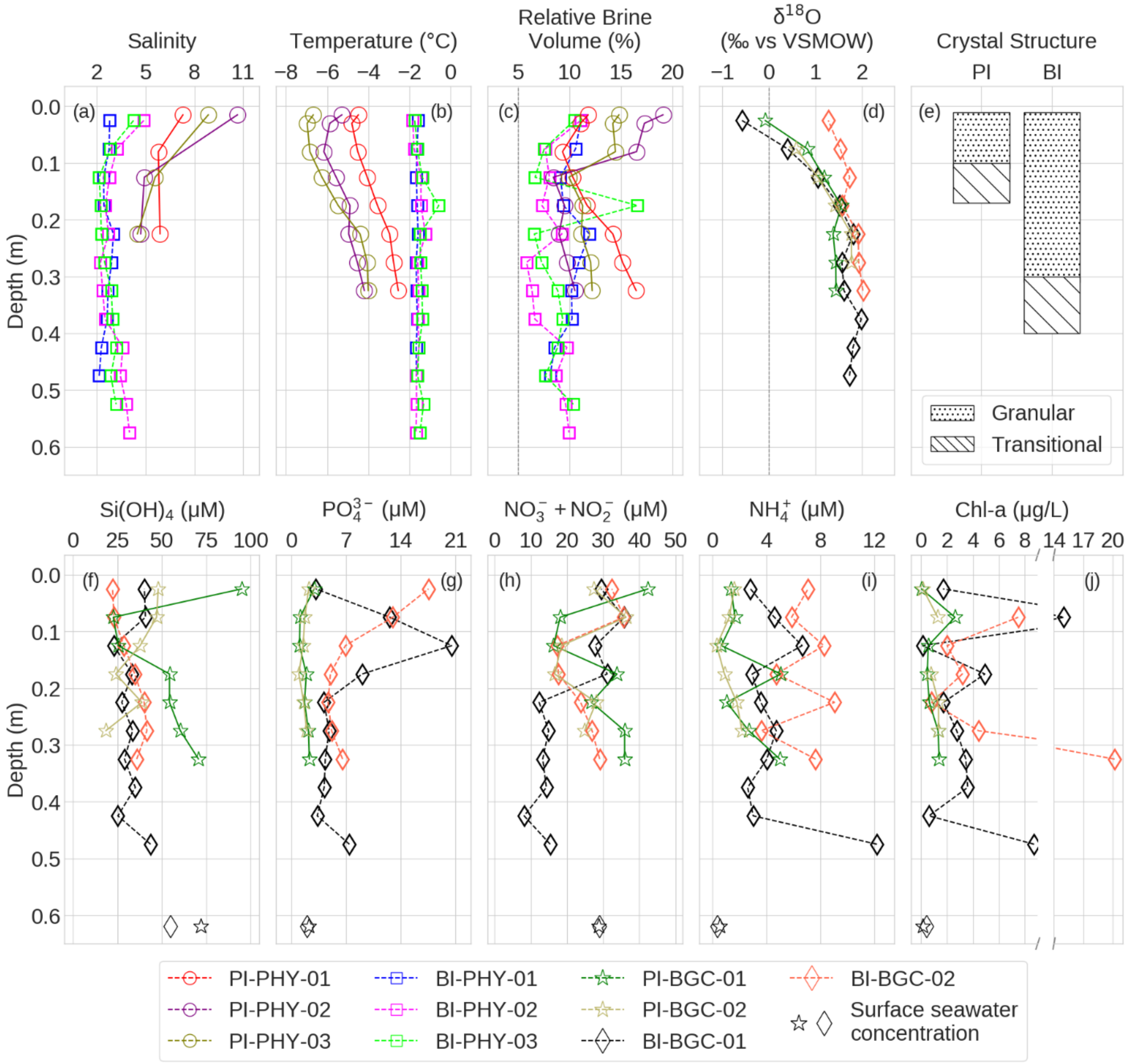

Figure D.1. True depth vertical profiles of (a) salinity, (b) temperature, (c) relative brine volume, (d) δ^{18}O, (e) crystal structure, (f-i) salinity normalised nutrients, (j) chlorophyll data for all the sea-ice cores from both ice types. Open symbols at the bottom of plots f-j indicate the surface seawater concentrations. Pancake ice (PI) cores are represented by solid lines and brash ice (BI) cores are represented by dashed lines. Profile colours correspond to Figure 6.4.

End